

MICROSTRUCTURAL EVOLUTION AND MECHANICAL  
PROPERTIES OF ULTRA-FINE GRAINED TUBULAR  
COMPONENTS PROCESSED BY SEVERE PLASTIC  
DEFORMATION

MOHSEN MESBAH

FACULTY OF ENGINEERING  
UNIVERSITY OF MALAYA  
KUALA LUMPUR

2020

**MICROSTRUCTURAL EVOLUTION AND  
MECHANICAL PROPERTIES OF ULTRA-FINE  
GRAINED TUBULAR COMPONENTS PROCESSED BY  
SEVERE PLASTIC DEFORMATION**

**MOHSEN MESBAH**

**THESIS SUBMITTED IN PARTIAL FULFILMENT OF  
THE REQUIREMENTS FOR THE DEGREE OF DOCTOR  
OF PHILOSOPHY**

**FACULTY OF ENGINEERING  
UNIVERSITY OF MALAYA  
KUALA LUMPUR**

**2020**

**UNIVERSITY OF MALAYA**  
**ORIGINAL LITERARY WORK DECLARATION**

Name of Candidate: **MOHSEN MESBAH**

Matric No: **KHA130081**

Name of Degree: **DOCTOR OF PHILOSOPHY**

Title of Thesis: **MICROSTRUCTURAL EVOLUTION AND MECHANICAL PROPERTIES OF ULTRA-FINE GRAINED TUBULAR COMPONENTS PROCESSED BY SEVERE PLASTIC DEFORMATION**

Field of Study: **MANUFACTURING PROCESSES**

I do solemnly and sincerely declare that:

- (1) I am the sole author/writer of this Work;
- (2) This Work is original;
- (3) Any use of any work in which copyright exists was done by way of fair dealing and for permitted purposes and any excerpt or extract from, or reference to or reproduction of any copyright work has been disclosed expressly and sufficiently and the title of the Work and its authorship have been acknowledged in this Work;
- (4) I do not have any actual knowledge nor do I ought reasonably to know that the making of this work constitutes an infringement of any copyright work;
- (5) I hereby assign all and every rights in the copyright to this Work to the University of Malaya ("UM"), who henceforth shall be owner of the copyright in this Work and that any reproduction or use in any form or by any means whatsoever is prohibited without the written consent of UM having been first had and obtained;
- (6) I am fully aware that if in the course of making this work I have infringed any copyright whether intentionally or otherwise, I may be subject to legal action or any other action as may be determined by UM.

Candidate's Signature

Date:

Subscribed and solemnly declared before,

Witness's Signature

Date:

Name:

Designation:

**MICROSTRUCTURAL EVOLUTION AND MECHANICAL PROPERTIES OF  
ULTRA-FINE GRAINED TUBULAR COMPONENTS PROCESSED BY  
SEVERE PLASTIC DEFORMATION**

**ABSTRACT**

The lightweight alloys have been widely used in various engineering applications such as automotive, aerospace, construction, and biomedical industries due to their low densities, high ductility, formability, and facile machining. However, the emerging trend for materials with high mechanical strength and plasticity hampers the widespread application of these alloys. Over the last two decades, severe plastic deformation (SPD) has been introduced as a promising approach for enhancement of the mechanical performance of the lightweight alloys through microstructural manipulations and grain refinement. However, the SPD techniques have been extensively utilized for the fabrication of non-tubular geometries and the studies on the manufacturing of ultra-fine-grained tubular components using SPD methods are scarce. The present research aims to study the microstructural evolution and mechanical properties of Al-1060, Brass70/30, ZK60, and WE43 Mg alloys processed by different SPD methods including tubular channel angular pressing (TCAP) and parallel tubular channel angular pressing (PTCAP). Accordingly, the main objective of this study is to investigate the possibility of fabricating ultrafine-grained (UFG) alloys via TCAP and PCAP techniques and explore the effects of the number of passes on microstructural evolution and mechanical properties of the SPD-processed alloys as compared with the as-received counterparts. Several characterization techniques, such as X-ray diffraction (XRD) analysis, optical microscope (OM), scanning electron microscope (SEM) combined with energy-dispersive X-ray spectroscopy (EDS), electron back-scattered diffraction (EBSD), transmission electron microscopy (TEM), and mechanical tests were employed to investigate the

microstructural and mechanical characteristics of UFG alloys. The obtained results confirmed the formation of homogeneous UFG structures with the minimum number of passes of 1 for Al and brass, as well as 3 for ZK60 and WE43. The minimum mean grain sizes obtained in TCAP-processed Al, as well as PTCAP-processed brass, ZK60 and WE43 were 0.48  $\mu\text{m}$ , 0.59  $\mu\text{m}$ , 0.9  $\mu\text{m}$ , and 2.2  $\mu\text{m}$  respectively. It was proposed that dynamic recrystallization as well as breaking and distributing of the precipitates at the newly-formed grains were the dominant phenomena after the SPD processes. The X-ray diffraction (XRD) profiles also confirmed the significant effect of the number of SPD passes on the microstructural characteristics of all four studied alloys. In terms of the mechanical properties, the hardness of the processed tubes increased and reached a maximum by increasing the number of SPD passes. The different SPD processes enhanced not only strength but also the ductility of the tubular component due to the simultaneous fine grain strengthening mechanism and homogeneous distribution of the intercomponent metallics in the alloy matrix. As a conclusion, the studied SPD processes exhibited significant potentials to generate UFG structures, leading to enhanced mechanical properties in the Al-1060, Brass70/30, ZK60, and WE43 Mg alloys.

Keywords: Severe plastic deformation; Ultrafine-grained alloys; Intermetallic compounds; Microstructure; Mechanical properties.

**EVOLUSI MIKROSTRUKTUR DAN SIFAT MEKANIKAL KOMPONEN TIUB  
BERBUTIR TERSANGAT HALUS MELALUI PROSES UBAH BENTUK  
PLASTIK KETERLALUAN**

**ABSTRAK**

Aloi ringan telah digunakan secara meluas dalam pelbagai aplikasi kejuruteraan seperti industri automotif, aeroangkasa, pembinaan, dan bioperubatan disebabkan oleh kepadatannya yang rendah, kemuluran tinggi, kebolehbentukan, dan pemesinan yang mudah. Walau bagaimanapun, trend yang muncul untuk bahan yang mempunyai kekuatan mekanikal dan keplastikan yang tinggi menghalang penggunaan aloi ini secara meluas. Sejak lebih dua dekad yang lalu, ubah bentuk plastik keterlaluan (SPD) telah diperkenalkan sebagai pendekatan yang menjanjikan untuk meningkatkan prestasi mekanikal aloi ringan melalui manipulasi mikrostruktur dan penghalusan butiran. Walau bagaimanapun, teknik SPD telah digunakan secara meluas untuk fabrikasi geometri bukan tiub dan kajian mengenai pembuatan komponen tiub ultra-halus menggunakan kaedah SPD adalah terhad. Penyelidikan ini menggunakan teknik SPD dalam penghasilan tiub berbutir tersangat halus (UFG). Penyelidikan ini bertujuan untuk mengkaji evolusi mikrostruktur dan sifat-sifat mekanikal aloi Al-1060, Brass70/30, ZK60, and WE43 Mg yang diproses oleh teknik SPD yang berbeza termasuklah pemampatan sudut saluran tiub (TCAP) dan pemampatan selari sudut saluran tiub (PTCAP). Oleh sebab itu, objektif utama kajian ini adalah untuk mengkaji kemungkinan fabrikasi UFG melalui teknik-teknik TCAP dan PTCAP dan meneroka kesan bilangan pasang pada evolusi mikrostruktur dan sifat-sifat mekanik aloi yang diproses oleh SPD berbanding dengan bahan yang tersedia. Beberapa teknik pencirian, seperti analisa pembelauan sinar-X (XRD), mikroskop optik (OM), pengimbasan mikroskop elektron (SEM) yang digabungkan dengan spektroskopi tenaga serakan (EDS), pembelauan balik serakan

elektron (EBSD), mikroskop elektron (TEM), dan ujian-ujian mekanikal telah digunakan. Hasil yang diperolehi mengesahkan pembentukan struktur UFG yang homogen dengan bilangan pas minimum 1 untuk Al dan tembaga, serta 3 untuk ZK60 dan WE43. Saiz minimum purata butiran yang diperolehi bagi Al yang diproses oleh TCAP, serta tembaga yang diproses PTCAP, ZK60 dan WE43 masing-masing 0.48  $\mu\text{m}$ , serta 0.59  $\mu\text{m}$ , 0.9  $\mu\text{m}$ , dan 2.2  $\mu\text{m}$ . Adalah dicadangkan bahawa pengkristalan semula secara dinamik serta pemecahan dan pengedaran mendakan pada butiran baru yang terbentuk adalah fenomena dominan selepas proses SPD. Profil pada XRD mengesahkan kepentingan kesan bilangan SPD pas keatas ciri-ciri mikrostruktur untuk semua aloi yang dikaji. Dari segi sifat mekanikal, kekerasan tiub yang diproses meningkat dan mencapai maksimum dengan meningkatkan bilangan pas SPD. Proses SPD yang berbeza tidak hanya mempertingkatkan kekuatan tetapi juga kemuluran komponen tiub kerana mekanisme pengukuhan serentak butiran halus dan pengedaran homogen antara komponen bahan logam dalam matriks aloi. Sebagai kesimpulan, proses SPD yang dikaji mempamerkan potensi yang penting untuk menghasilkan struktur UFG, yang menampilkan peningkatan sifat-sifat mekanikal dalam aloi-aloi Al-1060, Brass70/30, ZK60, dan WE43.

Keywords: Ubah bentuk plastik keterlaluan; Aloii berbutir tersangat halus; Sebatian antara logam; Mikrostruktur; Sifat mekanikal.

## ACKNOWLEDGEMENTS

First and foremost, I would like to express my sincere gratitude to my supervisors Prof. Datin Ir. Dr. Bushroa Binti Abdul Razak and Prof. Dr. Ghader Faraji for their encouragement, support, and guidance throughout my Ph.D. study. They have helped me in my research, creating environments for me to extend my potentials, and providing all kinds of opportunities for me to develop my academic capabilities. My thanks also extend to my colleagues and friends at the Centre of Advanced Manufacturing & Materials Processing (AMMP Centre), University of Malaya. Special thanks to the founder and current advisor of the AMMP, Prof. Ir. Dr. Mohd Hamdi Bin Abd Shukor for his invaluable advice.

It is my pleasure to acknowledge the significant help and beneficial discussions compassionately provided by Dr. Bahman Nasiri-Tabrizi in different stages of my research. I would like to thank WinTech Nano-technology Services (Singapore) for their outstanding transmission electron microscope (TEM) work, Dr. Mahmoud Ardakani at the Department of Materials, Faculty of Engineering, Imperial College London and also Hi-Tech Instruments Sdn Bhd. for performing precise EBSD analysis.

Most importantly, none of this would have been possible without the love of my family. I would like to present this achievement as a gift to my mother and father. It is their everlasting love, unconditional support, and understanding that strengthened my determination in pursuing this degree. Thank you both for giving me the strength to reach for the stars and chase my dreams. This research was fully funded by the Ministry of Higher Education (MOHE) and also Ministry of Science, Technology and Innovation (MOSTI), Malaysia with the high impact research (HIR) grant number of UM.C/625/1/HIR/MOHE/ENG/27 and the e-Science Fund grant number of 03-01-03-SF0788 respectively.

## TABLE OF CONTENTS

Abstract .....	iii
Abstrak .....	v
Acknowledgements .....	vii
Table of Contents .....	viii
List of Figures .....	xiv
List of Tables.....	xxi
List of Symbols and Abbreviations.....	xxii
<b>CHAPTER 1: INTRODUCTION.....</b>	<b>1</b>
1.1 Background .....	1
1.2 Problem Statement .....	3
1.3 Aim and Objectives.....	4
1.4 Scope of the Thesis .....	5
1.5 Thesis Outline .....	5
<b>CHAPTER 2: LITERATURE REVIEW.....</b>	<b>7</b>
2.1 Introduction.....	7
2.2 Severe Plastic Deformation (SPD) Methods for Tubular Components .....	8
2.2.1 Definition and History .....	9
2.2.2 SPD Modes.....	11
2.2.3 Grain Refinement Mechanism.....	14
2.3 Tubular Channel Angular Pressing (TCAP) and Process Parameters .....	15
2.3.1 Principles of TCAP .....	16
2.3.2 Effects of Channel Angle .....	19
2.3.3 Effects of Curvature Angle.....	23

2.3.4 Effects of the Deformation Ratio .....	26
2.3.5 Properties and Applications.....	28
2.3.6 TCAP-processed Metals and Alloys .....	30
2.3.6.1 Microstructural evolution and mechanical properties of magnesium-based alloys.....	30
(a) AZ91 magnesium alloy .....	30
(b) AZ31C magnesium alloy .....	34
2.3.6.2 Microstructural and mechanical properties of commercially pure copper	36
2.4 Parallel Tubular Channel Angular Channel (PTCAP) and Process Parameters .....	36
2.4.1 Principles of PTCAP .....	37
2.4.2 Effects of Channel Angle .....	39
2.4.3 Effects of Curvature Angle.....	44
2.4.4 Effects of the Deformation Ratio .....	46
2.4.5 Properties and Applications.....	49
2.4.6 PTCAP-processed Metals and Alloys .....	50
2.4.6.1 Microstructural and mechanical properties of magnesium-based alloys...	50
(a) AZ31 Magnesium alloy .....	50
(b) AZ91 Magnesium alloy.....	56
2.4.6.2 Microstructural and mechanical properties of aluminum-based alloys .....	58
(a) AA 5083 Aluminium alloy .....	58
(b) 6061 Aluminium alloy .....	59
(c) 7075 Aluminium alloy.....	61
2.4.6.3 Microstructural and mechanical properties of copper-based alloys .....	66
(a) Pure copper .....	66
(b) Cu–Zn Brass alloy .....	68
2.5 Summary of Literature Review .....	70

<b>CHAPTER 3: RESEARCH METHODOLOGY .....</b>	<b>71</b>
3.1 Materials.....	72
3.2 TCAP Processing .....	72
3.3 PTCAP Processing.....	74
3.4 Characterization Techniques.....	76
3.4.1 Physical and Structural Assessment.....	77
3.4.1.1 Phase analysis .....	77
3.4.1.2 Lattice constant and unit cell volume .....	77
3.4.1.3 Crystallite size ( $D$ ) and micro-strain ( $\eta$ ).....	78
3.4.1.4 Volume fraction of the grain boundary ( $f$ ).....	79
3.4.1.5 Defect density ( $D_d$ ) .....	79
3.4.2 Microstructural evolution analysis .....	80
3.4.2.1 Optical microscopy.....	80
3.4.2.2 Scanning electron microscopy (SEM) and energy-dispersive x-ray spectroscopy (EDS).....	81
3.4.2.3 Transmission electron microscopy (TEM).....	81
3.4.2.4 Electron backscattered diffraction (EBSD) .....	81
3.4.3 Mechanical Investigations.....	82
3.4.3.1 Vickers' Microhardness test .....	82
3.4.3.2 Stress-strain test.....	83
3.4.3.3 Nanoindentation test .....	83
<b>CHAPTER 4: RESULTS AND DISCUSSION .....</b>	<b>85</b>
4.1 Structural, Morphological and Mechanical Properties of UFG Al-1060 Tube Processed by TCAP.....	85
4.1.1 Phase Composition and Interplanar Spacing.....	85
4.1.2 Structural Features.....	87

4.1.2.1 Lattice constants and unit cell volume.....	88
4.1.2.2 Crystallite size and micro-strain .....	88
4.1.2.3 Volume fraction of the grain boundary .....	89
4.1.2.4 Defect and dislocation density.....	90
4.1.3 Microstructural Evolution Analysis .....	92
4.1.3.1 TEM analysis .....	92
4.1.3.2 EBSD Analysis .....	98
4.1.4 Mechanical Properties .....	102
4.1.4.1 Vickers microhardness.....	102
4.1.4.2 Stress-strain curve.....	103
4.1.4.3 Nanomechanical behaviour .....	104
4.2 Structural, Morphological and Mechanical Properties of 70cu-30zn Brass Tube Processed by PTCAP.....	106
4.2.1 Phase Composition and Interplanar Spacing.....	106
4.2.2 Structural Features.....	107
4.2.2.1 Lattice constants and unit cell volume.....	108
4.2.2.2 Crystallite size and micro-strain .....	108
4.2.2.3 Volume fraction of the grain boundary .....	109
4.2.2.4 Defect and dislocation density.....	110
4.2.3 Microstructural Evolution Analysis .....	112
4.2.3.1 Optical microscopy analysis .....	112
4.2.3.2 EBSD Analysis .....	113
4.2.4 Mechanical Properties .....	117
4.2.4.1 Stress-strain curve.....	117
4.2.4.2 Nanomechanical behaviour .....	117

4.3 Structural, Morphological and Mechanical Properties of ZK60 Mg Tube Processed by PTCAP.....	121
4.3.1 Phase Composition and Interplanar Spacing.....	121
4.3.2 Structural Features.....	122
4.3.2.1 Lattice constants and unit cell volume.....	123
4.3.2.2 Crystallite size and micro-strain.....	125
4.3.2.3 Volume fraction of the grain boundary.....	125
4.3.2.4 Defect and dislocation density.....	126
4.3.3 Microstructural Evolution Analysis.....	129
4.3.3.1 Optical microscopy analysis.....	129
4.3.3.2 SEM Analysis.....	133
4.3.4 Mechanical Properties.....	135
4.3.4.1 Vickers microhardness.....	135
4.3.4.2 Stress-strain curve.....	136
4.4 Structural, Morphological and Mechanical Properties of WE43 Mg Tube Processed by PTCAP.....	141
4.4.1 Phase Composition and Interplanar Spacing.....	141
4.4.2 Structural Features.....	143
4.4.2.1 Lattice constants and unit cell volume.....	143
4.4.2.2 Crystallite size and micro-strain.....	144
4.4.2.3 Volume fraction of the grain boundary.....	145
4.4.2.4 Defect and dislocation density.....	146
4.4.3 Microstructural Evolution Analysis.....	149
4.4.3.1 Optical microscopy analysis.....	149
4.4.3.2 SEM Analysis.....	151
4.4.4 Mechanical Properties.....	153

4.4.4.1 Vickers microhardness.....	153
<b>CHAPTER 5: CONCLUSIONS AND SUGGESTIONS FOR FUTURE WORK</b>	<b>156</b>
5.1 Feasibility of Obtaining UFG Structure in TCAP and PTCAP Methods .....	156
5.2 The Effect of Number of Passes on Microstructural Features .....	156
5.2.1 TCAP-processed Al-1060 .....	157
5.2.2 PTCAP-processed Brass70/30 .....	158
5.2.3 PTCAP-processed ZK60 Mg Alloy .....	159
5.2.4 PTCAP-processed WE43 Mg Alloy.....	160
5.3 The Effect of Number of Passes on Mechanical Behaviour .....	162
5.3.1 TCAP-processed Al-1060 .....	162
5.3.2 PTCAP-processed Brass70/30 .....	162
5.3.3 PTCAP-processed ZK60 Mg Alloy .....	163
5.3.4 PTCAP-processed WE43 Mg Alloy.....	163
<b>References .....</b>	<b>165</b>
List of Publications and Papers Presented .....	180
<b>APPENDIX .....</b>	<b>182</b>
Awards .....	182
Filed Patent.....	182
Successful Grant.....	182

## LIST OF FIGURES

<b>Figure 1.1:</b> Flowchart of the research activities.....	6
<b>Figure 2.1:</b> The element distortion in the direction of slip lines: (a) general case; (b) pure; and (c) simple shears as well as (d) Moore’s circles with rotation and (e) in the limit cases of pure and simple shears; $\eta\alpha$ and $\eta\beta$ exhibit the shear rates in the direction of the slip lines (Segal, 2002).....	13
<b>Figure 2.2:</b> Grain refinement mechanisms during SPD processes.....	15
<b>Figure 2.3:</b> (a) A schematic of TCAP and (b) the relevant factors (Mesbah et al., 2014). .....	17
<b>Figure 2.4:</b> (a) Model of Finite Elements and selected nodes from sample cross-section, (b–d) Effective strain contour resulting from finite element simulation within TCAP process with the second channel angle of 120°, 90° and 60°, respectively. (e) The effective strain diagram obtained from the FEM, across the sample thickness for different channel angles (Faraji et al., 2012b).....	20
<b>Figure 2.5:</b> (a-c) Contour of the effective stress dissemination obtained by FEM within TCAP process at various channel angles, and (d) effective stress amount across the tube sample thickness (Faraji et al., 2012b).....	21
<b>Figure 2.6:</b> Calculated pressing load obtained from FEM against ram displacement during TCAP with channel angles of 60°, 90°, and 120° (Faraji et al., 2012b).....	22
<b>Figure 2.7:</b> Impacts of curvature angles on equivalent plastic strain ( $\psi_1 = \psi_3$ ) ( $R/R_0=1.5$ , $\psi_2 = 90^\circ$ ) (Faraji et al., 2012c). ....	23
<b>Figure 2.8:</b> Impacts of curvature angles of $\psi_1 = \psi_3$ on the displacement force diagram obtained by FEM ( $R/R_0= 1.5$ , $\psi_2 = 90^\circ$ ) (Faraji et al., 2012c).....	24
<b>Figure 2.9:</b> (a-d) Effective plastic strain contour resulting from finite element simulation within TCAP process with the second curvature angles of $\psi_2 = 0^\circ, 28^\circ, 67.4^\circ$ and $90^\circ$ (e) Diagram of effective strain along the tube sample for different curvature angles (Faraji et al., 2012c).....	25
<b>Figure 2.10:</b> Influence of second curvature angle on the required loads in TCAP process ( $\psi_1 = \psi_3 = 0$ , $R/R_0= 1.2$ ) (Faraji et al., 2012c). ....	26

<b>Figure 2.11:</b> (a-c) The Effective plastic strain contour resulting from FEM, at diverse deformation ratios of 1.2, 1.5 and 1.8; (d) Path plots of equivalent plastic strain along the thickness at deformation ratios of 1.2, 1.5 and 1.8 (Faraji et al., 2012c).....	27
<b>Figure 2.12:</b> Influence of deformation ratio on the force-displacement diagram using FEM in comparison with experimental results (Faraji et al., 2012c).....	28
<b>Figure 2.13:</b> (a) An AZ91 specimen in the TCAP procedure, (b) optical images of the unprocessed body (a; initial $\alpha$ -Mg, b; eutectic $\alpha$ -Mg, c; $\beta$ ( $Mg_{17}Al_{12}$ )), (c) and (d) distinctive micro configurations of one-pass TCAP processed alloy; (e) microhardness values in the dissimilar sites and (f) microhardness against distance from TCAP treated tube end (Faraji et al., 2011c). ....	32
<b>Figure 2.14:</b> An AZ31C workpiece (a) before and (b) after TCAP along with the (c) tensile test sample; optical micrographs of the (d) unprocessed and processed samples after (e) one, (f) two, (g) three, and (h) four pass as well as mechanical behaviour as a function of the number of passes: (i) microhardness values, (j) elongation to failure, (k) $\sigma_{YS}$ , and (l) $\sigma_{UTS}$ (Mohammadi et al., 2015). ....	35
<b>Figure 2.15:</b> Schematic diagram of the PTCAP procedure (a) primary state, (b) the first and (c) second half-cycles as well as (d) die factors; schematic of the hybrid procedure, including (e) first and (f) second half-cycles of PTCAP.....	38
<b>Figure 2.16:</b> Influence of the channel angle on effective strain contour obtained by finite element method after (a) the first half pass, (b) the second half pass (Faraji & Mosavi Mashhadi, 2013b).....	40
<b>Figure 2.17:</b> Diagrams of strain values along the thickness of the sample at different channel angles obtained by the finite element method end of the second half pass (Faraji et al., 2013b).....	42
<b>Figure 2.18:</b> Effect of channel angle on the mean strain value and strain inhomogeneity index (Faraji et al., 2013b). ....	42
<b>Figure 2.19:</b> (a) The influence of channel angle on the force-displacement diagram in the PTCAP process (b) effect of the channel angle on the maximum force obtained by the finite element method.....	43
<b>Figure 2.20:</b> The impacts of curvature angle $\psi_1 = \psi_2$ on the imposed plastic strain through tube thickness. (Faraji et al., 2013b). ....	44
<b>Figure 2.21:</b> Impacts of the curvature angle on the mean strain and strain inhomogeneity index (Faraji et al., 2013b). ....	45
<b>Figure 2.22:</b> FE calculated load-displacement curves in different curvature angles (Faraji et al., 2013b).....	46

<b>Figure 2.23:</b> The effect of (K) value on the strain value through the PTCAP processed tube thickness (Faraji et al., 2013b).....	46
<b>Figure 2.24:</b> Effect of K value on the mean strain and strain inhomogeneity index (Faraji et al., 2013b).....	47
<b>Figure 2.25:</b> Effect of K value on (a) load-displacement curve and (b) the peak required load (Faraji et al., 2013b).....	48
<b>Figure 2.26:</b> Optical micrographs of the (a) unprocessed and (b) one, (c) two, and (d) three-pass PTCAP treated bodies as well as (e) a schematic view of the microstructural modification of AZ31 during PTCAP; (f) Engineering stress-strain plots of unprocessed, multi-pass processed specimens examined at 400° C and (g) two-pass PTCAP treated tube at a range of temperatures between 350° C and 450° C (Fata et al., 2016, 2017b).	51
<b>Figure 2.27:</b> Engineering stress-strain plots of AZ31 Mg tubes at (a) room temperature and (b) 400° C as well as (c) the feature of fractured samples following the tensile test. (Fata et al., 2017a).....	53
<b>Figure 2.28:</b> Optical images of AZ91 Mg alloys: (a) unprocessed, (b) 0P+TBE, (c) one pass, (d) 1P+TBE, (e) two-pass, (f) 2P+TBE, (g) three pass and (h) 3P+TBE processed tubes; true stress against true strain plots for the processed specimens compared to unprocessed sample: (i) one pass and 1P+TBE, (j) two-pass and 2P+TBE and (k) three pass and 3P+TBE samples as well as (l) $\sigma_{Yield}$ , $\sigma_{UTS}$ and elongation variations of the samples (Abdolvand et al., 2017b).....	57
<b>Figure 2.29:</b> Optical micrographs (a) annealed material, (b) PTCAP-processed AA aluminium 5083 alloy in the peripheral direction and (c) axial direction as well as the mechanical properties of (d) the annealed coarse-grained and (e) PTCAP-processed UFG tubes in axial and peripheral directions and (f) microhardness vs. distance in annealed and PTCAP-processed tube along axial and peripheral directions.....	59
<b>Figure 2.30:</b> The EBSD orientation imaging map (OIM) patterns, pole figures, and inverse pole figures, as well as boundary maps of (a,b) two and (c,d) four-pass PTCAP, processed specimen; (e) $\sigma_{Yield}$ , $\sigma_{UTS}$ , elongation and (f) microhardness of the processed tubes against PTCAP pass number (Faraji et al., 2015).....	61
<b>Figure 2.31:</b> Optical images of the PTCAP-processed alloy at 610° C in various circumstances; (a,c,e) one-pass for 5, 10 and 15 min, (b,d,f) two-pass for 5, 10 and 15 min (Meshkabadi et al., 2017).....	63
<b>Figure 2.32:</b> Optical micrographs of the two-pass PTCAP-processed specimens following reheating for 10 min at different temperatures of (a) 610, (b) 615, (c) 620 and (d) 625° C (Meshkabadi et al., 2017).....	64
<b>Figure 2.33:</b> Schematic view of the coarsening mechanism in PTCAP-processed specimens in the semi-solid zone (Meshkabadi et al., 2017).....	65

<b>Figure 2.34:</b> (a) The dislocation densities and (b) microhardness against equivalent plastic strain (compared to previous results) of the PTCAP processed tubes in terms of pass number, and bright-field TEM micrographs of the cross-sectional area of PTCAP processed tube after (c,f) one, (d,g) two, and (e,h) three-pass PTCAP procedure (Faraji et al., 2013a).....	67
<b>Figure 2.35:</b> (a) Deformed shapes of tube samples following quasi-static crushing test, which shows dissimilar deformation modes; (b) $\{1\ 1\ 1\}$ pole figures of the heat-treated and PTCAP processed specimens in the (b1,b2) axial and (b3,b4) circumferential directions, respectively; (c) force-displacement plots attained from axial compression tests and (d) total absorbed energy of heat-treated and PTCAP processed tubes (Afrasiab et al., 2014; Tavakkoli et al., 2015). .....	69
<b>Figure 3.1:</b> Flowchart of methodology. ....	71
<b>Figure 3.2:</b> (a) A schematic illustration of the TCAP process, (b) related parameters of the die, and (c) the experimental TCAP setup. ....	73
<b>Figure 3.3:</b> The schematic view of (a) primary state, (b) the first, (c) the second half-cycles of PTCAP, (d) die parameters, (e) utilized PTCAP die with its components, and (f) the experimental setup.....	74
<b>Figure 3.4:</b> (a) The exploded view drawing of PTCAP die, and (b) the exploded view of PTCAP manufactured die parts.....	76
<b>Figure 3.5:</b> The schematic of the employed techniques for characterization of the microstructural features of the processed tubes. ....	80
<b>Figure 3.6:</b> The schematic of the utilized techniques to assess the mechanical performance of the processed tubes. ....	82
<b>Figure 4.1:</b> XRD profiles of Al-1060 alloy (a) before and after (b) one, (c) two and (d) three TCAP passes as well as (e) the effect of strain on the direction of XRD patterns and (f) magnified XRD profiles in the range of $30^\circ \leq 2\theta \leq 50^\circ$ . ....	86
<b>Figure 4.2:</b> (a) Crystallite size ( $D$ ), (b) micro-strain ( $\eta$ ), (c) volume fraction of the grain boundary ( $f$ ), (d) defect density ( $D_d$ ), and (e) dislocation density ( $\rho$ ) of Al-1060 alloy prior to and after one, two and three TCAP passes.....	91
<b>Figure 4.3:</b> Different methods for strengthening Al-based alloys. ....	92
<b>Figure 4.4:</b> Bright (a, d, g) and dark (b, e, h) field TEM images and (c, f, i) grain size dispersal histogram of the cross-sectional micro configuration of the TCAP treated Al-1060 tubes following one, two and three passes. ....	94
<b>Figure 4.5:</b> TEM micrographs of the TCAP treated Al-1060 tubes following (a,b) one, (c,d) two and (e,f) three passes, demonstrating dislocations piled up to form subgrain	

boundary and higher magnification of dislocations in subgrain boundary (showed by red arrows)..... 96

**Figure 4.6:** The effect of the number of TCAP passes on grain size and grain shape factor of Al-1060 alloy..... 98

**Figure 4.7:** EBSD colour maps, boundary maps, pole figures, and grain diameter distributions obtained from the centre zone of the TCAP bodies exposed to (a-c, n) 0, (d-f, o) 1, (g-i, p) 2 and (j-l, q) 3 passes. Colour code utilized to clarify the crystallographic orientations on a standard stereographic projection (red: (0 0 1); blue: (1 1 1); green: (1 0 1)); (m) Schematic drawing of the tube coordinates system and position of the measured element by EBSD analysis..... 99

**Figure 4.8:** Distributions of the boundary misorientation angle acquired from the EBSD information of (a) unprocessed, (b) 1, (c) 2, and (d) 3 passes processed samples..... 101

**Figure 4.9:** (a) Microhardness of the processed tubes as well as (b) schematic of ring compression test and (b) true stress-strain curve of the unprocessed and processed Al-1060 tube through 1–3 passes TCAP resulted from tube compression tests. .... 103

**Figure 4.10:** (a) Typical load-penetration depth curves and (b) the module of elasticity of the unprocessed and TCAP processed samples. .... 105

**Figure 4.11:** (a) XRD patterns of 70Cu-30Zn brass alloy prior to and after one, two and three PTCAP passes and (b) magnified XRD patterns in the range of  $42^\circ \leq 2\theta \leq 52^\circ$ . .... 107

**Figure 4.12:** (a) Crystallite size ( $D$ ), (b) micro-strain ( $\eta$ ), (c) volume fraction of the grain boundary ( $f$ ), (d) defect density ( $D_d$ ), and (e) dislocation density ( $\rho$ ) of 70Cu-30Zn brass alloy before and after one, two and three PTCAP passes. .... 110

**Figure 4.13:** (a) Constitutional diagram of the Cu-Zn alloys and (b) solid-solution strengthening of 70Cu-30Zn brass alloy..... 112

**Figure 4.14:** OM images, EBSD orientation imaging map patterns and their corresponding boundary map as well as histograms for grain size distributions of the 70Cu-30Zn brass tube (a) before and after (b, d, e, h) first and (c, f, g, i) third passes of PTCAP. .... 115

**Figure 4.15:** The histograms of misorientation angle distribution after (a) first and (b) third pass of PTCAP. .... 116

**Figure 4.16:** (a) Tensile test location in the schematic view in the axial direction and (b) tensile engineering stress-strain curve of the 70Cu-30Zn brass tube before and after the first and third pass of PTCAP. .... 117

<b>Figure 4.17:</b> 3D SPM images of the indentation holes made in 70Cu-30Zn brass tube (a) before and after (b) first and (c) third pass of PTCAP as well as (d) the horizontal sections of the indentation hole at the Centre of the samples and (e) typical load-indentation depth curves. ....	119
<b>Figure 4.18:</b> (a) XRD profiles of ZK60 Mg alloy before and after one, two and three PTCAP passes as well as (b) the effect of strain on the direction of XRD patterns and magnified XRD profiles in the range of $30^\circ \leq 2\theta \leq 40^\circ$ . ....	121
<b>Figure 4.19:</b> (a) Crystallite size ( $D$ ), (b) micro-strain ( $\eta$ ), (c) volume fraction of the grain boundary ( $f$ ), (d) defect density ( $D_d$ ), and (e) dislocation density ( $\rho$ ) of ZK60 Mg alloy before and after one, two and three PTCAP passes. ....	126
<b>Figure 4.20:</b> Different methods for strengthening Mg-based alloys. ....	128
<b>Figure 4.21:</b> Optical micrographs of ZK60 Mg alloy perpendicular to the extrusion direction (a) before and after (b) one, (c) two and (d) three passes of PTCAP. ....	131
<b>Figure 4.22:</b> Comparing the number of PTCAP passes and the grain size achieved in different Mg alloys between the current study and the previous studies (Fata et al., 2017a; Fata et al., 2017b). ....	132
<b>Figure 4.23:</b> (a) “NavCam” image for macro navigation and SEM/EDS images of (b) as-received ZK60 Mg alloy (c) the processed tube perpendicular to the extrusion direction after third pass of PTCAP and (d) the EDX point analysis. ....	134
<b>Figure 4.24:</b> (a) Vickers microhardness values across the wall thickness of the as-received and PTCAP- processed tubes and (b) the average values of Vickers microhardness for each sample (c) compared to previous studies (Abdolvand et al., 2017b; Eftekhari et al., 2018; Faraji et al., 2017; Fata et al., 2017a; Fata et al., 2017b). ....	135
<b>Figure 4.25:</b> (a) Engineering stress–engineering strain curves for ZK60 Mg tube in the initial and PTCAP-processed conditions and (b) the strength variations of various Mg alloys processed by TCAP and PTCAP processes as well as (c) FI for the processed ZK60 (d) compared to previous studies (Abdolvand et al., 2017b; Eftekhari et al., 2018; Faraji et al., 2017; Fata et al., 2017a; Fata et al., 2017b). ....	137
<b>Figure 4.26:</b> XRD patterns of WE43 Mg alloy (a) before and after one, two and three PTCAP pass as well as (b) the influence of strain on the direction of XRD profiles and (f) magnified XRD reflections in the range of $30^\circ \leq 2\theta \leq 40^\circ$ . ....	141
<b>Figure 4.27:</b> (a) Crystallite size ( $D$ ), (b) micro-strain ( $\eta$ ), (c) volume fraction of the grain boundary ( $f$ ), (d) defect density ( $D_d$ ), and (e) dislocation density ( $\rho$ ) of WE43 Mg alloy before and after one, two and three PTCAP passes. ....	146

**Figure 4.28:** The dynamic dissolution of second-phase particles within the matrix in WE43 Mg alloy. .... 148

**Figure 4.29:** Optical micrographs of WE43 Mg alloy perpendicular to the extrusion direction (a) before and after (b) one, (c) two and (d,e) three passes of PTCAP..... 150

**Figure 4.30:** SEM micrographs and EDX spectra of the WE43 Mg alloy (a,b) prior to and (c,d) following three PTCAP passes. .... 152

**Figure 4.31:** (a) Vickers microhardness values along the thickness and (b) engineering stress–engineering strain curves for WE43 Mg tube before and after one, two and three passes of PTCAP..... 154

Universiti Malaysia

## LIST OF TABLES

<b>Table 2.1:</b> Grain size and ductility of AZ91 alloy at room temperature caused by a variety of SPD methods. ....	34
<b>Table 2.2:</b> A summary of the research findings on the ductility of SPD-processed AZ31. ....	55
<b>Table 3.1:</b> The chemical compositions of Al-1060, Cu-Zn brass, ZK60 Mg, and WE43 Mg Alloys used in this study. The values are reported in %wt.....	72
<b>Table 3.2:</b> TCAP die parameters and their values.....	73
<b>Table 3.3:</b> PTCAP Die parameters and their values.....	73
<b>Table 4.1:</b> Peak list of Al-1060 alloy before and after different TCAP passes.....	87
<b>Table 4.2:</b> Lattice constants and unit cell volume of unprocessed and TCAP-processed Al-1060. ....	88
<b>Table 4.3:</b> Lattice parameters and unit cell volume of the unprocessed and PTCAP-processed 70Cu-30Zn brass alloy. ....	108
<b>Table 4.4:</b> The mean values of the elastic modulus and hardness of the samples. ....	120
<b>Table 4.5:</b> Peak list of ZK60 Mg alloy before and after different PTCAP passes.....	123
<b>Table 4.6:</b> Lattice constants, unit cell volume and lattice mismatch of the unprocessed and PTCAP-processed ZK60 Mg alloy.....	124
<b>Table 4.7:</b> The tensile test results of ZK60 Mg alloy after PTCAP process compared to different thermo-mechanical processes (Dumitru et al., 2014; Fouad et al., 2011; He et al., 2010; Mostaed et al., 2014; Müller et al., 2009; Nový et al., 2009; Orlov et al., 2011; Shahzad et al., 2007; Shahzad et al., 2009; Vinogradov, 2017; Vinogradov et al., 2012). ....	140
<b>Table 4.8:</b> Peak list of WE43 Mg alloy before and after different PTCAP passes. ....	142
<b>Table 4.9:</b> Lattice constants, unit cell volume and lattice mismatch of the unprocessed and PTCAP-processed WE43 Mg alloy.....	143

## LIST OF SYMBOLS AND ABBREVIATIONS

<b>AFM</b>	Atomic Force Microscopy
<b>ARB</b>	ARB Accumulative Roll Bonding
<b>ASB</b>	Accumulative Spin-Bonding
<b>CEC</b>	Cyclic Extrusion Compression
<b>CFC</b>	Cyclic Flaring and Sinking
<b>CG</b>	Coarse-Grained
<b>CP</b>	Commercial Pure
<b>CR</b>	Cold Rolling
<b>D</b>	crystallite size
<b>D<sub>d</sub></b>	defect density
<b>d</b>	Grain size
<b>E</b>	Young modulus
<b>EBSD</b>	Electron Back-Scatter Diffraction
<b>ECAE</b>	Equal Channel Angular Extrusion
<b>ECAP</b>	Equal-Channel Angular Pressing
<b>ED</b>	Extrusion Direction
<b>EDM</b>	Electrical discharge machining
<b>EDS</b>	Energy Dispersive X-Ray Spectroscopy
<b>EPS</b>	Equivalent Plastic Strain
<b>FCC</b>	Face-Centred Cubic
<b>FEA</b>	Finite Element Analysis
<b>FEM</b>	Finite Element Method
<b>FESEM</b>	Field Emission Scanning Electron Microscopy
<b>FIB</b>	Focused Ion Beam
<b>(FWHM)</b>	The full width at half maximum
<b>FSW</b>	Friction Stir Welding
<b>GBS</b>	Grain Boundary Sliding
<b>GND</b>	Geometrically Necessary Dislocation
<b>GSF</b>	Grain Shape Factor
<b>HAGBs</b>	High-Angle Grain Boundaries
<b>HCP</b>	Hexagonal Close-Packed
<b>HPT</b>	High-Pressure Torsion
<b>HPTT</b>	High-Pressure Tube Twisting
<b>HV</b>	Vickers hardness

<b>IMCs</b>	Intermetallic compounds
<b><math>k_y</math></b>	The strengthening coefficient
<b>LAGBs</b>	Low-Angle Grain Boundaries
<b>LPSO</b>	Long Period Stacking Order
<b>MAF</b>	Multiaxial Forging
<b>MEMS</b>	Microelectromechanical Systems
<b>ND</b>	Normal Direction
<b>OM</b>	Optical Microscope
<b>PTCAP</b>	Parallel Tubular Channel Angular Pressing
<b>RC</b>	Repetitive corrugation
<b>RPTS</b>	Rubber Pad Tube Straining
<b>SEM</b>	Scanning Electron Microscope
<b>SPD</b>	Severe Plastic Deformation
<b>TCAP</b>	Tubular Channel Angular Pressing
<b>TCEE</b>	Tube Cyclic Expansion Extrusion
<b>TE</b>	Twist Extrusion
<b>TEM</b>	Transmission Electron Microscopy
<b>TCEC</b>	Tube Cyclic Extrusion Compression
<b>TD</b>	Transverse Direction
<b>UFG</b>	Ultrafine-Grained
<b>UTS</b>	Ultimate Tensile Strength
<b>XRD</b>	X-Ray Diffraction
<b><math>f</math></b>	Volume fraction of the grain boundary
<b><math>f_F</math></b>	Friction force
<b><math>f_N</math></b>	Normal force
<b><math>\delta</math></b>	Elongation to failure
<b><math>\varepsilon</math></b>	True strain
<b><math>\eta</math></b>	Micro-strain
<b><math>\mu</math></b>	Friction coefficient
<b><math>\sigma_0</math></b>	Friction stress
<b><math>\sigma_N</math></b>	Normal stress
<b><math>\sigma_{UTS}</math></b>	Ultimate strength
<b><math>\sigma_{ys}</math></b>	Yield stress
<b><math>\nu</math></b>	Poisson ration
<b><math>\varphi</math></b>	Channel angles
<b><math>\psi</math></b>	Corner angles

## CHAPTER 1: INTRODUCTION

### 1.1 Background

Lightweight metals such as aluminum (Al), magnesium (Mg), copper (Cu), and their alloys are desirable materials for use in different industries due to their lower density, high strength to weight, and durability. However, the sole usage of these materials in mass production is not cost-effective owing to the relatively lower strength, which requires costly alloying elements or energy-consuming heat treatments (Taban et al., 2010). Hence, the necessity for proposing new methods to enhance mechanical properties, including yield stress, tensile strength, and ductility is indispensable (Hirsch & Al-Samman, 2013).

Severe plastic deformation (SPD) has been widely studied over the last two decades as an effective approach to produce ultrafine-grained (UFG) lightweight metals and alloys with superior structural and mechanical properties. SPD refers to various metal forming procedures that apply extremely high strains, leading to exceptional refinement of grains (Verlinden, 2018). A negligible alteration in the overall dimensions of the workpiece is the unique feature of SPD processing. In this metalworking technique, a large strain could be applied by repeating the SPD processing. Retainment of the workpiece shape is another characteristic of the SPD techniques, which is obtained through the utilization of special tool geometries that prevent the free flow of the material and thereby produce significant hydrostatic pressure.

A number of SPD technologies such as equal channel angular pressing (ECAP) (Dyakonov et al., 2019), high-pressure torsion (HPT) (Edalati, 2019), and accumulative roll bonding (ARB) (Alizadeh & Dashtestaninejad, 2018) have been introduced for

development of varied UFG materials with excellent mechanical properties such as exceptional toughness and superplasticity, as well as electrical and optical properties (Furukawa et al., 2002). The novel and often extraordinary properties provided by SPD-processed materials compared with their conventional counterparts, provide promising potentials for their application in the fabrication of high-precision instruments, microelectromechanical systems (MEMS) (W.J. Kim & Sa, 2006) and biomedical implants (Latysh et al., 2006).

The mechanical properties of all polycrystalline materials are significantly determined by their average grain size ( $d$ ). According to the Hall–Petch equation, the yield stress ( $\sigma_{YS}$ ) is given by:

$$\sigma_{YS} = \sigma_0 + k_y d^{-1/2} \quad (\text{Eq. 1.1})$$

where  $\sigma_0$  is a material constant for the starting stress for dislocation movement (or the lattice resistance to dislocation motion) and  $k_y$  is the strengthening coefficient (a constant specific to each material) (Cordero et al., 2016). Eq. (1.1) indicates that the strength is increased with a reduction in the grain size; thus, superhard materials could be fabricated through the development of extremely small grains in their microstructures.

The grain size of polycrystalline materials also plays a major role in dictating many other critical properties. In particular, smaller grain sizes present higher resistance to plastic flow compared to the coarse-grained counterparts, leading to their higher applicability in superplastic forming operations at elevated temperatures.

This phenomenon has led to the development of UFG and nanostructured materials, defined as polycrystalline materials with  $d$  values of 100 nm to 1  $\mu\text{m}$  and below 100 nm, respectively. However, in order to be defined as bulk UFG materials, some additional requirements such as fairly homogeneous and reasonably equiaxed microstructure as well as grain boundaries with high angles of misorientation are required.

The presence of elevated fractions of high angle grain boundaries is important to achieve advanced and unique mechanical properties (Valiev, 2004).

## 1.2 Problem Statement

Common SPD methods such as equal channel angular pressing (ECAP), high pressure torsion (HPT), and accumulative roll bonding (ARB) are mostly for producing the bulk shape of alloys.

Although lightweight tubular components are widely applicable in many branches of engineering such as aircraft, automotive, cooling towers, pressure vessels, pipelines, and offshore platforms, the production of tubular components with promising mechanical properties remains a primary challenge in material science. To this aim, several SPD processes such as high-pressure tube twisting (HPTT) (Tóth et al., 2009), tube cyclic extrusion compression (TCEC) (Babaei & Mashhadi, 2014a), and stagger spinning (Xia et al., 2014) have been developed to produce UFG structures with tubular geometries.

However, limitations such as low production rates, material inhomogeneity, and complexity of the process have restricted their widespread applicability for mass production. Therefore, the effective fabrication of tubular shaped components has urged industries to solve this issue by developing a new class of SPD processes with the capability of producing tubular UFG alloys including Al, Mg, and Cu-based alloys in various applications, especially in commercial strategy and implementation using higher strain levels.

For this purpose, the tubular channel angular pressing (TCAP) was proposed as a valuable technique for the fabrication of UFG tubes by (Faraji et al., 2011c). With regards to the TCAP capabilities, a parallel tubular-channel angular pressing (PTCAP) method

was also introduced as a new SPD process suitable for fabricating UFG and nanostructured tubes by the same group (Faraji et al., 2012a).

However, to the best of our knowledge, there are no comprehensive experimental outputs on the processing of Al-1060, Cu-Zn Brass, ZK60, and WE43 Mg alloys by the TCAP and PTCAP methods to produce tubular UFG alloys for different engineering applications. This suggests that the possibility assessment of the fabrication of tubular UFG alloys by the proposed SPD processes is a big challenging task that has been considered in the present project.

### 1.3 Aim and Objectives

The present study aims to investigate the microstructural evolution and mechanical properties of Al, Mg, and Cu-based alloys processed by different SPD processes including tubular channel angular pressing (TCAP) and parallel tubular channel angular pressing (PTCAP). To achieve this aim, the following objectives were defined:

1. To determine the minimum number of passes required to obtain UFG structure in Al-1060, Cu70-30Zn Brass, ZK60, and WE43 Mg alloys via TCAP and PTCAP methods.
2. To explore the microstructural features of the processed alloys in terms of alteration in lattice parameters, volume of unit cell, crystallite size ( $D$ ), micro-strain ( $\eta$ ), volume fraction of the grain boundary ( $f$ ), and defect density ( $D_d$ ).
3. To analyze the mechanical behaviour of the processed alloys in terms of microhardness, yield strength ( $\sigma_{YS}$ ), ultimate tensile strength ( $\sigma_{UTS}$ ), and elongation to failure ( $\delta$ ).

## **1.4 Scope of the Thesis**

The present work aspires to incorporate the materials science and mechanical engineering to develop new configurations of Al-1060 alloy, Cu-Zn Brass, ZK60, and WE43 Mg alloys with appropriate microstructural properties and superb mechanical durability. The development of such improved alloys requires the optimization of the processing parameters. The processed specimens need to also be characterized regarding phase and chemical purity, size, and morphology, as well as mechanical strength. Thus, several characterization techniques including X-ray diffractometry (XRD), field emission scanning electron microscopy (FESEM), energy dispersive spectroscopy (EDS), Vickers hardness tester, and tensile test were utilized. It should be noted that the comprehensive nanomechanical assessments by nanoindentation and structural changes by transmission electron microscopy (TEM) and grain misconfiguration by electron backscatter diffraction (EBSD) fall beyond the scope of this research and can be executed in further work. However, in some cases, in order to demonstrate the capability of these characterization methods in an insightful understanding of the UFG alloys, TEM, EBSD, and nanoindentation techniques were employed.

## **1.5 Thesis Outline**

The current thesis is organized into five chapters. Following this introductory chapter, chapter two gives a review of relevant literature, from the overview of different SPD processes, especially TCAP and PTCAP methods and their influential parameters on microstructure and mechanical properties of lightweight materials processed through different methods. Information about the materials, methods employed for the material characterization, and analysis of the processed components are demonstrated in chapter three. Chapter four presents the results obtained from experimental procedures and the relevant discussion. In this chapter, the feasibility of the proposed processes for producing UFG alloys and enhancing their mechanical behaviour are provided. Finally, chapter five



## CHAPTER 2: LITERATURE REVIEW

### 2.1 Introduction

In traditional metal forming procedures, for instance, forging, extrusion, and rolling, the applied plastic strain is normally below 2.0. While the processes are executed up to few passes, the amount of plastic strain will typically raise more than 2.0, and consequently, the thickness and the diameter of the sample will turn into very thin, which are improper for structural components. Thus, many SPD processes are proposed to impose controlled deformation - large strain on the bulk substance without altering the configuration (Azushima et al., 2008). As established by the Hall–Petch mechanism (Eq. 1-1), a reduction in the grain size causes an enhancement in the material strength (Mahmoodian et al., 2019). Thus, the objective of the SPD process for producing UFG metal is to fabricate lightweight components with high mechanical strength and reliability (Azushima et al., 2008). In addition, to produce the UFG structure, the end outcomes should be free from defects and reasonably porosity free, improving the mechanical performance of the material (Zhu & Liao, 2004).

Numerous SPD methods and procedures have been invented and developed during last few years, for instance, ECAP (Jafarlou et al., 2016), high pressure torsion (HPT) (Edalati et al., 2018), and accumulative roll bonding (ARB) (Saito et al., 1999). These three methods are amongst the most common ones, which are typically employed for the production of bulk shaped alloys. There are also other SPD processing techniques such as twist extrusion (TE), multiaxial forging (MAF) (Salandari-Rabori et al., 2018), cyclic extrusion compression (CEC), continuous SPD processes (Y. Huang & Prangnell, 2007), repetitive corrugation (RC), rotary die ECAP, and integrated extrusion and ECAP (Tyagi & Banerjee, 2017) which are in the less common use category. Despite the widespread

use of tubular components in the industry, few SPD procedures have been proposed for the production of UFG tubes, for example, TCAP (Faraji et al., 2011c, 2012e), PTCAP (Faraji et al., 2012a), high-pressure tube twisting (HPTT) (Tóth et al., 2009), cyclic flaring and sinking (CFS) (Torabzadeh et al., 2016), accumulative spin-bonding (ASB) (Mohebbi & Akbarzadeh, 2010), rubber pad tube straining (RPTS) (Shapourgan & Faraji, 2016), and tube cyclic expansion extrusion (TCEE) (Babaei et al., 2014b). Several reviews on the SPD processes and UFG materials are available in the literature (Elias et al., 2013; Estrin & Vinogradov, 2013; Kawasaki et al., 2012; Langdon, 2007; Toth & Gu, 2014; Valiev & Langdon, 2006; C. Wang et al., 2012; Zhilyaev & Langdon, 2008), but almost none is available on the SPD methods for tubular components. A comprehensive appraisal of the SPD methods of tubular parts was recently published by Faraji and Kim (Faraji & Kim, 2017), wherein it was reported that UFG tubes in a laboratory-level can be fabricated using these SPD procedures. However, fabrication and characterization of TCAP and PTCAP for the development of UFG and nanostructured tubes have not been yet fully documented. Therefore, the present study makes available perceptive knowledge about the definition and history, principles, mechanisms of the microstructural refinement, and mechanical features of TCAP and PTCAP processed substances.

## **2.2 Severe Plastic Deformation (SPD) Methods for Tubular Components**

Over the past decades, numerous efforts have been done to design effectual SPD procedures proper for fabricating cylindrical tubes (Faraji et al., 2017). Herein, we present only the UFG tubes produced by TCAP and PTCAP methods. In this part, we are focusing on the introduction of tube SPD procedures, SPD modes, and grain refinement mechanisms.

### 2.2.1 Definition and History

SPD is a more common term, which refers to a category of the processes of working with metals including very large strains and naturally a multifaceted stress condition or high shear, causing an elevated imperfection density and equiaxed UFG structure ( $d < 500$  nm) or nanocrystalline configuration ( $d < 100$  nm) (Wei et al., 2004). A brief overview of the past of SPD is provided in this division.

The utilization of intense strains is not an unprecedented approach in the processes of working with metals, which is employed since ancient times. With common forming processes like drawing, rolling, and forging, adequately large strains can be achieved at different temperatures (Segal, 2018). The general skeleton for the development of dislocation configurations at modest strains is taken into consideration. This frame is also expanded to greater strains that are present throughout rolling and drawing (Segal, 2018). As a result of the initial investigation, a novel method of unrestricted straining via torsion under compression (HPT) was employed on the processing of a variety of substances, where a remarkable microstructural modification caused by extremely large shear strains was detected. Afterward, this approach was expanded further, and novel methods for the evolution of simple shear into probable industrial functions were proposed (Segal, 2018), which motivated deep investigation on the utilization of SPD for potential functions in advanced technology.

In connection with the grain refinement, X-ray analysis was performed, which was the only existing method for the examination of such fine configurations at the time (Segal, 2018). After that, TEM analysis was performed on the profoundly HPT-treated specimens and provided special inspections on a very small scale structure (Segal, 2018). Accordingly, the description of some terms like dislocation-free grains with sharp high-angle boundaries (HABs) was possible, which is consistent with the current definition of

UFG structures (Segal, 2018). From 1980 to 1990, an extensive program on SPD was started, where the strain hardening, treating, and recrystallizing of single crystals were studied. Nonetheless, this method could only fabricate very small specimens, which was not of industrial interest, thus was limited to academic interest only. The circumstances altered following the invention of a novel SPD process in 1972 known as ECAP. The ECAP changed the SPD into an effortless forming process that could be used on large billets from a variety of substances under different working circumstances. Thus, wide studies were conducted on ECAP from 1970 to 1986. For the first time, UFG bulk specimen was produced and its mechanical behaviour and physical features were explored. Particularly, a substantial rise in  $\sigma_{YS}$  and  $\sigma_{UTS}$  with keeping satisfactory ductility for hardening situation, further reinforcement by deformation process, and characteristic development of particular elastic, magnetic and superconductive substances were established.

These findings have brought about dramatic changes in materials production processes, as a result, extensive studies are conducted focusing on increasing efficiency and eliminating constraints over the past decades. It should be noted again that novel deformation processes caused two milestones in the times past of SPD: first, the HPT recognized SPD as a systematic approach, and the second, ECAP changed this approach into a powerful technique with the ability to produce various nanostructured and UFG substance (Segal, 2018).

Currently, a variety of SPD procedures are developed for different substances with different shapes. Nonetheless, there are many restrictions of their application to industrial uses, particularly those with a multifaceted configuration. Exploration of SPD procedures is typically executed on small specimens, effortless instruments and intensive work processes, which does not comply with the practical requirements. Without consideration

of the preferred mode of deformation, each SPD procedure possesses certain mechanical factors. In addition, some features such as processing cost, simplicity, reliability, and mainly the capability of scale-up fabrication should be considered. knowing that most of this data is unknown, further attempts are required for the commercialization of SPD. This suggests that different SPD methods should be reviewed and re-evaluated for industrial-scale to diminish the risk and costs (Segal, 2018).

### 2.2.2 SPD Modes

The phrase “mode of deformation” is typically utilized in combination with specific procedures of material examination without particular characterization. A more sufficient description of the mode of deformation is on the basis of the features of strain, strain rate tensors, and stress (Segal, 2002). For strains higher than 1, that are normal throughout SPD, impacts of flexibility and hardening may be disregard, the substance functioning is resembling a perfect rigid-plastic body. Besides, for easiness, the two-dimensional and homogeneous plastic flows are considered below. Substantial deformation of such substance is explained via the theory of flow by the strain rate ( $T_{\dot{\epsilon}}$ ) and stress ( $T_{\sigma}$ ) tensors towards the principal shear stresses ( $\alpha$ - and  $\beta$ -slip lines). Given that the plastic flow is autonomous of the hydrostatic pressure,  $T_{\sigma}$  values regularized by the material yield stress are equal. The element distortion in the direction of slip lines, i.e. general case, pure shear, and simple shear as well as Moore’s circles with rotation and in the limit cases of pure shear and simple shear is illustrated in Figure 2.1(Segal, 2018).

Tensors  $T_{\dot{\epsilon}}$  would be regularized using the efficient von Mises shear strain rate to contrast the dissimilar strain rate states (Segal, 2018):

$$\eta = \frac{\eta_\alpha + \eta_\beta}{2} \quad (\text{Eq. 2.1})$$

where  $\eta_\alpha$  and  $\eta_\beta$  are  $du/d\beta$  and  $dv/d\alpha$ , respectively.  $u$  and  $v$  are also velocity components in the direction of slip lines of  $\alpha$  and  $\beta$ .

The regularized tensors  $T_{\xi/\eta}$  fluctuate depending on the dispersal of shears between the slip lines, which is appraised using the deformation type coefficient (Segal, 2018):

$$C = \frac{\eta_\alpha - \eta_\beta}{2\eta} \quad (\text{Eq. 2.2})$$

where the  $C$  is scalar and dimensionless.

In one restricted situation, the rates of shear strain are homogeneously dispersed between both slip lines:  $\eta_\alpha = \eta_\beta$  and  $C = 0$ , which fits pure shear (Figure 2.1(b)). The rate of shear strain is localized in the direction of  $\alpha$  or  $\beta$ -slip line with  $\eta_\alpha = 2\eta$  and  $C = 1$  and  $\eta_\beta = 2\eta$  and  $C = -1$ , respectively, in a different restricted condition which symbolizes a simple shear in the direction of either the  $\alpha$ - or  $\beta$ -slip lines (Figure 2.1(c)). The coefficient  $C$  alters in the range of  $-1 \leq C \leq 1$  and all probable modes of deformation are restricted between pure and simple shears for the reason that the two slip lines are equivalent. In accordance with Eqs. 2.1 and 2.2, the tensor of regularized strain rate can be determined into two parts as follows (Segal, 2018):

$$T_{\xi/\eta} = \{0,0,0,1,1,0\} + \{0,0,0,C,-C,0\} \quad (\text{Eq. 2.3})$$

The beginning Eq. 2.3 is a symbol of the regularized pure shear, but the next division stands for the regularized speed of rigid rotation. The factors  $\eta$ ,  $C$  and  $\omega$  correspond to the shear strain rates  $\eta_\alpha$ ,  $\eta_\beta$ , linear strain rates  $\xi_\alpha$ ,  $\xi_\beta$ , and angle speed of rigid rotation in the direction of the slip lines (Segal, 2018):

$$\xi_\alpha = \xi_\beta = 0, \eta_\alpha = \eta(1 + C), \eta_\beta = \eta(1 - C), \omega = \eta C \quad (\text{Eq. 2.4})$$

This equation exhibits that  $C$  is the regularized speed of rigid rotation  $C = \omega/\eta$ . In addition, similar rates of strain along arbitrary coordinate axes  $x$  and  $y$  are (Segal, 2018):

$$\xi_{xx} = -\xi_{yy} = \eta \sin 2\varphi, \eta_{xy} = \eta(\cos 2\varphi + C), \eta_{yx} = \eta(\cos 2\varphi - C), \omega = \eta C \quad (\text{Eq. 2.5})$$

where  $\varphi$  points out an angle between the  $x$ -axis and  $\alpha$ -slip line in the counter-clockwise direction. The rigid rotation is generally abandoned in the classic model of plasticity. Nevertheless, this feature plays a key role in materials with a distinct configuration. Figure 2.1(d) shows a geometrical illustration of Eqs. 2.3, 2.4, and 2.5 by the Moore circle. The Moore circles for all probable modes of deformation between pure shear (centre  $O$ ), simple shear in the direction of the  $\alpha$ -slip line (centre  $O_1$ ), as well as simple shear in the direction of the  $\beta$ -slip line (centre  $O_2$ ) are shown in Figure 2.1(e) (Segal, 2018).

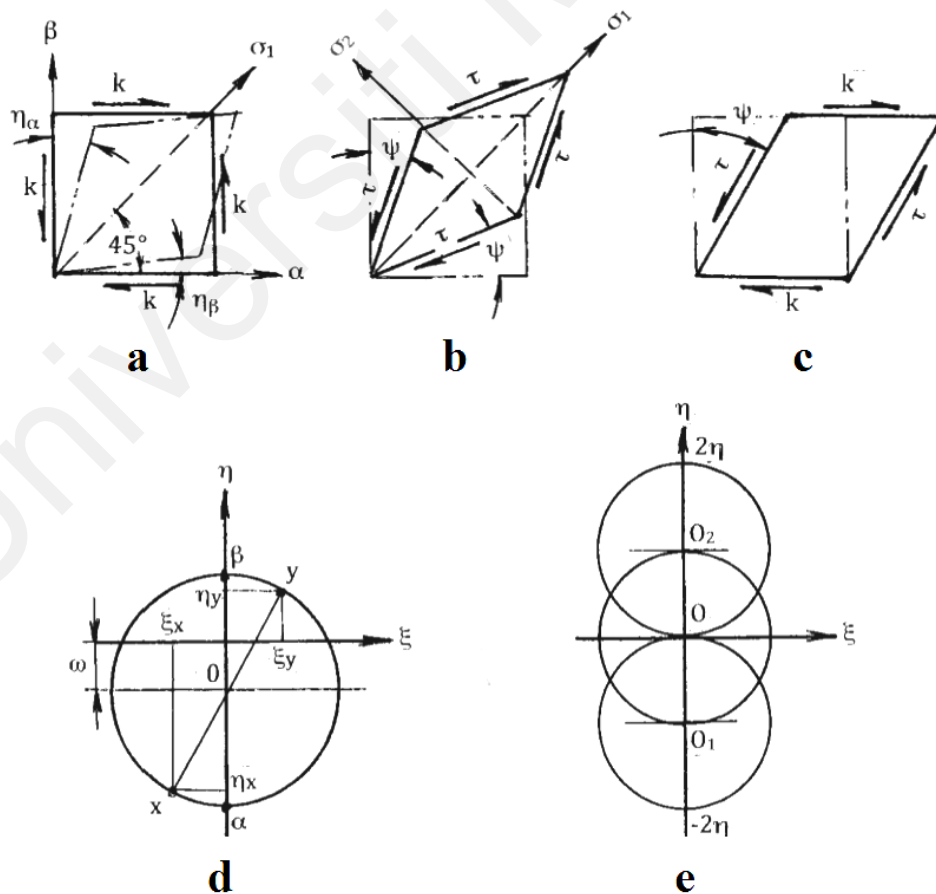


**Figure 2.1:** The element distortion in the direction of slip lines: (a) general case; (b) pure; and (c) simple shears as well as (d) Moore's circles with rotation and (e) in the limit cases of pure and simple shears;  $\eta\alpha$  and  $\eta\beta$  exhibit the shear rates in the direction of the slip lines (Segal, 2002).

### 2.2.3 Grain Refinement Mechanism

The grain refinement during SPD has attracted huge attention during the past few years. SPD is an extension of common straining at ambient temperatures consisting of origins as well as reciprocal action of various imperfections, which creates low-angle domain boundaries. Successive structural distortions throughout the SPD comprises crumbling through grain dividing as well as the development of micro-shear bands, twins, and cellblocks by additional evolution of low-angle boundaries (LABs) into HABs as a consequence of incessant and interrupted dynamic recrystallization.

From Figure 2.2, the mechanisms of microstructural refinement are still unclear; nonetheless, the influences of rigid rotation, texture development, localization of shear band, hardening, and overlap attributable to the altering of loading trails are commonly reported. In accordance with the foregoing arguments, the mode of deformation has a great impact on the microstructural features. Bridgman (Bridgman, 1937) was the first who revealed an excellent microstructural refinement during a simple shear caused by the HPT. On the contrary, the wire drawing works on SPD by Langford and Cohen (1976) and other authors discovered fibrous micro configurations with sub-arrangements of cells and sub-particles which were not fresh grains.

The same flake-like micro configuration is also observed during rolling with great diminution and near-pure-shear manner. On the other hand, Hirsch et al. (1988) reported extremely-fine microstructure in the case of rolling in macro-shear bands, wherein the deformation type was altered from pure to simple shear. Some efforts are also made to pile up dislocations, restrain recovery, and expand strain-persuaded UFG configurations via rolling at very low temperatures. Notwithstanding the great compactness of dislocations, conversely, no refinement was observed in the case of cryogenically processed copper at a strain equal to 5 (Y. Wang et al., 2003). It was only after strains

higher than 5, that fresh grains with HABs began to come into sight as a result of the incessant dynamic recrystallization by fragment rotation. A straight assessment of structural improvement by simple and pure shears is also presented (Angella et al., 2013). A number of reports are also presented and compared to a range of SPD processes in connection with the structural refinement. Wherein the same general trend was observed in which a simple shear can be brought upon by a rise in the mode of deformation that makes the SPD procedures more efficient for grain refinements (Segal, 2018). So, a simple shear can be sorted as the most favorable type of microstructural modification during SPD.

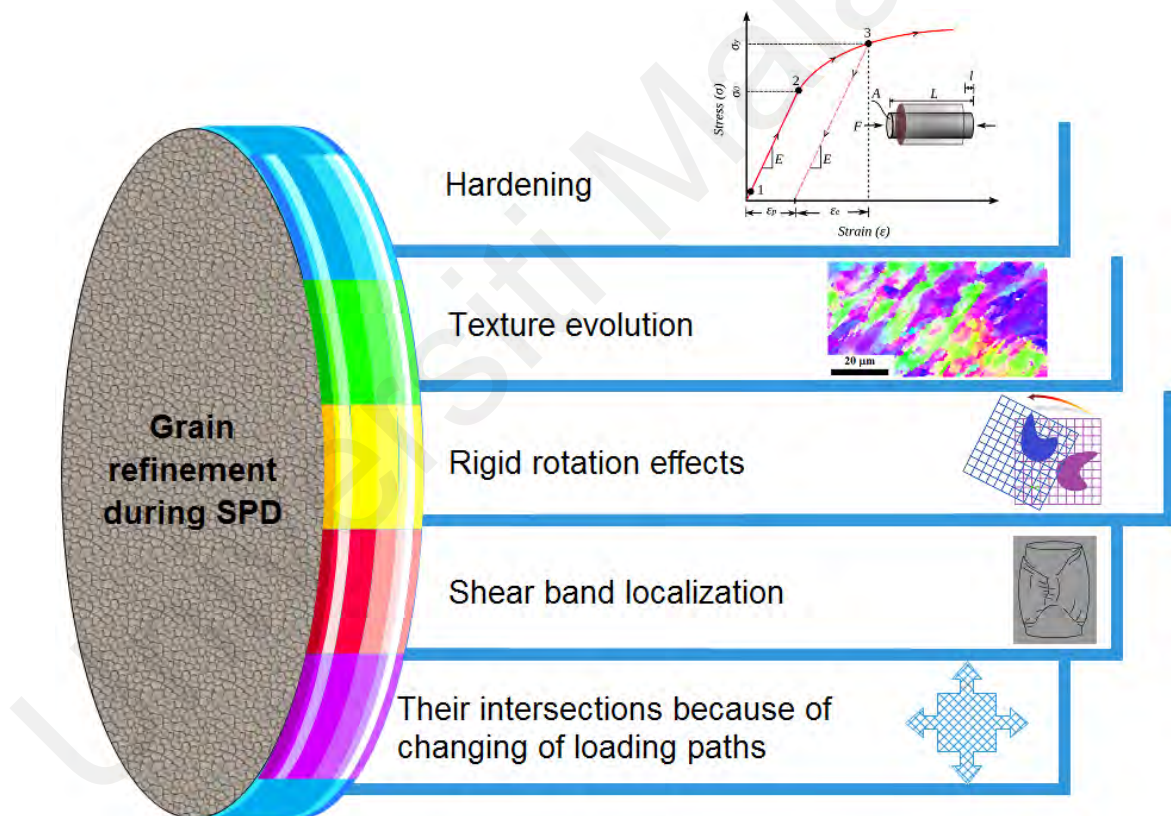


**Figure 2.2:** Grain refinement mechanisms during SPD processes.

### 2.3 Tubular Channel Angular Pressing (TCAP) and Process Parameters

Based on the literature, the structural evolution under identical circumstances intensely counts on the mechanics of procedure, which discriminate SPD from common manufacturing processes, making an exceptional material refinement. Segal found that

the performance of an ECAP die could be compromised by a die scheme, which seems easy with sharp corners. It is particularly cautioned versus the utilization of dies with a corner arc, which results in the incidence of a broadly extended fan-like plastic region (Segal, 2002), which is equal to a synthetically enhanced friction that scatters the shear and creates a substantial strain incongruousness. Regrettably, this vital caution was unnoticed in several investigations, where a basic die plan with a rounded outer corner was employed (Pérez, 2004). In this neglect, an excessive cost should be excluded as a result of significant incongruousness of the processed configuration, together with a reduction in the hydrostatic compressive stress and the practicality of the substance. On the contrary, by following the proposed advice, specimens with homogeneous micro configuration can be formed (Estrin et al., 2013). Faraji et al. (2011c) developed the first effective TCAP method on the basis of ECAP without its limitations in the processing of tubular materials. It should be noted that the TCAP process proposed herein is consistent with the central advice of Segal.

### **2.3.1 Principles of TCAP**

The conventional description of the TCAP is revealed in Figure 2.3 (Faraji et al., 2011c). The die consists of three angular deformation zones. This method is based on creating shear stresses. The tube is placed in the space between the mandrel and the cylinder, then by extruding the punch, the metal tube is extruded into the angular channel. Subsequently, it will undergo severe shear strain and also plastic deformation by passing through the three symmetrical areas. At the end of the process, it returns to its original dimensions and can be repeated.

The die variables are also illustrated in Figure 2.3(b). These factors make some influences on the processing load and the deformation mechanism (Faraji et al., 2012b).

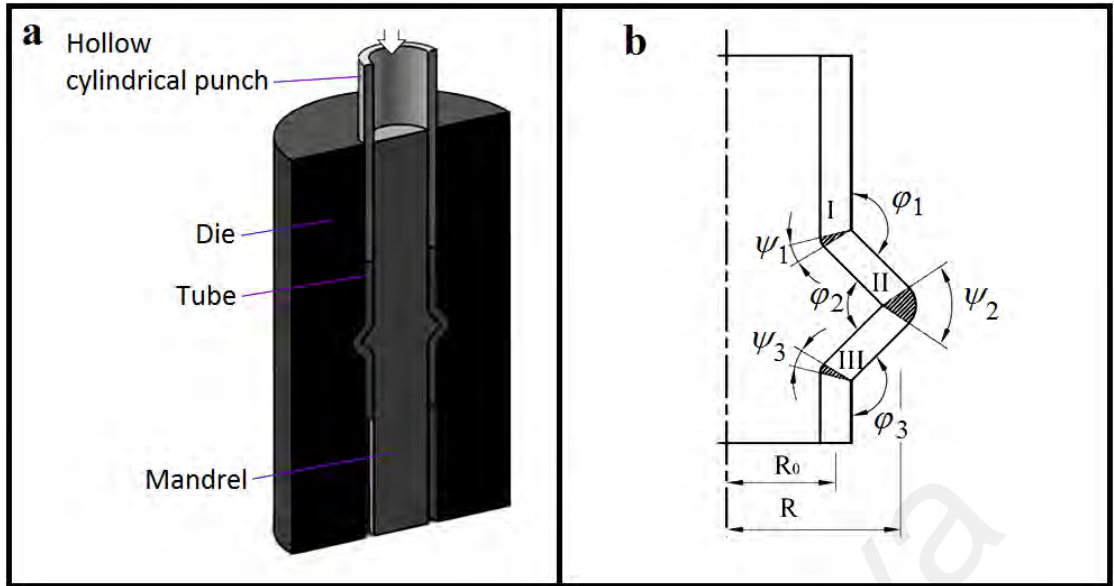


**Figure 2.3:** (a) A schematic of TCAP and (b) the relevant factors (Mesbah et al., 2014).

During common ECAP, strain status can be regarded as a simple shear, whereas in TCAP extra radial and circumferential tensile in zone *b* as well as compressive strains in zone *c* exists. The following equation can be utilized to determine the accumulated strain caused by three successive common ECAP with channel angles  $\phi$  ( $135^\circ$ ,  $90^\circ$ , and  $135^\circ$ ) and corner angles  $\psi$  ( $0^\circ$ ,  $90^\circ$ , and  $0^\circ$ ) (Faraji et al., 2011c):

$$\bar{\epsilon} = \frac{2 \cot(\phi/2 + \psi/2) + \psi \csc(\phi/2 + \psi/2)}{\sqrt{3}} \quad (\text{Eq. 2.6})$$

Therefore, the accumulated equivalent strain caused by three successive common ECAP is 1.863 that is the total amount for the plastic strains caused by Eq. 2.6. Due to the presence of radial and circumferential strains in the TCAP process, the entire equivalent strain will be more than 1.863. The precise amount of entire amassed strain ( $\bar{\epsilon}_T$ ) in the TCAP process can be determined using Eq. 2.7, that is caused by the general engineering plasticity equation and the geometry of Figure 2.3(b) (Faraji et al., 2011c):

$$\bar{\epsilon}_T = \sum_{i=1}^3 \left[ \frac{2 \cot(\phi_i/2 + \psi_i/2) + \psi_i \csc(\phi_i/2 + \psi_i/2)}{\sqrt{3}} \right] + 2\bar{\epsilon}_\theta \quad (\text{Eq. 2.7})$$

$$\bar{\varepsilon}_\theta = \frac{2}{\sqrt{3}} \varepsilon_\theta \quad (\text{Eq. 2.8})$$

$$\varepsilon_\theta = \ln \frac{R}{R_0} \quad (\text{Eq. 2.9})$$

where  $R$  and  $R_0$  are the tube radii in the channel zone and final tube, respectively. Ultimately, the entire equivalent strain following  $N$  passes of TCAP can be represented with the equation shown below (Faraji et al., 2011c):

$$\bar{\varepsilon}_{TN} = N \left\{ \sum_{i=1}^3 \left[ \frac{2 \cot(\varphi_i/2 + \psi_i/2) + \psi_i \csc(\varphi_i/2 + \psi_i/2)}{\sqrt{3}} \right] + 2\bar{\varepsilon}_\theta \right\} \quad (\text{Eq. 2.10})$$

According to Eq. 2.7, the entire corresponding plastic strain in the TCAP process is about 2.2 which is higher in contrast to the three-pass ECAP (1.863). Extensive studies on the influence of friction circumstances are conducted so far (Faraji et al., 2012d). The semi-circular shape of the procedure in relation to the triangular geometry is also examined through the finite element method (FEM) (Faraji et al., 2012e).

It is reported that a smaller force, improved lower hydrostatic stress and strain uniformity can be attained from the semi-circular geometry. A rise in the angles of die revealed a similar trend for a semi-circular channel. On account of the importance of process load, few attempts are also accomplished with the purpose of reducing the force of TCAP procedure by means of the ultrasonic vibration-assisted process (Faraji et al., 2014a). It was found that the processing load was somewhat reduced by employing the ultrasonic vibration onto the punch. Nonetheless, the utilization of ultrasonic vibration toward the die caused a substantial decrease in force. As the force was directed into the radial direction, the requisite load might be reduced up to 80% (Faraji et al., 2014a) for the reason that the ultrasonic vibration drastically declines the coefficient of friction and the friction force is a great division of the TCAP load (Siddiq & El Sayed, 2012).

### 2.3.2 Effects of Channel Angle

According to the parameters shown in Figure 2.3(b) and assuming that in the die design, channel angles of  $(\varphi_1)$  and  $(\varphi_3)$  are equal to each other ( $(\varphi_1)=(\varphi_3)$ ), the only independent parameter that  $(\varphi_1)$  and  $(\varphi_3)$  are also geometrically a function of it would be channel angles of  $(\varphi_2)$  and the values of  $60^\circ$ ,  $90^\circ$ , and  $120^\circ$  will be examined for it.

The microstructure and deformation behaviour of materials are straightly associated with the amount of strain and also the distribution pattern. Thus, effective strain analysis is very important (S. Xu et al., 2008). Figure 2.4(b-d) demonstrates the effective strain contour resulting from finite element simulation within the TCAP process with the second channel angle of  $120^\circ$ ,  $90^\circ$ , and  $60^\circ$ , respectively. The value of the coefficient of friction is assumed to be 0.05. It is clear from these figures that the smaller angle causes the higher effective strain of plastic and the worst strain homogeneity. Measured values of effective strain along TCAP processed tube with different aforementioned angles shown in Figure 2.4(e) diagrams. It is clear from this figure that increasing the angle of the second channel reduces the equivalent plastic strain (Faraji et al., 2012b). The equivalent plastic strains of 1.65–2.15 ( $1.9 \pm 0.25$ ), 2.15–2.85 ( $2.5 \pm 0.35$ ), and 2.5–3.75 ( $3.125 \pm 0.625$ ) have been attained after one pass TCAP with channel angles of  $120^\circ$ ,  $90^\circ$ , and  $60^\circ$ , respectively. That is to say, the percentage of strain variations in thickness in relation to specimens made with channel angles of  $120^\circ$ ,  $90^\circ$ , and  $60^\circ$  are 13.1%, 14%, and 20%. In simple terms, the effect of channel angle on strain homogeneity for angles of  $60^\circ < \varphi_2 < 90^\circ$  is less than its effect on the angles of  $90^\circ < \varphi_2 < 120^\circ$ .

Figure 2.4(e) implies that the maximum equivalent plastic strain occurred in the inner surface of the sample for all channel angles. By considering at the shear zone I (Figure 2.3(b)) and Figure 2.4(d) it can be concluded that the uppermost strain was gained at the inner surface, unlike ECAP. This can be due to the presence of peripheral strain at the

TCAP process which is not present in the ECAP process, which leads the imposing pressure towards the internal mandrel surface. (Faraji et al., 2012b).

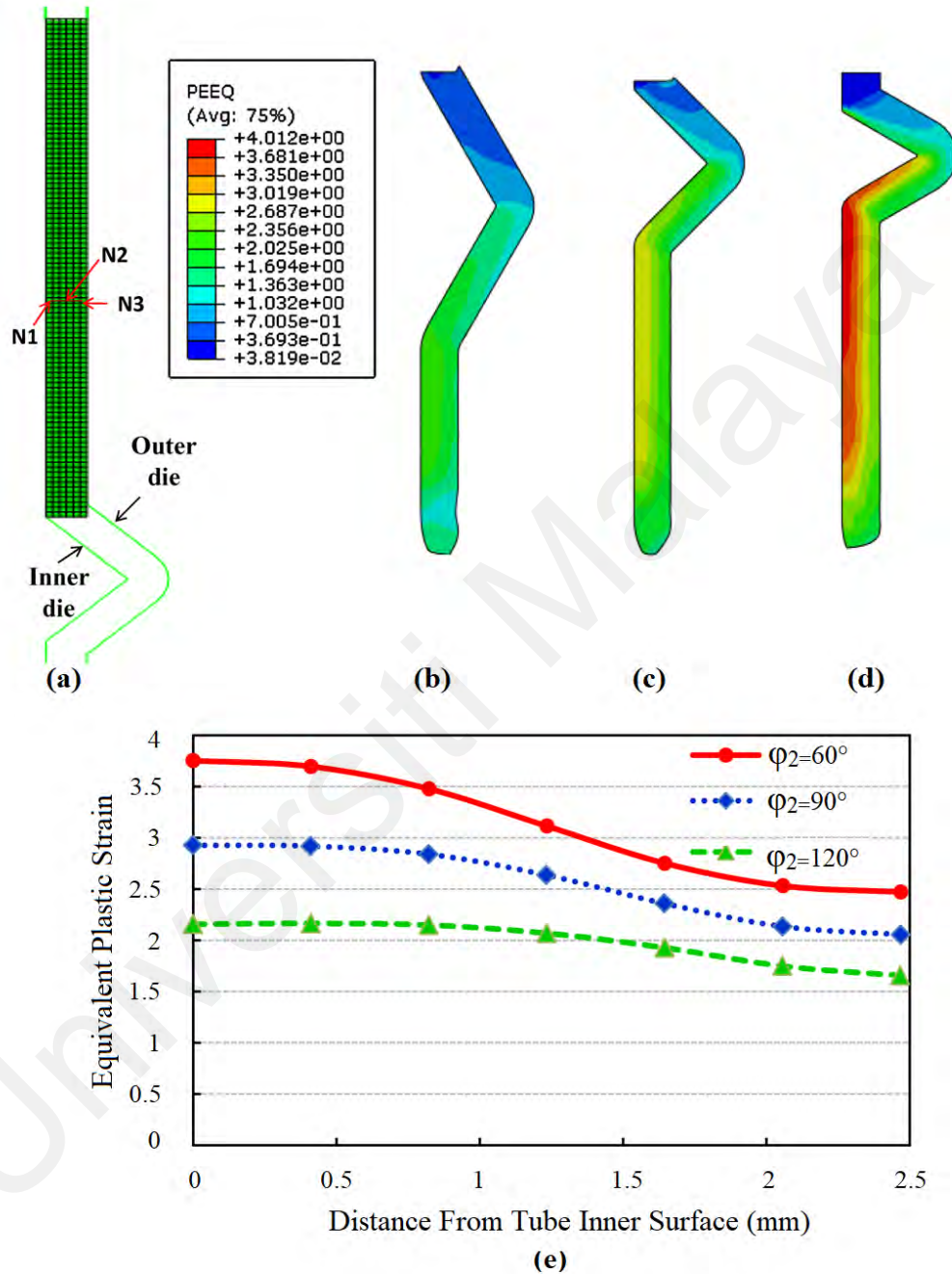


**Figure 2.4:** (a) Model of Finite Elements and selected nodes from sample cross-section, (b–d) Effective strain contour resulting from finite element simulation within TCAP process with the second channel angle of 120°, 90° and 60°, respectively. (e) The effective strain diagram obtained from the FEM, across the sample thickness for different channel angles (Faraji et al., 2012b).

Figure 2.5 (a–c) demonstrates the contour of the effective stress dissemination obtained by FEM within the TCAP process at various channel angles. By applying the strain contour analysis in the deformation area, it may be possible to obtain further information about the plastic region and shear deformation (Nagasekhar et al., 2007).

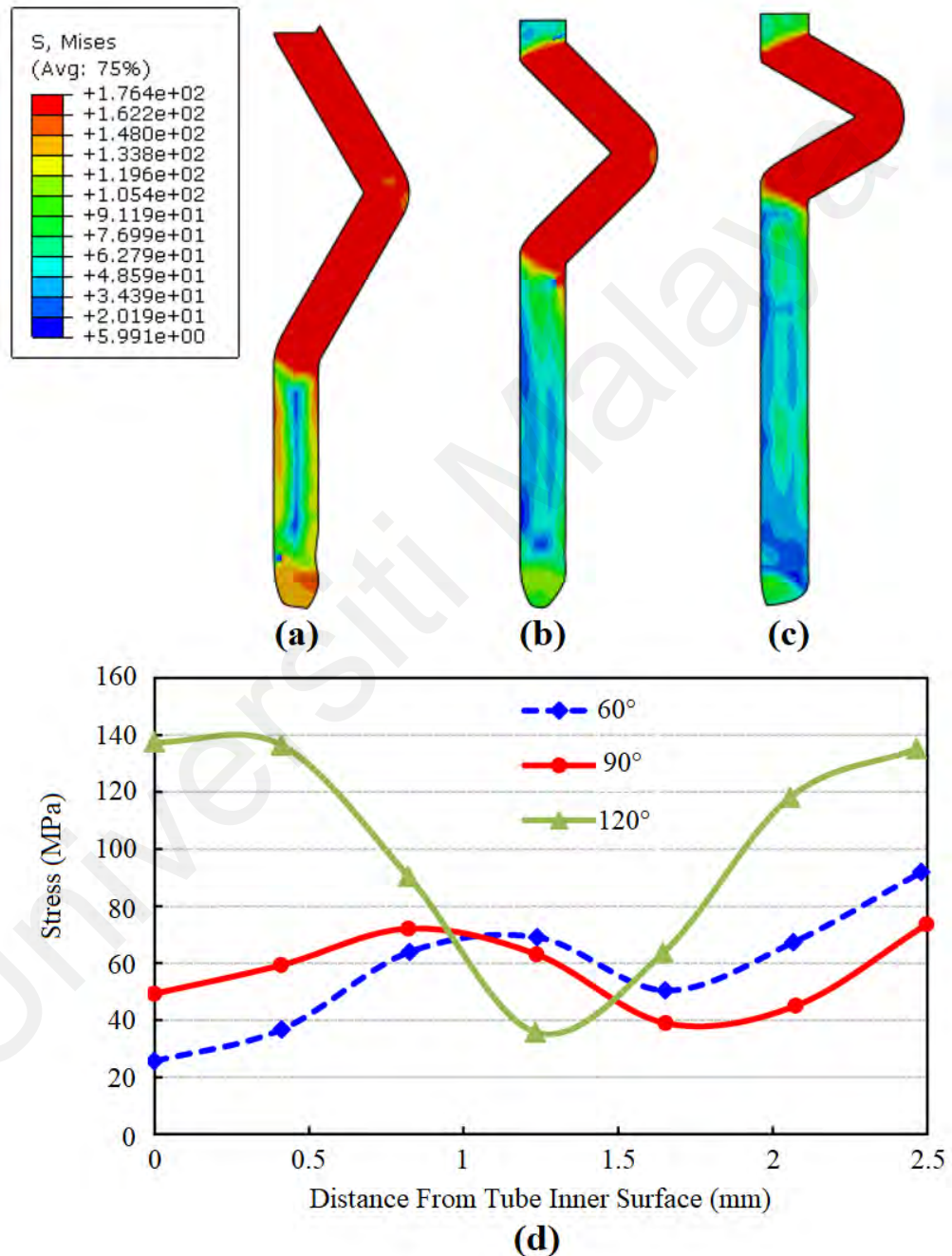


**Figure 2.5:** (a-c) Contour of the effective stress dissemination obtained by FEM within TCAP process at various channel angles, and (d) effective stress amount across the tube sample thickness (Faraji et al., 2012b).

Figure 2.5 Illustrates that for all the considered channel angles, fully plastic zones are located between the shear regions. Figure 2.5(d) shows the effective stress amount across the tube sample thickness. It can be found that the best stress homogeneity occurs at an angle of  $90^\circ$  and the worst happens at  $120^\circ$ . Perhaps the (worst-case) homogeneity is because of the existence of the separation zone at  $120^\circ$  angle. (Faraji et al., 2012b).

Figure 2.6 represents the calculated pressing load obtained from FEM against ram displacement throughout TCAP by various channel angles where no BP was applied. Besides, the friction coefficient was considered 0.05. It reveals that the force diagrams are different for various channel angles. The required force decreases with increased angle. Nevertheless, in these graphs, there are three incline alterations. With the increase in the channel angle, incline alteration abruptly decreases. A significant trait in force figures is that all curves converge to a certain value near the end. It can be ascribed to the friction force value. It can be due to increasing the tube passing trace as a consequence of increasing the channel angle by assuming the geometry of Figure 2.3(b). (Faraji et al., 2012b).

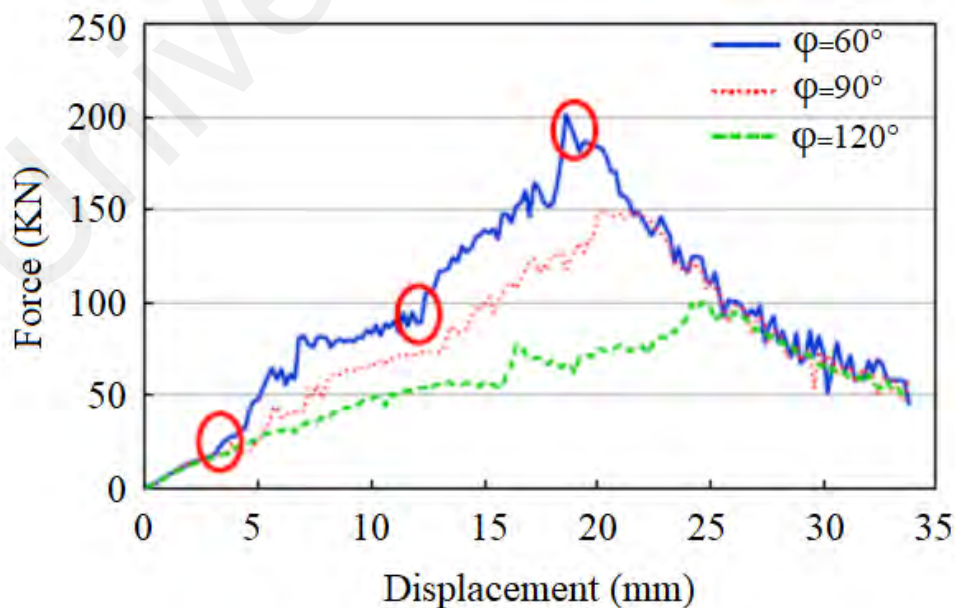


**Figure 2.6:** Calculated pressing load obtained from FEM against ram displacement during TCAP with channel angles of  $60^\circ$ ,  $90^\circ$ , and  $120^\circ$  (Faraji et al., 2012b)

### 2.3.3 Effects of Curvature Angle

Figure 2.7 demonstrates the equivalent plastic strain across the tube thickness in the TCAP process at various curvature angles ( $\psi_1 = \psi_3$ ) of  $0^\circ$ ,  $17^\circ$ ,  $35.5^\circ$ , and  $45^\circ$ . As it can be seen, an enhancement in the curvature angle value caused an increment in the equivalent strain at the internal surface area of the tubular sample. Nevertheless, it doesn't have a substantial consequence on the external surface area strain. In other words, the strain homogeneity will be increased once the curvature angles of  $\psi_1 = \psi_3$  increase (Faraji et al., 2012c).

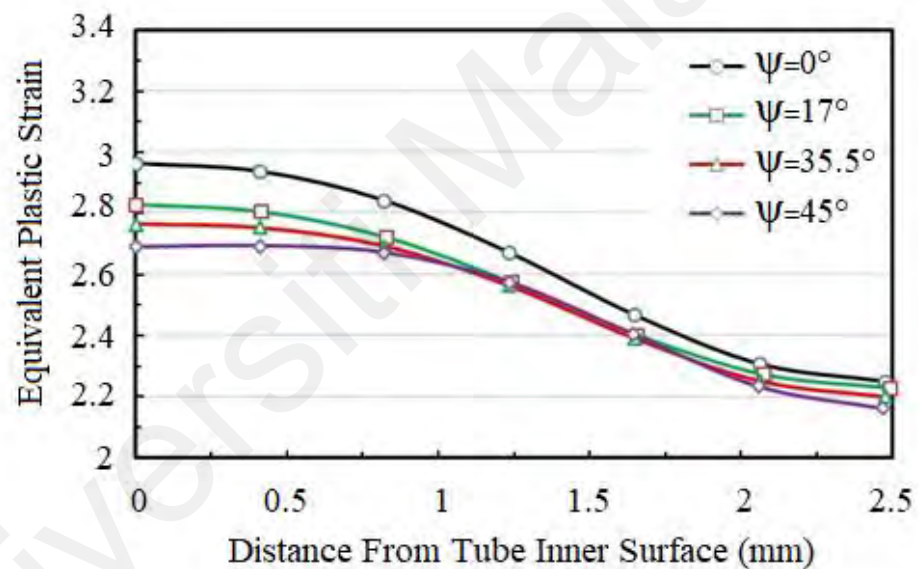


**Figure 2.7:** Impacts of curvature angles on equivalent plastic strain ( $\psi_1 = \psi_3$ ) ( $R/R_0 = 1.5$ ,  $\psi_2 = 90^\circ$ ) (Faraji et al., 2012c).

The impacts of curvature angles of  $\psi_1 = \psi_3$  on displacement force diagram have been shown in Figure 2.8 in which the values of  $R/R_0$  is equal to 1.5 and  $\psi_2$  is equal to  $90^\circ$ . According to the above graphs, it can be found that the values of curvature angles did not have a noteworthy effect on the mandatory load. By considering Figure 2.7 and Figure 2.8, It can be determined which in process of TCAP, choosing the higher value of

curvature angles, will possibly improve homogeneity and consistency deprived of any substantial effect on the required process loads (Faraji et al., 2012c).

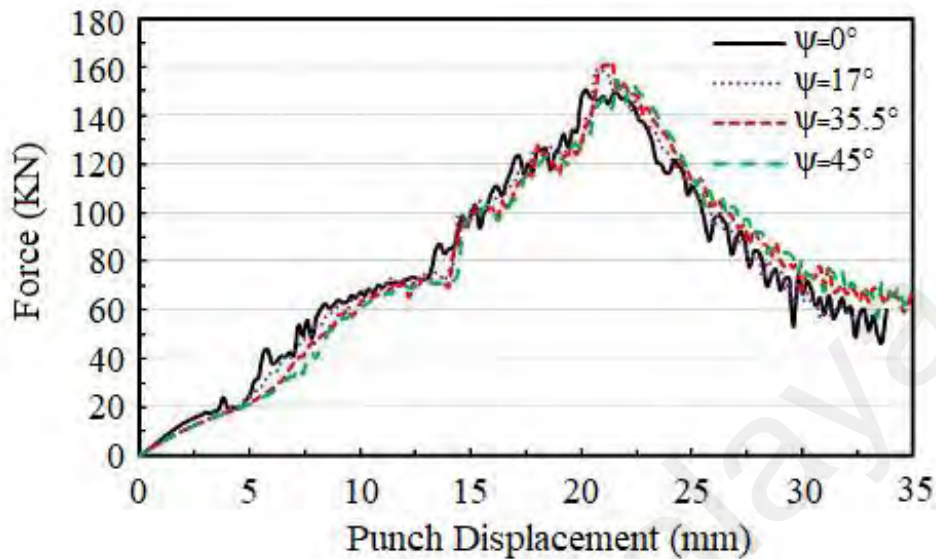


**Figure 2.8:** Impacts of curvature angles of  $\psi_1 = \psi_3$  on the displacement force diagram obtained by FEM ( $R/R_0 = 1.5$ ,  $\psi_2 = 90^\circ$ ) (Faraji et al., 2012c).

The Effective plastic strain contour resulting from FEM, through the angles of curvature  $\psi_2 = 0^\circ, 28^\circ, 67.4^\circ$  &  $90^\circ$ , correspondingly is illustrated in Figure 2.9 (a-d). As can be observed, increasing the  $\psi_2$  leads to decreasing the rate of strain. This phenomenon was also observed in the ECAP method (H.S. Kim, 2002).

Numerical values of corresponding plastic strain along the tube thickness consistent to curvature angles of  $\psi_2 = 0^\circ, 28^\circ, 67.4^\circ$ , and  $90^\circ$  are exposed in Figure 2.9(e). It can be observed that the maximum and minimum strain values happen at the outer and inner surfaces of the processed metal tube correspondingly. In addition, the homogeneity of strain enlarged once the  $\psi_2$  was amplified up to  $67.4^\circ$ . By enhancing the  $\psi_2$  to  $90^\circ$  the trend will change and maximum and minimum strains occurred in the interior and exterior surfaces of the sample (Faraji et al., 2012c).

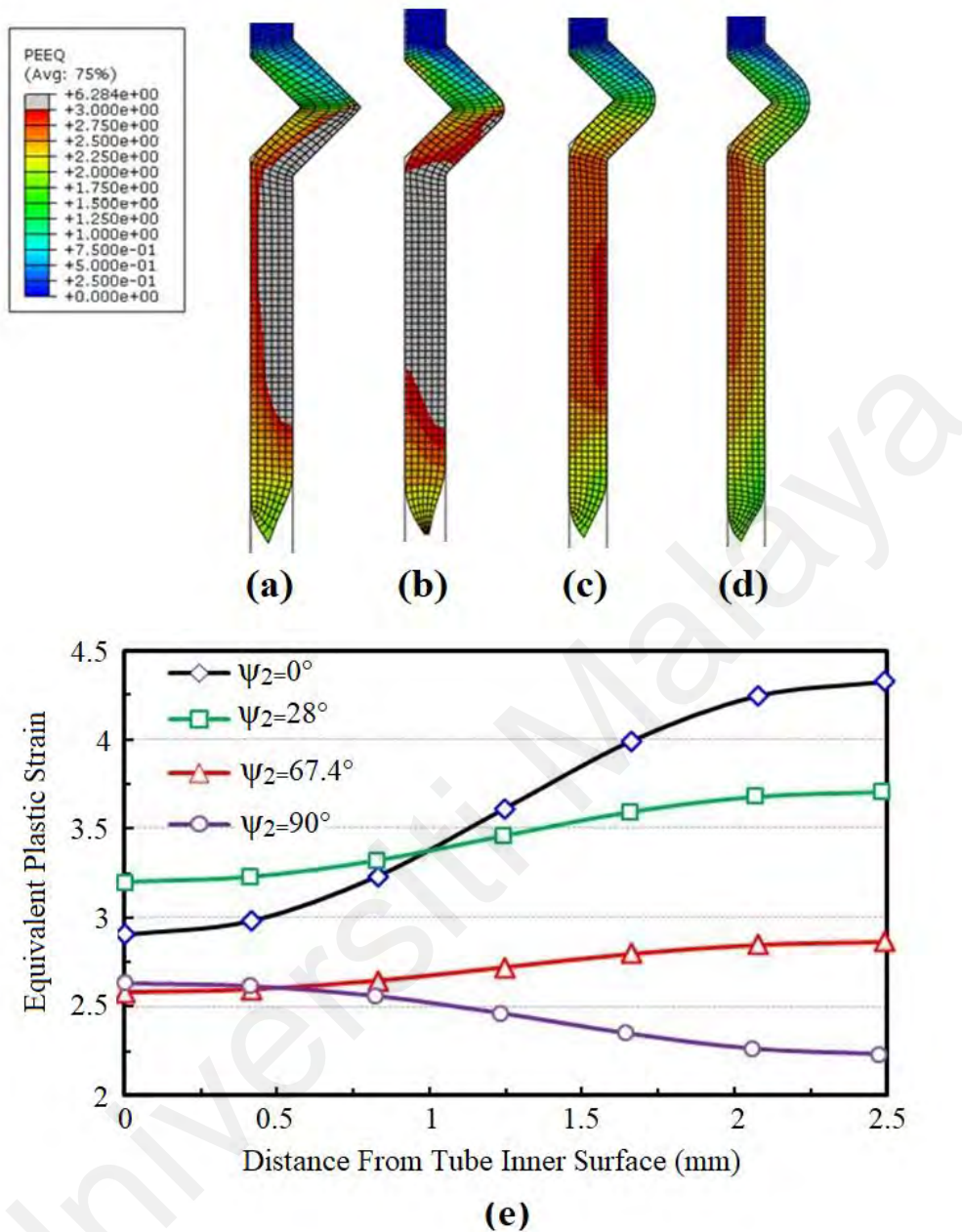


**Figure 2.9:** (a-d) Effective plastic strain contour resulting from finite element simulation within TCAP process with the second curvature angles of  $\psi_2 = 0^\circ$ ,  $28^\circ$ ,  $67.4^\circ$  and  $90^\circ$  (e) Diagram of effective strain along the tube sample for different curvature angles (Faraji et al., 2012c)

Figure 2.10 describes the impacts of the second curvature angle ( $\psi_2$ ) on the mandatory loads in the TCAP method, while the  $\psi_1$  is equal to  $\psi_3$  equal to zero, and the deformation ratio  $R/R_0$  is equal to 1.2. Also, and according to the above figure, it can be concluded that by raising the second curvature angle the obligatory load will lower down. Bearing

the strain homogeneity in mind and the needed force for performing the process lead to a finding that the optimum value for  $\psi_2$  would be equal to  $90^\circ$  (Faraji et al., 2012c).

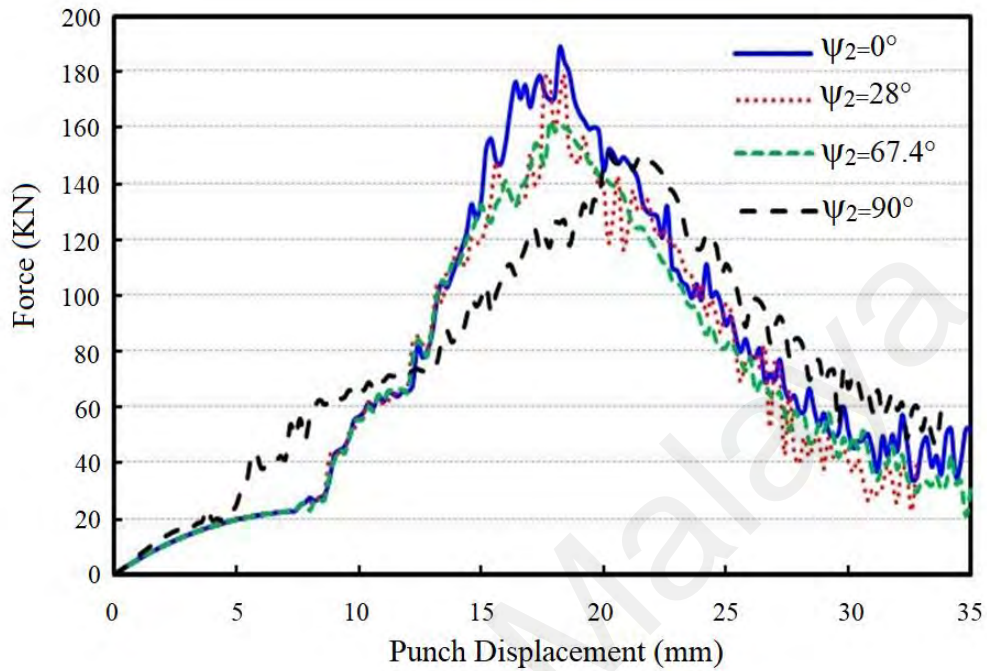
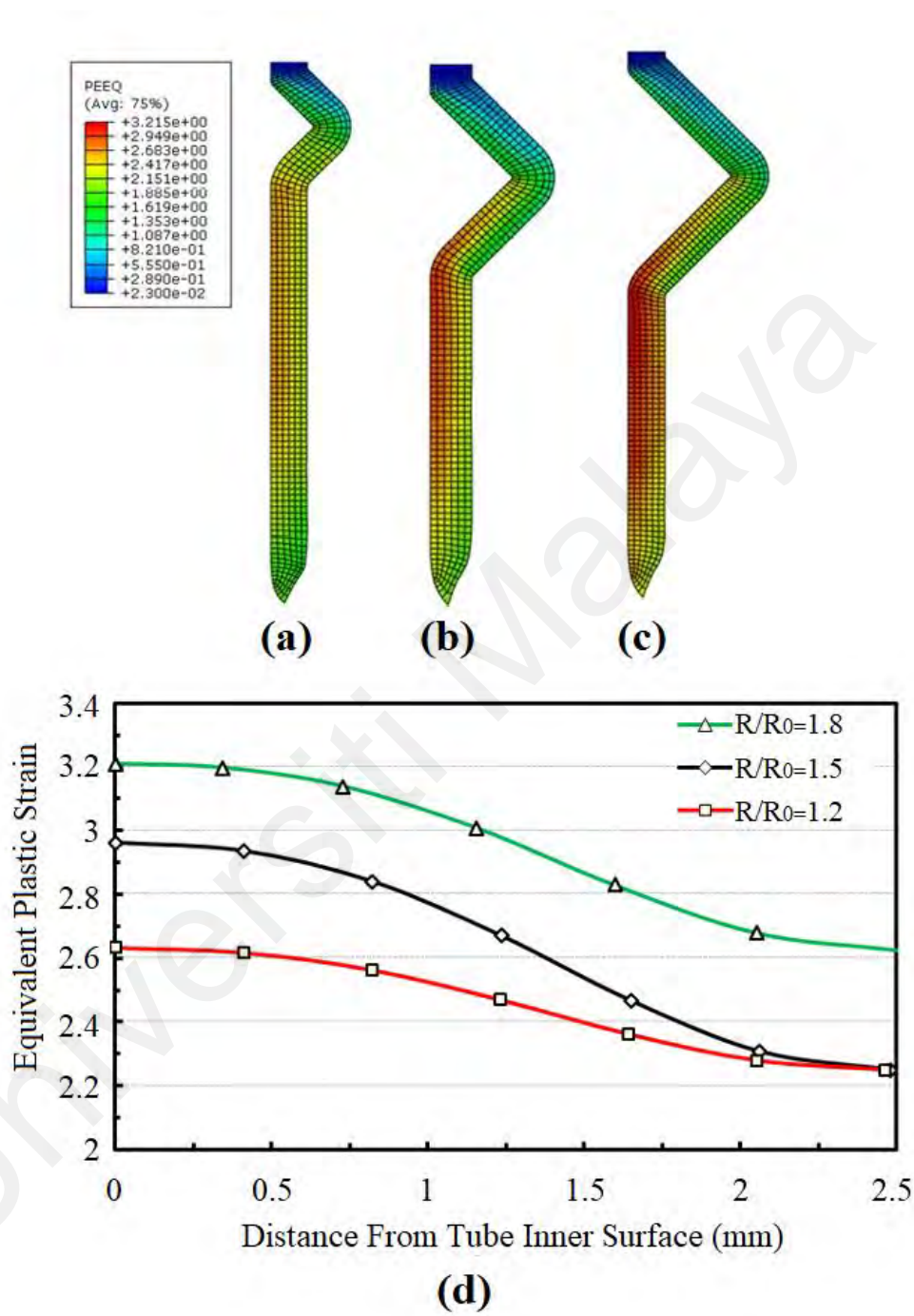


**Figure 2.10:** Influence of second curvature angle on the required loads in TCAP process ( $\psi_1 = \psi_3 = 0$ ,  $R/R_0 = 1.2$ ) (Faraji et al., 2012c).

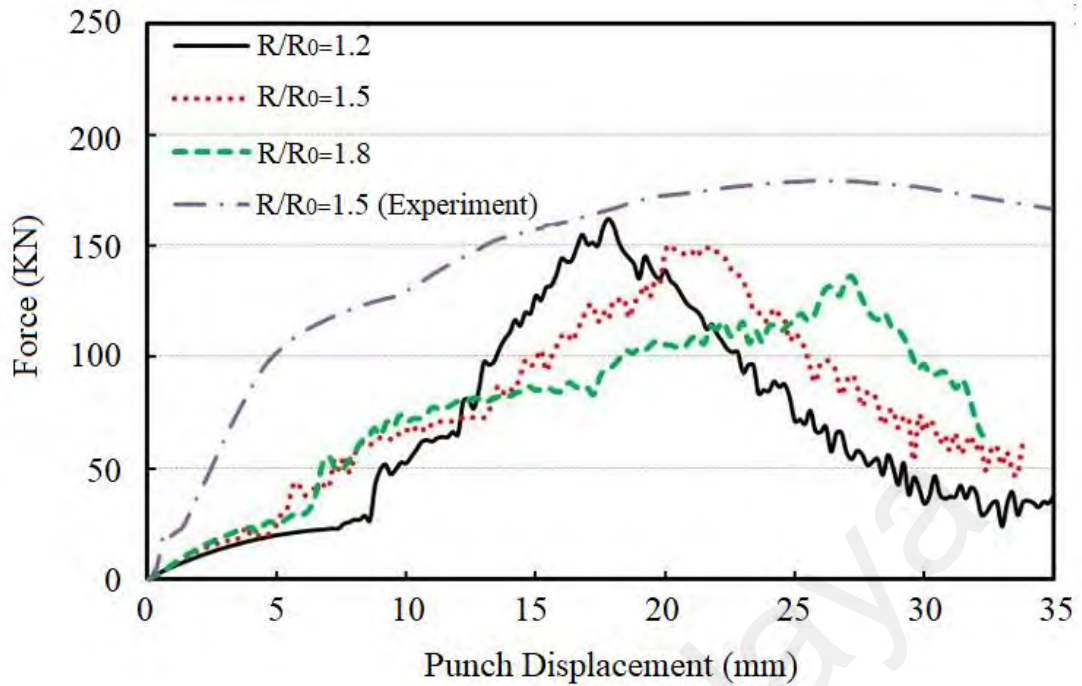
### 2.3.4 Effects of the Deformation Ratio

Figure 2.11(a-c) displays equivalent plastic strain contours consistent to 3 diverse deformation ratios ( $R/R_0$ ) of 1.2, 1.5, & 1.8. It's clear that the bigger deformation ratio will cause superior equivalent plastic strain. The quantified strain amount correlated to Figure 2.11(a-c) has been shown in the graphs of Figure 2.11(d). It is clear that in the TCAP procedure by deformation ratio of 1.2, 1.5, & 1.8, the equivalent values of plastic strains of 2.25-2.65 ( $2.45 \pm 0.2$ ), 2.25-2.95 ( $2.6 \pm 0.35$ ), and 2.65-3.05 ( $2.85 \pm 0.2$ ) will be achieved after exerting single pass of TCAP one-to-one. Therefore, strain alteration in various deformation ratios of 1.2, 1.5, & 1.8 are 8.1%, 13.4%, & 7%, respectively. This implies that there is no identical trend between strain homogeneity and deformation ratio

variation. The best strain homogeneity is attained in the deformation ratios of 1.8 and the worst one gained at 1.5.



**Figure 2.11:** (a-c) The Effective plastic strain contour resulting from FEM, at diverse deformation ratios of 1.2, 1.5 and 1.8; (d) Path plots of equivalent plastic strain along the thickness at deformation ratios of 1.2, 1.5 and 1.8 (Faraji et al., 2012c).



**Figure 2.12:** Influence of deformation ratio on the force-displacement diagram using FEM in comparison with experimental results (Faraji et al., 2012c).

Figure 2.12 displays the influence of deformation ratio on the force-displacement diagram using FEM and also a comparison among FE and obtained experimental results in the deformation ratio of  $R/R_0$  equal to 1.5 in TCAP procedure. This figure allows the conclusion that increasing the deformation ratio reduces the maximum force required by the process. So from the point of view of strain homogeneity and low force, selecting a more deformation ratio (here till 1.8) is recommended. (Faraji et al., 2012c).

### 2.3.5 Properties and Applications

Investigations of the UFG material properties revealed exceptional features connected with successful grain refinement. The  $\sigma_{YS}$  and  $\sigma_{UTS}$ , and hardness, as well as ductility, are basically reliant on microstructural features of metal. A perfect industrial component is required to possess elevated mechanical strength and fracture toughness as well as adequate ductility. Nevertheless, a desirable equilibrium of elevated mechanical strength

and ductility is a critical issue that needs to be carefully evaluated (Valiev et al., 2002). A rise in the mechanical strength through microstructural modification, consistent with the Hall–Petch equation, could also result in a probable reduction in ductility. This suggests that UFG materials with improved mechanical strength and elevated ductility are uncommon.

Actually, metals could be strong or ductile, but the simultaneous combination of both properties are rare. During the past decades, achieving a proper balance of elevated mechanical strength and ductility has received considerable interest (An et al., 2008; Y. Lin et al., 2012; Zhao et al., 2008; Zhao et al., 2006). Although the precise justifications for the elevated ductility are vaguely specified, based on the literature, the high ductility of UFG materials is ascribed to the occurrence of different phenomena, such as microstructural refinement with high-angle grain boundaries (Zhao et al., 2006), high angle grain boundaries together with low interior dislocation densities (Y. Lin et al., 2012), bimodal grain size scattering (Y. Wang et al., 2002), nano-twins development (C.X. Huang et al., 2015), and UFG alloy with nano-sized precipitates (Y.-K. Lee et al., 2007). The activation of these mechanisms may be ascribed to the processing parameters, for instance, hydrostatic compressive stress, strain rate, thermal treatments, as well as the composition of materials.

Constrained ductility was found for roughly various SPD treated specimens, thus future orientations in tubular components should be towards improving both mechanical strength and ductility for the reason that in most functions, the tubes are deformed to produce engineering constituents by means of forming procedures like tube hydroforming that takes advantage of ductile metals (Faraji et al., 2008).

In this regard, TCAP as an innovative high strain procedure is proper for deforming tubular bodies, wherein the tube substance is exposed to SPD using intermittent pressing

toward the inside of the tubular angular channel along with three shear regions. The strain–stress state and flow pattern of TCAP are contrasting those of common ECAP. This procedure comes with an extra compressive strain and radial tensile for the reason that the diameter of tube alters during the procedure and returns to the preliminary status in the last part. Thus, according to the capabilities of TCAP for producing UFG metals and alloys, its potentiality to simultaneously improve strength and ductility should be carefully assessed (Faraji et al., 2017). In the following section, some instances of metals and alloys processed by TCAP are described in details in terms of microstructural features, mechanical strength, and ductility.

### **2.3.6 TCAP-processed Metals and Alloys**

#### **2.3.6.1 Microstructural evolution and mechanical properties of magnesium-based alloys**

##### **(a) AZ91 magnesium alloy**

To demonstrate the feasibility of the TCAP procedure, an AZ91 Mg alloy was treated by Faraji et al. (2011c); (Faraji et al., 2014b). Cylindrical tubes were attained from as-cast ingots. In the TCAP die, the channel angles were  $\varphi_1 = \varphi_3 = 135^\circ$  and  $\varphi_2 = 90^\circ$ . In addition, the curvature angle and the outer corner angle  $\psi_2$  was  $90^\circ$  (Faraji et al., 2014b), while both the  $\psi_1$  and  $\psi_3$  were equal to  $0^\circ$ . The TCAP experimentations were executed at  $300^\circ\text{C}$  under a pressing velocity of  $5\text{ mm min}^{-1}$ . Figure 2.13(a) shows an AZ91 specimen in the TCAP procedure (Faraji et al., 2011c). It is reported that the diameter of the tube enlarged during the procedure and reverted to the primary dimension in the last part of the TCAP. The optical micrograph of the unprocessed sample is illustrated in Figure 2.13(b), which displays a distinctive dendritic configuration with an initial Mg implanted in a  $\text{Mg}_{17}\text{Al}_{12}$  network with an average grain size of  $150\ \mu\text{m}$ . In the processed alloy

(Figure 2.13 c and d), many equiaxed and dynamically recrystallized grains were observed. It is reported that the dynamic recrystallization in AZ91 alloy during SPD could happen at 300° C (Faraji et al., 2011b).

From the optical micrographs of the processed sample, the one-pass TCAP procedure has led to the refinement of the microstructure from the primary value of ~150 to ~1.5  $\mu\text{m}$ . Nevertheless, some undissolved  $\text{Mg}_{17}\text{Al}_{12}$  phases were observed in the microstructure. They also studied the microstructural alterations during TCAP parallel to the extrusion direction and found that there was almost no grain refinement in some areas. The deformation mode in these regions was constrained compression and unaffected the microstructural modification. In these circumstances, the intermetallic  $\text{Mg}_{17}\text{Al}_{12}$  turned into partly dissolved owing to the procedure temperature (Faraji & Asadi, 2011a). Nonetheless, the insufficient time did not let entire homogenization happen during the TCAP procedure. This shows that the segregation was declined, but not completely eliminated (S. Xu et al., 2006).

In view of the fact that diffusion of Al in Mg was rather gradual, the intermetallic  $\text{Mg}_{17}\text{Al}_{12}$  was present merely in zones of high Al-content as soon as cooling down from the processing temperature of 300° C. Based on the literature, the microstructural refinement of the AZ91 Mg alloy is drastically influenced by the amassed strain amounts. The feeding of the tube material into the shear region I lead to microstructural modification due to the shear strains. It is well-established that the deformation shear component plays a key function in the microstructural modification during SPD (Faraji et al., 2011b). The development of dynamically recrystallized twins as a consequence of the temperature of the procedure and the shear strain was also perceived.

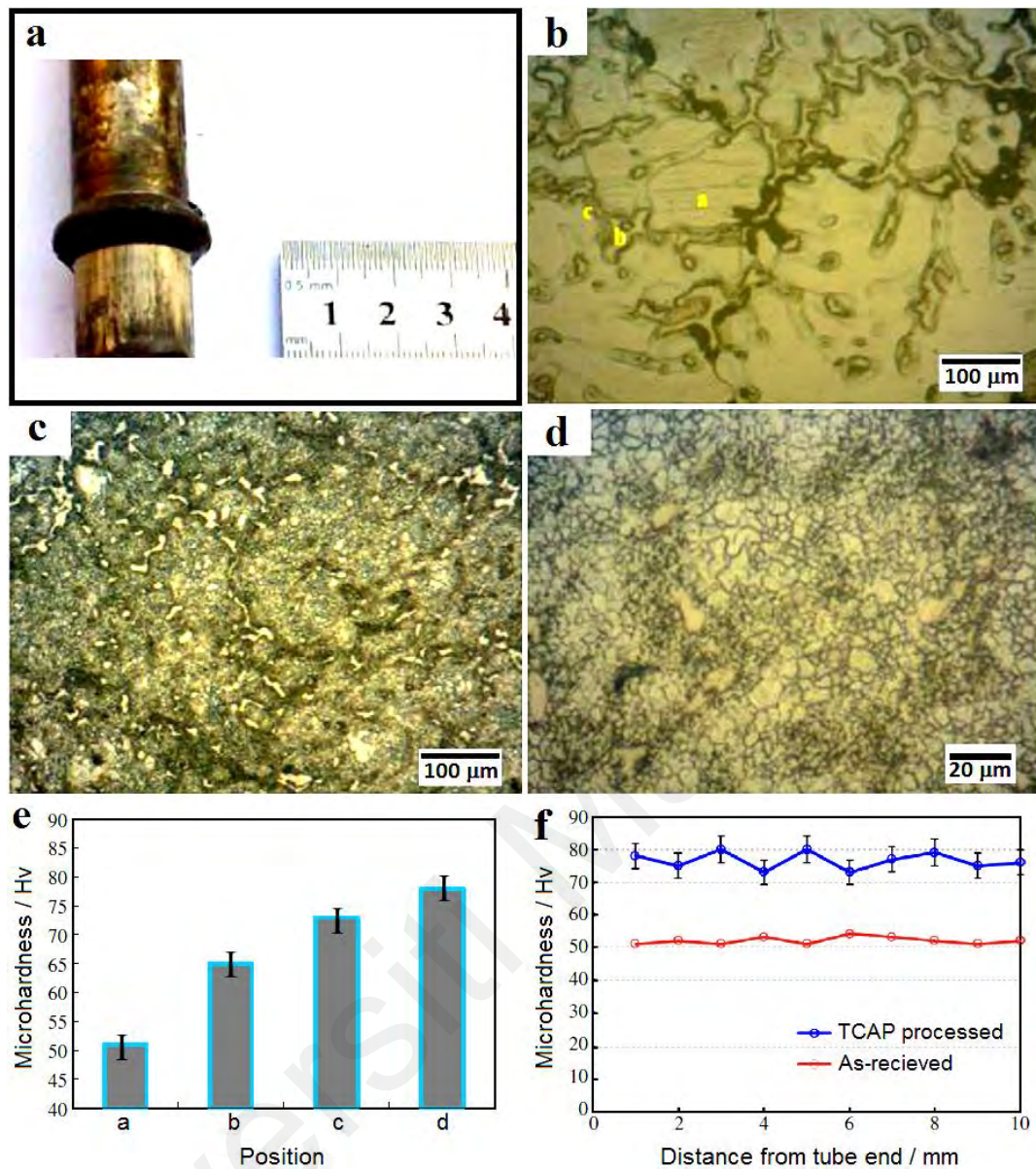


**Figure 2.13:** (a) An AZ91 specimen in the TCAP procedure, (b) optical images of the unprocessed body (a; initial  $\alpha$ -Mg, b; eutectic  $\alpha$ -Mg, c;  $\beta$  ( $Mg_{17}Al_{12}$ )), (c) and (d) distinctive micro configurations of one-pass TCAP processed alloy; (e) microhardness values in the dissimilar sites and (f) microhardness against distance from TCAP treated tube end (Faraji et al., 2011c).

According to Figure 2.13(e), the hardness enhanced remarkably for the TCAP treated tube transverse cutting following shear region I, attaining the utmost amount at the region following shear region III. It is obvious that the TCAP procedure enhanced the microhardness value to 78 HV from the primary amount of 51 HV. The microhardness of the tube is severely enhanced following passing every shear region. In general, it is approved that the hexagonal close-packed (hcp) metals like magnesium display a robust

reliance of mechanical strength and hardness on the microstructural features attributable to the lack of slip systems (Kleiner et al., 2004). The rise in the hardness value of the AZ91 alloy can be caused by the microstructural modification and to the dissolution and dispersal of the  $\beta$  phase. The  $Mg_{17}Al_{12}$  phase is a hard and brittle phase that is dispersed over the grain boundaries (Chino et al., 2003). Here, variations in microhardness are visible which are probably caused by the presence of several grains with larger average grain size and massive  $\beta$  phases that possess inferior hardness compared to the grain refined areas and dispersed  $\beta$  phase zones with elevated hardness (Faraji et al., 2011b). The microhardness variations of the treated tube in Figure 2.13(f) demonstrate that there exists a good uniformity throughout the length of the tube.

In another research, Reshadi et al. (2015) investigated the influence of deformation speed (1, 10, 20, 50, and 100 mm min<sup>-1</sup>) and temperature (150 and 250 °C) on magnesium AZ91 during TCAP. The results indicated that a rise in the ram speed caused superior strength and inferior elongation. Moreover, at a steady punch speed, a rise in the temperature of the process resulted in a diminution in the mechanical strength, while the elongation somewhat enhanced. The results also showed that the grain size of the processed alloy reduced to ~1  $\mu$ m from the primary amount of ~150  $\mu$ m. In general, the utilization of very low punch speeds throughout the SPD of hcp metals is an influential approach for improving the UFG hcp metals ductility whereas preserving the high mechanical strengths. The mean grain size and also elongation value at room temperature for the AZ91 alloy from various SPD processes are presented in Table 2.1. As can be seen, the TCAP treated sample at 250 °C at lower punch speed has the utmost ductility at room temperature relative to other processes. This confirms the high potentiality of the TCAP process for enhancing the ductility of high strength UFG AZ91 Mg alloy at fairly lower temperatures.

**Table 2.1:** Grain size and ductility of AZ91 alloy at room temperature caused by a variety of SPD methods.

Method	Temperature (°C)	Number of passes	Strain rate (s <sup>-1</sup> )	Average grain size (μm)	Ductility	Reference
ECAP	270	8	$5 \times 10^{-4}$	1.2	5	[73]
ARB	375	1	$10^{-3}$	0.5	2.2	[74]
ARB	375	4	$10^{-3}$	< 1	2.4	[74]
TCAP	250	1	$10^{-3}$	~2.4	9.7	[72]
TCAP	150	1	$10^{-3}$	~1	7	[72]

(b) *AZ31C magnesium alloy*

In addition to AZ91 alloy, the pass-number influence on the microstructural evolution and mechanical behaviour of the TCAP treated AZ31C Mg alloy at 300° C was studied by Mohammadi et al. (2015). In this regard, the pressing process was executed via four-passes over AZ31C Mg tubes and in each pass, the specimen was exposed to mechanical assessments. Figure 2.14(a–c) shows an AZ31C workpiece prior to and after the TCAP along with the tensile test sample (Mohammadi et al., 2015). Moreover, optical micrographs of the unprocessed and processed samples after one, two, three, and four passes of TCAP, as well as the mechanical behaviour as a function of the TCAP pass number are also shown in this figure.

From the optical micrographs in Figure 2.14(e–h), TCAP led to the significant refinements in the microstructure and accordingly an average grain size of around 6, 7.5, 7.2, and 7.8 μm was obtained after one, two, three and four TCAP passes, respectively. These micrographs confirm the development of the recrystallized grains along with the coarse grains surrounded by ultrafine grains after the TCAP process. The results of microhardness assessment showed that the hardness value of the one-pass specimen increased around 29%, however, no significant changes in the microhardness were observed as the number of TCAP passes raised to four (Figure 2.14(i)). According to Figure 2.14(j), there was no significant improvement in elongation. In addition,  $\sigma_{Yield}$  and  $\sigma_{UTS}$  increased to 1.97 and 1.49 times compared to the unprocessed sample (Figure

2.14(k) and (l)). A substantial intensification in mechanical strength was monitored after two-passes of TCAP, whereas a higher number of passes had no major effect (Mohammadi et al., 2015).

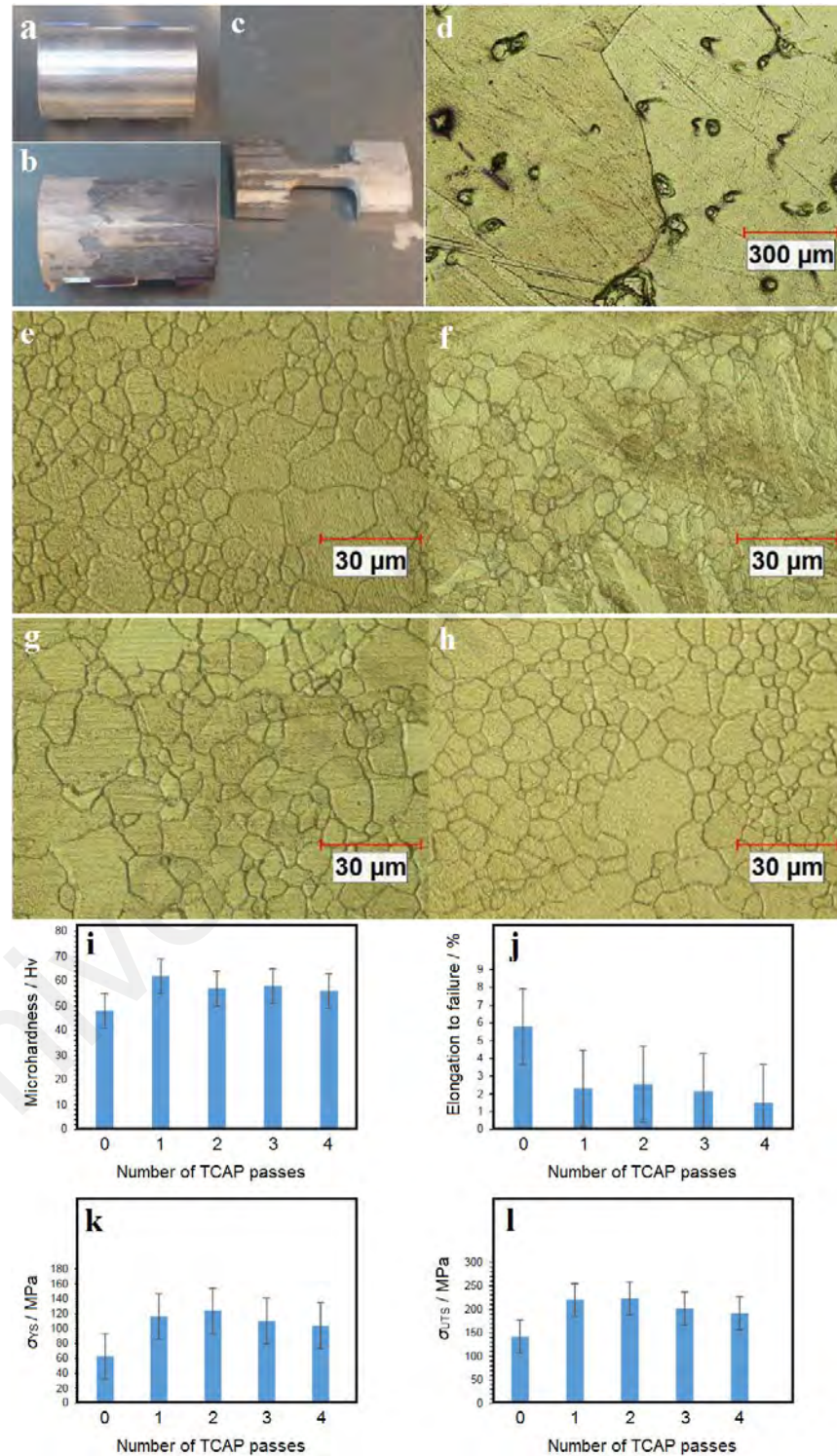


**Figure 2.14:** An AZ31C workpiece (a) before and (b) after TCAP along with the (c) tensile test sample; optical micrographs of the (d) unprocessed and processed samples after (e) one, (f) two, (g) three, and (h) four pass as well as mechanical behaviour as a function of the number of passes: (i) microhardness values, (j) elongation to failure, (k)  $\sigma_{YS}$ , and (l)  $\sigma_{UTS}$  (Mohammadi et al., 2015).

### **2.3.6.2 Microstructural and mechanical properties of commercially pure copper**

The perfection of SPD effectiveness by declining the pressing load is a major challenge for the industrialization of these methods. In this regard, Faraji et al. (2014a) studied the effects of ultrasonic vibration amplitudes in axial and radial directions on the deformation performance and requisite punch force of the TCAP of the commercially pure copper tube using the FEA. The numerical results showed that the level of the required effectual strain and the consistency of strain spreading increased by utilizing the ultrasonic vibration. Moreover, higher ultrasonic vibration amplitude resulted in a rise in effectual strain and augmentation of strain distribution. On the other hand, simulation results revealed that the utilization of ultrasonic vibration requires an inferior pressing force to perform the TCAP procedure. A much lower punch load is also needed by adding the vibration amplitude. It was found that the effect of radial directional ultrasonic vibration is a more prevailing feature compared to the axial one, on both strain functioning and pressing force. It seems that the ultrasonic vibration of TCAP die is more important compared to the ultrasonic vibration of either mandrel or punch (Faraji et al., 2014a).

### **2.4 Parallel Tubular Channel Angular Channel (PTCAP) and Process Parameters**

Although it is capable of applying high hydrostatic compressive stress to the substance, that is vital for attaining UFG configuration with high-angle grain boundaries (Estrin et al., 2013), there is an important restriction in the TCAP procedure which is the amount of required processing load. In general, the whole process load is the summation of deformation and frictional forces. The deformation force stays steady as the tube length is altered. Nonetheless, the friction force varies severely for long tubes, and subsequently, the total force will enhance. There is a constraint in the tube length owing to the hollow geometry of the cylindrical punch with restricted  $\sigma_{YS}$  and buckling strength ( $\sigma_{cr}$ ). As the

length of the tube enhances, the length of the hollow punch is required to be raised, leading to a reduction in  $\sigma_{cr}$ . The ultimate constraint on the length of a tube treated in this process is reliant on a grouping of parameters including thickness and diameter of the tube, the tube material, lubricant, and die geometry. For instance, the tube length must not surpass ~40 mm for the processes in Faraji et al. using the AZ91 tubing (Faraji et al., 2011c), otherwise, the punch will not succeed. Therefore, the reduction of the processing load may be an important contest for SPD processes. To overcome this problem, Faraji et al. (2012a) introduced the PTCAP process in 2012.

#### 2.4.1 Principles of PTCAP

Generally, the PTCAP procedure is composed of two half-cycles as schematically illustrated in Figure 2.15. From Figure 2.15(a), on the brink of the process, the primary tube is put into the gap between the mandrel and die. In the first half-cycle, the tube substance is extruded by the first punch into an angular tubular channel possessing two axisymmetric shear regions, so that the tube diameter increases (Figure 2.15(b)).

The tube substance, in the second half-cycle, is next re-extruded into the shear regions through the second punch at the other end of the tube. This procedure may be replicated as many times as required to achieve a distinct strain, without any variation to the transverse cutting of the sample.

A high plastic strain can be formed in the shear region due to the accumulative shear strain at each pass. Tensile and compression circumferential strains are attained throughout the first and second half cycles of the PTCAP process, respectively. In this type of SPD process, taking into account the presence of radial and circumferential strains (Estrin et al., 2013), the total accumulated plastic strain ( $\bar{\epsilon}_{TN}$ ) level after N PTCAP passes

arising from the shear and normal strains can be determined using the following relationship (Faraji et al., 2014b), which is developed from the die geometry (Figure 2.15 (d)) and engineering plasticity equation (C. Wang et al., 2012):

$$\bar{\epsilon}_{TN} = 2N \left\{ \sum_{i=1}^2 \left[ \frac{2 \cot(\varphi_i/2 + \psi_i/2) + \psi_i \operatorname{cosec}(\varphi_i/2 + \psi_i/2)}{\sqrt{3}} \right] + \bar{\epsilon}_\theta \right\} \quad (\text{Eq. 2.11})$$

where  $\bar{\epsilon}_{TN}$ ,  $N$ ,  $\varphi_i$ , and  $\psi_i$  are respectively total accumulated plastic strain, number of PTCAP passes, channel angles, and curvature angles.

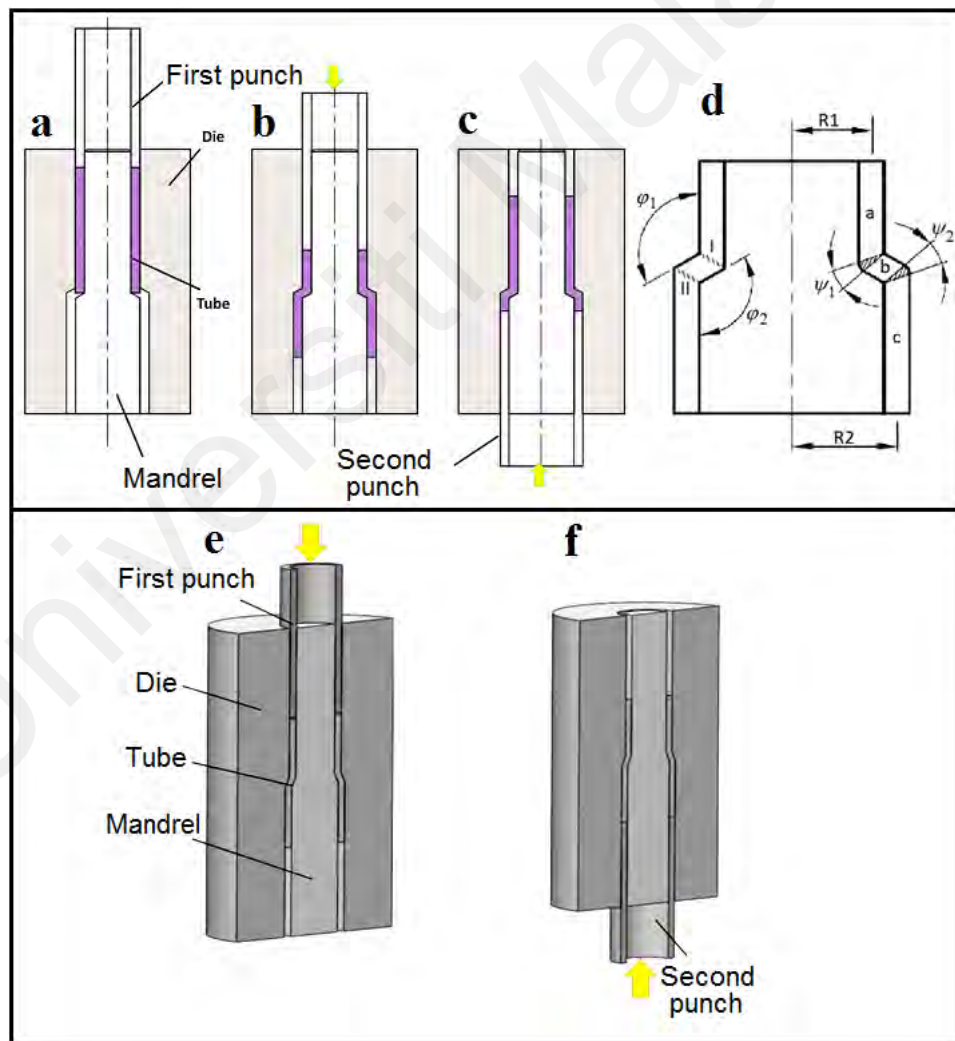


**Figure 2.15:** Schematic diagram of the PTCAP procedure (a) primary state, (b) the first and (c) second half-cycles as well as (d) die factors; schematic of the hybrid procedure, including (e) first and (f) second half-cycles of PTCAP.

In this equation,  $\bar{\varepsilon}_\theta = \frac{2}{\sqrt{3}}\varepsilon_\theta$  and  $\varepsilon_\theta = \ln \frac{R_2}{R_1}$ , where  $R_1$  and  $R_2$  are shown in Figure 2.15(h). In accordance with this equation, the proposed process applies an equivalent plastic strain of  $\sim 1.8$  after each PTCAP pass. Therefore, the strain values after the second and third PTCAP pass were 3.6 and 5.4, respectively. Compared to the TCAP procedure,  $\sim 60\%$  lower process load could be employed in the PTCAP method (Faraji et al., 2012a). This is a major benefit of the PTCAP, where the processing of longer tubes is achievable compared to the TCAP procedure.

In order to investigate the effective parameters on deformation behaviour and the required load of the PTCAP process, various items including; channel angle, curvature angles, and deformation ratio should be taken into account. Thus, in this section, the effects of the aforementioned parameters on plastic deformation behaviour, imposed strain, and strain homogeneity will be discussed.

#### 2.4.2 Effects of Channel Angle

In order to examine the effect of the channel angle  $\varphi_1 = \varphi_2$  shown in Figure 2.15(d), six different angles were considered. Here the curvature angle is equal to zero, and the coefficient of friction was assumed 0.05. Figure 2.16 demonstrates the influence of channel angle  $\varphi_1 = \varphi_2$  on the plastic strain contour variation after the first and also the second half cycle of the PTCAP process. As can be seen by increasing the value of the channel angle, the imposed strain level will be decreased at the end of both half passes. By performing the first-half pass, some tube thinning is observed due to the existence of peripheral tensile strains which can be associated with the enhancement of the tube diameter. So, the thickness of the tube is lesser than its original amount. (Faraji et al., 2012b).

From Figure 2.16(a), it can be figured out that minimum tube thinning is happened in the channel angle  $100^\circ$ . The reason behind this phenomenon can be associated with the presence of advanced hydrostatic pressure in this situation in comparison with other cases. This phenomenon similarly occurs in the multi-pass ECAP process (H.S. Kim, 2002).

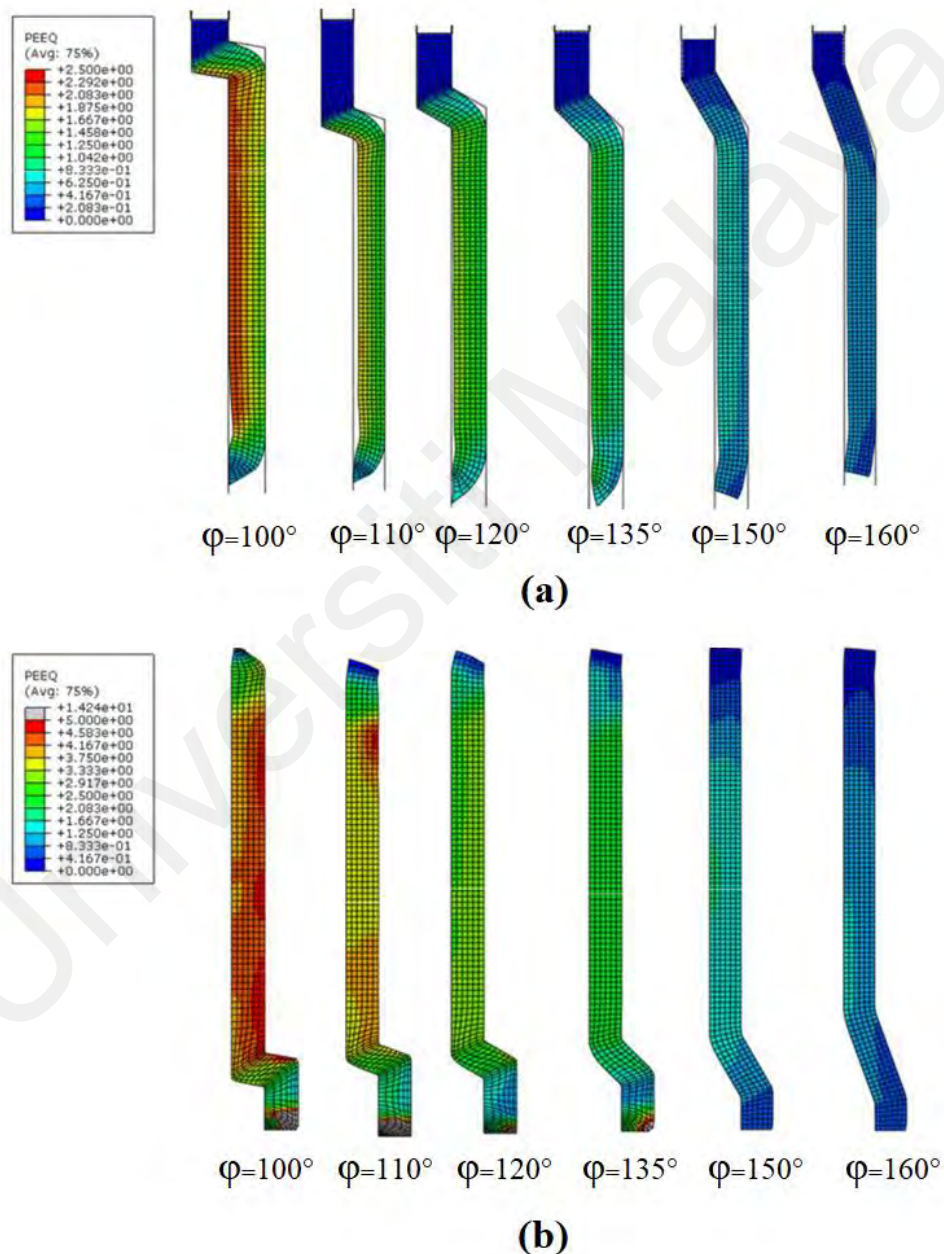
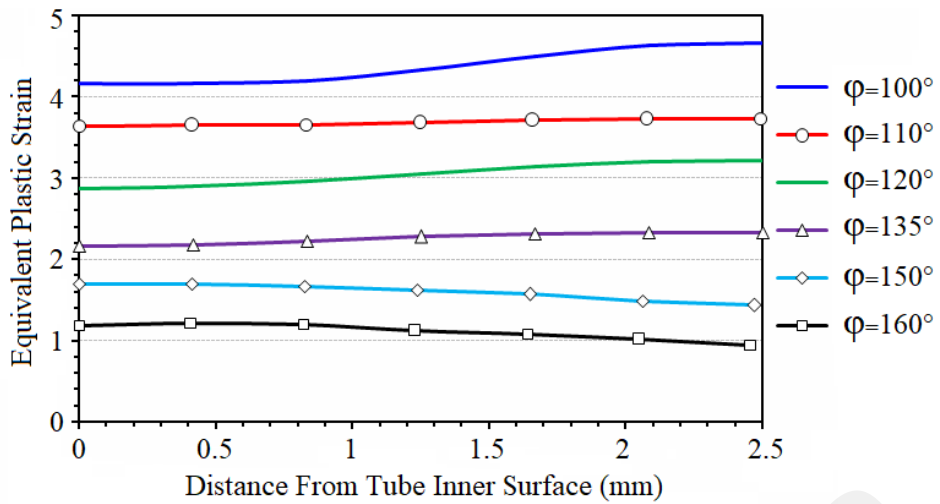


**Figure 2.16:** Influence of the channel angle on effective strain contour obtained by finite element method after (a) the first half pass, (b) the second half pass (Faraji & Mosavi Mashhadi, 2013b).

The existence of hydrostatic pressure in the first corner resulted from the next corners leads to compensation for some tube thinning. The tube thinning has its highest value at channel angles of 110° and the lowest value at 100°. By taking the tail part of the processed tube into account, after performing the first half pass according to Figure 2.16 (a), it can be figured out that the wasted useless part of the tube can be decreased by raising the amount of the channel angle. Nevertheless, tube thinning is retaliated in the second half pass owing to the enforcement of compressive peripheral strains caused by a reduction in the tube diameter.

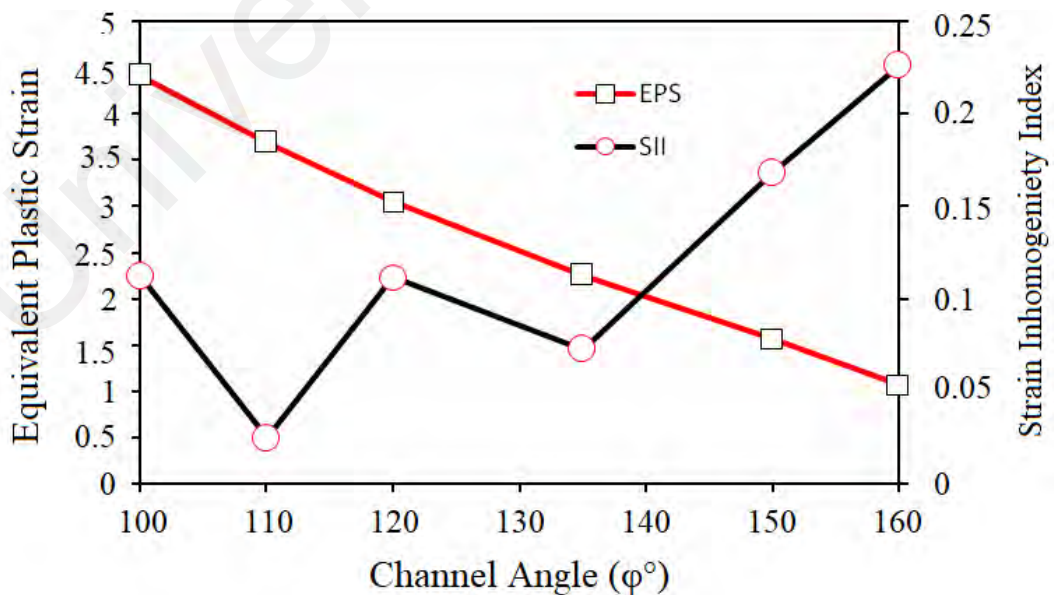
It can be discovered from Figure 2.16(b) that the tube attains its original size after each complete pass in almost all channel angles. This is the main characteristic of SPD processes. (Faraji et al., 2013b).

Figure 2.17 demonstrates the effective plastic strain values along the tube thickness for different angles of the channel in the process PTCAP sample. It is observed that by increasing the channel angle, the effective strain value decreases. Up to 135°, the strain value on the internal surface of the tube is slightly less than the strain value on the external surface. At angles above 135°, this trend is changed. Perhaps the development of a second-corner empty space at angles above 135 degrees could be the reason. According to this figure, the average effective strain along the thickness for channel angles of 100°, 110°, 120°, 135°, 150°, and 160°, are respectively 4.4, 3.7, 3.05, 2.25, 1.55 and 1.05. Internal microstructure homogeneity and therefore the amount of homogeneity in hardness evaluation will be significantly changed by the homogeneity of imposed plastic strains. Hence, Strain inhomogeneity index was specified to express the strain inhomogeneity as  $SII = (\epsilon_{Max} - \epsilon_{Min}) / \epsilon_{Ave}$  where  $\epsilon_{Max}$ ,  $\epsilon_{Min}$  and  $\epsilon_{Ave}$  designate highest, lowest and average equivalent plastic strains throughout the processed tube thickness, one-to-one (Faraji et al., 2013b).

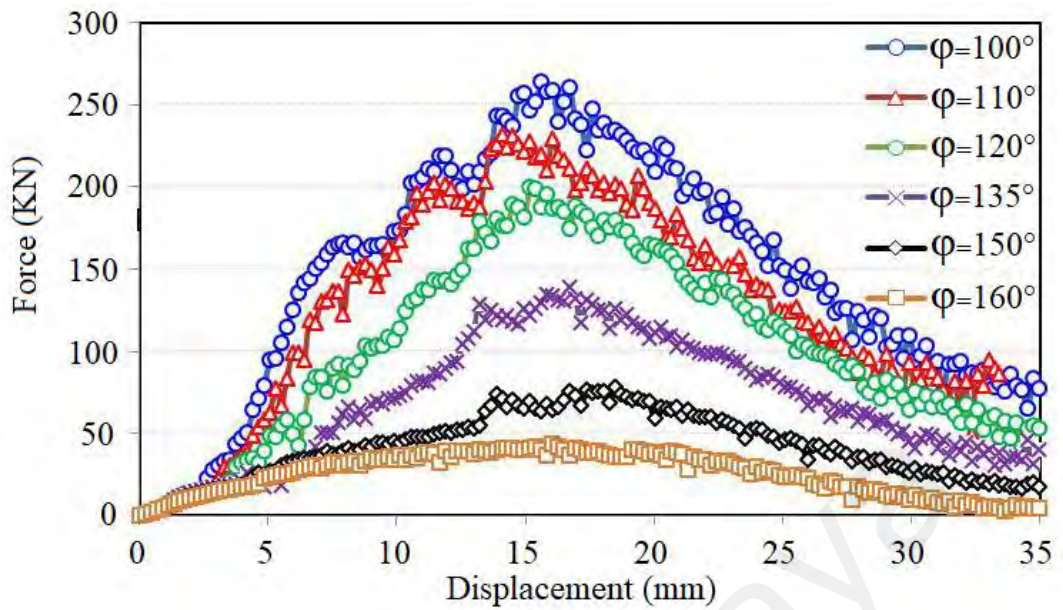


**Figure 2.17:** Diagrams of strain values along the thickness of the sample at different channel angles obtained by the finite element method end of the second half pass (Faraji et al., 2013b).

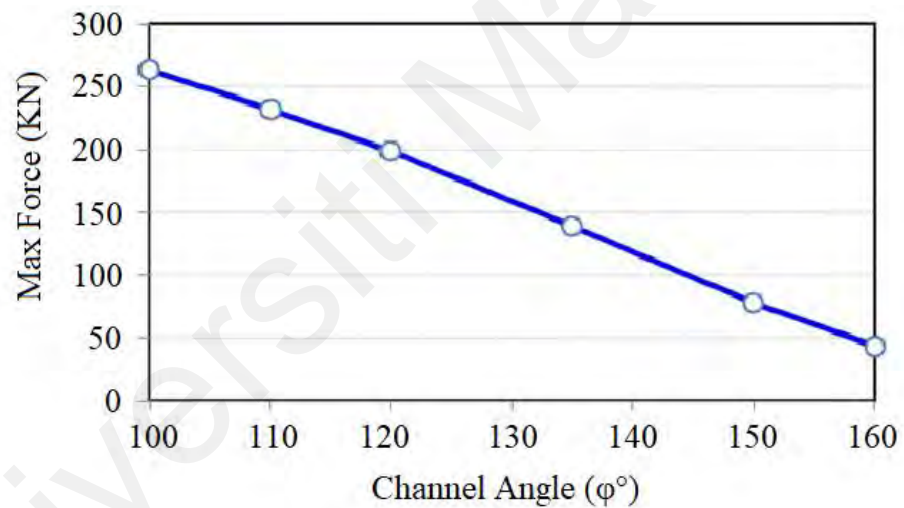
Figure 2.18. illustrates the impacts of channel angle on strain inhomogeneity index. It can be found that the process of strain alteration shows almost a linear relationship. Furthermore, in the SII graph, there is no specific trend until the angle of 135° but there are increases after 135°. In other words, enhancements of the channel angle after 135°, lead improvements in the strain inhomogeneity index.



**Figure 2.18:** Effect of channel angle on the mean strain value and strain inhomogeneity index (Faraji et al., 2013b).



(a)



(b)

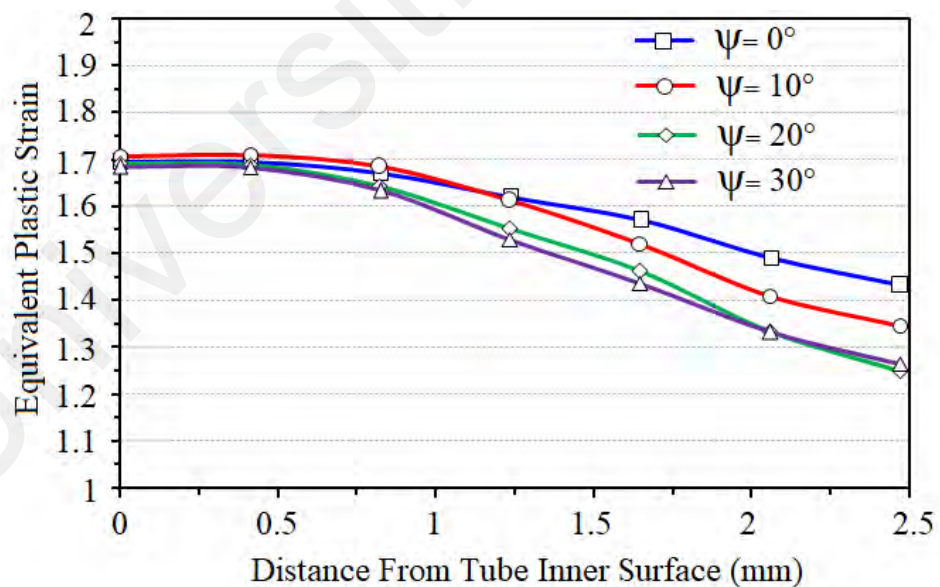
**Figure 2.19:** (a) The influence of channel angle on the force-displacement diagram in the PTCAP process (b) effect of the channel angle on the maximum force obtained by the finite element method

Figure 2.19(a) displays the influence of the channel angle on the force-displacement diagram in the PTCAP process. Increasing the channel angle reduces the essential process force, and thus choosing higher values of channel angles would be more desirable in terms of required equipment and the cost of the process. In the force history, it's remarkable

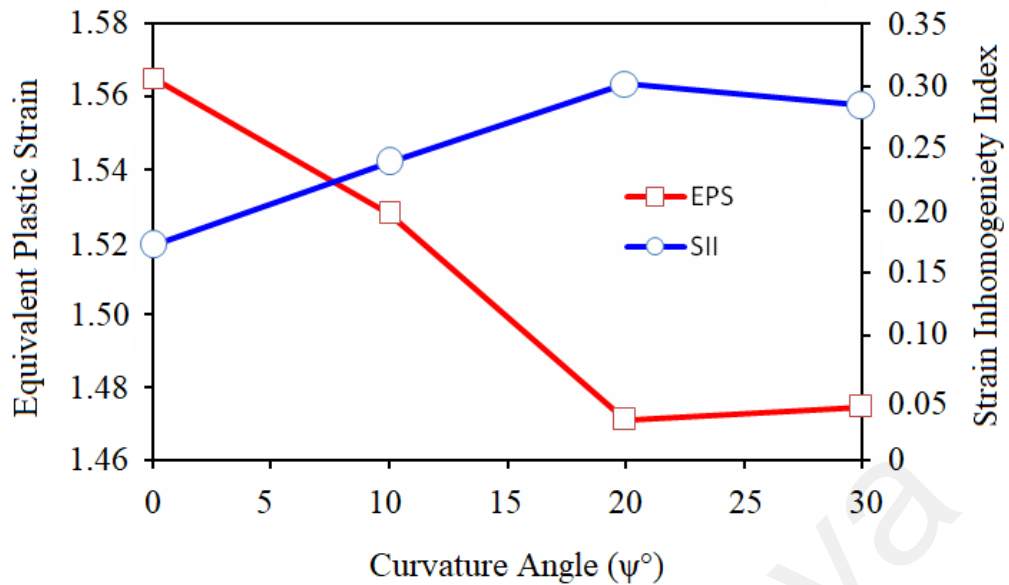
that all the graphs approach to a lower value. The reason behind this phenomenon can be associated with the friction force, in which a normal force multiplied by a friction coefficient in the Coulomb friction model (Faraji et al., 2012d). The peak loads consistent with diverse channel angles have been shown in Figure 2.19(b). It is clear that the curve trend appears to be almost linear (Faraji et al., 2013b).

### 2.4.3 Effects of Curvature Angle

Figure 2.20 demonstrates the impacts of curvature angle  $\psi_1 = \psi_2$  on the imposed plastic strain through the PTCAP processed tube thickness. The variation of the curvature angle does not affect the strain value at the inner surface of the tube but increasing the curvature angle decreases the effective strain value at the outer surface of the tube. This means that strain homogeneity decreases with increasing curvature angle.



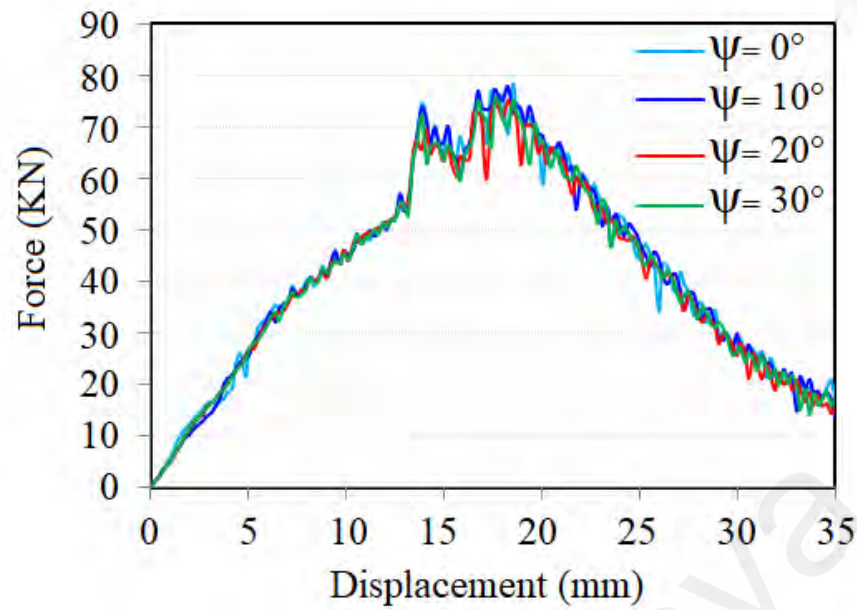
**Figure 2.20:** The impacts of curvature angle  $\psi_1 = \psi_2$  on the imposed plastic strain through tube thickness. (Faraji et al., 2013b).



**Figure 2.21:** Impacts of the curvature angle on the mean strain and strain inhomogeneity index (Faraji et al., 2013b).

The mean strain variations and strain inhomogeneity index with the variation of the curvature angle along the thickness of the PTCAP processed tube has been shown in Figure 2.21. The mean strain value decreases by increasing the curvature angle up to  $20^\circ$ , whereas increasing the curvature angle to the values above  $20^\circ$ , almost does not affect it. In addition, this enhancement will lead to an increase in the strain inhomogeneity index. Hence, the strain homogeneity is better at lower curvature angles. (Faraji et al., 2013b).

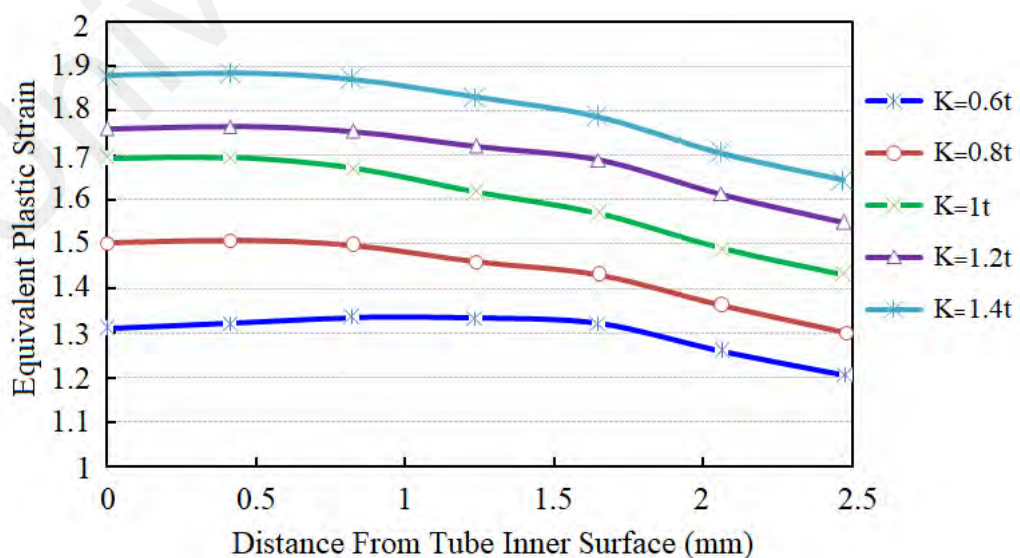
Figure 2.22 presents the effect of the curvature angle on the displacement force diagram in the PTCAP process. A comparison of the diagrams at different angles of curvature shows that changing the angle of curvature does not have much effect on the required force in the PTCAP process. Accordingly, it leads to a finding that choosing the curvature angle of zero would be the best option.



**Figure 2.22:** FE calculated load-displacement curves in different curvature angles (Faraji et al., 2013b).

#### 2.4.4 Effects of the Deformation Ratio

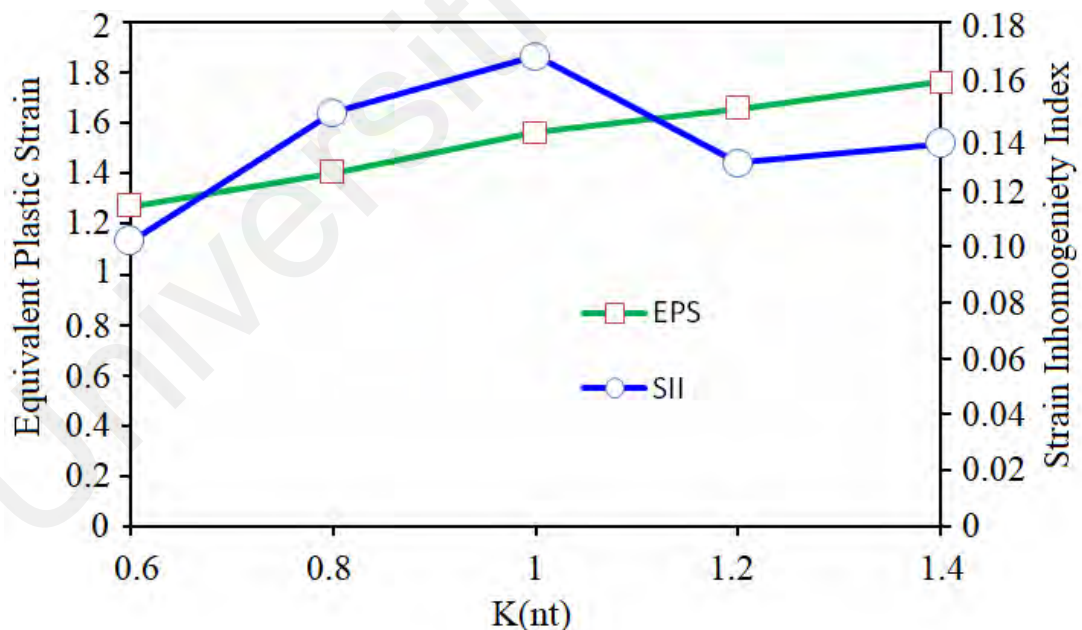
To study the impacts of the deformation ratio, the variable of  $K = R2 - R1$  was defined. Then, different  $K$  values of  $0.6t_0$ ,  $0.8t_0$ ,  $1t_0$ ,  $1.2t_0$ , and  $1.4t_0$  were considered. The effect of deformation ratio ( $K$  value), on the strain value through the PTCAP processed tube thickness has been shown in Figure 2.23.



**Figure 2.23:** The effect of ( $K$ ) value on the strain value through the PTCAP processed tube thickness (Faraji et al., 2013b).

The figure demonstrates an increase in the deformation ratio leading to an increase in the amount of imposed strain. This increase is not due to the applied shear strain at the corners, but because of the increase in the vertical strain due to the alteration in tube diameter. All the curves have the same trend so that the strain in the inner surface of the tube is more than that of the outer surface.

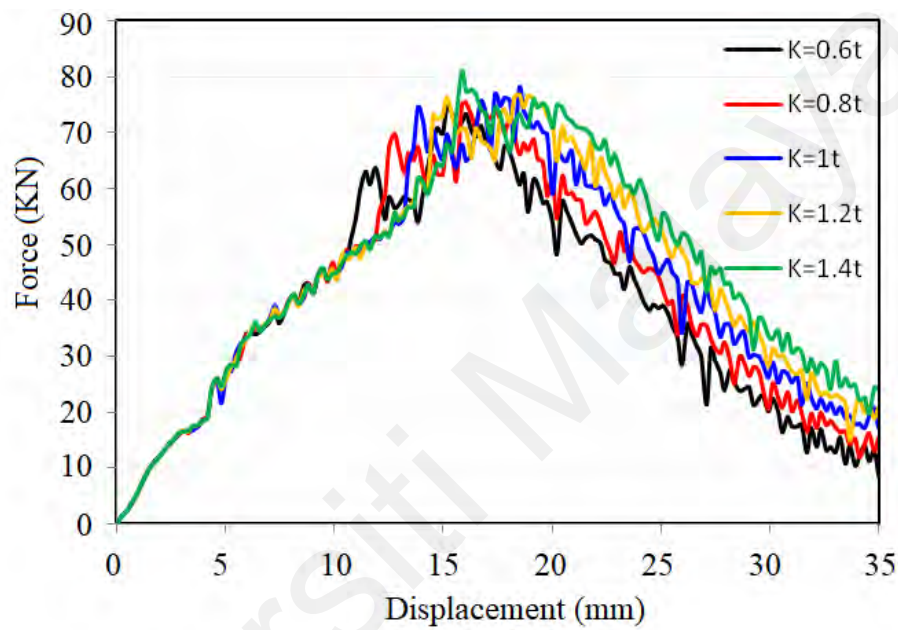
Figure 2.24 displays the influence of K value on the strain inhomogeneity index and mean equivalent strain. The mean equivalent plastic strain increases almost linearly with the increase of K value. Since the total effective strain comprises the normal and shear components, the increase in linear trend can be caused by an increase in the normal strain contribution to the total effective strain value. Also, as can be seen at the above figure, there is no specific trend in the strain inhomogeneity index curve. Nevertheless, the best strain homogeneity could be reached in K equal to 0.6 and the worst at K=1, separately.



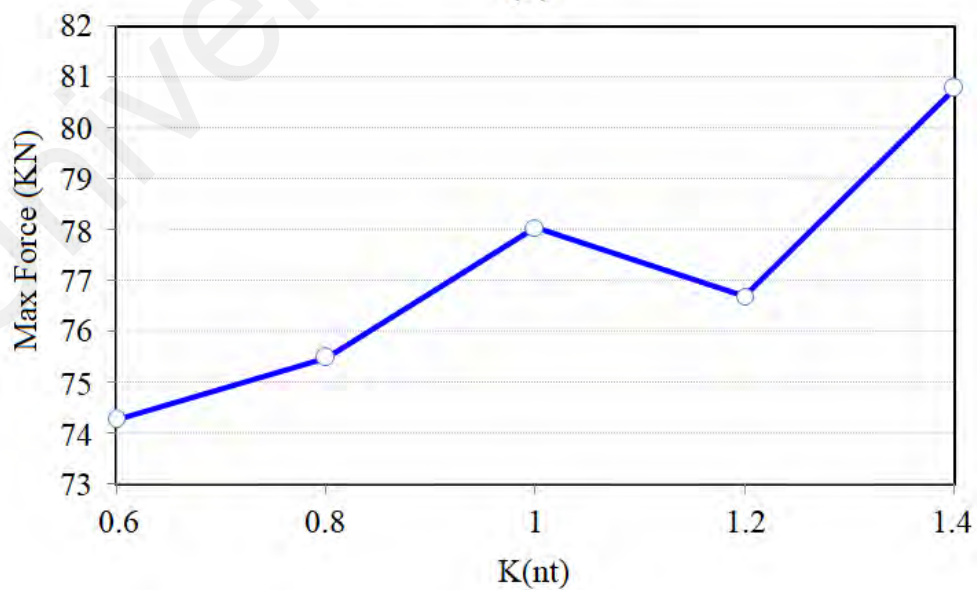
**Figure 2.24:** Effect of K value on the mean strain and strain inhomogeneity index (Faraji et al., 2013b).

Figure 2.25(a) demonstrates the impacts of K value on the load-displacement curve in the PTCAP process. All diagrams follow a similar trend, and the difference in the position

of maximum force is due to the increase in the tube trace length between the two consecutive shear zones in greater quantities of  $K$  which consequently causes the diagram to be drawn to the right. The peak load versus  $K$  value has been shown in Figure 2.25(b). It can be discovered that an increase in the  $K$  value leads to an increase in the peak load. Therefore, it could be concluded that choosing the  $K$  value of (0.6) would be the best choice in terms of gaining the best strain homogeneity and lowest process load.



(a)



(b)

**Figure 2.25:** Effect of  $K$  value on (a) load-displacement curve and (b) the peak required load (Faraji et al., 2013b).

### 2.4.5 Properties and Applications

As mentioned above, all tube SPD processes give rise to considerable enhancement of mechanical strength with the loss of ductility. In fact, only in some rare cases both of these features have been improved concurrently. For instance, a PTCAP procedure followed by the TBE of AZ31 Mg alloy at 250° C and up to a strain of around 2.8 caused a dramatic improvement in  $\sigma_{UTS}$  to ~330 MPa and 13% elongation (Abdolvand et al., 2015b). In this case, elevated hydrostatic stress and plastic strains at the TBE process led to the further grain refinement to ~3  $\mu\text{m}$ , where the development of equiaxed with a large misorientation was observed. At the same time, comparatively lower mechanical strength (210 MPa) and elongation (5%) were attained from TCAP of AZ31 Mg alloy at a strain of ~6.6 at 300° C compared to the hybrid approach (PTCAP+TBE). One of the major directions of the SPD processing of tubes is their utilization as the structural modules in actual applications. Therefore, the evaluation of other properties and special capacities, for instance, pressure-bearing capability for high-pressure tubing purpose, superplastic performance, crushing feature with axial loading, fatigue behaviour, and thermal conductivity as well as formability for hydroforming target is very important for the further development of the SPD processes in various applications.

Among these properties, only the pressure-bearing ability (Abdolvand et al., 2015a) and crushing behaviour of the SPD processed tubes are investigated so far. Afrasiab et al. (2014) reported an outstanding energy-absorption ability of UFG brass tubes processed by PTCAP and indicated that the microstructural refinement caused alterations in the post-buckling modes of the thin-walled brass tube, thereby resulted in a significant increase in the capability of energy-absorption from 49.56 to 162.51 J and 197 J in the case of the first and second passes of the treated tubes, respectively (Afrasiab et al., 2014). They proved that the UFG and nanostructured thin-walled tubes exhibit a superb

capability of energy-absorption, which has improved around four times relative to the coarse-grained structures (Afrasiab et al., 2014).

Additionally, from the perspective of industrial application, the pressure-bearing capability of a tube specimen is more significant compared to uniaxial tensile performance. In this regard, it is found that the nanostructured and UFG tubes processed by the PTCAP possess an outstanding pressure-bearing ability compared to the coarse-grained structures (Abdolvand et al., 2015a). Moreover, the bursting pressure of the UFG tube enhanced prominently to 93 MPa following just the one-pass PTCAP from an initial value of 43.3 MPa in the case of the coarse-grained sample. Besides, the bursting pressure of 88 MPa following two-pass and 81.3 MPa after three-pass PTCAP was achieved (Abdolvand et al., 2015a).

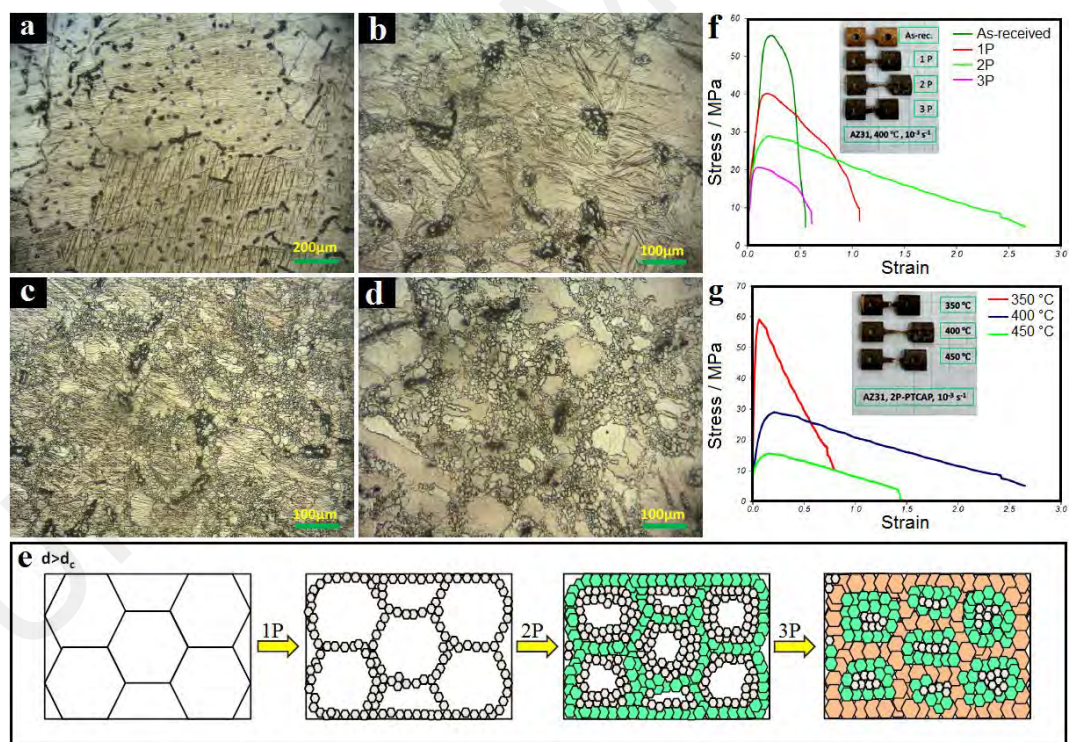
#### **2.4.6 PTCAP-processed Metals and Alloys**

##### **2.4.6.1 Microstructural and mechanical properties of magnesium-based alloys**

###### **(a) AZ31 Magnesium alloy**

As mentioned above, a hybrid approach including PTCAP and TBE is recommended by Abdolvand et al. (2015b) for the fabrication of thin-walled UFG AZ31 Mg tubes. The results indicated that the microhardness of the processed tube enhanced drastically to 70 HV from a primary value of 38 HV. In a similar approach, Fata et al. (2018) employed a mix of two processes: PTCAP and TBE at 300° C to produce an UFG AZ31 Mg tube. They studied the microstructural evolution, hardness, fractography behaviour and tensile features of the processed specimens at room temperature. To appraise the hot tensile ductility of the processed bodies, the analysis was also done at a high temperature of 400° C, after that the fractured surface of the tensile specimens was assessed. The microstructural observations exhibited a bimodal configuration composed of large grains

surrounded by many smaller ones. This microstructural modification resulted in a simultaneous increase in hardness and mechanical strength at room temperature and also caused an elevated elongation of around 181% at 400° C. The fractographic SEM micrographs also revealed the incidence of typically ductile fracture in the specimens pulled at 400° C. The same group also employed the PTCAP procedure on AZ31 Mg alloy tubes to attain an UFG configuration (Fata et al., 2016, 2017b). Figure 2.26(a) shows the microstructure of the unprocessed alloy with an average grain size of around 520  $\mu\text{m}$ . Figure 2.26(b–d) also displays the microstructure of multi-pass PTCAP processed tubes. From these micrographs, new finer grains are developed in the direction of the primary grain boundaries and a necklace-like array is formed, which is in good agreement with previous observations (Figueiredo & Langdon, 2009).



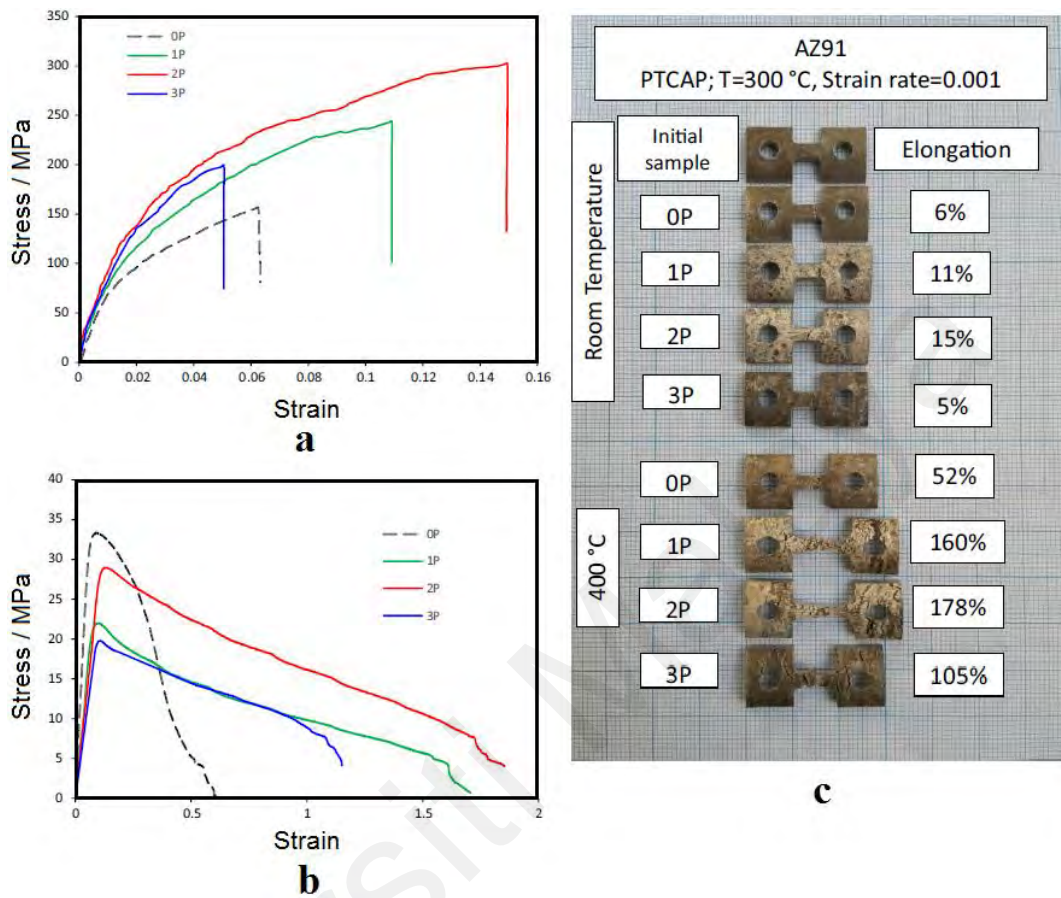
**Figure 2.26:** Optical micrographs of the (a) unprocessed and (b) one, (c) two, and (d) three-pass PTCAP treated bodies as well as (e) a schematic view of the microstructural modification of AZ31 during PTCAP; (f) Engineering stress-strain plots of unprocessed, multi-pass processed specimens examined at 400° C and (g) two-pass PTCAP treated tube at a range of temperatures between 350° C and 450° C (Fata et al., 2016, 2017b).

Figure 2.26(e) illustrates a schematic view of the grain refinement mechanism of AZ31 Mg alloy during PTCAP on the basis of pass number, where the grain nucleation in the direction of the pre-existed boundaries in lower PTCAP passes and their expansion by elevated PTCAP passes resulted in a roughly equiaxed grain configuration in the AZ31 Mg alloy tube. From Figure 2.26(f), the two-pass PTCAP processed specimen possesses 263% elongation to failure at 400° C. Accordingly, to examine the effect of temperature, the two-pass PTCAP processed specimen was chosen to pull out at a range of temperatures between 350° C and 450° C, as shown in Figure 2.26(g).

From this figure, the maximum amount of mechanical strength is achieved at 350° C. Nonetheless, this specimen was quickly cracked at a fairly low elongation of ~79%. Although around 50% lower peak strength was detected at 400° C relative to the 350° C counterpart, the specimen showed a more dynamic process and the elongation increased to 263%. The result also revealed a diminishing behaviour in the mean grain size along the gripper section to the failure tip of the fractured UFG specimen. The hardness enhanced from the gripper zone to the end of the gauge section close to the fracture tip. However, the hardness declined at the fracture tip because of the development of cavity and micro-voids in this region during the tensile test.

Fata and his group in a complementary study evaluated the hot tensile behaviour of the UFG AZ31 Mg alloy tube processed by PTCAP in terms of pass number at 300° C (Fata et al., 2017a). As shown in Figure 2.27(a), a rise in the strain caused a significant increase in mechanical strength and elongation of the processed tubes at room temperature. The unprocessed sample showed a poor softening behaviour because of having a coarse grain structure. In contrast, a good softening property was achieved following the PTCAP procedure due to the grain refinement by dynamic recrystallization, nucleation, and

coarsening of  $\beta$  phase precipitates as well as grain growth during the tensile deformation (Faraji et al., 2012f).



**Figure 2.27:** Engineering stress-strain plots of AZ31 Mg tubes at (a) room temperature and (b) 400° C as well as (c) the feature of fractured samples following the tensile test. (Fata et al., 2017a)

This behaviour strictly counts on the deformation temperature. The results showed that the mechanical strength enhanced to around 92% following the second-pass PTCAP, while only 56% increase in strength was detected after the first-pass PTCAP. The elongation relatively enhanced also at room temperature. From Figure 2.27(b) and (c), the maximum elongation of 178% was obtained for the two-pass PTCAP treated tube at 400° C tensile test, while an elongation of 105% was observed in the case of three-pass processed tube, which was most likely caused by the grain growth and microcrack development during the third-pass PTCAP procedure (Fata et al., 2017a).

In another study, they also investigated the deformation trend of the AZ31 Mg alloy tubes treated by multi-pass PTCAP, where the tensile assessment was done at a range of temperatures between 25° C and 450° C. The strain rate sensitivity exponent ( $m$ ) was also calculated for the four-pass PTCAP treated tube, at 350, 400 and 450° C and strain rates of  $10^{-2}$ ,  $10^{-3}$  and  $10^{-4} \text{ s}^{-1}$ , where the mean value of  $m$  coefficients was around 0.3 (Eftekhari et al., 2018).

Based on the microstructural investigations, a bimodal configuration was observed following the first-pass of PTCAP, while additional PTCAP passes resulted in a significant microstructure refinement and uniformity. In consequence of the sliding of grain boundary as the governing deformation mechanism, an elevated elongation to failure of ~281% was attained at 450° C and an inferior strain rate of  $10^{-4} \text{ s}^{-1}$ . Additionally, the Vickers microhardness results indicated that due to the significant microstructure refinement, the value of hardness increased particularly by rising the pass number of PTCAP. The fractographic SEM micrographs also indicated that a considerably ductile rupture took place in all examined specimens (Eftekhari et al., 2018). A summary of the research findings on the ductility of SPD-processed AZ31 Mg alloy are summarized in Table 2.2 (Eftekhari et al., 2018; Fata et al., 2016, 2017b; Figueiredo et al., 2009; Figueiredo & Langdon, 2010; Kang et al., 2008; Lin et al., 2005; Xu et al., 2015).

It was found that the grain size plays a significant role in attaining the superplastic performance. For instance, the eight-pass ECAP processed specimen with a mean grain size of 0.7  $\mu\text{m}$  exhibited a high elongation to failure of 460%. Another vital factor in the superplasticity is temperature, where the impact of temperature during the tensile test on the variations of elongation to failure is reported by Figueiredo et al. (2010). Among all the processed AZ31 alloy tubes, the four-pass PTCAP treated specimen pulled at 450° C and  $10^{-4} \text{ s}^{-1}$  possesses the best elongation to failure of 281%. Besides, according to this

table, four-pass PTCAP treated specimens pulled at 450° C and  $10^{-3} \text{ s}^{-1}$  as well as 400° C and  $10^{-4} \text{ s}^{-1}$  have high elongations to failure of 256% and 233%, respectively.

**Table 2.2:** A summary of the research findings on the ductility of SPD-processed AZ31.

No.	Initial condition	Type	Process	<sup>1</sup> IGS ( $\mu\text{m}$ )	<sup>2</sup> FGS ( $\mu\text{m}$ )	<sup>3</sup> TTT ( $^{\circ}\text{C}$ )	<sup>4</sup> TSR ( $\text{s}^{-1}$ )	Elongation (%)	Ref.
1	Extruded	Rod	ECAP/200°C/4P	9.4	2.2	350	$1 \times 10^{-4}$	960	[87]
2	Extruded	Rod	ECAP/200°C/8P	2.5	0.7	150	$1 \times 10^{-4}$	460	[91]
3	Drawn	Rod	HPT (RP)/10Turns/6GPa	35	0.11	150	$1 \times 10^{-3}$	355	[92]
4	Extruded	Rod	ECAP/200°C/6P	9.4	1.6	200	$3.3 \times 10^{-4}$	210	[93]
5	Extruded	Rod	ECAP/200°C/6P	9.4	1.6	150	$3.3 \times 10^{-4}$	160	[93]
6	As-cast	Rod	ECAP/300°C/5P	223	3.8	350	$1 \times 10^{-2}$	156	[94]
7	Extruded	Rod	ECAP/200°C/6P	9.4	1.6	177	$3.3 \times 10^{-3}$	130	[93]
8	As-cast	Tube	PTCAP/300°C/2P	520	8	400	$1 \times 10^{-3}$	263	[85]
9	As-cast	Tube	PTCAP/300°C/2P	520	8	450	$1 \times 10^{-3}$	145	[85]
10	As-cast	Tube	PTCAP/300°C/1P	520	11	400	$1 \times 10^{-3}$	106	[86]
11	Extruded	Tube	PTCAP/300°C/4P	43	6.8	450	$1 \times 10^{-4}$	281	[90]
12	Extruded	Tube	PTCAP/300°C/4P	43	6.8	450	$1 \times 10^{-3}$	256	[90]
13	Extruded	Tube	PTCAP/300°C/4P	43	6.8	400	$1 \times 10^{-4}$	233	[90]
14	Extruded	Tube	PTCAP/300°C/2P	43	8.2	450	$1 \times 10^{-3}$	210	[90]
15	Extruded	Tube	PTCAP/300°C/1P	43	11	450	$1 \times 10^{-3}$	200	[90]
16	Extruded	Tube	PTCAP/300°C/4P	43	6.8	400	$1 \times 10^{-3}$	182	[90]
17	Extruded	Tube	PTCAP/300°C/2P	43	8.2	400	$1 \times 10^{-3}$	180	[90]
18	Extruded	Tube	PTCAP/300°C/4P	43	6.8	350	$1 \times 10^{-4}$	175	[90]
19	Extruded	Tube	PTCAP/300°C/1P	43	11	400	$1 \times 10^{-3}$	162	[90]
20	Extruded	Tube	PTCAP/300°C/4P	43	6.8	450	$1 \times 10^{-2}$	160	[90]
21	Extruded	Tube	PTCAP/300°C/4P	43	6.8	350	$1 \times 10^{-3}$	144	[90]

<sup>1</sup>Initial grain size

<sup>2</sup>Final grain size

<sup>3</sup>Tensile testing temperature

<sup>4</sup>Tensile strain rate

(b) *AZ91 Magnesium alloy*

The AZ91 Mg alloy is one of the most widely used Mg alloys due to productiveness in relation to cost, high mechanical strength, and desired castability (S.W. Xu et al., 2009). Nevertheless, Mg-based alloys possess poor ductility because of the hcp crystal configuration and abundant dendritic second phases that limit their broad applications (Mabuchi et al., 1997). Even though several attempts are made to produce UFG tubes by the PTCAP procedure, few studies have addressed PTCAP processing of AZ91 Mg tubes as a widespread industrial product. Abdolvand et al. (2017a) investigated AZ91 Mg tubes processed by PTCAP at 300° C and evaluated the microstructural features and mechanical behaviour of the experimental outputs. Improvement in mechanical strength, hardness, and ductility were noted following the PTCAP procedure.

From the microstructural assessments, the average grain size drastically reduced from 150 µm for the unprocessed tube to 3.8 µm in the case of the three-pass PTCAP processed tube. The utmost mechanical strength of around 108% was found for the two-pass PTCAP processed tube, while the strength of the one-pass processed tube is only enhanced about 62.5%. Meanwhile, the mechanical properties of the three-pass PTCAP processed tube were degraded as a result of the development of microcracks on the surface. A rise in elongation at room temperature and hardness was also detected. The same group, in another research (Abdolvand et al., 2017b), studied the microstructural evolution and mechanical behaviour of UFG AZ91 thin-walled tubes processed by a hybrid approach (PTCAP+TBE). From Figure 2.28(a–h), a significant microstructure refinement was obtained following the hybrid procedure, so that the mean grain size reduced to 12.4, 9.8 and 8.8 µm from an initial value of ~150 µm after one, two and three-pass combined process, respectively. This behaviour can be explained by the key role of shear strains in the grain refinement (Shin et al., 2002). Figure 2.28(i–k) show the tensile true stress-strain plots of the processed AZ91 Mg alloy tubes following the different number of passes at

room temperature. As can be seen, the  $\sigma_{YS}$  and  $\sigma_{UTS}$  enhanced considerably to 150 and 354 MPa for the 2P+TBE tube, from the primary values of 86 and 166 MPa, respectively.

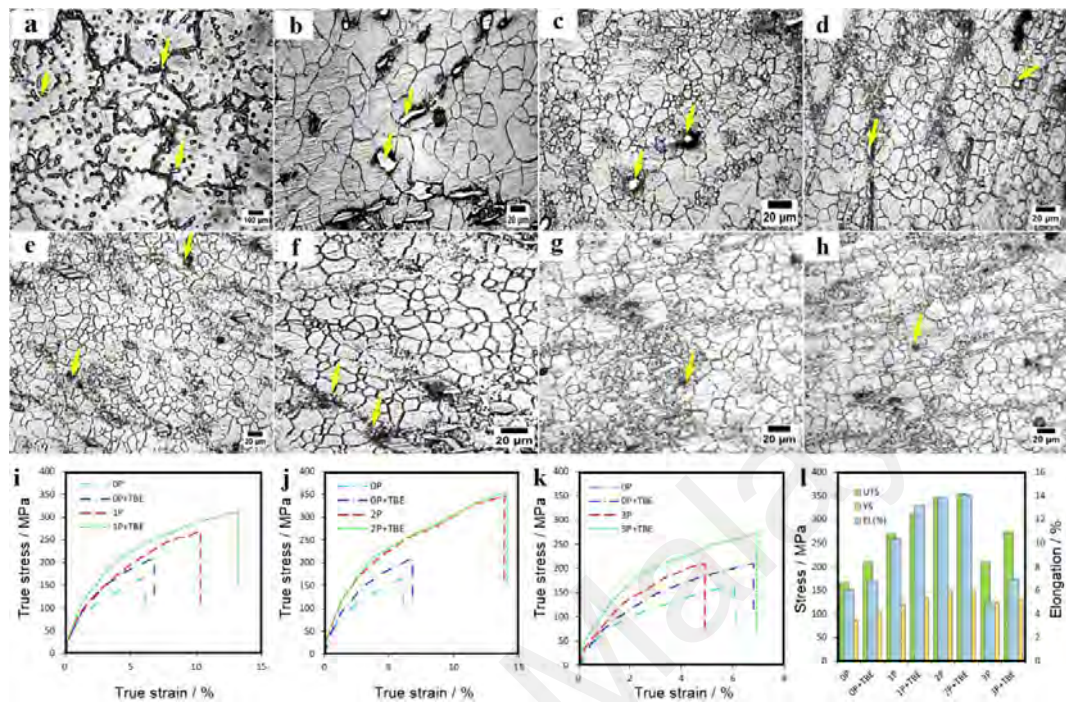


**Figure 2.28:** Optical images of AZ91 Mg alloys: (a) unprocessed, (b) 0P+TBE, (c) one pass, (d) 1P+TBE, (e) two-pass, (f) 2P+TBE, (g) three pass and (h) 3P+TBE processed tubes; true stress against true strain plots for the processed specimens compared to unprocessed sample: (i) one pass and 1P+TBE, (j) two-pass and 2P+TBE and (k) three pass and 3P+TBE samples as well as (l)  $\sigma_{Yield}$ ,  $\sigma_{UTS}$  and elongation variations of the samples (Abdolvand et al., 2017b).

In general, the main reason for the mechanical weakness of the as-cast AZ91 Mg alloy is the non-uniform distribution of the  $\beta$  phase precipitates at the grain boundaries (Faraji et al., 2011a), while the uniform dispersal of the recrystallized grains and raising the density of dislocation following the SPD process can cause a significant increase in the mechanical strength (Sakai & Miura, 2011). Based on some previous findings on the SPD procedure of AZ31 and AZ61 Mg alloys, raising the strain resulted in an improvement in the elongation and a reduction in the strength as a consequence of texture evolution and grain refinement (Jin et al., 2005). However, both mechanical strength and elongation improvement of AZ91 Mg alloy was observed with increasing strain, as shown in Figure 2.28(l). These differences between the AZ91 alloy and other AZ alloy series could be

ascribed to the elevated volume fraction of the  $\beta$  phase precipitates and more uniform grain size distribution, which is accountable for improved elongation. The hydro-bulge analysis revealed that the bursting pressure raised to 220, 246 and 195 bar for one, two, and three-pass thin-walled tubes, respectively, from the primary value of 160 bar (Abdolvand et al., 2017b).

#### **2.4.6.2 Microstructural and mechanical properties of aluminum-based alloys**

##### **(a) AA 5083 Aluminium alloy**

Aluminium tubes have a wide range of applications in industries (Javidikia & Hashemi, 2017), due to the flexibility, strength, and high resistance against corrosion. Although some properties such as hardness, microstructure (Afrasiab et al., 2015; H.S. Kim et al., 2001), energy absorption capability (Afrasiab et al., 2014) and fracture behaviour (Fata et al., 2016) of UFG tubes have been examined by the PTCAP process, the anisotropic properties of AA aluminium 5083 have not been investigated. Recently, Javidikia et al. (2017) studied the mechanical anisotropic behaviour of UFG AA 5083 tubes produced via the PTCAP process.

Based on the results obtained from the UFG of AA 5083 tubes using the PTCAP procedure and mechanical anisotropy (Figure 2.29), the following points can be noted: First, UFG tubes gave less anisotropy compared to the coarse-grained samples. Second, greater strength (about 579 MPa) was obtained along the peripheral direction inside the PTCAP-processed tube, although it was about 334 MPa along the axial direction. Third, there was an improvement in the final strength, about 25 and 44% along with the axial and peripheral directions, respectively. From the comparisons between the UFG and PTCAP-processed tube with CG, the elongation to failure of the former decreases to 43% inside the axial direction and roughly 18% in the peripheral direction. Additionally, an

increase of about 250 MPa along the axial direction and 460 MPa along the peripheral direction was observed. Finally, the peripheral direction showed increased hardness and strength compared to the axial direction. This gave a close agreement with the anisotropy of tensile properties and this phenomenon was confirmed through distinct textures in the mechanical properties (Javidikia et al., 2017).

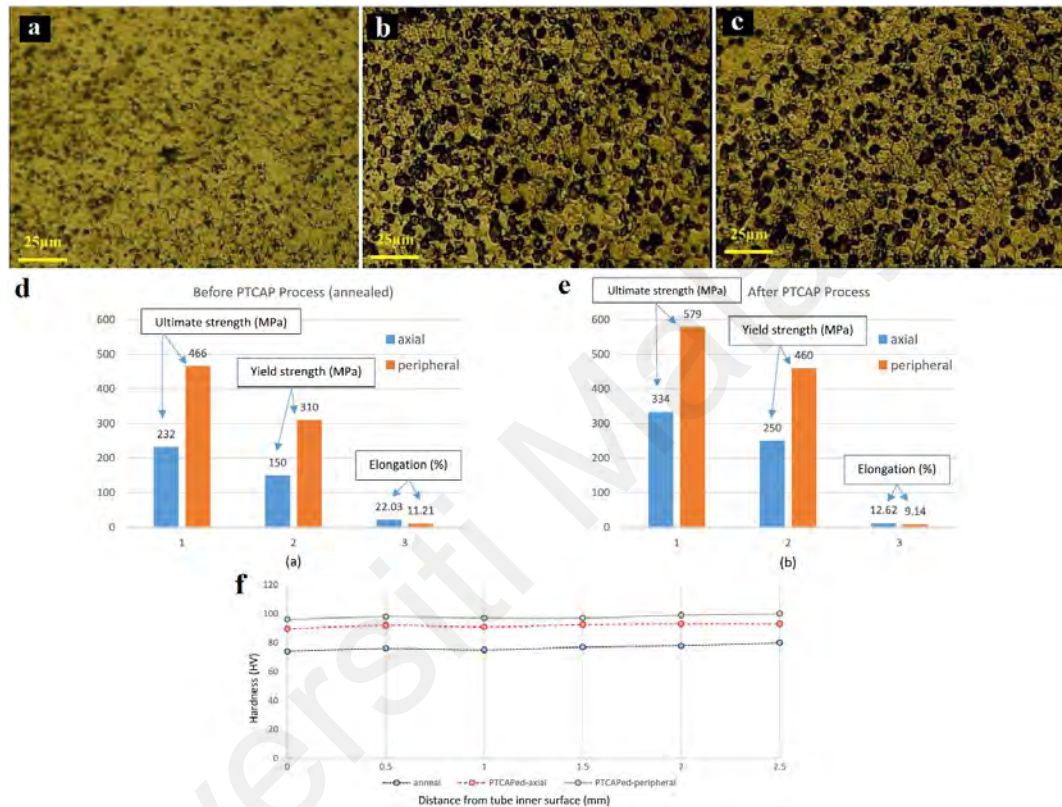


**Figure 2.29:** Optical micrographs (a) annealed material, (b) PTCAP-processed AA aluminium 5083 alloy in the peripheral direction and (c) axial direction as well as the mechanical properties of (d) the annealed coarse-grained and (e) PTCAP-processed UFG tubes in axial and peripheral directions and (f) microhardness vs. distance in annealed and PTCAP-processed tube along axial and peripheral directions.

### (b) 6061 Aluminium alloy

It was found that roughly two-thirds of all extrudates consist of Al-based alloys, and 90% belong to the 6xxx series (H.S. Kim et al., 2001). Moreover, among many Al-based alloys, the age-hardened Al-6061 alloy is widely utilized in a variety of industrial applications due to its good combination of strength and formability. Accordingly, numerous attempts are made to produce UFG Al-6061 alloy by different SPD methods,

such as ECAP (Jining et al., 2005), HPT (Das et al., 2012) and ARB (Rezaei et al., 2011). However, no investigations are made for the preparation and characterization of the Al-6061 alloy by the TCAP and PTCAP processes. Faraji et al. (2015) applied the multi-pass PTCAP procedure to fabricate UFG Al-6061 alloy tubes, where the influence of the pass number on the microstructural refinement and mechanical behaviour were examined.

The EBSD analysis in Figure 2.30(a) and (b) show that the lengthened sub-grains or grains with around 800 nm in size with a large fraction of low-angle grain boundaries are developed following two-pass PTCAP. As shown in Figure 2.30(c) and (d), the elongated sub-grains have changed to roughly equiaxed grains with ~400 nm in size with a large misorientation following four-pass PTCAP procedure.

After four-pass PTCAP ( $e \sim 6.4$ ), the  $\sigma_{YS}$  and  $\sigma_{UTS}$  also enhanced by 2.1 and 1.6 times, respectively, relative to the annealed specimen (Figure 2.30(e)). Ductile rupture with a wide necking region and numerous big dimples were present in the heat-treated specimen, whereas the fine dimples and restricted ductile fracture characteristics were detected in the UFG specimens. Also, the microhardness of the processed tube improved by ~63% following the three-pass PTCAP process, while the further rise in the pass number did not affect the microhardness, as illustrated in Figure 2.30(f) (Faraji et al., 2015).

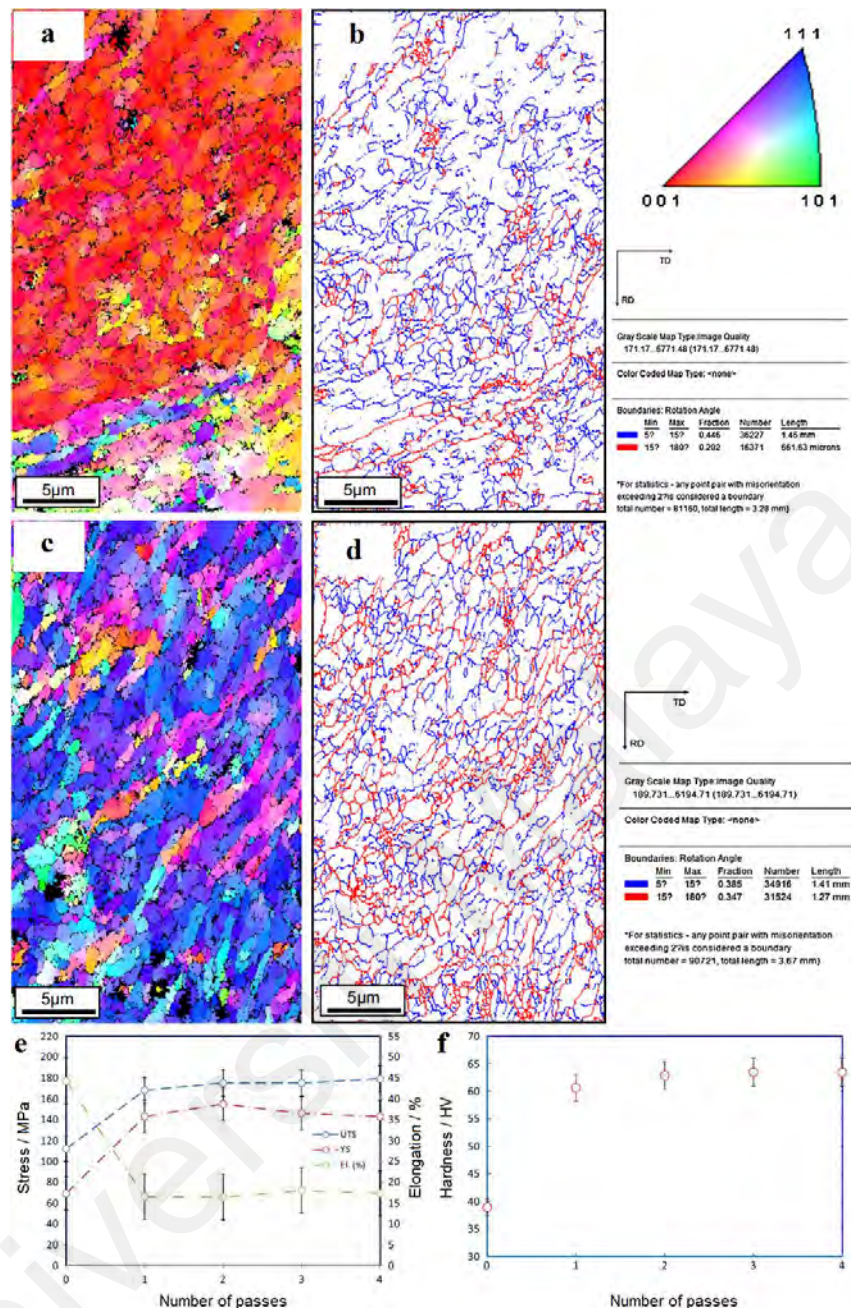


**Figure 2.30:** The EBSD orientation imaging map (OIM) patterns, pole figures, and inverse pole figures, as well as boundary maps of (a,b) two and (c,d) four-pass PTCAP, processed specimen; (e)  $\sigma_{Yield}$ ,  $\sigma_{UTS}$ , elongation and (f) microhardness of the processed tubes against PTCAP pass number (Faraji et al., 2015).

### (c) 7075 Aluminium alloy

The 7075 aluminium alloy is light weight and high strength alloy with wide applications possesses some characteristics that can be compared to those of soft steel (Javdani et al., 2016). Turning to the special physical properties, this alloy is an outstanding alternative for steel owing to the elevated strength to weight ratio. Seeing that

it is commonly shaped via a pricey machining process caused by the somewhat lower ductility in metal forming processes, the semi-solid forming of this alloy is vital. Efforts are made to attain a spheroidal morphology of this alloy for semi-solid forming. Some other investigations have utilized ECAP as a strain-persuading step in the strain-induced and melt activated (SIMA) approach.

Ashouri et al. (2008) employed the one to four-pass ECAP procedure to assess the influences of strain on the morphology and shape factor of reheated A356 alloy. Hossein Nedjad et al. (2008) also studied that a combination of ECAP and isothermal heating in the semi-solid state resulted in a semi-solid billet with the spheroidal solid phase. In this regard, Meshkabadi et al. (2017) evaluated the microstructural features of PTCAP-treated tubes in the semi-solid state to clarify the appropriate factors for the succeeding forming procedure. By appraising the impacts of process parameters, for instance, the pass number, reheating time and temperature, the proper circumstances for attaining a refined microstructure were established.

Moreover, the uniformity of the microstructure was also examined. Such a microstructure for tubular parts is an important advantage in fabricating large and complex parts, at the same time as using the benefits of semi-solid forming like diminished production steps and low process loads.

From Figure 2.31(a–f), the increase of the pass number from one to two, changes the grain size drastically, while only slight variations are observed in the shape factor. In addition, as the pass number raised, a homogeneous distribution was achieved, and the spherical formation took place quicker.

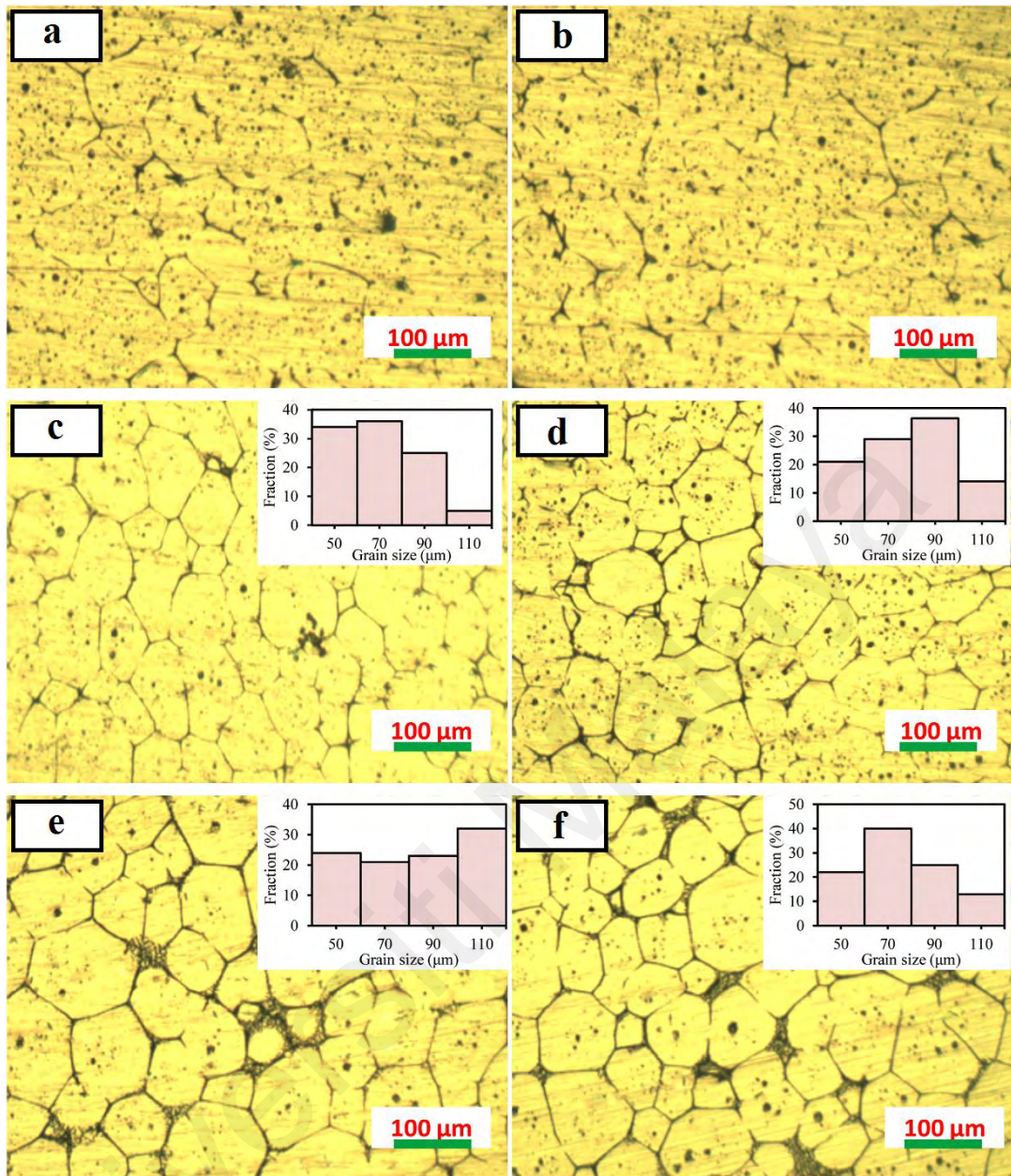


**Figure 2.31:** Optical images of the PTCAP-processed alloy at 610° C in various circumstances; (a,c,e) one-pass for 5, 10 and 15 min, (b,d,f) two-pass for 5, 10 and 15 min (Meshkabadi et al., 2017).

Besides, when the temperature raised, the size of solid particles reduced primarily and then increased, and became more spherical in a progressive state, as shown in Figure 2.32(a–d). The suitable circumstances for the subsequent semi-solid forming processes are at a reheating temperature of 620 °C, where the mean grain size was < 100 μm, while the shape factor was > 0.7. Appropriateness of 620° C for the semi-solid forming processes was established by the homogeneous distribution of the grains.

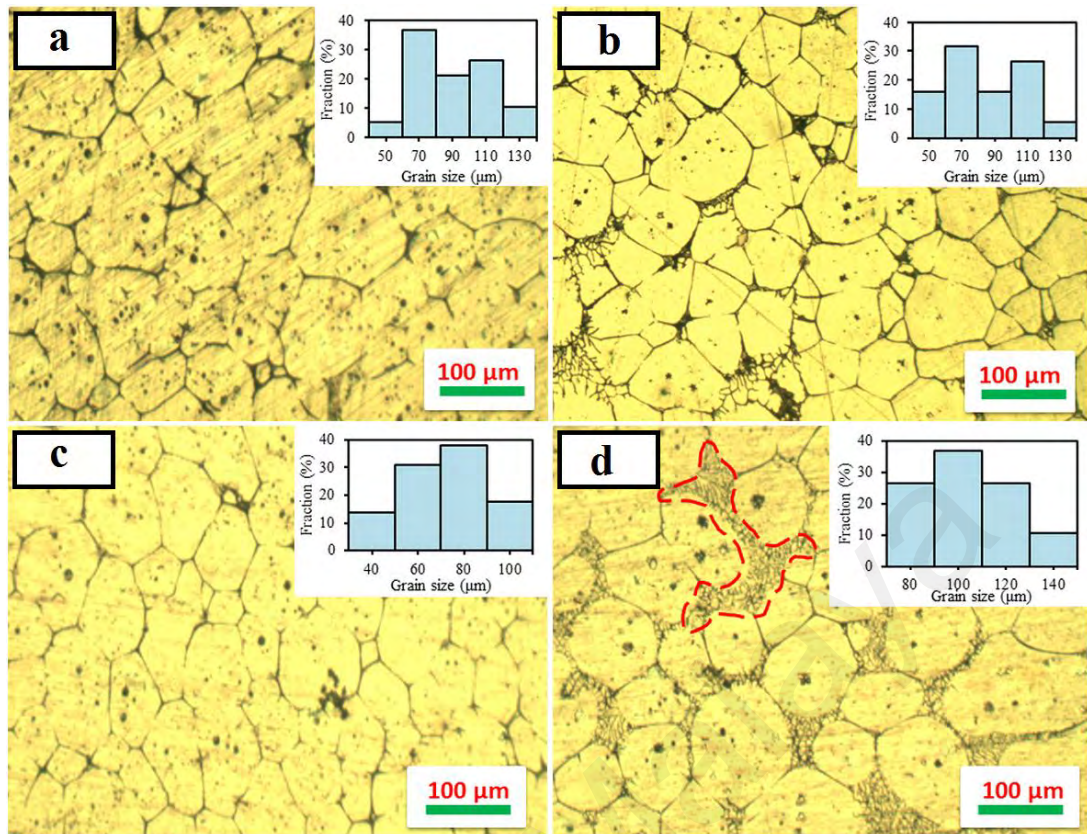


**Figure 2.32:** Optical micrographs of the two-pass PTCAP-processed specimens following reheating for 10 min at different temperatures of (a) 610, (b) 615, (c) 620 and (d) 625° C (Meshkabadi et al., 2017).

The deformation mechanism of the PTCAP processed specimens in the semi-solid region is demonstrated in Figure 2.33. As it is known, the application of a cold working process such as the PTCAP increases the number and density of dislocations in the material (Faraji et al., 2013a). The dislocations are dispersed in the matrix and form sub-grain boundaries in the microstructure. The greater amount of cold-work by increasing the pass number of PTCAP promotes greater misorientation angle and dislocations, which are reorganized to create new high angle grain boundaries.

Ultimately, an equilibrium between the dislocation formation and the reorganization in grain boundaries is achieved, which results in the development of the UFG configurations (Faraji et al., 2013a).

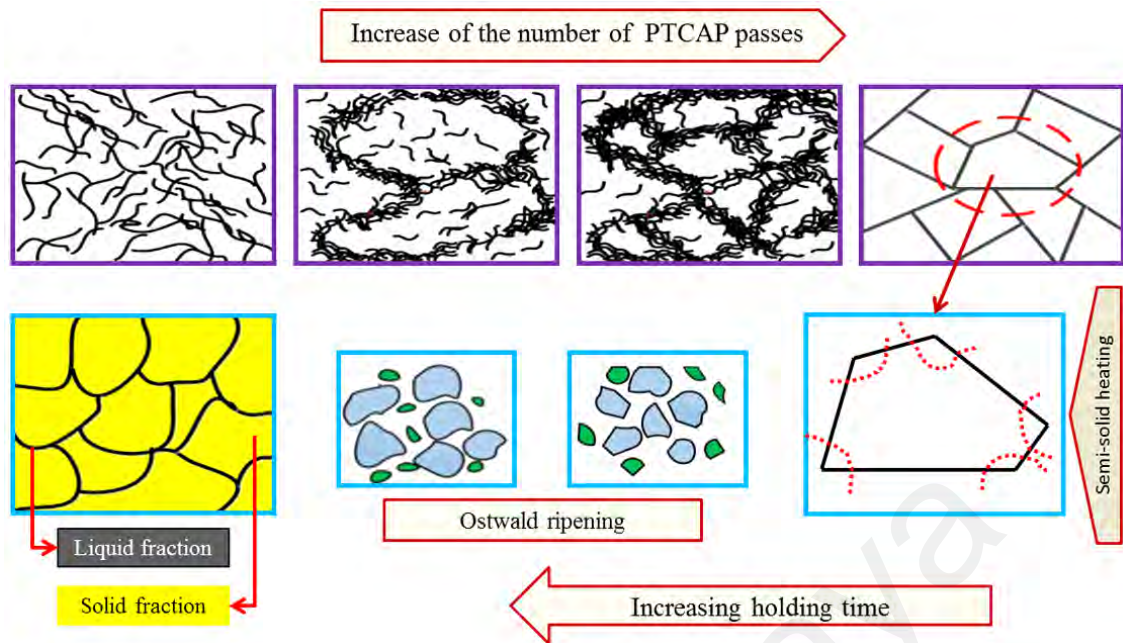


**Figure 2.33:** Schematic view of the coarsening mechanism in PTCAP-processed specimens in the semi-solid zone (Meshkabadi et al., 2017).

The stored strain energy is released by reheating the UFG configurations attained from the SPD. The sharp edges of the polygon like configuration are detached progressively due to the diffusion occurrence, followed by the formation of a liquid phase in the recrystallized boundaries. In the end, the liquid fraction enhances, whereas the Ostwald ripening mechanism is actuated and a spherical configuration comprising solid particles surrounded by a liquid phase is developed (Meshkabadi et al., 2017).

The results also showed that both the grain size and shape factor rose with the heating time. The dispersal of the solid particles depended significantly on the holding time. Comparisons of the grain size and shape factor between the ECAP and PTCAP-processed Al-based alloys in the same circumstances showed a high capability of the PTCAP as a strain-inducing stage to obtain an appropriate microstructure of semi-solid forming, particularly for tube formed specimens. Besides, the hardness tests indicated that the two-pass PTCAP processed specimens possessed higher hardness compared to the one-pass

processed samples in all cases. At an elevated reheating time and temperature, the variation in the hardness values was insignificant (Meshkabadi et al., 2017).

#### **2.4.6.3 Microstructural and mechanical properties of copper-based alloys**

##### **(a) *Pure copper***

Faraji et al. (2012a) applied the PTCAP method to a commercially pure copper, where a substantial microstructure refinement attained an average grain size of 150–300 nm following one-pass PTCAP procedure. The FEA outputs indicated that an equivalent plastic strain of  $3\pm 0.05$  could be obtained at the end of the second cycle of PTCAP, whereas it was  $3\pm 0.4$  at the end of the TCAP. This shows an outstanding strain uniformity through the length and thickness of the PTCAP processed tube. In addition, the numerical data showed that the PTCAP method required 57% lower loads than the TCAP method. Thus, PTCAP has two important advantages of requiring a lower load while achieving an excellent strain homogeneity. In a complementary study, the same group (Faraji et al., 2013a), processed a commercially pure copper through multi-pass PTCAP and the influences of the pass number on the microstructural refinement and the dislocation density were also examined.

From the TEM images and dislocation densities in Figure 2.34(a) and (c–h), elongated sub-grains with interior tangled dislocations are developed in the first pass. The density of interior dislocations through the elongated grains reduced the following two pass. A further increase in the PTCAP pass caused an approximate disappearance of the elongated grains and equiaxed grains with grain size around 150 nm were developed as a consequence of dynamic recovery. The dislocation densities were also calculated by hardness indentation size effect using the Nix–Gao model (Faraji et al., 2013a).

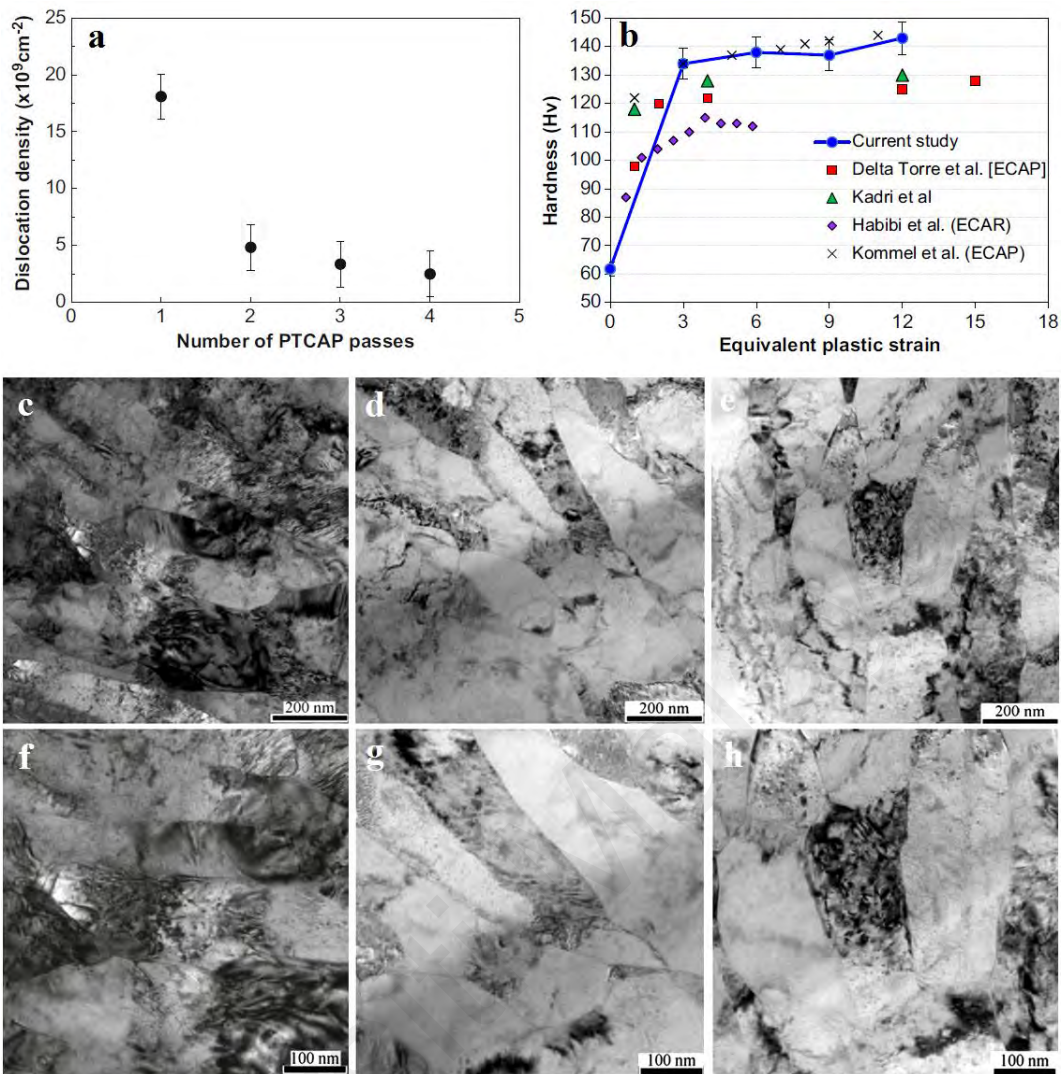


**Figure 2.34:** (a) The dislocation densities and (b) microhardness against equivalent plastic strain (compared to previous results) of the PTCAP processed tubes in terms of pass number, and bright-field TEM micrographs of the cross-sectional area of PTCAP processed tube after (c,f) one, (d,g) two, and (e,h) three-pass PTCAP procedure (Faraji et al., 2013a).

The results indicated that a rise in the pass number of PTCAP results in a reduction in the dislocation densities. It can be seen that the dislocation density has declined from  $18.1 \times 10^9 \text{ cm}^{-2}$  in the first-pass to  $2.48 \times 10^9 \text{ cm}^{-2}$  following four-pass PTCAP. The TEM observations corroborated the determined values from the Nix–Gao model. From Figure 2.34(b), the microhardness of the four-pass PTCAP processed tube increased to  $\sim 142 \text{ HV}$  from the primary value of around  $62 \text{ HV}$ . A substantial rise occurred following one-pass PTCAP, but the hardness value became saturated in the following passes (Faraji et al., 2013a).

(b) *Cu–Zn Brass alloy*

Brass tubes find broad applications in numerous industries owing to the good corrosion resistance and durability. Based on the available literature, the mechanical behaviour of metals can be drastically improved by microstructural refinements using various SPD processes. Afrasiab et al. (2014) studied the energy absorption capability of nanostructured Cu–Zn thin-walled tubes. In other studies, they also investigated the severe mechanical anisotropy of high-strength UFG Cu–Zn tubes processed by PTCAP (Afrasiab et al., 2015; Tavakkoli et al., 2015; Tavakkoli et al., 2016). Diverse deformation types of axisymmetric concertina-folding, three- and two-lobes diamond modes were detected in the case of the heat-treated, one-pass, and two-pass PTCAP processed tubes, respectively, as shown in Figure 2.35(a).

The corresponding textures in Figure 2.35(b) confirm the severe anisotropy in the mechanical behaviour, where the  $\{1\ 1\ 1\}$  plane was rotated around  $90^\circ$  with reorientation toward the radial direction following the PTCAP procedure, whereas it was scattered with a small texture to the extrusion direction in the heat-treated specimen.

As shown in Figure 2.35(c), the mean forces of 5.2, 16.1, and 18.8 KN are recorded for the heat-treated, processed tubes following one and two-pass PTCAP, respectively. A substantial rise in the capability of energy absorption from an initial value of 49.56 J for the annealed tube to 162.51 and 197 J was found for the one and two-pass PTCAP processed tubes, respectively (Figure 2.35(d)). It was reported that a rise in the absorbed energy is a prominent capability of the nanostructured and UFG tubes contrasted to the coarse-grained tubes (Afrasiab et al., 2014; Tavakkoli et al., 2015).

The results showed that higher strength of around 1220 and 580 MPa along the peripheral and axial direction was attained, respectively, in the PTCAP processed tube.

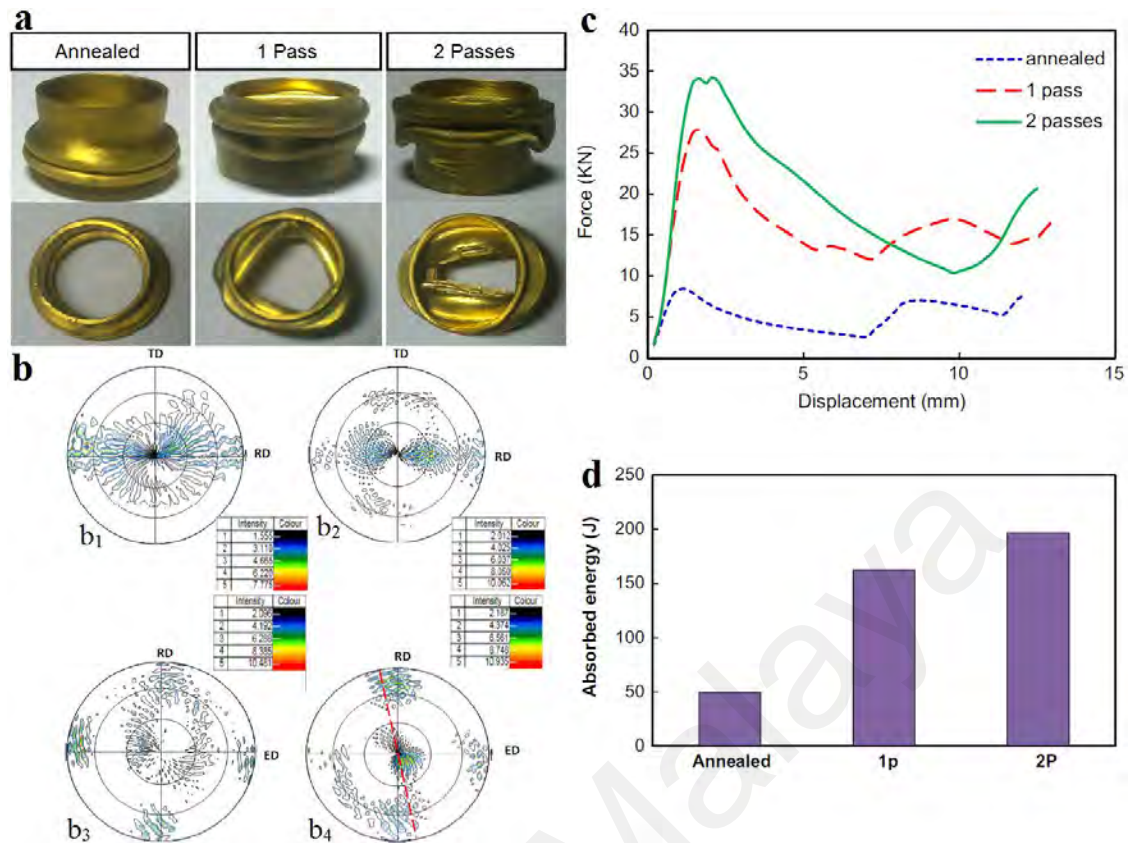


**Figure 2.35:** (a) Deformed shapes of tube samples following quasi-static crushing test, which shows dissimilar deformation modes; (b)  $\{1\ 1\ 1\}$  pole figures of the heat-treated and PTCAP processed specimens in the (b<sub>1</sub>,b<sub>2</sub>) axial and (b<sub>3</sub>,b<sub>4</sub>) circumferential directions, respectively; (c) force-displacement plots attained from axial compression tests and (d) total absorbed energy of heat-treated and PTCAP processed tubes (Afrasiab et al., 2014; Tavakkoli et al., 2015).

In addition, the elongation to failure of the UFG PTCAP processed tube reduced to 80% and 53% in the axial and peripheral directions, respectively, contrasted to the coarse-grained tube. The  $\sigma_{YS}$  also enhanced to about 224% along the axial direction and 182% along the peripheral direction. The results of hardness tests revealed that the hardness in the peripheral direction was greater compared to the axial direction, which shows a good conformity with the anisotropy of tensile features (Fata et al., 2018). In a complementary study, we also studied the nano-mechanical behaviour and microstructural refinement of UFG brass tubes processed by PTCAP, where an enhancement in the mechanical performance of the brass tube was observed after the SPD processing (Mesbah et al., 2016).

## 2.5 Summary of Literature Review

The application of adequate stress on various metals and their alloys inevitably gives rise to plastic deformation. The severely deformed materials commonly lead to failure due to the incapability towards plastic deformation. Nevertheless, if plastic deformation restoration mechanisms (dynamic recovery or dynamic recrystallization) dominate throughout, the ability of a substance to initiate plastic deformation can be increased, which contributes to the microstructural modification by arranging line defects into surface imperfections. There are several techniques for performing SPD, the most notable case is the ECAP.

In addition, TCAP is an efficient technique for the preparation of nanostructured and ultrafine-grained UFG tubes. With regards to the capabilities of TCAP, the PTCAP technique is also an established and innovative SPD process, wherein the deformation includes two half-cycles which are influenced by a number of factors including deformation ratio, curvature angle, and channel angle. The microstructural evolution, mechanical behaviour and potential applications of these methods for producing UFG Al, Mg, and Cu-based tubular components have not been yet explored. Thus, the main focus of the next chapter is on the characterization of TCAP and PTCAP processed Al-1060, Cu-Zn Brass, ZK60, and WE43 Mg alloys as lightweight alloys in engineering applications.

## CHAPTER 3: RESEARCH METHODOLOGY

This chapter provides the details of starting materials, SPD processing, experimental procedures, and analysis methods. The applied methodology in this research could be categorized into five main parts. The Al-1060, Cu-Zn Brass, ZK60, and WE43 Mg alloys were firstly processed using TCAP or PTCAP methods. The structural features of the SPD-processed samples were secondly measured and compared with those of unprocessed workpieces. Thirdly, a comparative assessment was carried out to compare the microstructural evolution of the SPD-processed and unprocessed workpieces. The tensile strength and microhardness of the samples were then measured as selected mechanical properties and ultimately, the mechanisms of grain refinement and mechanical performance increment in SPD-processed samples were realized. Figure 3.1 shows the flowchart of methodology.

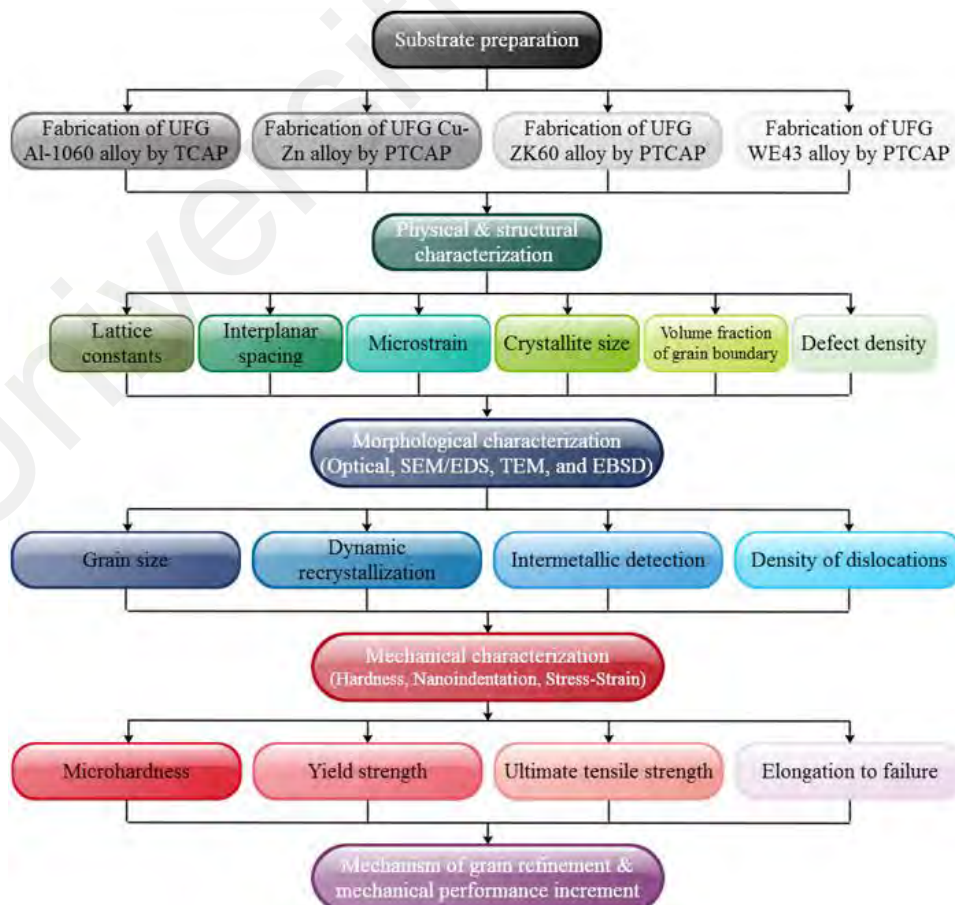


**Figure 3.1:** Flowchart of methodology.

**Table 3.1:** The chemical compositions of Al-1060, Cu-Zn brass, ZK60 Mg, and WE43 Mg Alloys used in this study. The values are reported in %wt.

Element	Al-1060	70-30 Cu-Zn Brass	ZK60	WE43 Mg
Al	99.60	-	0.005	-
Cu	0.05	69.00	-	0.02
Fe	0.35	0.06	-	-
Mg	0.03	-	Remain	Remain
Mn	0.03	-	0.025	0.14
Si	0.25	-	-	0.009
Ti	0.03	-	-	-
V	0.05	-	-	-
Zn	0.05	30.87	5.5	0.18
Nd	-	-	-	3.65
Ni	-	-	-	0.003
Zr	-	-	0.5	0.47
Pb	-	0.07	-	-
Y	-	-	-	3.9

### 3.1 Materials

An as-cast commercial pure Al-1060 (99.6%), commercial 70-30 Cu-Zn brass, ZK60, and WE43 Mg alloys in the form of ingot and extruded bars were used as the starting materials. The chemical compositions of these alloys are summarized in Table 3.1.

### 3.2 TCAP Processing

Al-1060 cylindrical tube samples with outer diameters of 20 mm, thicknesses of 2.5 mm, and lengths of 40 mm were formed by machining. The samples were then annealed at 350 °C for 2 h to attain a homogeneous and recrystallized microstructure.

Figure 3.2(a) demonstrates a schematic of TCAP procedure applied in this study. A hollow cylindrical punch was used to press the tube into a crevice in the middle of the die and mandrel that forms a tubular angular channel with three shear zones I, II, and III. The cross-section of the tube remains constant before and after the process. In the multi-pass TCAP, the procedure was repeated to develop unique strains without a decrease in the cross area of the workpiece. The TCAP facility composes of a die and mandrel with three

intersecting channels, a plunger, and a hydraulic press. The die and the plunger were made from tool steel and heat-treated to achieve a Rockwell hardness of 55 HRC. Before pressing, the tubes and plunger were lubricated using molybdenum disulfide ( $\text{MoS}_2$ ) as an inorganic lubricant. The die geometry is shown in Figure 3.2(b) resulted in the imposed strain of  $\sim 2.2$  according to Eq. (2.10) after each individual pass. The die parameters and their values are shown in Table 3.2.

The TCAP tests were performed in one, two, and three passes by an INSTRON press machine with a speed of  $10 \text{ mm}\cdot\text{min}^{-1}$  at room temperature. The experimental setup including the die and press is shown in Figure 3.2(c).

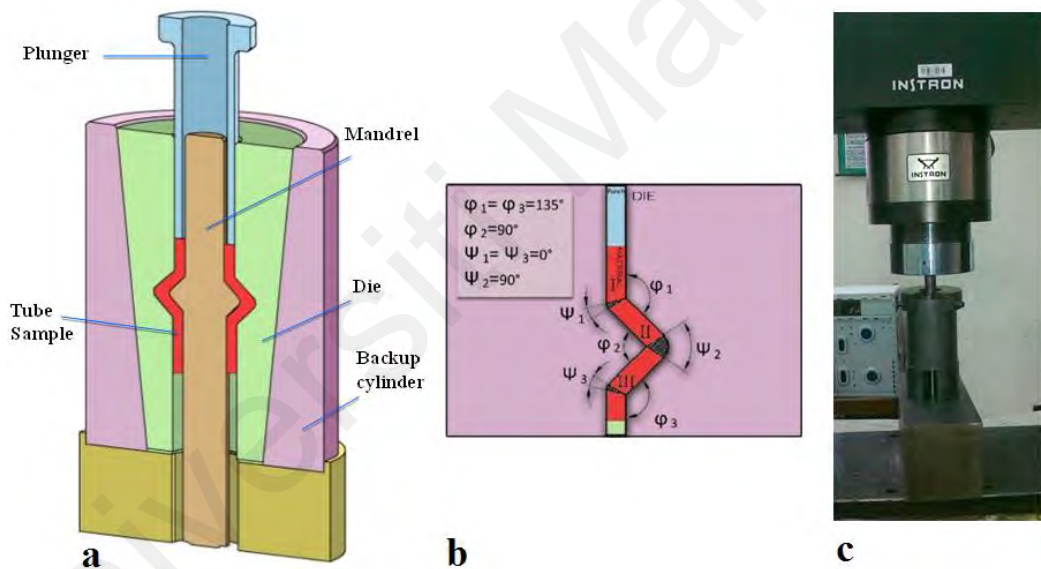


**Figure 3.2:** (a) A schematic illustration of the TCAP process, (b) related parameters of the die, and (c) the experimental TCAP setup.

**Table 3.2:** TCAP die parameters and their values.

$R/R_0$	$R_0$ (mm)	$t_0$ (mm)	$(\varphi_1, \varphi_3)$ ( $^\circ$ )	$\varphi_2$ ( $^\circ$ )	$\psi_1, \psi_3$ ( $^\circ$ )	$\psi_2$ ( $^\circ$ )
1.2	8.75	2.5	135	90	0	90

**Table 3.3:** PTCAP Die parameters and their values.

Material	$\varphi_i$ ( $^\circ$ )	$\psi_1, \psi_2$ ( $^\circ$ )	$R_1$ (mm)	$R_2$ (mm)
Tool steel	150	0	8.75	11.25

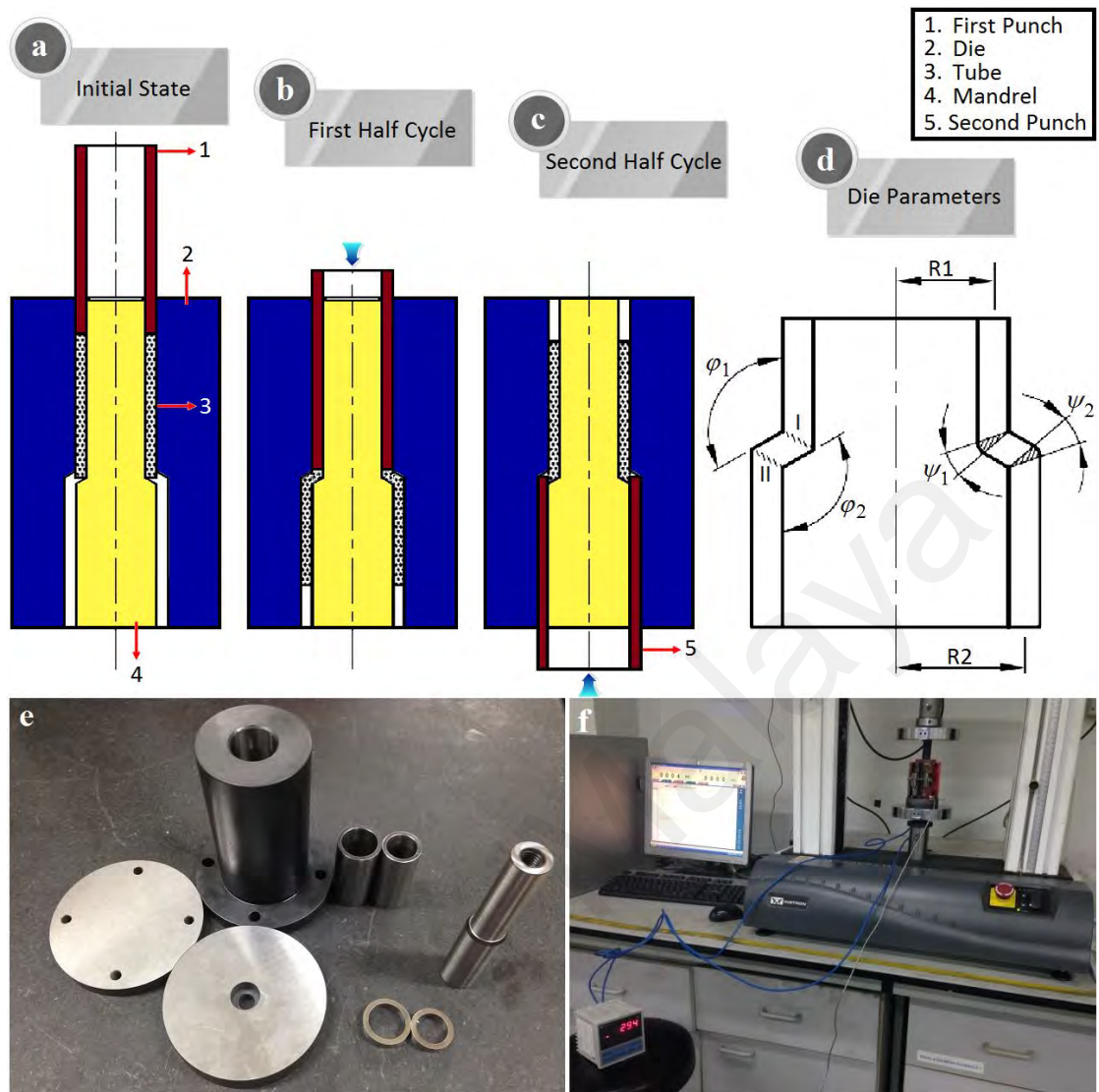


**Figure 3.3:** The schematic view of (a) primary state, (b) the first, (c) the second half-cycles of PTCAP, (d) die parameters, (e) utilized PTCAP die with its components, and (f) the experimental setup.

### 3.3 PTCAP Processing

The commercial 70-30 Cu-Zn brass, ZK60, and WE43 Mg alloys received in the form of ingot and extruded bars. Then, they were machined into cylindrical tube samples with outer diameters of 20 mm, thicknesses of 2.5 mm, and a length of 40 mm. In the case of 70-30 Cu-Zn brass, the tubes were annealed at 600° C for 1 h to achieve a homogeneous micro-structure. A PTCAP die with the channel ( $\phi_i$ ) and curvature ( $\psi_1, \psi_2$ ) angles of 150° and 0°, respectively was fabricated from hot-worked tool steel H13 and hardened to 55 HRC (Table 3.3). The SPD processes were then executed by an INSTRON press machine.

The PTCAP processes (one to three passes) were conducted at room temperature for 70-30 Cu-Zn brass and at 300° C for ZK60 and WE43 Mg alloys with a ram speed of 5 mm min<sup>-1</sup>. Moreover, MoS<sub>2</sub> was applied to the die and workpiece interface to reduce the friction between the material and the die.

The PTCAP process was carried out in two half-cycles, as illustrated in Figure 3.3(a–d). In this technique, the primary tube was preliminarily placed into the space between the mandrel and die (Figure 3.3(a)), followed by shoving into the deformation zone, which was comprised of a tubular channel with two shear areas, using the first punch (Figure 3.3(b)). Afterward, the tube was pushed backwards into the same shear area via the second punch to recover its preliminary dimensions (Figure 3.3(c)). No rotation of the tube towards the die was made between two half cycles.

A high plastic strain can be formed in the shear region due to the accumulative shear strain in each pass. The tensile and compression circumferential strains are attained throughout the first and second half cycles of the PTCAP process, respectively. In accordance with Figure 3.3(d) and Eq. 2.11, this type of SPD process applies an equivalent plastic strain of ~ 1.8 after each PTCAP pass. Therefore, the strain values after the second and third PTCAP pass were 3.6 and 5.4, respectively. The PTCAP die and its components, as well as the experimental setup, are shown in Figure 3.3(e) and (f). Figure 3.4(a) and (b) also show the exploded view drawing of PTCAP die and exploded view of PTCAP manufactured die parts, respectively.

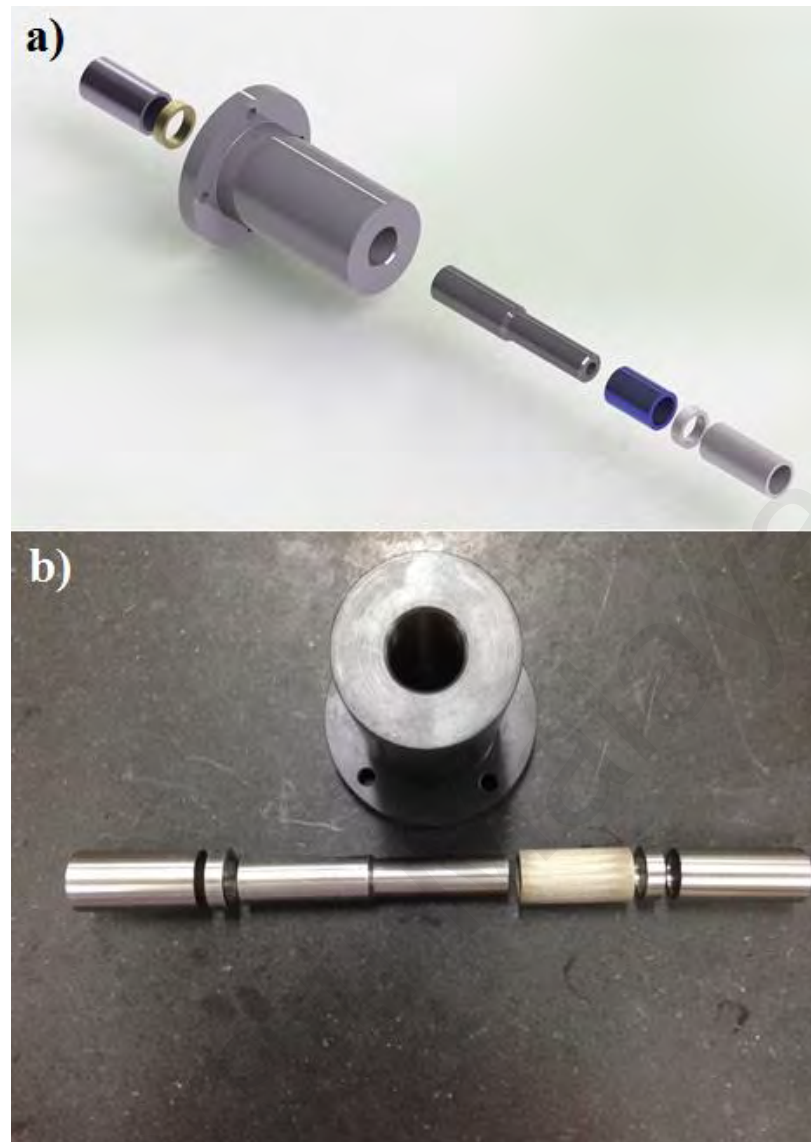


**Figure 3.4:** (a) The exploded view drawing of PTCAP die, and (b) the exploded view of PTCAP manufactured die parts

### 3.4 Characterization Techniques

Prior to the characterization, the unprocessed and SPD-processed samples were cut in a perpendicular direction to the extrusion direction. The samples were then grinded using SiC papers in the range of 400-2400 grits. To obtain a smooth surface, the surfaces of all samples were then polished by diamond suspension with a mesh size of 6, 3, and 1  $\mu\text{m}$ . The mirror-like surfaces were obtained by final vibratory polishing using Buehler VibroMet® 2 Vibratory Polisher with 0.05  $\mu\text{m}$  colloidal silica for 4 h. The samples were

removed from the polisher, washed thoroughly with distilled water, rinsed in alcohol, and blow-dried prior to the tests.

### **3.4.1 Physical and Structural Assessment**

#### **3.4.1.1 Phase analysis**

The X-ray diffraction (XRD) analyses were carried out in different  $2\theta$  ranges (PANalytical Empyrean X-ray diffractometer) using  $Cu-K\alpha$  radiation ( $\lambda = 0.154$  nm) to investigate the phase compositions of the UFG tubes. The XRD profiles were analysed using "HighScore Plus" software and the diffraction data were compared to the standards compiled by JCPDS and Material Project (MP), which included card numbers #004-0770 for Mg, #004-0787 for Al, #040-1334 for MgZn, #034-0457 for MgZn<sub>2</sub>, #16-0854 for Mg<sub>24</sub>Y<sub>5</sub>, #050-1333 for  $\alpha$ -brass, as well as mp-1401 for ZrZn<sub>2</sub> and mp-864889 for ZrZn<sub>3</sub>. It should be noted that due to the unavailability of standard codes for Zr<sub>3</sub>Zn<sub>2</sub> intermetallic compound (IMCs), the relevant characteristic peaks were only compared with those reported in previous studies (Dumitru et al., 2014; Zakiyuddin & Lee, 2018).

#### **3.4.1.2 Lattice constant and unit cell volume**

The routine XRD analyses, in general, fail to provide adequate crystallographic data required for accurate determination of the physical properties of the UFG tubes processed by TCAP and PTCAP. Therefore, a more subtle inspection was necessary to achieve a comprehensive assessment. Here, the interplanar spacing ( $d_{hkl}$  values) derived from the XRD profiles and Equation (3.1) were employed to determine the cubic and hexagonal lattice constants,  $a$ ,  $b$ , and  $c$ , using Eqs. 3.2 and 3.3, respectively (Cullity & Stock, 2001):

$$\lambda = 2d_{hkl} \sin \theta_{hkl} \quad (\text{Eq. 3.1})$$

$$\frac{1}{d_{hkl}^2} = (h^2 + k^2 + l^2) \frac{1}{a^2} \quad \text{Cubic (Al, Cu-Zn)} \quad (\text{Eq. 3.2})$$

$$\frac{1}{d_{hkl}^2} = \frac{4}{3} \left( \frac{h^2 + hk + k^2}{a^2} \right) + \frac{l^2}{c^2} \quad \text{Hexagonal (Mg)} \quad (\text{Eq. 3.3})$$

where  $h, k, l$  are the Miller indices of the reflection planes. The unit cell volumes ( $V$ ) of the cubic and hexagonal structures were also calculated using Eq. (3.4) and Eq. (3.5), respectively (Cullity et al., 2001):

$$V = a^3 \quad (\text{Eq. 3.4})$$

$$V = \sqrt{\frac{3}{2}} a^2 c \quad (\text{Eq. 3.5})$$

In addition, the in-plane and out-of-plane strains in the hexagonal structures were estimated using the lattice parameters with the unstrained Mg lattice parameters to determine the lattice mismatch, according to Eq. (3.6) and Eq. (3.7) (Cheong et al., 2014):

$$\varepsilon_a = \frac{a - a_0}{a_0} \quad \text{In-plane strain} \quad (\text{Eq. 3.6})$$

$$\varepsilon_c = \frac{c - c_0}{c_0} \quad \text{Out-of-plane strain} \quad (\text{Eq. 3.7})$$

### 3.4.1.3 Crystallite size ( $D$ ) and micro-strain ( $\eta$ )

Hereon, the  $D$  and  $\eta$  values were determined using X-ray line profile analysis, based on the Williamson-Hall equation (Williamson & Hall, 1953):

$$\beta^2 = \frac{X^2}{\cos^2 \theta} + Y^2 \tan^2 \theta \quad (\text{Eq. 3.8})$$

where  $X = 0.9\lambda/D$  and  $Y = 4\eta$ .  $\beta$ ,  $K$ ,  $\theta$ ,  $\lambda$ ,  $\eta$  and  $D$  are the full width of the Bragg peak at half maximum, shape constant, Bragg's angle, wavelength of the X-ray source, micro-strain, and crystallite size, respectively.

#### 3.4.1.4 Volume fraction of the grain boundary ( $f$ )

When a crystallite is assumed as a sphere with diameter  $D$ , delimited by a shell of the grain boundary with a hypothetical thickness ( $t$ ) of 1 nm, the volume fraction of the grain boundary ( $f$ ) is roughly determined by the following equation (Sun & Froes, 2002):

$$f = 1 - \left[ \frac{D}{(D + t)} \right]^3 \quad (\text{Eq. 3.9})$$

#### 3.4.1.5 Defect density ( $D_d$ )

The  $D_d$  values in the crystals of the processed specimens were also calculated using Eq. (3.10) as follows (Badran et al., 2017):

$$D_d = \frac{1}{D^2} \quad (\text{Eq. 3.10})$$

Moreover, in view of the fact that dislocations are the most important defects in SPD-processed specimens, their density ( $\rho$ ) can be interpreted in terms of  $D$  and  $\eta$  by the following formula (Bera et al., 2013):

$$\rho = \frac{2\sqrt{3}\langle\eta^2\rangle^{1/2}}{Db} \quad (\text{Eq. 3.11})$$

where  $b$  is the magnitude of the Burgers vector of dislocation equal to  $(a/3\langle 11\bar{2}0 \rangle)$  for a hcp Mg alloy and  $a$  is the relevant lattice constant.

### 3.4.2 Microstructural evolution analysis

The employed techniques to characterize the microstructural features of the processed tubes are illustrated in Figure 3.5.



**Figure 3.5:** The schematic of the employed techniques for characterization of the microstructural features of the processed tubes.

#### 3.4.2.1 Optical microscopy

For the optical microscopy analyses, the processed tubular specimens were cut in a perpendicular direction to the direction of extrusion. The specimens were then ground with SiC paper until the 2400-grit. Subsequently, the specimens were polished with the diamond paste using an oil-based lubricant. The ultimate polishing was carried out using an oxide polishing suspension. To detect the grain boundaries, an etchant with a chemical composition of 4.2 g picric acid ( $C_6H_3N_3O_7$ ,  $\geq 98\%$ , Sigma-Aldrich), 50 ml ethanol, 20 ml of distilled water, and 10 ml of acetic acid ( $CH_3COOH$ ,  $\geq 99.8\%$ , Sigma-Aldrich) was utilized. The microstructural analyses were performed on the etched samples via an optical microscope.

#### **3.4.2.2 Scanning electron microscopy (SEM) and energy-dispersive x-ray spectroscopy (EDS)**

For a detailed microscopic examination, the samples prepared for optical microscopic studies were also scrutinized by SEM (SU3500) combined with EDS at an accelerating voltage of 15 kV for the determination of the chemical compositions. Navcam is short for navigational camera. Navcams typically take wide angle photographs that are used to plan the next moves of the object tracking.

#### **3.4.2.3 Transmission electron microscopy (TEM)**

In order to obtain an insightful understanding of the microstructural differences of the UFG and unprocessed alloys TEM investigations were also performed in some cases using a FEI Tecnai TF20 machine at the accelerating voltage of 200 KV. For these tests, the tubular samples were cut in a direction perpendicular to the extrusion direction. The lamella samples were then taken at the area along the middle of the tube thickness, followed by twin-jet polishing in a mixture of 30 % nitric acid (HNO<sub>3</sub>) and 70% carbinol at minus 30° C.

#### **3.4.2.4 Electron backscattered diffraction (EBSD)**

EBSD was also performed to investigate the microstructural and crystallographic characterizations of some UFG specimens. In these investigations, grain boundaries were identified when the misorientation between two neighboring measurement points was more than 2°. Therefore, grain boundaries with misorientation less than 2° could not be detected in the analysis. Microstructural investigations were conducted using Hikari XP EBSD Camera, attached to Schottky Field Emission SEM (SU5000) at 20 kV and 1.4 nA electron beam during the measurements. The EBSD analysis was executed in a wholly computer-monitored automated EBSD (TSL-OIM), with a step size of 0.07 µm.

### 3.4.3 Mechanical Investigations

Figure 3.6 shows the schematic of the utilized techniques to assess the mechanical performance of the processed tubes.



**Figure 3.6:** The schematic of the utilized techniques to assess the mechanical performance of the processed tubes.

#### 3.4.3.1 Vickers' Microhardness test

The Micro-hardness test procedure, ASTM E-384, specifies a range of light loads using a diamond indenter to make an indentation that is measured and converted to a hardness value. It is very useful for testing on a wide type of materials as long as test samples are carefully prepared. Usually, the prepared samples are mounted in a plastic medium to facilitate preparation and testing. The indentations should be as large as possible to maximize the measurement resolution.

The Vickers' microhardness tests were performed on the rings extracted from the central portions of the pressed materials. The cross-sectional samples with heights of 10 mm were cold mounted, grounded until 2400-grits and polished with alumina at room temperature. The Vickers microhardness tests were then carried out at room temperature using a FM-1e microhardness instrument at a load of 100 gf with a dwell time of 10 s. The hardness values were reported as the mean of four spots recorded in a cross-shape around each certain point at a distance of 0.15 mm.

### 3.4.3.2 Stress-strain test

In this study, the assessment of engineering stress-strain curves was carried out to determine  $\delta$ ,  $\sigma_{YS}$ , and  $\sigma_{UTS}$  in order to investigate any possible alteration in the mechanical properties of the processed tubes. Hence, the selected specimens were cut using Electrical Discharge Machining (EDM) throughout the extruding direction with standard reported dimensions. Afterward, the wire cut samples were polished via 1200-2400 grit silicon carbide papers and sonicated in acetone for 10 min at 40 W. The tensile tests were carried out for the SPD-processed specimens at room temperature with a strain rate of  $5.0 \times 10^{-4} \text{ S}^{-1}$  using INSTRON tensile tester machine.

### 3.4.3.3 Nanoindentation test

The nanomechanical properties of the UFG alloys were characterized by the nanoindentation technique using a Triboindenter 750 Ubi system (Hysitron Inc., USA) equipped with a Berkovich indenter. The tests were performed in three steps and according to the ISO 14577 standard (14577, 2002; ISO-14577-1, 2002).

In the first step, the indenter tip was pressed into specific sites of the material by applying an increasing normal load. When the normal load reached a pre-set maximum value, the second step was initiated in which the indenter was held at the maximum normal load for a period of time to minimize the effects of material rate-dependent behaviour. In the third step, the normal load was reduced until partial or complete relaxation occurred. Following one cycle of loading, holding, and unloading, a hole with nanometer dimensions was formed. During the test, a high-precision instrument continuously recorded the values of load and displacement. The indenter was penetrated into the specimens with a maximum normal load of 6.5 mN. The speeds for each loading and unloading step were also kept constant. However, the loading, holding, and unloading

times were set at 30 s, 10 s, and 30 s, respectively. In each region, at least four nanoindentation experiments were performed. The scanning probe microscopy (SPM) images were taken before and after indentation tests to measure the sample deformation.

Universiti Malaya

## CHAPTER 4: RESULTS AND DISCUSSION

### 4.1 Structural, Morphological and Mechanical Properties of UFG Al-1060 Tube Processed by TCAP

#### 4.1.1 Phase Composition and Interplanar Spacing

Figure 4.1(a–d) shows the XRD profiles of the Al-1060 alloy prior to and following one, two and three TCAP passes. As can be seen, the same characteristic peaks corresponding to the cubic Al (JCPDS#004-0787) are obtained in all specimens. In fact, no intermetallic phase has been revealed, which is related to the nature of the alloy. However, the intensity of the characteristic peak decreased drastically after TCAP due to excessive strain-induced and precipitates fragmentation (Hilšer et al., 2018). It is obvious that the (1 1 1) growth plane has not changed after the TCAP process.

From this figure and Table 4.1, there are some discrepancies in XRD profiles as the number of passes increases. First, all characteristic reflections were slowly moved to higher angles after the first, second and third TCAP pass. This manner suggests that the SPD can cause isotropic compression of the Al lattice, where shifting to the higher angles hints the decrease of the volume cell of the Al throughout the TCAP, respectively. Second, on account of the reduction in the crystallite size and increase in the micro-strain, peak broadening took place with the increase in the number of TCAP pass. Third, the intensity of the diffraction peaks diminished considerably as a result of the structural evolution like excessive strain induced during the TCAP. According to Figure 4.1(e) and (f), it is obvious that the direction of XRD reflections is influenced by both non-uniform and uniform strains so that no peak broadening is detected and the group transverse reflecting planes exhibit a homogeneous equilibrium  $d$  spacing ( $d_0$ ) in the absence of strain. In contrast, the reflecting plane spacing becomes larger than  $d_0$  and the peak shifts

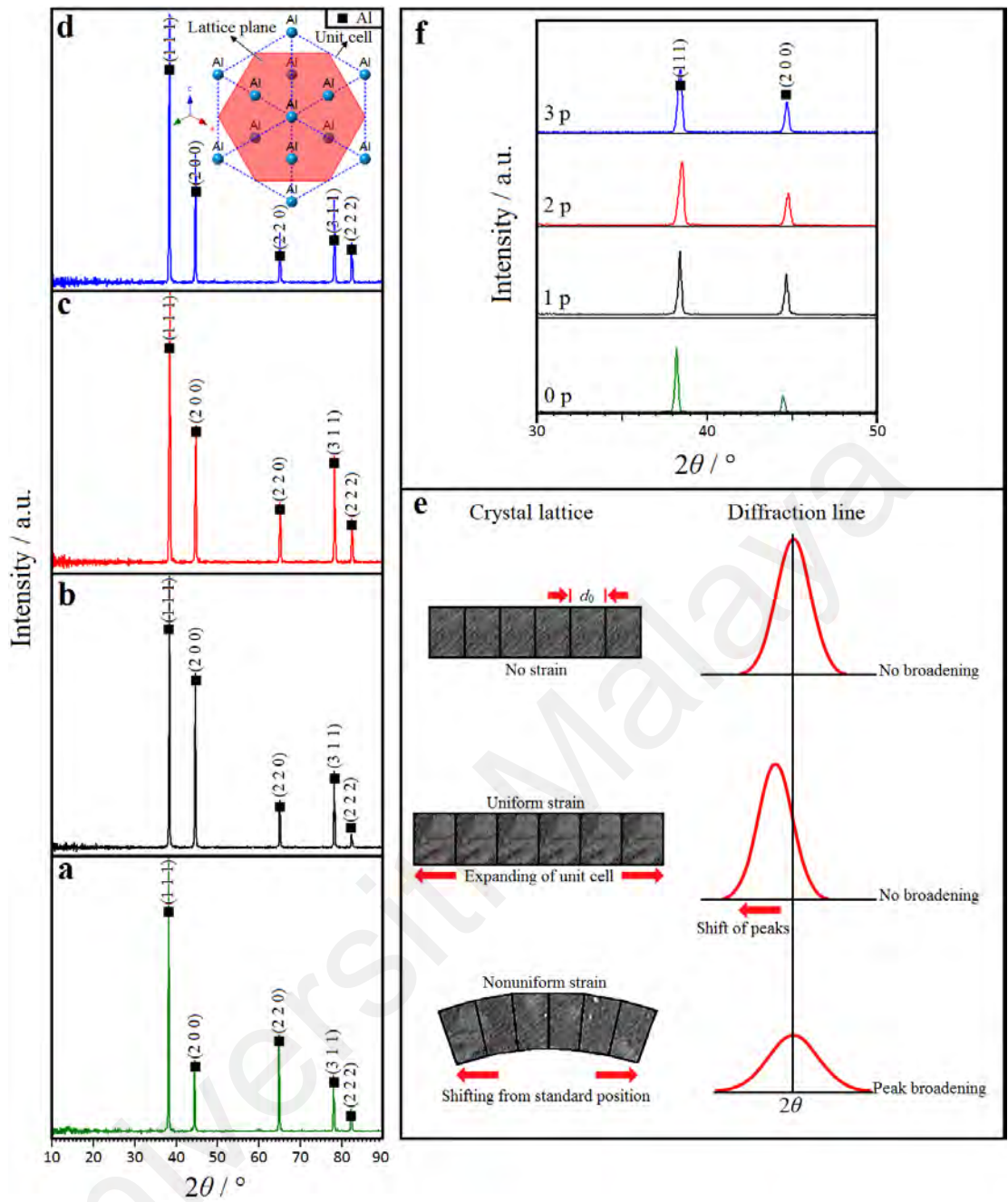


**Figure 4.1:** XRD profiles of Al-1060 alloy (a) before and after (b) one, (c) two and (d) three TCAP passes as well as (e) the effect of strain on the direction of XRD patterns and (f) magnified XRD profiles in the range of  $30^\circ \leq 2\theta \leq 50^\circ$ .

to the lower angles in the presence of a uniform tensile strain at right angles. No peak broadening is also perceived similar to the prior model. In the third case, the non-uniform strain results in the bending of grains, where the plane spacing is larger than  $d_0$  on the top side (tension), but it is less than  $d_0$  on the bottom side (compression), and it is equal to  $d_0$  somewhere between top and bottom (Nasiri-Tabrizi, 2014). Accordingly, in the present

case, the running of different TCAP passes is associated with the concurrent presence of uniform and non-uniform strains, which has led to both peak broadening and peak shift.

#### 4.1.2 Structural Features

In this section, the main structural features of the TCAP-processed Al-1060 alloy, including lattice parameters, volume of unit cell, micro-strain, crystallite size, the volume fraction of the grain boundary and defect density are presented.

**Table 4.1:** Peak list of Al-1060 alloy before and after different TCAP passes.

Pass	No.	$2\theta$ (°)	FWHM (°2 $\theta$ .)	h	k	l	$d_{hkl}$ spacing (Å)	Height (cts.s <sup>-1</sup> )
0	1	38.1954	0.1535	1	1	1	2.35631	1539.11
	2	44.4400	0.1535	2	0	0	2.03863	396.62
	3	65.0667	0.0936	2	2	0	1.43590	291.91
	4	78.0106	0.1560	3	1	1	1.22388	299.27
	5	82.2464	0.1560	2	2	2	1.17124	125.16
1	1	38.3904	0.1279	1	1	1	2.34479	1495.95
	2	44.6359	0.1535	2	0	0	2.03014	937.40
	3	65.0272	0.1023	2	2	0	1.43430	263.45
	4	78.1713	0.1560	3	1	1	1.22176	414.87
	5	82.3827	0.1872	2	2	2	1.16964	71.32
2	1	38.5569	0.2558	1	1	1	2.33505	895.84
	2	44.7929	0.1535	2	0	0	2.02339	454.50
	3	65.1344	0.1791	2	2	0	1.43220	199.75
	4	78.2794	0.1872	3	1	1	1.22035	369.49
	5	82.4933	0.1560	2	2	2	1.16836	151.42
3	1	38.4407	0.2132	1	1	1	2.34184	1136.66
	2	44.6835	0.1421	2	0	0	2.02809	536.78
	3	65.0637	0.1066	2	2	0	1.43359	208.29
	4	78.2192	0.1300	3	1	1	1.22113	345.85
	5	82.3923	0.1300	2	2	2	1.16953	165.50

**Table 4.2:** Lattice constants and unit cell volume of unprocessed and TCAP-processed Al-1060.

Number of passes	<i>a</i> -axis (Å)	<i>b</i> -axis (Å)	<i>c</i> -axis (Å)	<i>V</i> (Å <sup>3</sup> )
0	4.0600	4.0600	4.0600	66.94
1	4.0526	4.0526	4.0526	66.56
2	4.0471	4.0471	4.0471	66.29
3	4.0510	4.0510	4.0510	66.48

#### 4.1.2.1 Lattice constants and unit cell volume

To determine the cubic lattice parameters and unit cell volume of Al-1060 alloy prior to and after TCAP Eqs. (3.2) and (3.4) were used and the calculated values are given in Table 4.2. From the data given in this table, the TCAP led to a small shrinkage of the lattice constants and volume of unit cell. The standard lattice parameters value ( $a = b = c$ ) for Al (JCPDS#004-0787) is 4.0494 Å. Based on the data presented in Table 4.2, the lattice constant reduced from the initial value of 4.0600 Å for the unprocessed specimen to 4.0526, 4.0471 and 4.0510 Å following the first, second and third TCAP pass, respectively. Accordingly, the unit cell volume decreased from the initial value of 66.94 Å<sup>3</sup> for the unprocessed sample to 66.56, 66.29 and 66.48 Å<sup>3</sup> after the first, second and third TCAP pass, respectively. As mentioned above, this shrinkage in lattice constants and unit cell volume of Al can be explained by very high strains induced during the TCAP process (Hilšer et al., 2018). A similar trend was also observed by Murashkin et al. (2015), measuring the evolution of the lattice parameters of the SPD-processed Al.

#### 4.1.2.2 Crystallite size and micro-strain

In accordance with the XRD profiles in Figure 4.1 and peak list of Al-1060 alloy following one, two, and three passes in Table 4.1, an augmentation in the FWHM was detected by rising number of passes, which was caused by the lessening of the crystallite size  $D$  and rising of the micro-strain  $\eta$ . Based on the obtained data from Eq. 3.8 and the

relevant bar charts in Figure 4.2(a) and (b), the alterations of  $D$  and  $\eta$  in Al-1060 alloy prior to and following one, two and three TCAP passes are linear. In fact, in the case of the unprocessed sample, the crystallite size and lattice strains were  $364 \pm 16$  nm and 0.08%, respectively. However, after the first, second and third TCAP passes these values reached  $91 \pm 16$  nm and 0.1%,  $68 \pm 16$  nm and 0.14% as well as  $60 \pm 16$  nm and 0.18%, respectively. This indicates a linearly decreasing trend in crystallite size and an increasing trend in the lattice strain of the TCAP-processed Al-1060 alloy. These calculations also show that the smallest  $D$  and the utmost  $\eta$  values were achieved in the third pass of the operation, which corroborates that the UFG Al-1060 tube processed by three passes of TCAP is much more strained compared to the other specimens. Comparable findings are reported for crystallite size and micro-strain in the ECAP-processed commercial Al-based alloy by XRD analysis (Charfeddine et al., 2014); nonetheless, as these calculations are first presented for the TCAP-processed Al-1060 alloy, further studies are needed to attain optimal quantities.

#### 4.1.2.3 Volume fraction of the grain boundary

According to Eq. 3.9, it is expected that due to a significant reduction in the crystallite size, fraction of grain boundary is significantly increased with the increasing number of passes. As can be seen in Figure 4.2(c), the TCAP processing of Al-1060 alloy also resulted in significant alterations in  $f$  from 0.8% for the unprocessed sample to 3.2, 4.3 and 4.8% in this case, two and three-passed specimens, respectively. This dramatic increase in the fraction of grain boundary can have substantial effects on the level of crystallographic defects like dislocation, where the size and the orientation of different adjoining crystals can have a severe impact on the dislocation of nucleation and multiplication (Kheradmand et al., 2010). These alterations in the alloy structure

undoubtedly have significant effects on the microstructural evolution and mechanical behaviour of the TCAP-processed Al-1060 alloy, which will be discussed in the following sections.

#### 4.1.2.4 Defect and dislocation density

The density of crystallographic defects as a symbol of interruptions of regular patterns in crystalline solids can be estimated in terms of crystallite size in the processed alloys.

These defects include:

- (i) Point defects like vacancy, which are imperfections that happen only at or around a single lattice point,
- (ii) Line defects like dislocations, which can be explained by gauge theories,
- (iii) Planar defects, that involve grain boundaries, stacking faults and twin boundary,
- (iv) Bulk defects, which cover three-dimensional macroscopic or bulk imperfections, such as pores, cracks, or inclusions, voids, and impurities.

Herein,  $D_d$  values, which covers all types of crystallographic defects, was determined using Eq. (3.10) (Badran et al., 2017). In addition, in view of the fact that for severe plastic deformed specimens, dislocations are the most important line defects (as mentioned above), its density was calculated in terms of lattice constants, crystallite size and micro-strain using equation Eq. (3.11) (Badran et al., 2017).

Figure 4.2(d) demonstrates that  $D_d$  enhances linearly as the number of passes increases, signifying the impact of the number of TCAP passes on the defect density of the Al-1060 alloy. Among the specimens, the three-passed tube possessed the highest defect density and accordingly exhibited a significant increase in  $D_d$  compared to the unprocessed sample. From Figure 4.2(e), it is also obvious that the dislocation density as the main line

defect increases with the number of TCAP passes and maybe saturated at the higher strain depending on the material and the processing temperature. It should be noted that the saturation of the dislocation density is a result of the dynamic equilibrium between the duplication and the obliteration of dislocations (Gubicza, 2015).

In general, there are different metallurgical mechanisms for strengthening Al-based alloys. These strengthening mechanisms are vital because pure aluminum is soft to use for engineering applications. In Figure 4.3 different methods for the strengthening of Al-based alloys are illustrated, including work hardening (cold working), solid solution strengthening, dispersion strengthening, and precipitation strengthening.

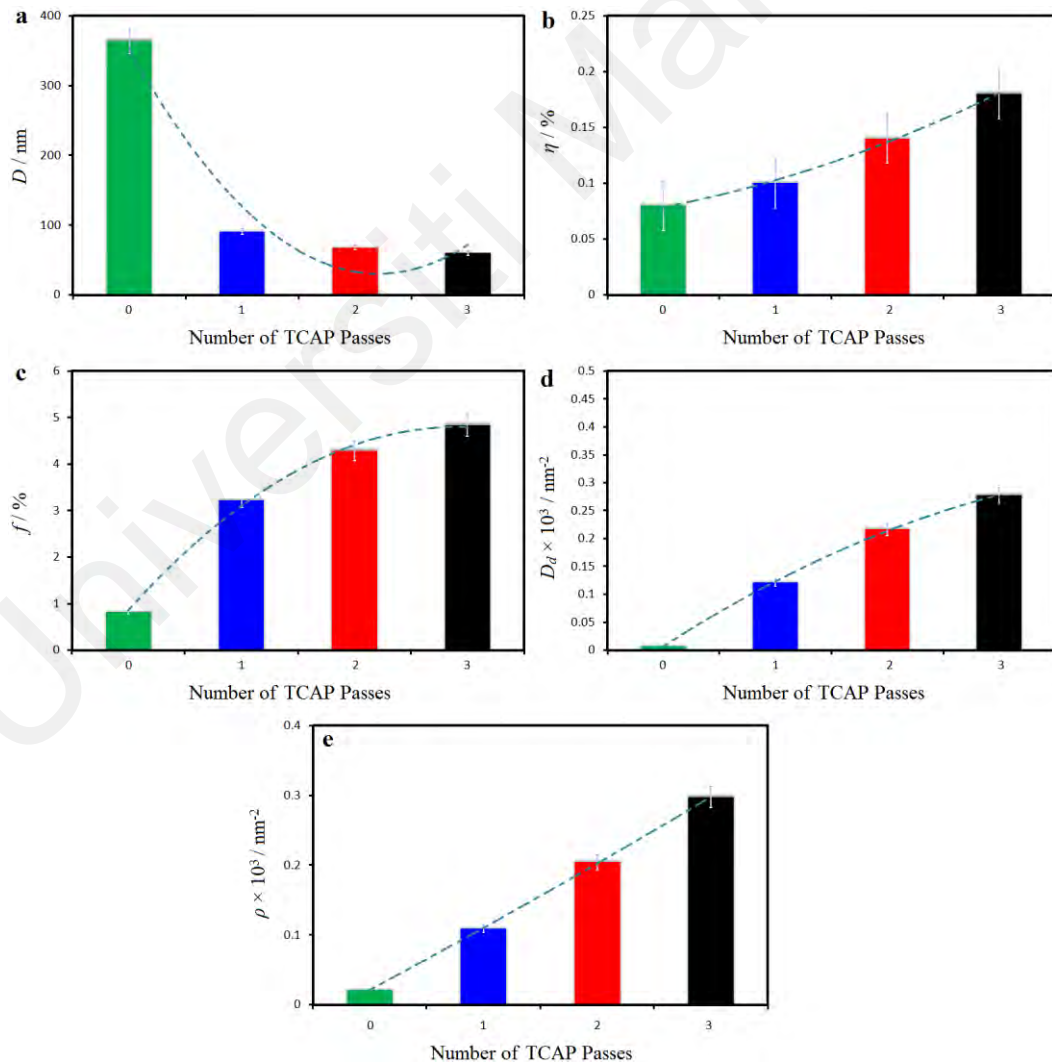


**Figure 4.2:** (a) Crystallite size ( $D$ ), (b) micro-strain ( $\eta$ ), (c) volume fraction of the grain boundary ( $f$ ), (d) defect density ( $D_d$ ), and (e) dislocation density ( $\rho$ ) of Al-1060 alloy prior to and after one, two and three TCAP passes.

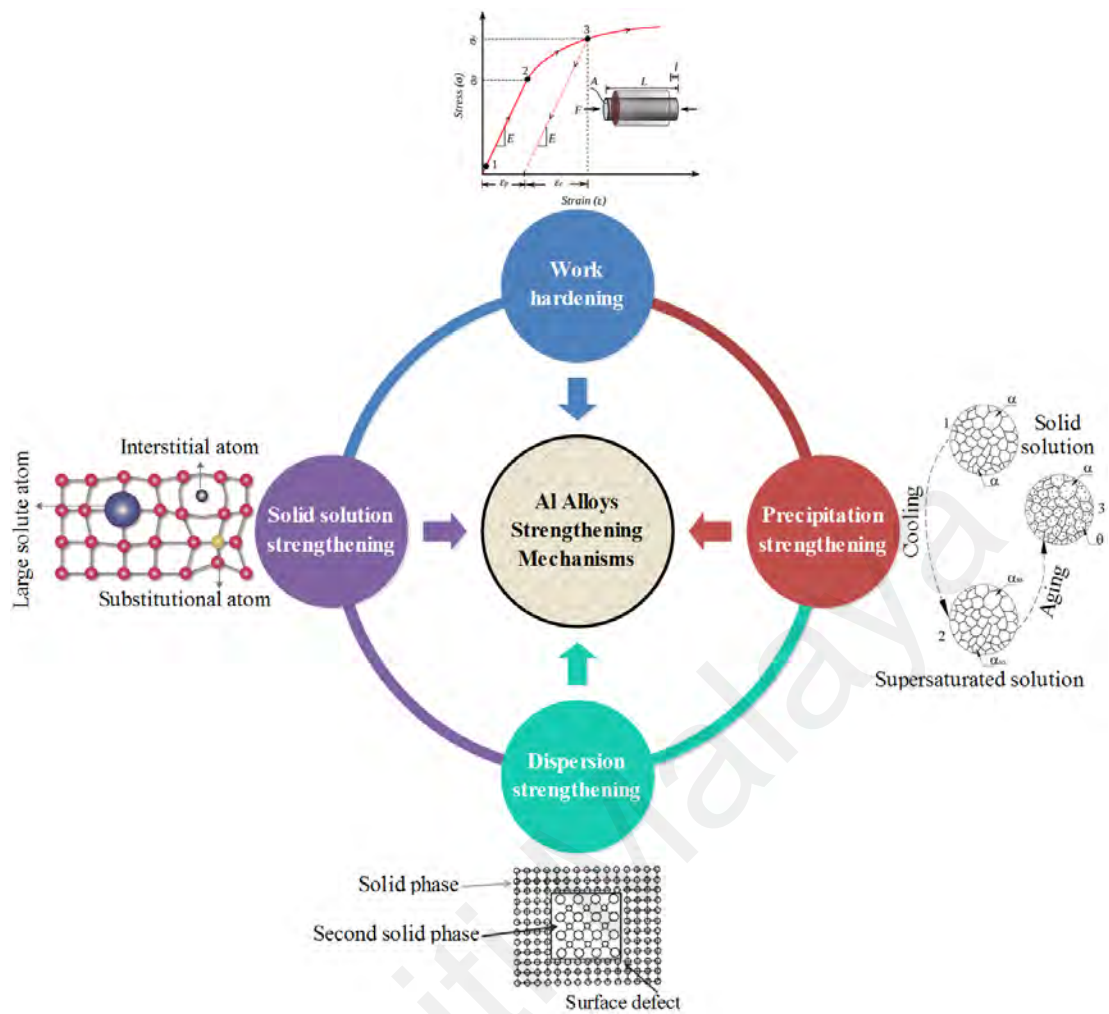


**Figure 4.3:** Different methods for strengthening Al-based alloys.

This suggests that strengthening of Al-based alloys can be tailored via a variety of grouping of mechanisms. However, in 1xxx alloys like Al-1060 alloys, due to the lack of alloying elements, the alloy can mainly be strengthened by work hardening (Gubicza, 2015). This description corroborates that in the TCAP-processed Al-1060 tube work hardening plays the central role in strengthening.

### 4.1.3 Microstructural Evolution Analysis

#### 4.1.3.1 TEM analysis

Figure 4.4(a) and (b) show the bright and dark field TEM micrographs of the cross-sectional microstructure of the TCAP processed Al-1060 tube after one pass ( $\epsilon \sim 2.2$ ), respectively. The TEM micrographs show that the microstructure consists of elongated

subgrains in which high fraction of low angle grain boundaries could be seen. Results from EBSD analysis of ECAP processed aluminum samples in the early passes showed that in this stage most of the grain boundaries have low misorientation angle (Basavaraj et al., 2009; Sabirov et al., 2013). This type of aligned subgrains, similar to a band structure could also be seen in the microstructure of ECAP processed pure aluminum after the early passes (Yoon et al., 2008). The array of elongated subgrains is aligned almost at an angle of  $45^\circ$  or less to the radial direction of the tube. In general, on comparing the bright and dark field TEM micrographs, a large misorientation among neighboring grains is observed.

The bright and dark field TEM micrographs of TCAP processed samples through two passes ( $\epsilon \sim 4.4$ ) are shown in Figure 4.4(d) and (e), respectively. The arrays of elongated subgrains observed in one pass processed sample have mostly transformed into nearly equiaxed subgrains and grains by the two-pass TCAP process. Comparison of the dark and bright field micrographs shows that the microstructure of the two-pass processed sample contains a large number of grain and subgrains having low angle boundaries similar to one pass sample microstructure. The boundaries mainly have low angle misorientations. This observation is also seen in the microstructure of pure aluminum after four passes of ECAP ( $\epsilon \sim 4$ ) (Tóth et al., 2009). Similar to the one-pass process, the grain boundaries are still unclear. The fraction of unclear boundaries is smaller compared to one pass processed sample. The bright and dark field TEM micrographs of the TCAP processed sample after three passes ( $\epsilon \sim 6.6$ ) show that further increase in the number TCAP passes causes the grain boundaries to be distinguishable as observed in Figure 4.4(g) and (h). This has indicated that the subgrains in the micrographs in Figure 4.4(d) and (e) have changed to equiaxed grains with high angle grain boundaries.

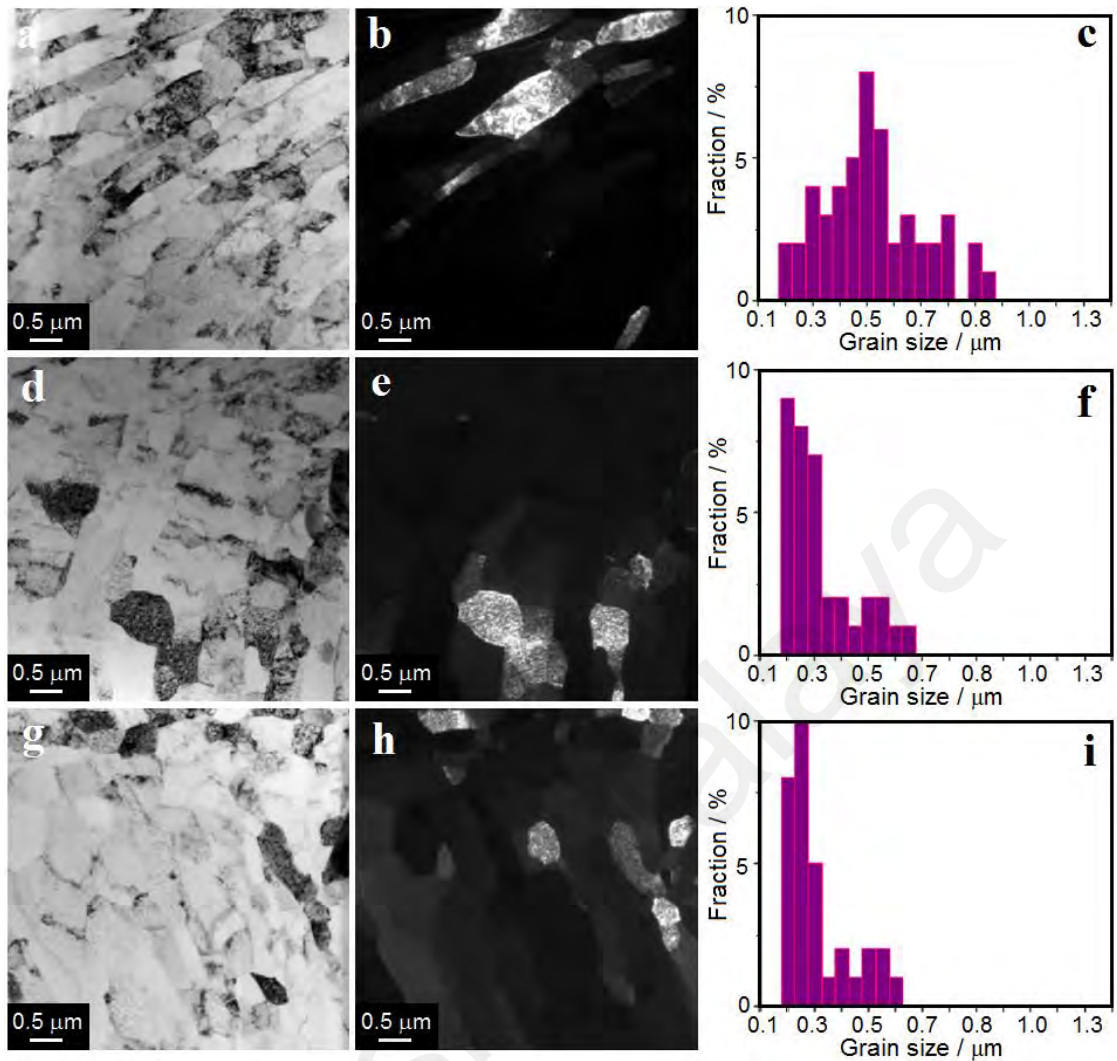


**Figure 4.4:** Bright (a, d, g) and dark (b, e, h) field TEM images and (c, f, i) grain size dispersal histogram of the cross-sectional micro configuration of the TCAP treated Al-1060 tubes following one, two and three passes.

This phenomenon is evident when TEM micrographs in Figure 4.4 are compared. The results also support the use of the dark field TEM technique to evaluate the microstructure of UFG materials, where high angle boundaries are easily distinguishable. Comparing the dark field TEM images shown in Figure 4.4(b, e, h), it can be seen that increasing the number of TCAP passes leads to an increase in the fraction of high angle grain boundaries, which are easily distinguishable in the dark field images in the three-pass processed sample. This qualitative result is consistent with the quantitative EBSD result achieved in previous works (Mohebbi et al., 2010; Sabirov et al., 2013). Most of the newly developed grains after the third pass may have low grain interior dislocation densities.

Due to the lower work hardenability of UFG materials with smaller grain size compared to fine-grained materials (S.H. Lee et al., 2002), it may be expected that in the sample processed via higher number of passes, smaller equiaxed grains nearly free of dislocations are formed. Faraji et al. (2012f) showed that an increase in the number of PTCAP passes caused a decrease in the density of dislocations in the grain interiors. The results are in good agreement with previous work conducted on pure copper via PTCAP (Salimyanfard et al., 2011).

TEM micrographs of the TCAP treated Al-1060 tubes following one, two and three TCAP passes are shown in Figure 4.5, demonstrating dislocations piled up to form subgrain boundary and higher magnification of dislocations in subgrain boundary (showed by red arrows). In this figure, the grains are divided into subgrains by the subgrain boundaries, where the dislocation substructures are also formed as a result of the SPD process. As shown in Figure 4.5(a, c and e), these boundaries included a series of dislocations loaded on a particular plane. It is found that dynamic recovery can happen in Al due to the high stacking fault energy that results in the organization of dislocations into low-angle ( $2\text{--}5^\circ$  misorientation) subgrain boundaries (Yadav & Bauri, 2012).

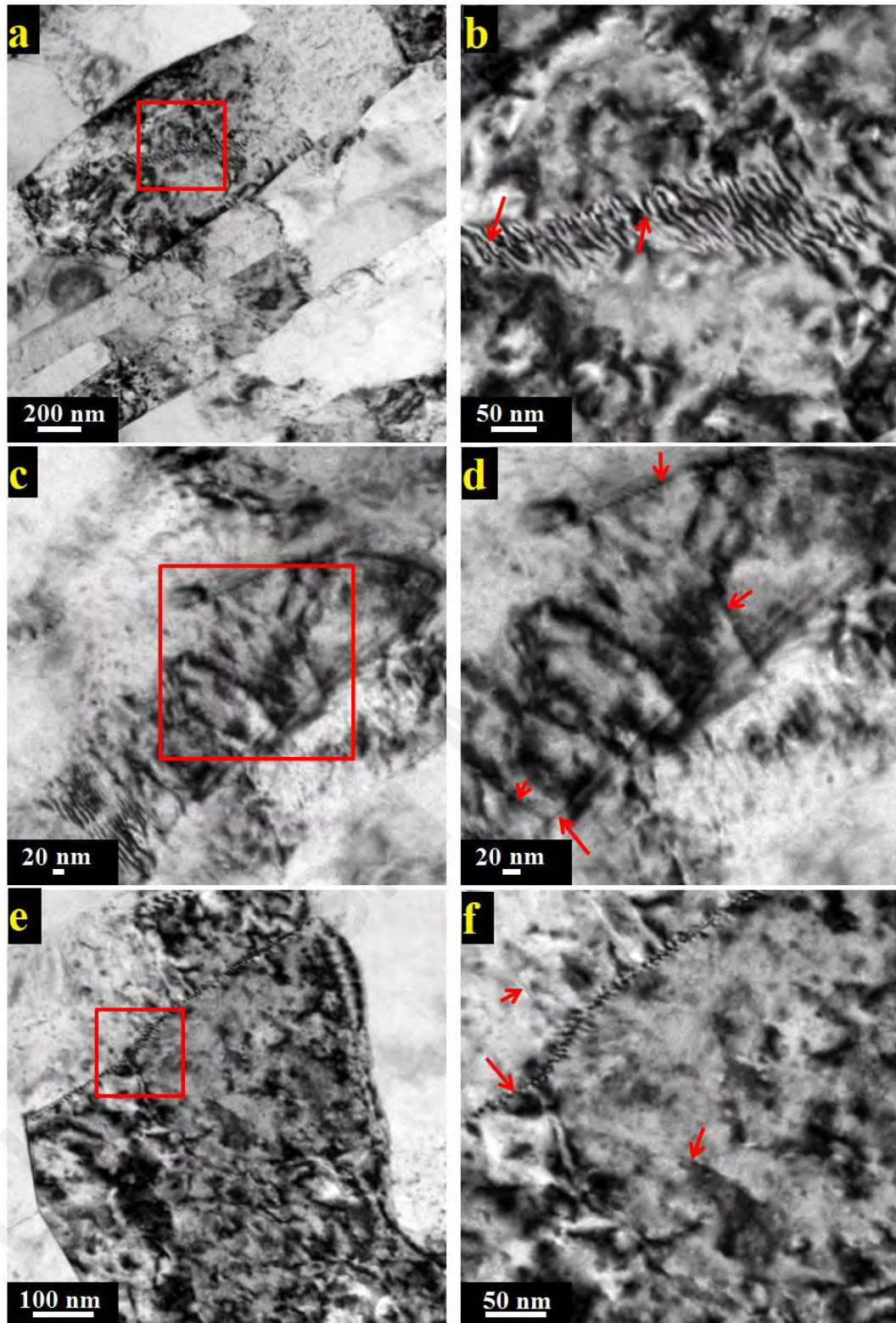


**Figure 4.5:** TEM micrographs of the TCAP treated Al-1060 tubes following (a,b) one, (c,d) two and (e,f) three passes, demonstrating dislocations piled up to form subgrain boundary and higher magnification of dislocations in subgrain boundary (showed by red arrows).

The dislocations are created as the TCAP deformations are absorbed in the subgrain boundaries and the misorientation increases to convert them into low-angle grain

boundaries ( $5\text{--}15^\circ$ ). In Figure 4.5(b, d, and f), the greater magnification of dislocations into the subgrain boundary is evident. A continuous dynamic process of recrystallization turned these low angle boundaries into high angle boundaries, resulting in the fine-grained structure (Yadav et al., 2012).

The quantitative values of the shape and size of the grains are shown in Figure 4.6. Grain shape factor (GSF) is defined as  $GSF = d_1/d_2$  to quantify the shape of grains in which  $d_1$  and  $d_2$  are the mean values of the long and short diameter of the grains. The high value of GSF corresponds to elongated grain shapes, whereas GSF value close to unit corresponds to equiaxed grain shape. Here, to calculate GSF more than 50 grains are considered. As mentioned earlier, in the early stages of the TCAP process, the elongated grain structure is formed. When the number of TCAP passes increases to three, elongated grains and subgrains almost disappear, and equiaxed grains are formed.

Figure 4.6 indicates that the GSF value decreases when the number of TCAP passes is increased. After three passes, the GSF value decreased to 1.3 from the initial value of 4.2 in the processed sample after one pass. Measurements of the grain sizes from TEM micrographs also show that one pass of the TCAP process has refined the microstructure from the initial annealed condition having grain sizes of about  $53\ \mu\text{m}$  to a microstructure and new subgrains with grain sizes of around  $460\ \text{nm}$ . It is worth noting that there is presence of distinctly elongated subgrains having  $\sim 100\ \text{nm}$   $d_2$ , and more than  $\sim 1\ \mu\text{m}$   $d_1$  values. Figure 4.6 and histograms in Figure 4.4(c, f, i) show that when the process undergoes the second pass the elongated subgrains with  $460\ \text{nm}$  size have morphed to a combination of new grains and subgrains of about  $320\ \text{nm}$  in sizes. On third TCAP pass, the elongated grains and subgrains almost disappear, and equiaxed grains of about  $310\ \text{nm}$  is formed. These results reflect the findings of previous reports on the SPD processing of aluminum alloys. Reihanian et al. (2008b) reported mean grain sizes of  $380\ \text{nm}$  for

commercially pure aluminum samples after eight passes ECAP (route  $B_c$ ) process, which is almost in good agreement with the current results (Mesbah et al., 2014). The grain size of UFG high purity aluminum (99.999%) after eight passes ECAP was reported to be 1.1  $\mu\text{m}$  (Kawasaki et al., 2009).

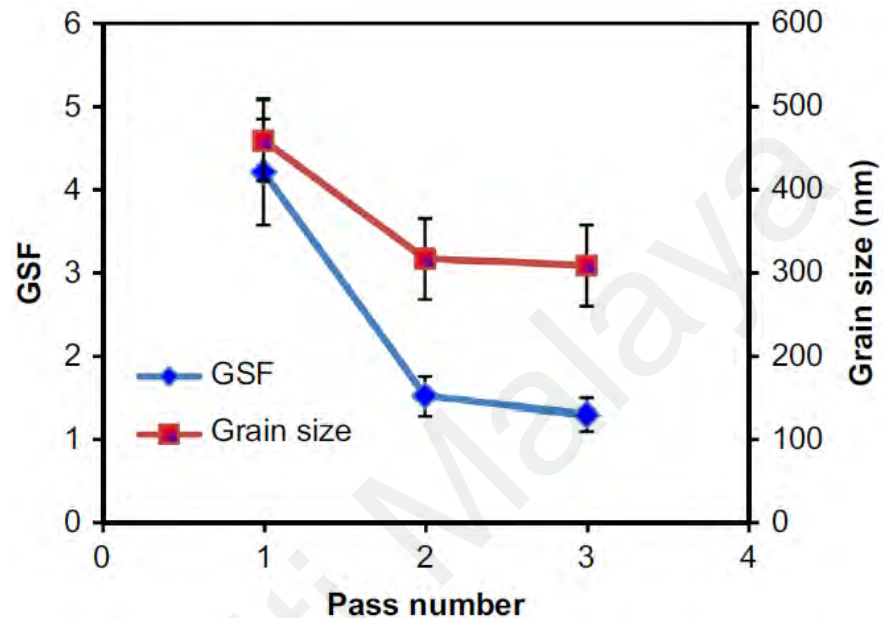


**Figure 4.6:** The effect of the number of TCAP passes on grain size and grain shape factor of Al-1060 alloy.

#### 4.1.3.2 EBSD Analysis

Figure 4.7 shows EBSD colour maps, boundary maps, pole figures, and grain diameter distributions obtained from the centre zone of the TCAP bodies exposed to different passes. Colour code utilized to clarify the crystallographic orientations on a standard stereographic projection (red: (0 0 1); blue: (1 1 1); green: (1 0 1)). The schematic drawing of the tube coordinates system and position of the measured element by EBSD analysis is also demonstrated in Figure 4.7(m). The colour maps are presented in Figure 4.7(a), (d), (g), and (j) indicates that the crystallographic orientation of the grains is parallel to the extrusion direction consistent with the key stereographic triangle presented in the

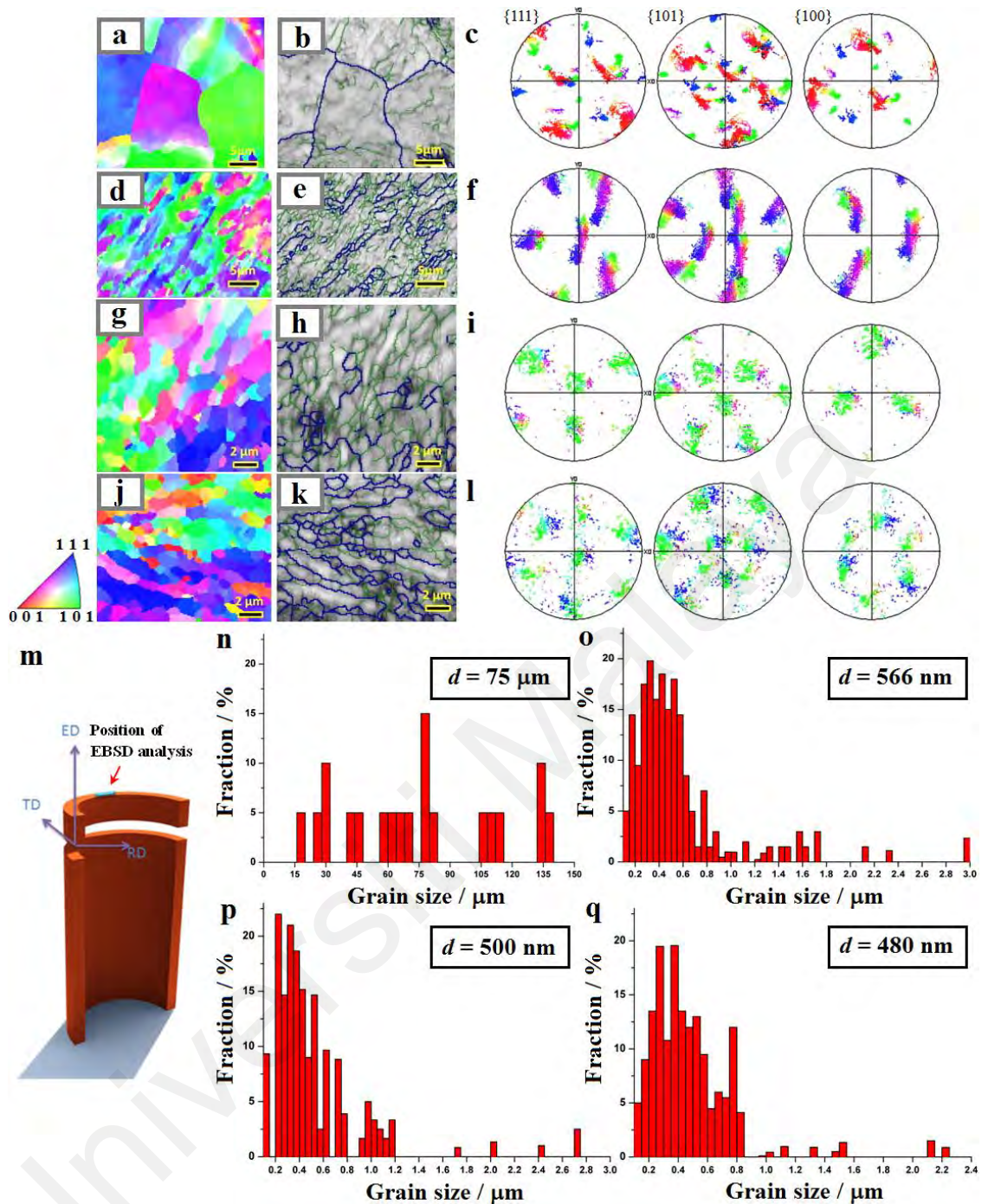


**Figure 4.7:** EBSD colour maps, boundary maps, pole figures, and grain diameter distributions obtained from the centre zone of the TCAP bodies exposed to (a-c, n) 0, (d-f, o) 1, (g-i, p) 2 and (j-l, q) 3 passes. Colour code utilized to clarify the crystallographic orientations on a standard stereographic projection (red: (0 0 1); blue: (1 1 1); green: (1 0 1)); (m) Schematic drawing of the tube coordinates system and position of the measured element by EBSD analysis.

Figure 4.7(b), (e), (h), and (k) displays the corresponding grain boundary maps, wherein the high angle grain HAGBs (i.e. the boundaries which have a relative misorientation larger than  $15^\circ$ ) are shown as blue lines, and the LAGBs (i.e. those

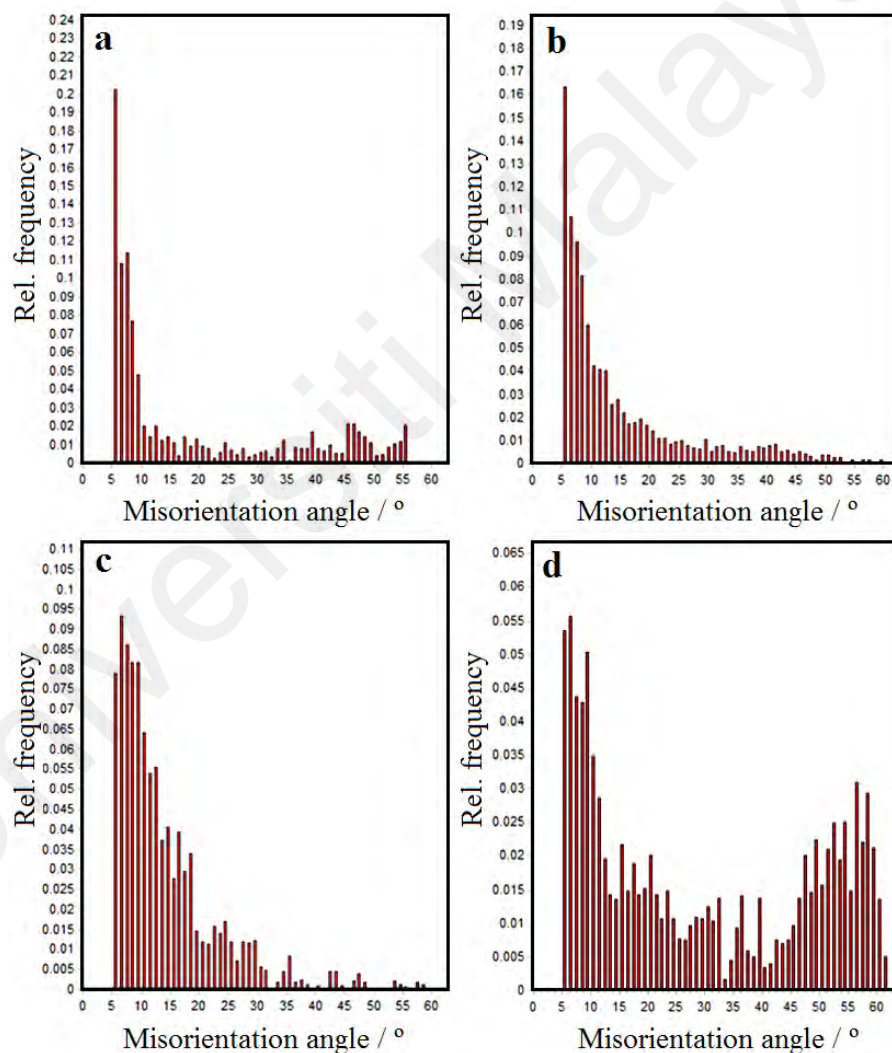
boundaries which have a relative misorientation from  $2^\circ$  to  $15^\circ$ ) are shown as green lines, respectively. Misorientations and boundaries less than  $2^\circ$  were not considered in the maps due to the inaccuracy in the EBSD measurements (Schwartz et al., 2000). An elongated grain microstructure was observed in the EBSD map along the TCAP induced shear bands. Also, several subgrains were evident in the grains' interior structure, which were mostly oriented along the shear direction, building a  $45^\circ$  angle with the PD.

Figure 4.7(c, f, i, and l) presents the pole figures of the unprocessed and TCAP processed tubes acquired using the EBSD technique in a particular position shown in Figure 4.7(m). It is clear that the processing route leads to the shear texture and the intensity of texture raise as the number of passes increases. From the (1 1 1), (1 0 1) and (1 0 0) pole figures of the initial sample in Figure 4.7(c), it can be seen that as-received material has a strong cube texture. In accordance with Figure 4.7(f), remarkable changes in texture can be observed after only one pass TCAP. It can be seen that the intensities of the texture increase from the first to the third pass and thus the overall intensity of the third pass is stronger than one pass. This shows that the texture of the first pass and the third pass is close to ideal, while the deviation from ideal texture is obvious for the second pass. Figure 4.7(n–q) demonstrates the relating histogram for the grain size of the TCAP-processed Al-1060 alloy.

From Figure 4.7(n), which illustrates the actuarial variation of grain size, the average size of the unprocessed sample was around  $75\ \mu\text{m}$ . In the first pass in Figure 4.7(o), the mean grain size diminished from a preliminary grain size of  $75\ \mu\text{m}$  to  $566\ \text{nm}$ , where 9.88% of grains were in the nano regime and the maximum area fraction was related to the diameter of  $0.325\ \mu\text{m}$ . According to Figure 4.7(p), an average grain size of about  $500\ \text{nm}$  was achieved for 2 pass sample, wherein the maximum grain size was around  $2.725\ \mu\text{m}$  and 15.73% of the grains had the diameter of nanometer range. In 3 pass processed

sample (Figure 4.7(q)), the utmost grain size was about  $0.825\ \mu\text{m}$  and the average grain size was around  $480\ \text{nm}$ . These results are consistent with the quantitative EBSD result attained in former works (Mohebbi et al., 2010; Reihanian et al., 2008a; Sabirov et al., 2013).

Figure 4.8 shows the fractions of grain boundaries (as a percentage) schemed as a function of the boundary misorientation angle for unprocessed and processed samples through different numbers of passes.



**Figure 4.8:** Distributions of the boundary misorientation angle acquired from the EBSD information of (a) unprocessed, (b) 1, (c) 2, and (d) 3 passes processed samples.

From this figure, the misorientation distribution displays two simultaneous evolution types. First, a nonstop rise in the occurrence of high-angle misorientation toward the value

range of 50–60°, and second, a modest rise in misorientation values in the range of 15°–25° because of the conversion of subgrains into grains. Once the misorientation reaches the higher-range distribution, the range increase stops. However, a substantial portion of misorientation in the range of 15–25° continues primarily due to the conversion of subgrains to grains, or a process of grain refining achieves its saturation limit (Cabibbo et al., 2005; Kawasaki et al., 2009). It is clear from Figure 4.8(d) that after 3 passes TCAP, the LAGBs are marginal and on the contrary HAGBs surrounded the crystallites by their majority.

#### **4.1.4 Mechanical Properties**

##### **4.1.4.1 Vickers microhardness**

Hardness measurements were taken on the tube cross-section normal to the extrusion direction. Figure 4.9(a) shows the Vickers microhardness of the processed tube versus the number of passes. The hardness increased notably after the first pass and remained almost constant in the subsequent passes. This phenomenon is in good agreement with the previous reports (Sabirov et al., 2013). The microhardness increased from an initial value of 32.9–49.4 HV after the first pass of TCAP, an increase of about 50%. The enhancement in the hardness of the pure Al could be attributed to the grain refinement as outlined in the well-known Hall–Petch relationship. The hardness increased notably as the grain structure was refined and the dislocations were accumulated significantly. After the first pass, increasing the number of subsequent TCAP passes did not affect microhardness, most probably due to the saturation of the grain sizes. Similar saturation behaviour was also seen in ECAP processing of Cu (Salimyanfard et al., 2011), Ni (Raju et al., 2008), Ti (Gunderov et al., 2013) and Mg-based alloy (Sitdikov et al., 2008).

#### 4.1.4.2 Stress-strain curve

Ring-shaped specimens with a thickness of 1 mm, length of 6 mm and an outer diameter of 18 mm were prepared by machining the sections along the axis of the TCAP processed tube as shown in Figure 4.9(b). The compression load was applied parallel to the extrusion direction. Figure 4.9(c) shows the result of the compression test, indicating the stress-strain curves of the TCAP processed tubes for different numbers of passes, which resulted from the compression test.

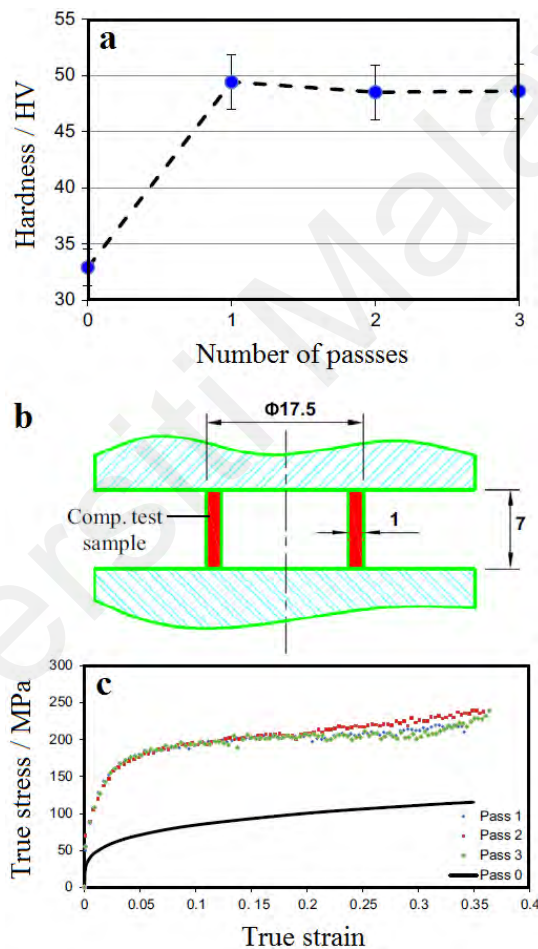


**Figure 4.9:** (a) Microhardness of the processed tubes as well as (b) schematic of ring compression test and (c) true stress-strain curve of the unprocessed and processed Al-1060 tube through 1–3 passes TCAP resulted from tube compression tests.

The comparison made on the TCAP processed tubes with an unprocessed coarse-grained Al-1060 shows a notable increase in the yield and ultimate strength. The yield and ultimate strengths for all TCAP processed cases are 2.5 and 2.3 times higher than

those in the coarse-grained state. It is noticed that the TCAP processed sample shows a short transient high hardening rate at the early stage of deformation, up to a strain of about 0.05, followed by almost perfect plastic deformation with very low strain hardening during deformation. Compression tests were conducted up to a specified strain and the samples did not show any sign of failure, similar to the compression test results of UFG Al produced by ECAP (Sabirov et al., 2013). As mentioned, the most notable improvement was obtained on the first TCAP pass, the subsequent increase in TCAP passes did not show any further improvements.

#### 4.1.4.3 Nanomechanical behaviour

Typical load-penetration depth curves of the unprocessed and TCAP-processed Al-1060 alloy are shown in Figure 4.10(a). These curves plainly demonstrate that the final indentation depth decreased in the TCAP-processed sample for different passes compared to the unprocessed specimen. The hardness values from these curves using the so-called Oliver-Pharr method were estimated (Oliver & Pharr, 1992), where hardness values of 0.83, 1.05, 1.21 and 1.3 GPa were achieved for 0, 1, 2 and 3 passes processed samples, respectively. This shows that the TCAP-processed samples had higher hardness compared to the unprocessed sample; however, the hardness enhancement in the first pass was higher than that of the next passes. On the other hand, the elastic modulus as one of the resistance to being deformed elastically can be determined from the load-displacement information of the nanoindentation test using Oliver and Pharr equation as follows (Oliver et al., 1992):

$$\frac{1}{E_r} = \frac{1 - \nu^2}{E} + \frac{1 - \nu_i^2}{E_i} \quad (\text{Eq. 4.1})$$

where  $E$  and  $\nu$  are the elastic modulus and Poisson's ratio of the test sample,  $E_i$  and  $\nu_i$  are the elastic modulus and Poisson's ratio of indenter tip, and  $E_r$  is the reduced elasticity modulus of material, which is obtained from the nanoindentation test based on the Oliver–Pharr method (Oliver et al., 1992).

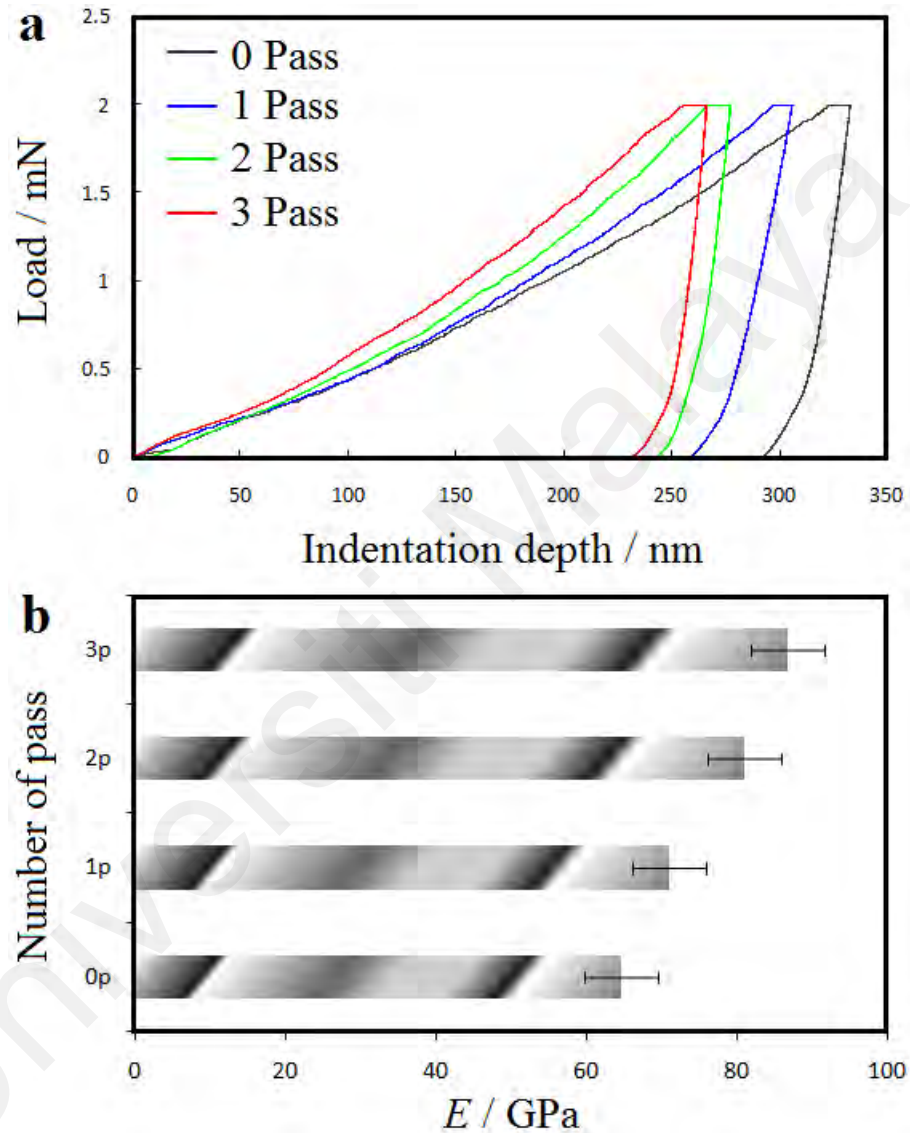


**Figure 4.10:** (a) Typical load-penetration depth curves and (b) the module of elasticity of the unprocessed and TCAP processed samples.

For calculating the elastic modulus of the Al-1060 samples, the values of  $\nu = 0.33$ , and  $\nu_i = 0.07$  and  $E_i = 1140$  GPa were considered in Eq. 4.1. The values used for  $\nu_i$  and  $E_i$  are taking into account the technical data accessible for the related Triboindenter system. Based on the obtained data presented in Figure 4.10(b), values of elastic modulus of the

TCAP-processed samples were greater than that of the unprocessed tube. Also, an increase in the TCAP passes has prompted an increment in the module of elasticity, which could be considered as an important feature of the SPD processed materials.

## **4.2 Structural, Morphological and Mechanical Properties of 70Cu-30Zn Brass Tube Processed by PTCAP**

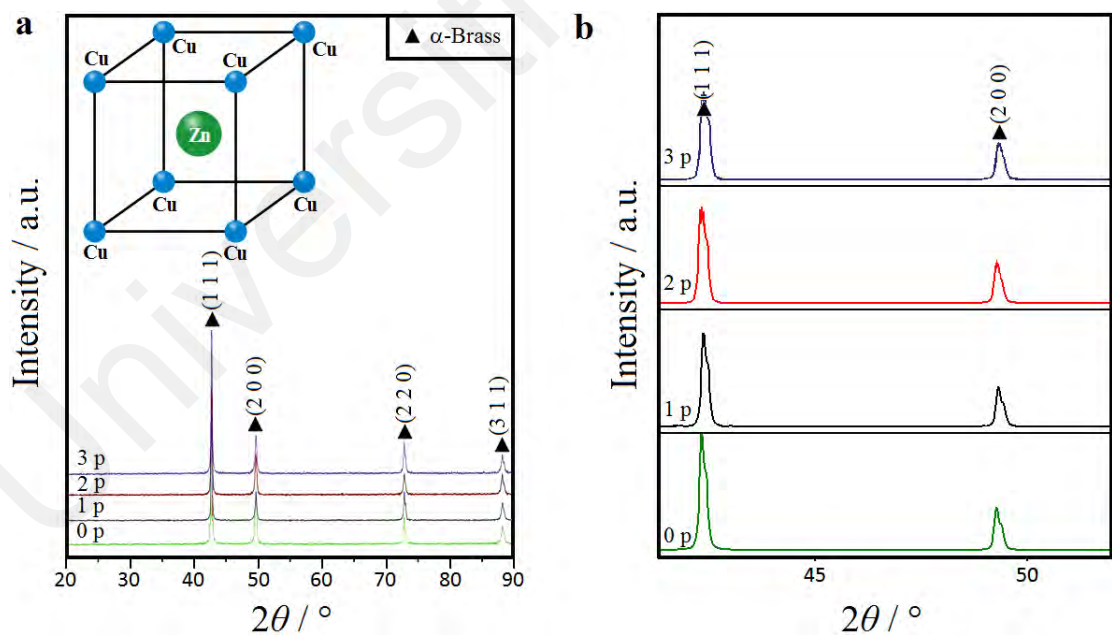
### **4.2.1 Phase Composition and Interplanar Spacing**

Figure 4.11(a) displays the XRD patterns of the 70Cu-30Zn brass alloy before and after one, two and three PTCAP passes. In accordance with these profiles, all detected characteristic peaks are assigned to the face-centered cubic (fcc) crystal configuration of  $\alpha$ -brass (see the inset in Figure 4.11(a)), which are consistent with standard (JCPDS#050-1333). These diffraction peaks are as follows: (1 1 1) plane at  $2\theta = 42.325^\circ$ , (2 0 0) plane at  $2\theta = 49.275^\circ$ , (2 2 0) plane at  $2\theta = 72.245^\circ$ , and (3 1 1) plane at  $2\theta = 87.455^\circ$ . As can be seen, the preferential orientation in all cases is along the (1 1 1) plane, which is in good agreement with the previous studies (Pineau, 2015). No characteristic peak of Cu or Zn was observed here, confirming the formation of a homogenous  $\alpha$  crystal configuration. This crystal structure takes place when Zn dissolves into Cu, creating a solid solution of homogeneous composition (Benisek et al., 2014). By an increase in the number of passes, some alterations were observed in the XRD profiles as shown in Figure 4.11(b). For instance, with increasing the number of passes, the brass-derived XRD peaks declined in both sharpness and intensity, which could be caused by the excessive strain induced by the PTCAP, which is associated with a significant increase in lattice imperfections (Faraji et al., 2012a). In addition, peak broadening occurred due to the further reduction in the crystallite size and intensification in the micro-strain by increasing the number of PTCAP passes. Moreover, all diffraction peaks were gradually shifted to higher angles after the

PTCAP processing, showing a reduction in the brass unit cell volume. From Figure 4.11(b), the direction of XRD reflections has been impacted by both non-uniform and uniform strains because both peak shifting and broadening were detected prior to and after the PTCAP, which is matched with the results obtained from TCAP-processed Al-1060 alloy.

#### 4.2.2 Structural Features

The structural features of the PTCAP-processed 70Cu-30Zn brass alloy, involving lattice constants, unit cell volume, crystallite size, micro-strain, the volume fraction of the grain boundary and defect density are provided in the following subsections.



**Figure 4.11:** (a) XRD patterns of 70Cu-30Zn brass alloy prior to and after one, two and three PTCAP passes and (b) magnified XRD patterns in the range of  $42^\circ \leq 2\theta \leq 52^\circ$ .

**Table 4.3:** Lattice parameters and unit cell volume of the unprocessed and PTCAP-processed 70Cu-30Zn brass alloy.

Number of Passes	<i>a</i> -axis (Å)	<i>b</i> -axis (Å)	<i>c</i> -axis (Å)	<i>V</i> (Å <sup>3</sup> )
0	3.6710	3.6710	3.6710	49.47
1	3.6690	3.6690	3.6690	49.39
2	3.6660	3.6660	3.6660	49.27
3	3.6600	3.6600	3.6600	49.03

#### 4.2.2.1 Lattice constants and unit cell volume

As mentioned above, Eqs. 3.2 and 3.4 were utilized to calculate the fcc lattice constants and unit cell volume of 70Cu-30Zn brass alloy before and following PTCAP. From Table 4.3, PTCAP gave rise to a substantial shrinkage in lattice structure of  $\alpha$ -brass. The standard lattice constant and unit cell volume values for  $\alpha$ -brass (JCPDS#050-1333) are 3.6961 Å and 50.49 Å<sup>3</sup>, respectively. However, the obtained data showed that the lattice constant decreased from the initial value of 3.6710 Å for the unprocessed sample to 3.6690, 3.6660 and 3.6600 Å after the first, second and third PTCAP pass, respectively. These reductions in lattice constants have resulted in unit cell contraction from the initial value of 49.47 Å<sup>3</sup> for the unprocessed specimen to 49.39, 49.27 and 49.03 Å<sup>3</sup> after the first, second and third PTCAP pass. These alterations in lattice features can be attributed to the excessive strain induced by the PTCAP (Faraji et al., 2013b).

#### 4.2.2.2 Crystallite size and micro-strain

According to the XRD patterns in Figure 4.11, an increase in the FWHM of the characteristic peaks was observed with increasing the number of passes. This behaviour is caused by the shrinking of the crystallite size and intensifying the micro-strain. Therefore, to better understand the effect of PTCAP on the refinement mechanism of the present system, the calculation of these parameters is vital (Charfeddine et al., 2014).

The determined values from Eq. 3.8 and the corresponding graphs in Figure 4.12(a), the structural variations of  $D$  and  $\eta$  in 70Cu-30Zn brass alloy are linear and accordingly the crystallite size reduced from the initial value of  $106 \pm 16$  nm for the unprocessed sample to  $102 \pm 16$  nm after the first pass of PTCAP and then decreased to  $82 \pm 16$  nm with increasing the number of passes up to two. Finally, the smallest crystallite size ( $73 \pm 16$  nm) was obtained after 3 passes. In a similar trend,  $\eta$  reduced from 0.01% for the unprocessed workpiece to 0.02, 0.04, and 0.59% following the first, second and third pass of PTCAP, respectively (Figure 4.12(b)). This result indicates that the minimum  $D$  and the maximum  $\eta$  values were obtained in the third pass of the process due to the much more strained structure compared to the other samples.

#### 4.2.2.3 Volume fraction of the grain boundary

In view of the fact that the determination of volume fraction of grain boundary depends on the crystallite size, a significant increase in  $f$  value is expected with decreasing crystallite size (Eq. 3.9). From Figure 4.12(c), the PTCAP processing of 70Cu-30Zn brass alloy caused substantial variations in  $f$  value from 2.8% for the unprocessed specimen to 2.9, 3.6 and 4.0% for the first, second and third pass, respectively. This structural evolution plays an important role in nucleation and duplication of dislocation (Kheradmand et al., 2010) and thereby has profound effects on the microstructural features and mechanical performance of the PTCAP-processed Al-1060 alloy, which will be explained in the following sections.

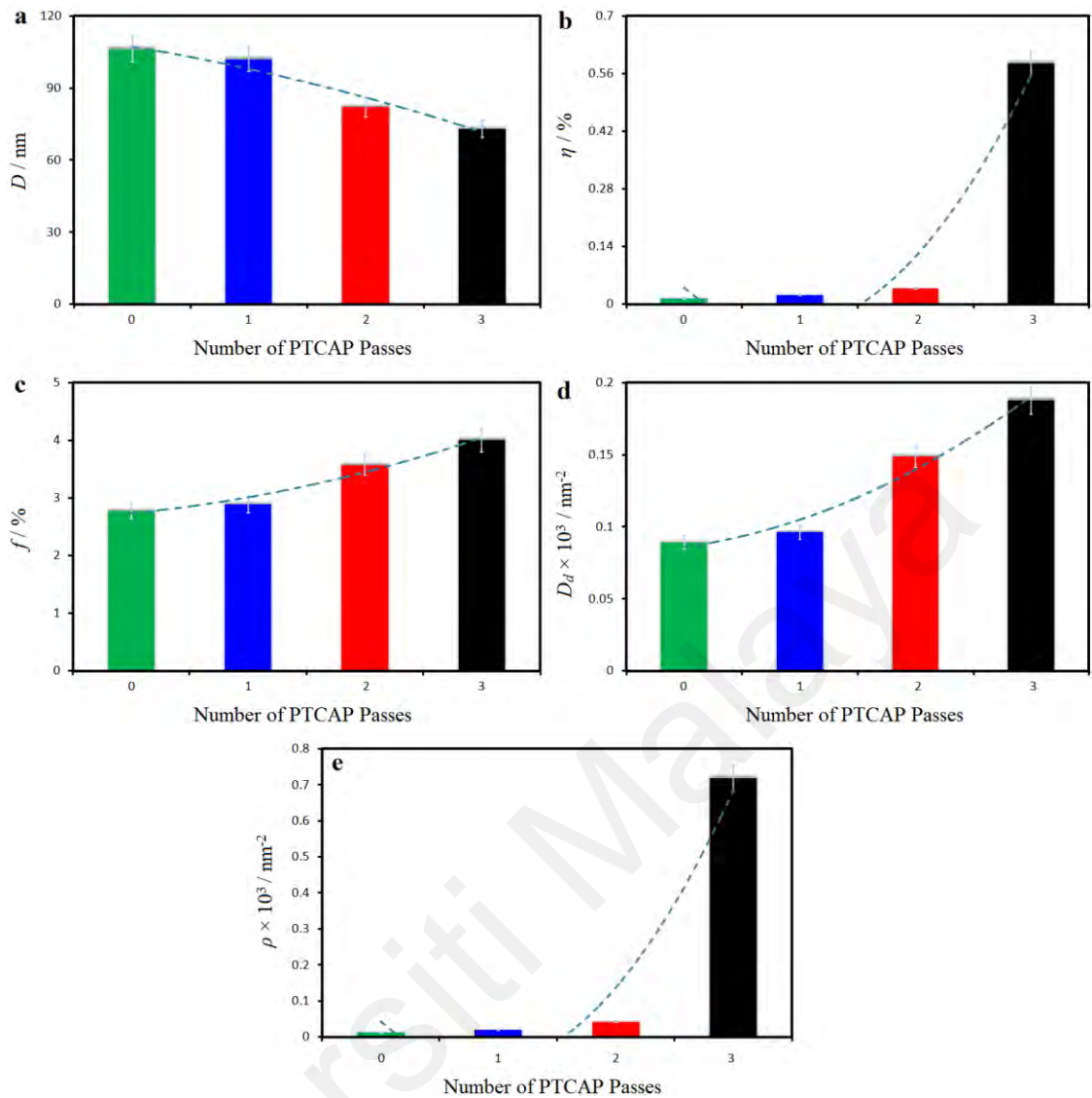


**Figure 4.12:** (a) Crystallite size ( $D$ ), (b) micro-strain ( $\eta$ ), (c) volume fraction of the grain boundary ( $f$ ), (d) defect density ( $D_d$ ), and (e) dislocation density ( $\rho$ ) of 70Cu-30Zn brass alloy before and after one, two and three PTCAP passes.

#### 4.2.2.4 Defect and dislocation density

Here,  $D_d$  as a representative of crystallographic imperfections was calculated using Eq. 3.10. Given that for SPD-processed tubes, dislocation is the main line defects, its density was also determined to take into account other structural features including lattice parameters, crystallite size and micro-strain using equation Eq. 3.11 (Bera et al., 2013). As shown in Figure 4.12(d and e), with increasing the number of passes, the level of the defect and dislocation density has risen drastically and reached an utmost following the third pass. This reveals that the lessening in crystallite size and subgrain with increasing

imposed strain are ascribed to the rise in dislocation density. As grain refinement during the SPD processes like PTCAP generally begins by the arrangement of dislocations into low energy configurations, for instance, LAGBs (Gubicza, 2015).

As already mentioned, there are four major strengthening mechanisms for metals which are based on preventing both movement and proliferation of dislocation or making it energetically undesirable for the dislocation to shift. Among them, solid-solution strengthening is a common procedure for Cu (Maki et al., 2013), where small amounts of an alloying element (like Zn) added to molten Cu can absolutely dissolve and develop a uniform configuration (Figure 4.13(a and b)). Additional amounts of the alloying element will not dissolve at some point; the precise amount is determined by the solid solubility of the specific element in Cu. An alloy with Zn added to Cu is known as brass; the resulting alloy is softer and more ductile than their counterparts. The basic distinction between different kinds of brasses is conditional on their crystal configurations including alpha ( $\alpha$ ), alpha-beta ( $\alpha/\beta$ ) and beta ( $\beta$ ) brasses (Figure 4.13(a)).

From the XRD profiles in Figure 4.11, the processed brass in the present study is alpha-type because around 30.87% Zn dissolved into Cu and formed a solid-solution of homogenous composition. The precipitation hardening is another copper strengthening method, which includes quenching a supersaturated solid-solution from a high temperature, then reheating to a lower temperature (aging) to allow the excess solute to precipitate out and generate a second phase. Of course, this type of strengthening is often observed in Cu-based alloys comprising beryllium (Be), chromium (Cr), nickel (Ni), or zirconium (Zr). However, in the present case, this mechanism is not active owing to the type of alloy ( $\alpha$ -brass) and the lack of these alloying elements. This confirms that in the PTCAP-processed 70Cu-30Zn brass tube, solid-solution strengthening is the main mechanism as schematically illustrated in Figure 4.13(b).

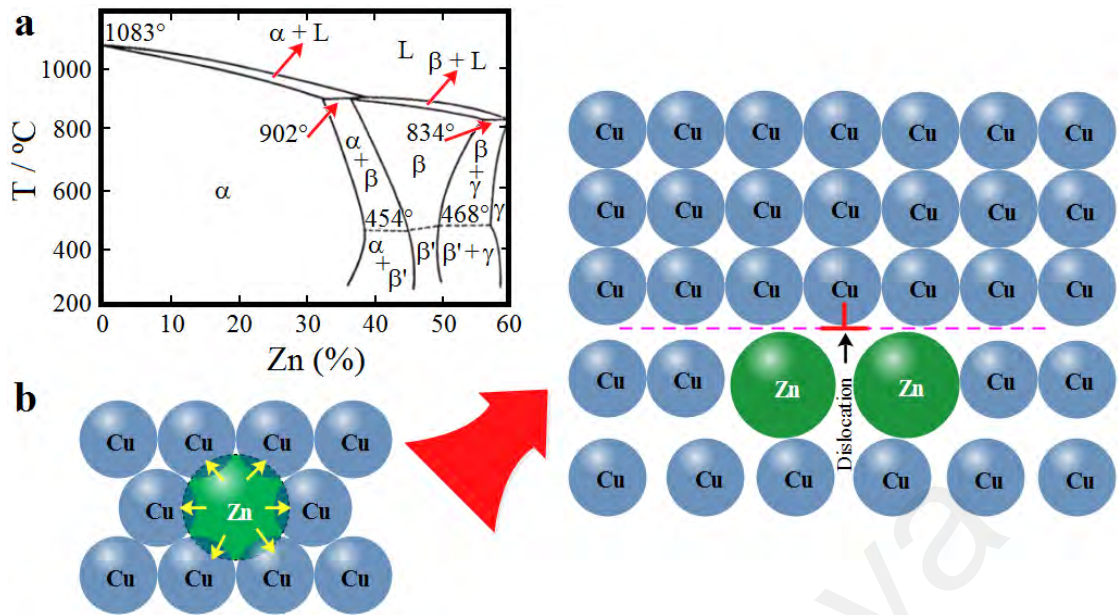


**Figure 4.13:** (a) Constitutional diagram of the Cu-Zn alloys and (b) solid-solution strengthening of 70Cu-30Zn brass alloy.

### 4.2.3 Microstructural Evolution Analysis

#### 4.2.3.1 Optical microscopy analysis

With the aim of understanding the performance of materials, it is essential to create an appropriate linkage between the phenomena happening at the proper scale of the microstructure and the material properties. The morphological features of the SPD-processed materials depend not only on the composition and crystal structure but also on the level of accumulated strain during the process. Under the circumstances described in the experimental part, we made observations by optical microscopy and EBSD to the grain's morphology and evolution.

Figure 4.14(a–c) shows OM images of the 70Cu-30Zn brass tube before and after the first and third passes of PTCAP. As shown in Figure 4.14(a), a recrystallized microstructure with a mean grain size of  $\sim 70 \mu\text{m}$  was formed in the case of the unprocessed 70Cu-30Zn brass tube (heat-treated at  $600^\circ\text{C}$ ). After the first pass of PTCAP in Figure 4.14(b) significant changes in morphology and size of the particles and thereby

a substantial refinement was observed. With further increasing the number of PTCAP passes, more refinement to the nanometer regime occurred due to the higher accumulated strain and stress concentration on the grain boundaries (Figure 4.14(c)).

#### 4.2.3.2 EBSD Analysis

Figure 4.14(d–i) displays EBSD orientation (which distinguished the microstructural changes during the PTCAP process perpendicular to the direction of the extrusion) imaging map patterns and their corresponding boundary map as well as histograms for grain size distributions of the 70Cu-30Zn brass alloy prior to and following the first and third passes of PTCAP.

Based on the EBSD analysis, there were a lot of grains and subgrains with a high fraction of (LAGBs) after the first pass of the PTCAP process, which is related to the capability of PTCAP to refine the microstructure of the 70Cu-30Zn brass alloy. Recrystallized grains in FCC metals, because of the large deformations at room temperatures, have been reported by Salimyanfard et al. (2011) and C. Xu et al. (2003). Results from optical microscopy analysis of four passes ECAP-processed Al-6061 samples showed that most of the elongated grains became uniformly distributed as explained by Tham et al. (2007), which was inconsistent with one pass PTCAP-processed sample microstructure and the subgrains in the EBSD micrographs transformed to equiaxed grains with HAGBs after the third pass of PTCAP.

The blue lines in Figure 4.14(e and g) exhibit the HAGBs and a misorientation angle above  $15^\circ$ , the same as the LAGBs with the red lines. After the first pass of PTCAP, the low-angle misorientation is dominant in the boundaries, whereas HAGBs were prevailing following three passes.

Herein, the corresponding histograms for grain size distributions of the first and third passes of PTCAP were evaluated. Based on the obtained results in Figure 4.14(h and i), the diameter of 0.64  $\mu\text{m}$  has the maximum area fraction, where the average grain size decreased from the initial value of 75  $\mu\text{m}$  to 780 nm after the first pass of PTCAP. Also, it is remarkable that the maximum diameter of grains in the first pass is 2.78  $\mu\text{m}$ . Following the third pass of PTCAP, the average grain size of about 590 nm was achieved, where the utmost grain diameter was about 2.15  $\mu\text{m}$  and the maximum area fraction belonged to the grains by the approximate size of 0.52  $\mu\text{m}$ .

In this regard, different results are presented in previous reports (Zhao et al., 2005; Zhao et al., 2007). For instance, the mean grain size of 17 nm after five passes HPT for brass (Cu–30 wt.% Zn) processed sample was reported by Zhao et al. (2005). In another research, a mean grain size of 110 nm was reported for the samples processed by HPT + CR process (Zhao et al., 2007).

It should be noted that as the grains continue to refine by successive passes, the formation of LAGBs is suppressed. This is related to the fact that the HAGBs can efficiently absorb the dynamically generated dislocations. The accumulated strain values were strongly influenced by the grain size of the brass alloy such that with increasing the accumulated strain, grains were refined more and more until saturation value as reported by Faraji et al. (2012a). This microstructural observation confirms that UFG and nanostructured tubular components can be acquired by different passes of the PTCAP process.

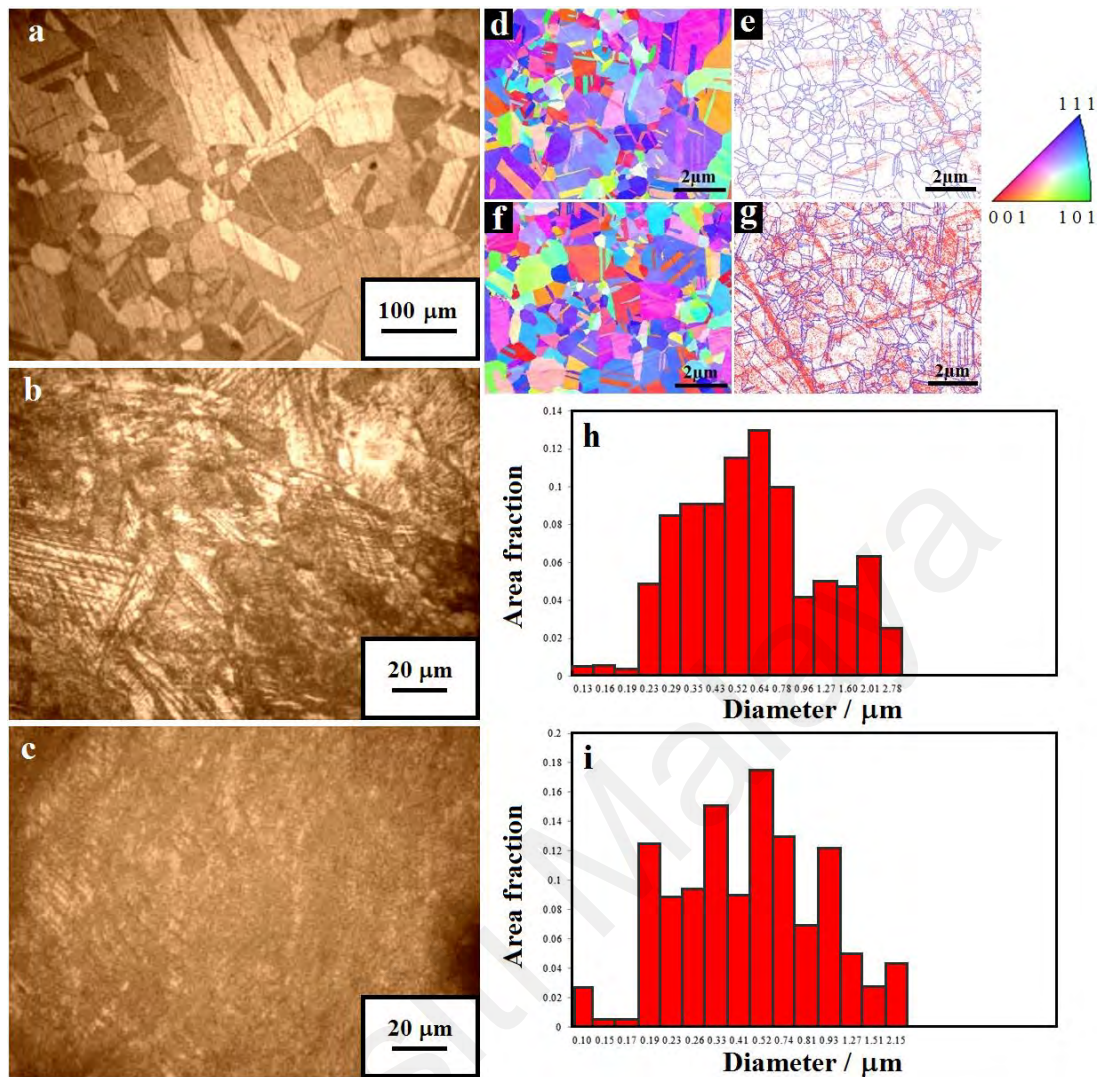


**Figure 4.14:** OM images, EBSD orientation imaging map patterns and their corresponding boundary map as well as histograms for grain size distributions of the 70Cu-30Zn brass tube (a) before and after (b, d, e, h) first and (c, f, g, i) third passes of PTCAP.

Figure 4.15 displays the histograms which represent the average distribution of grain boundaries' fractions plotted as a function of the boundary misorientation angle for first and third passes of PTCAP samples. According to Figure 4.15(a), After the first pass the microstructure mainly consists of LAGBs (60%) while after the third pass, the area fraction of HAGBs is  $\sim$ (66%). ( Figure 4.15(b)). The misorientation distribution displayed two simultaneous evolutionary types: (i) a continuous ascent in the incidence of high-angle misorientation in the direction of the value range of  $55^{\circ}$ – $60^{\circ}$ , and (ii) a moderate increase in misorientation values in the range of  $2^{\circ}$ – $15^{\circ}$  (up to 30% of the total amount of

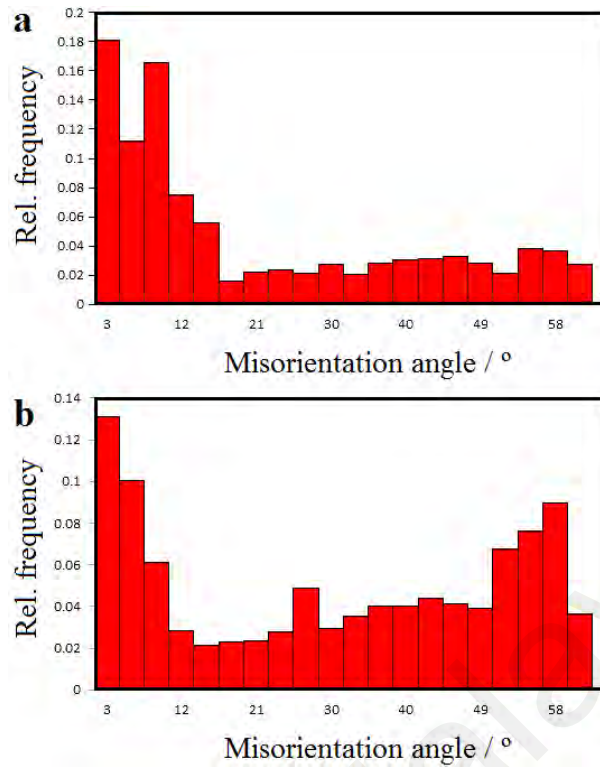


**Figure 4.15:** The histograms of misorientation angle distribution after (a) first and (b) third pass of PTCAP.

misorientation, after the third pass) owing to the exchange of subgrains into grains. Meanwhile, the misorientation rises to the higher-range distribution with no more increment.

A substantial portion of the misorientation in the range of  $15^{\circ}$ – $25^{\circ}$  continued mainly as a result of the exchange of the subgrains to grains, or a process of grain refining which achieves its saturation limit.

Following the third pass of PTCAP, the LAGBs were found to be marginal. In fact, HAGBs surround the crystallites by their majority. These results are consistent with the findings of the previous study (El-Danaf et al., 2007).

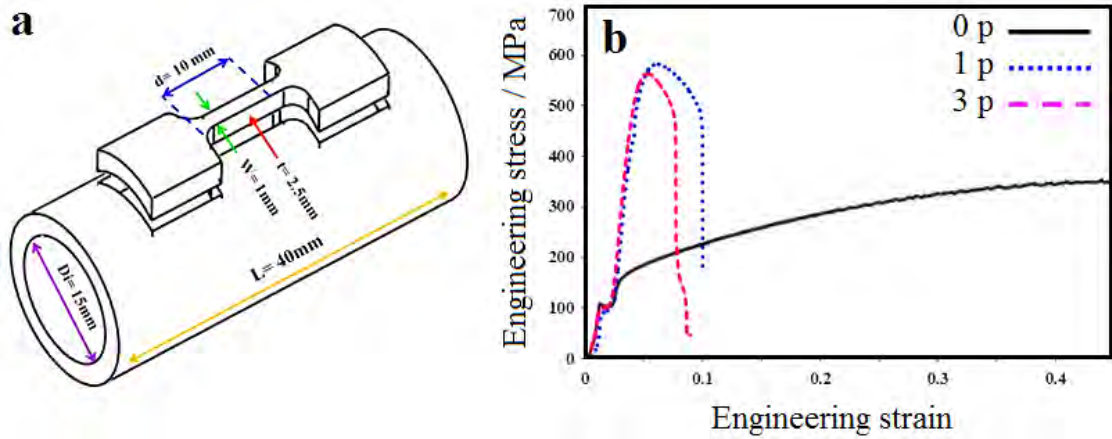


**Figure 4.16:** (a) Tensile test location in the schematic view in the axial direction and (b) tensile engineering stress-strain curve of the 70Cu-30Zn brass tube before and after the first and third pass of PTCAP.

## 4.2.4 Mechanical Properties

### 4.2.4.1 Stress-strain curve

Tensile test location in the schematic view in the axial direction and tensile engineering stress-strain curve of the 70Cu-30Zn brass tube before and after the first and third pass of PTCAP are shown in Figure 4.16(a) and (b), respectively. From this curve, a significant rise in  $\sigma_{YS}$  and  $\sigma_{UTS}$  was detected for the PTCAP-processed specimens, which can be caused by the grain refinement during the PTCAP processing (Faraji et al., 2012a). In contrast, there was a substantial diminution in elongation to failure ( $\delta$ ) following the first and third pass of PTCAP. It should be mentioned that no significant increase was observed in mechanical strength and elongation to failure ( $\delta$ ) with increasing the number of passes from 1 to 3. This behaviour can be ascribed to the saturation in the grain size as already reported in the previous studies (Sabbaghianrad et al., 2014).

### 4.2.4.2 Nanomechanical behaviour

The mechanical behaviour of the SPD-processed alloys like 70Cu-30Zn brass tube can be analyzed by the macro- or micro-scale tests. Nonetheless, such examination may also

have some drawback for instance: (a) First, standard sample preparation is time-consuming and costly; (ii) Secondly, it is very difficult to create pre-cracks in brittle alloys; (iii) the mechanical strength values are somewhat higher than the actual values; (iv) in some test, for instance, microhardness assessment, unwelcome cracks may form in addition to the major crack, which can perturb the stress field and affects the toughness (Karimzadeh & Ayatollahi, 2014). Alternatively using the nanoindentation test, the possibility of creating small cracks declines because the threshold load to cause cracking is remarkably inferior than the Vickers indentation test, where the highly restricted applied loads and locating of nanoindenters make available a precise assessment of the load, the beginning of fracture and other mechanical features of the processed tubes (Kruzic et al., 2009).

In general, during nanoindentation testing, there are numerous concerns that necessitate being well thought-out if high-quality information is to be attained as testing the bulk workpieces. In the case of soft materials, one of the main matters in assessing mechanical behaviour is the accurateness of the determined contact area because of the pile-up around the indenter resulting in a substantial rise in the contact area. During this test, the mechanisms of deformation and, thus the prevailing dislocation nucleation and propagation events are multifaceted. This suggests that the fraction of the pile-up is not constantly proportional to the load of indentation and its figure can change. Accordingly, a precise assessment of mechanical features needs to determine the contact area by another technique, for instance, SPM or SEM images (Moharrami & Bull, 2014). Here, SPM micrographs attained using the indenter tip following the completion of the main indentation cycle were appraised to compute the pile-up heights and widths observed in the unprocessed tube, and the outputs were contrasted to those from the processed tubes under similar indentation circumstance.

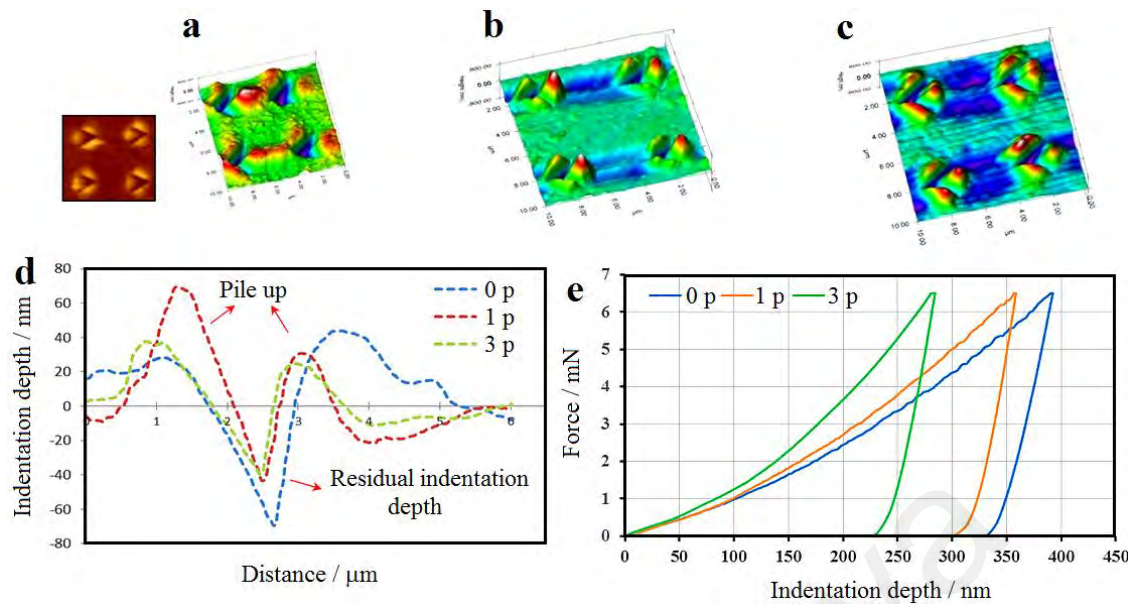


**Figure 4.17:** 3D SPM images of the indentation holes made in 70Cu-30Zn brass tube (a) before and after (b) first and (c) third pass of PTCAP as well as (d) the horizontal sections of the indentation hole at the Centre of the samples and (e) typical load-indentation depth curves.

Figure 4.17(a–e) shows 3D SPM images of the indentation holes made in the 70Cu-30Zn brass tube prior to and following the first and third pass of PTCAP as well as the horizontal sections of the indentation hole at the Centre of the samples and typical load-indentation depth curves. From the 3D SPM observations in Figure 4.17(a–c), no radial cracks are observed around the holes in all cases. In addition, it was observed that the pile-up amount that detected in the processed tubes was significantly higher than that of the unprocessed workpiece (Figure 4.17(d)). This behaviour can be explained on the basis of the work hardening behaviour of the material (Oliver et al., 1992).

According to this figure, it is also clear that the residual indentation depth of the unprocessed tube is more than the PTCAP processed samples, which means that this workpiece possessed a more plastic deformation. This behaviour is in direct relation to the plasticity index, where more plasticity index value will cause more pile up and residual indentation depth in the specimen and will be discussed in this section. Figure 4.17(e) illustrates the typical load-displacement curves obtained from the nanoindentation

experiments performed on the unprocessed and processed samples. Evaluation of the load-displacement curves reveals that the maximum indentation depth has changed by increasing the number of PTCAP passes, where the maximum indentation depth is much more in the case of the unprocessed sample in comparison with PTCAP processed samples. It is remarkable that the indentation depth with maximum value was considered for material with lower strength. The maximum indentation depth at a constant load for 0, 1, and 3 passes PTCAP samples were 335, 300, and 230 nm, respectively. As already mentioned, the elastic modulus is one of the important mechanical properties, which can be obtained from the load-displacement data of the Nanoindentation experiment (Oliver et al., 1992). Here, for calculating this feature, the values of  $\nu = 0.33$ ,  $\nu_i = 0.07$ , and  $E_i = 1140$  GPa were considered in Eq. (4.1) on the basis of the technical data available for the related Triboindenter system. The mean values of the elastic modulus and hardness of the samples are presented in Table 4.4.

Based on this table, the mean values of the elastic modulus and hardness of the processed brass after the first and third pass of PTCAP are  $75.1 \pm 1.65$  GPa and  $2.625 \pm 0.11$  GPa as well as  $103.86 \pm 3.36$  GPa and  $2.832 \pm 0.14$  GPa, respectively. Which are significantly higher than those of the unprocessed tube with the elastic modulus of  $64.08 \pm 1.34$  GPa and hardness of  $1.645 \pm 0.07$  GPa. These values are in good agreement with previous research (Afrasiab et al., 2014; Haghshenas et al., 2012) and can be attributed to the strain hardening and grain refinement as indicated in the well-known Hall-Petch relationship (Faraji et al., 2012a).

**Table 4.4:** The mean values of the elastic modulus and hardness of the samples.

Sample	Elastic modulus (GPa)	Hardness (GPa)
0 Pass	$64.08 \pm 1.34$	$1.645 \pm 0.07$
1 Pass	$75.1 \pm 1.65$	$2.625 \pm 0.11$
3 Pass	$103.86 \pm 3.36$	$2.832 \pm 0.14$

### 4.3 Structural, Morphological and Mechanical Properties of ZK60 Mg Tube Processed by PTCAP

#### 4.3.1 Phase Composition and Interplanar Spacing

Figure 4.18(a) shows the XRD profiles of the ZK60 Mg alloy before and after one, two and three PTCAP passes. In all cases, the main characteristic peaks corresponding to the  $\alpha$ -Mg (JCPDS#004-0770) matrix are prominent. Small peaks attributed to the Mg–Zn, and Zn–Zr intermetallic phases such as the rhombohedral MgZn (JCPDS#040-1334), hexagonal MgZn<sub>2</sub> (JCPDS#034-0457), cubic ZrZn<sub>2</sub> (mp-1401) and hexagonal ZrZn<sub>3</sub> (mp-864889) are also detected. The presence of Zr<sub>3</sub>Zn<sub>2</sub> precipitates in addition to the  $\alpha$ -Mg and other intermetallic phases were observed in the processed samples (Dumitru et al., 2014). It is obvious that the (1 0 1) growth plane was changed to (0 0 2) plane after the PTCAP process. It should be noted that Zr did not form any secondary phases with Mg.

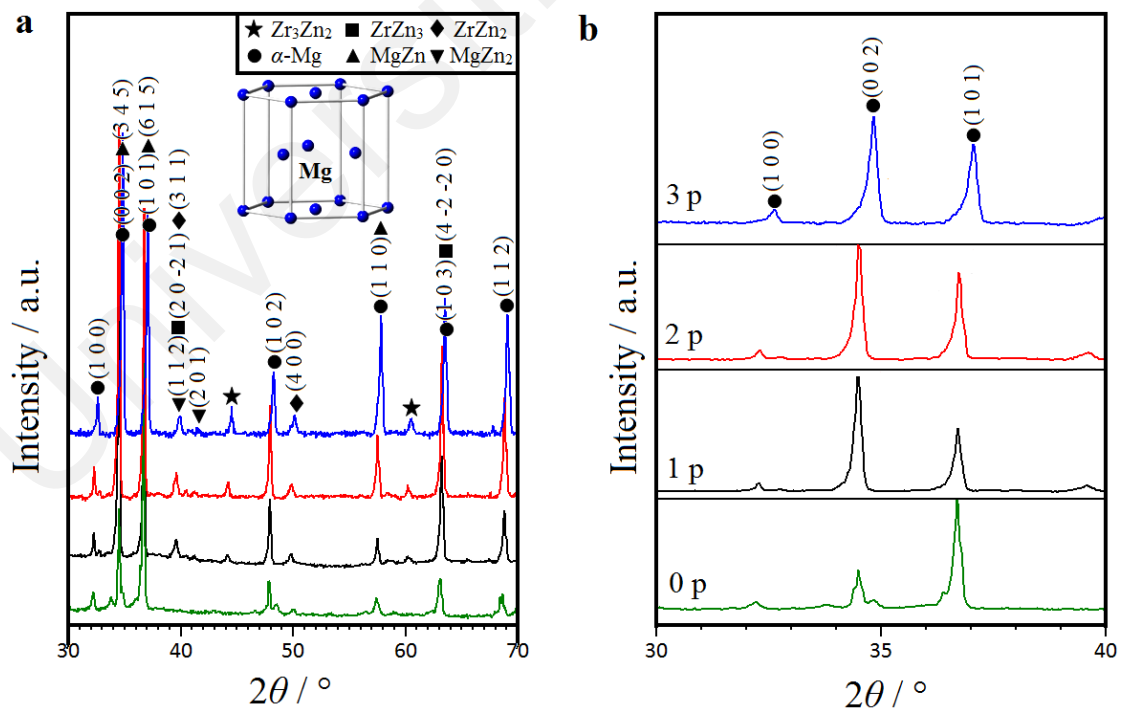


**Figure 4.18:** (a) XRD profiles of ZK60 Mg alloy before and after one, two and three PTCAP passes as well as (b) the effect of strain on the direction of XRD patterns and magnified XRD profiles in the range of  $30^\circ \leq 2\theta \leq 40^\circ$ .

As can be seen in Figure 4.18(a) and Table 4.5, similar XRD patterns were obtained after different PTCAP passes. However, there are some discrepancies over the number of passes increase. First, all characteristic reflections are gradually shifted to higher angles, signifying that the deformation process led to an isotropic compression of the  $\alpha$ -Mg. The reflection shift to the higher angles also implies the decrease of the volume cell of the  $\alpha$ -Mg during the SPD process. Second, as a consequence of the diminution in the crystallite size and rise in the micro-strain, peak broadening occurs with the increase in the number of PTCAP passes. Third, the intensity of the diffraction peaks decreases drastically due to the structural changes during the PTCAP process.

From Figure 4.18(b), it is noted that the direction of XRD reflections is affected by both non-uniform and uniform strains, and the group transverse reflecting planes exhibit a homogeneous equilibrium  $d$  spacing ( $d_0$ ) in the absence of strain. In contrast, the reflecting plane spacing becomes larger than  $d_0$  and the peak shifts to the lower angles in the presence of a uniform tensile strain at right angles. In the third case, the non-uniform strain results in the bending of grains, where the plane spacing is larger than  $d_0$  on the top side (tension), but it is less than  $d_0$  on the bottom side (compression), and it is equal to  $d_0$  somewhere between top and bottom (Nasiri-Tabrizi, 2014). Accordingly, in the present case, the running of different PTCAP passes is associated with the concurrent presence of uniform and non-uniform strains, which has led to both peak broadening and peak shift.

### 4.3.2 Structural Features

In the following subsections, the structural features of the unprocessed and PTCAP-processed ZK60 Mg alloy are presented.

**Table 4.5:** Peak list of ZK60 Mg alloy before and after different PTCAP passes.

Pass	No.	2 $\theta$ . ( $^{\circ}$ )	FWHM ( $^{\circ}$ )	h	k	l	$d_{hkl}$ -spacing ( $\text{\AA}$ )	Height (cts s $^{-1}$ )
0	1	32.2138	0.1279	1	0	0	2.7789	963.83
	2	34.4964	0.1023	0	0	2	2.6000	5088.13
	3	36.6829	0.1791	1	0	1	2.4499	14803.76
	4	48.5195	0.3070	1	0	2	1.8763	500.36
	5	57.4165	0.3070	1	1	0	1.6050	845.08
	6	63.0944	0.1023	1	0	3	1.4735	1850.51
	7	68.6437	0.0936	1	1	2	1.3662	1179.51
1	1	32.2632	0.1023	1	0	0	2.7747	835.46
	2	34.4788	0.1535	0	0	2	2.60131	12115.41
	3	36.702	0.1279	1	0	1	2.44868	6610.55
	4	47.9188	0.1023	1	0	2	1.89844	2232.25
	5	57.5061	0.1023	1	1	0	1.60266	886.1
	6	63.2095	0.1248	1	0	3	1.46988	3950.1
	7	68.7971	0.1560	1	1	2	1.36349	1750.99
2	1	32.2891	0.1023	1	0	0	2.77254	808.33
	2	34.5008	0.1535	0	0	2	2.5997	9506.75
	3	36.7281	0.1023	1	0	1	2.447	7133.04
	4	47.9464	0.1023	1	0	2	1.89741	2309.4
	5	57.5135	0.1023	1	1	0	1.60247	1555.41
	6	63.2305	0.1248	1	0	3	1.46944	3799.96
	7	68.8145	0.1560	1	1	2	1.36319	2494.39
3	1	32.6215	0.1535	1	0	0	2.74504	636.01
	2	34.8326	0.1535	0	0	2	2.57569	5056.11
	3	37.0503	0.1279	1	0	1	2.42646	3698.26
	4	48.2695	0.1279	1	0	2	1.88547	1042.83
	5	57.8188	0.1279	1	1	0	1.59474	1977.73
	6	63.5096	0.1560	1	0	3	1.46365	2268.89
	7	69.0943	0.1872	1	1	2	1.35835	1991.81

#### 4.3.2.1 Lattice constants and unit cell volume

As previously mentioned in Chapter 3, in order to determine the hexagonal lattice parameters and the corresponding unit cell volume of Mg-based alloys prior to and after PTCAP, Eqs. 3.3 and 3.5 were employed. The lattice parameters, volume of unit cell and lattice mismatch of the unprocessed and the PTCAP-processed ZK60 Mg alloy are summarized in Table 4.6.

**Table 4.6:** Lattice constants, unit cell volume and lattice mismatch of the unprocessed and PTCAP-processed ZK60 Mg alloy.

Number of passes	<i>a</i> -axis (Å)	<i>b</i> -axis (Å)	<i>c</i> -axis (Å)	<i>V</i> (Å <sup>3</sup> )	$\epsilon_a$ (%)	$\epsilon_c$ (%)
0	3.209(8)	3.209(8)	5.208(1)	46.44	-0.016	-0.027
1	3.203(5)	3.203(5)	5.198(7)	46.20	-0.203	-0.238
2	3.202(5)	3.202(5)	5.200(7)	46.19	-0.234	-0.200
3	3.200(2)	3.200(2)	5.191(5)	46.03	-0.296	-0.372

From the data given in this table, the PTCAP resulted in a small decrease in the lattice parameters and volume of unit cell, which is consistent with the results of other studies (Charfeddine et al., 2014). The standard lattice constants for Mg (JCPDS#004-0770),  $a_0$  and  $c_0$ , are 3.2095 and 5.2104 Å, respectively. According to data presented in Table 3,  $a$  decreased from the initial value of 3.209(8) Å (unprocessed sample) to 3.203(5), 3.202(5), and 3.200(2) Å after the first, second and third PTCAP pass, respectively. However, the changes in  $c$  parameter were not linear; first, it reduced from 5.208(1) Å (unprocessed specimen) to 5.198(7) Å after the first PTCAP pass and then increased to 5.200(7) Å following the second PTCAP pass, and eventually reached a minimum value of 5.191(5) Å in the three-pass sample. Furthermore, a decrease in the unit cell volume was observed by the increase of the number of PTCAP passes and reached a minimum of 46.03 Å<sup>3</sup> after three passes. The results also show that the lattice mismatch of the processed samples are insignificant, which demonstrates that there are small strain values (~ 0.2–0.372%) as the ZK60Mg tubes are processed by different passes in the PTCAP process. The highest values of the  $\epsilon_a$  (~ 0.296) and  $\epsilon_c$  (~ 0.372%) are related to the three passed sample. The negative value of the strain's points to the in-plane and out-of-plane strains in  $\alpha$ -Mg which is compressive (Cheong et al., 2014).

In accordance with the XRD profiles in Figure 4.18 and peak list of ZK60 Mg alloy after different PTCAP passes in Table 4.5, an increase in the FWHM by increasing the number of passes is generally attributable to two effects of the SPD on the crystal

structure; first is the reduction of the crystallite size  $D$  and the second is the increase of the micro-strain  $\eta$  (Charfeddine et al., 2014).

#### 4.3.2.2 Crystallite size and micro-strain

Figure 4.19 shows the structural features of the ZK60 Mg alloy before and after one, two and three PTCAP passes. The values acquired, are depicted in Figure 4.19(a and b), which indicates that the PTCAP process led to the lattice distortions between 0.19 and 0.25% and severe refinements of the microstructure to nanometer crystallite size with an average of  $68 \pm 8$ ,  $61 \pm 8$  and  $51 \pm 8$  nm after one, two and three PTCAP passes, respectively. It is noticeable that the minimum  $D$  and the maximum  $\eta$  values are attained after three PTCAP passes, which indicates that the UFG–ZK60Mg tube processed by three passes of PTCAP is much more strained compared to the other tubes. Nonetheless, investigations on the structural features of severely deformed ZK60 Mg alloys by PTCAP is still in the early stages (Ungár et al., 2001). For instance, comparable results are reported for crystallite size and micro-strain in severely deformed copper and commercial aluminum alloy by XRD analysis (Charfeddine et al., 2014; Gubicza et al., 2005).

#### 4.3.2.3 Volume fraction of the grain boundary

As mentioned above, the volume fraction of grain boundary was estimated using Eq. 3.9. As can be seen in Figure 4.19(c), the PTCAP processing of ZK60 Mg alloy led to changes in the  $f$  value from 4.3% for the one-passed sample to 4.8% for the two-passed specimen and finally reached a maximum of 5.7% after three PTCAP passes.

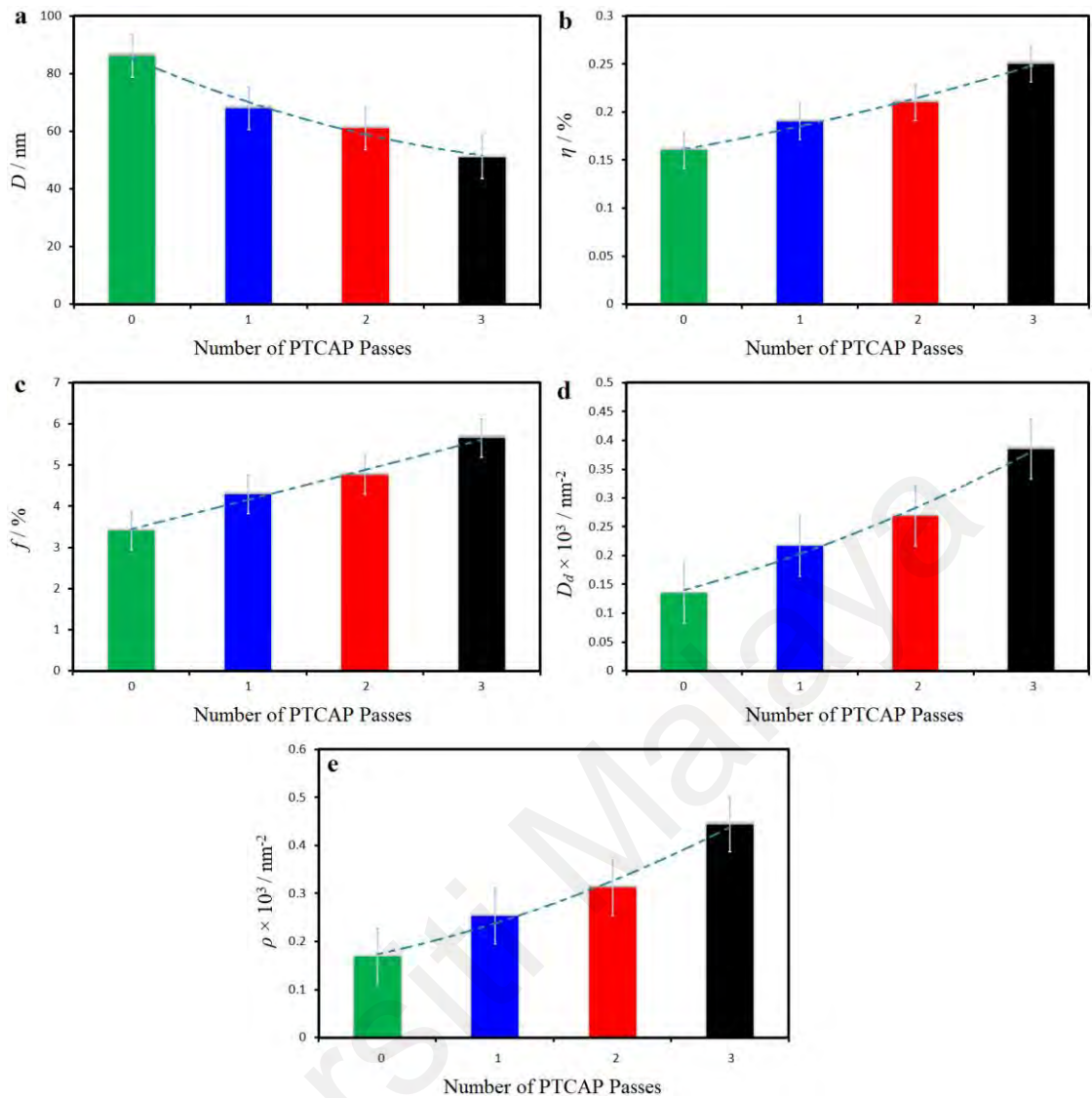


**Figure 4.19:** (a) Crystallite size ( $D$ ), (b) micro-strain ( $\eta$ ), (c) volume fraction of the grain boundary ( $f$ ), (d) defect density ( $D_d$ ), and (e) dislocation density ( $\rho$ ) of ZK60 Mg alloy before and after one, two and three PTCAP passes.

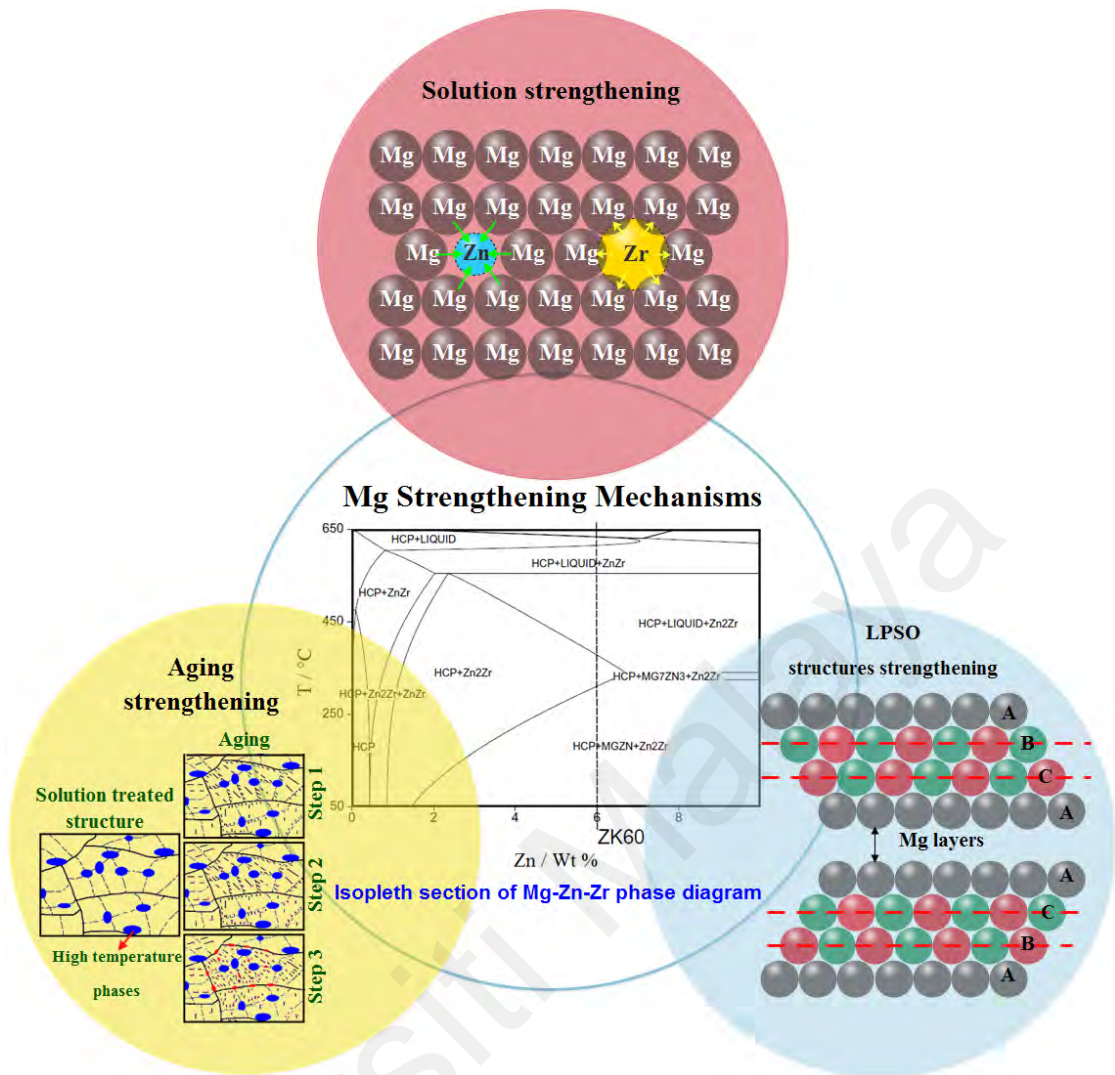
#### 4.3.2.4 Defect and dislocation density

Figure 4.19(d) also depicts that  $D_d$  increases linearly as the number of passes increases. This corroborates the effects of SPD and the number of passes on the  $D_d$  of the ZK60 Mg alloy, where the  $D_d$  of the three-passed sample increases by  $\sim 184\%$  compared to the unprocessed specimen. This behaviour can be ascribed to the processing conditions, e.g. like higher equivalent strain in three-passed specimen compared to the other samples, which resulted in more lattice defects, such as concentration of vacancies, density and

feature of dislocations, kind and fraction of grain boundaries (Bera et al., 2013; Tavakkoli et al., 2015). Thus, the performance of UFG ZK60 Mg alloy can be tailored by an appropriate selection of the production methodology. This result is also in accordance with previous reports that the  $D_d$  of the UFG structure is enhanced by the increase in the number of SPD passes (Mesbah et al., 2014; Tyagi et al., 2017). From Figure 4.19(e), it is clear that the dislocation density increases with the number of PTCAP passes which is associated with structural changes during the process (Bera et al., 2013).

It should be mentioned that the rate of increase in the dislocation density shows a rising propensity with the rise in the number of PTCAP passes. Although it is essential to know whether or how such a mechanism could affect the performance of the UFG–ZK60 Mg tubes in relevant industries, it is beyond the scope of this research, as the present work is focused on the microstructural and mechanical analysis as well as the structural changes in terms of the number of PTCAP passes. Hence, additional efforts are required to recognize the precise relationship between the level of strain hardening and the functionality of the UFG–ZK60 Mg tubes.

As already mentioned above, there are different strengthening mechanisms for metallic alloys depending on the type of alloy and production considerations. In the present alloy (ZK60 Mg), Zn (5.49 wt%) is considered as an advantageous alloying element for increasing mechanical strength by making age-hardening response, developing IMCs, and refining grain size. Accordingly, in Mg-based alloys, different strengthening mechanisms can occur conditionally upon the chemical composition of alloys, including solution strengthening, long-period stacking order (LPSO) strengthening as well as aging strengthening (Tyagi et al., 2017), as shown in Figure 4.20.



**Figure 4.20:** Different methods for strengthening Mg-based alloys.

Among them, the aging precipitation of ZK60 consists of the GP zone and the  $\beta'$  (MgZn) phase, wherein the  $\beta'$  phase is the main precipitate in the system and is so stable that can be turned to an equilibrium phase via a long-term aging process. It was also reported that the cutting of  $\beta'$  precipitates by dislocations is the main strengthening mechanism of the  $\beta'$  precipitates in the ZK60 Mg alloy, rather than the bowing of dislocations between the precipitates (W.C. Liu et al., 2009). This shows that the aging strengthening mechanism is a shear mechanism and thus the mechanical behaviour of the ZK60 Mg alloy can be enhanced by enhancing the density of the  $\beta'$  phase.

### 4.3.3 Microstructural Evolution Analysis

#### 4.3.3.1 Optical microscopy analysis

Figure 4.21 shows the optical micrographs of ZK60 Mg alloy perpendicular to the extrusion direction before and after one, two and three passes of PTCAP. From this figure, the distribution of grain size and the process of homogenization is changed with the increase in the number of PTCAP passes. As shown in Figure 4.21(a), the initial as-received material possesses almost coarse grains with a mean grain size of  $\sim 90 \mu\text{m}$ . In addition to these coarse  $\alpha$ -Mg grains, fine particles with a discontinuous network precipitated primarily at the grain boundaries. These fine particles include mainly the  $\beta'$  phase (MgZn) as well as other Mg–Zn, and Zn–Zr intermetallic compounds such as MgZn<sub>2</sub>, ZrZn<sub>2</sub>, and ZrZn<sub>3</sub>. According to Figure 4.21(b–d), the microstructural features of the samples have completely changed after being exposed to the strain levels of 1.8, 3.6 and 5.4 in one, two and three PTCAP pass.

These alterations become more pronounced with the increase of the level of accumulated strain. In the case of the one-passed sample, the grains in various areas are refined which corroborates the effect of the PTCAP process on the microstructural refinement. From Figure 4.21(b), after one pass of PTCAP a bimodal structure which is a combination of coarse grains with a mean size of  $\sim 7 \mu\text{m}$  and recrystallized fine grains of  $\sim 1.5 \mu\text{m}$  is formed. Such a structure is also observed in other studies (Abdolvand et al., 2017b), which is caused by partial dynamic recrystallization during the SPD process. In general, the most common reason for microstructural refinement in Mg at high temperatures is the presence of dynamic recrystallization and nucleation of smaller grains around the main grain boundaries.

These regions possess high energies and are suitable sites for nucleation. This behaviour is related to the stress concentration on the grain boundaries and consequently,

the activation of slip systems (Fata et al., 2017b), where many twins occur in the primary grains owing to the lack of slip systems in hcp metals. Accordingly, an accumulated strain and dynamic recrystallization can initiate the development of a homogeneous structure. However, at higher temperatures, microstructural refinement is less affected by the dynamic recrystallization which is due to the grain growth (Tan & Tan, 2003).

In Figure 4.21(c), as the level of accumulated strain increased to 3.6 in the second PTCAP pass, it can be seen that the remaining coarse grains of the previous steps have become smaller ( $\sim 2 \mu\text{m}$ ), and the  $\beta'$  phase, as well as other intermetallic compounds, were found broken into relatively smaller particles and distributed in the microstructure. Finally, after three PTCAP passes (Figure 4.21(d)), a more homogeneous and finer microstructure was formed, where a uniform distribution of  $\beta'$  and other intermetallic compounds inside the refined  $\alpha$ -Mg matrix with a mean size of  $\sim 0.9 \mu\text{m}$  is clearly visible leading to an enhancement in the mechanical behaviour and the formability of the UFG-ZK60 Mg tube (Abdolvand et al., 2017b). From this figure, the fraction of secondary phases (intermetallic particles) did not change with the increase in the number of PTCAP passes. As it would be expected, in view of the fact that these intermetallic particles are formed during casting, further SPD steps should not alter the total amount.

Nonetheless, consistent with Figure 4.21, the size and distribution of these secondary phases are different. In addition, some unrecrystallized areas are visible in the microstructure of the one-passed specimen, which was reported in SPD processing of AZ91 alloy at high temperatures and medium strain levels (Faraji et al., 2011b). By increasing the number of PTCAP passes, the volume fraction of the unrecrystallized areas decreases and eventually disappears after three passes. The mechanism of the grain refinement after this SPD process can be elucidated by dynamic recrystallization and deformation twins, which takes place throughout the hot deformation of the ZK60 alloy,

where at the outset primary grains are fragmented by the twins and dynamically recrystallized grains are bounded by the twin boundaries. Subsequent to each pass and by the increase of the shear strain, the grain boundaries with low angle progressed and changed to grain boundaries with high angle, precipitates can be cut in small blocks and distributed at the newly developed dynamically recrystallized grains.

As described above, the as-received alloy with an average grain size of 90  $\mu\text{m}$  is replaced by fine grains of around 0.9  $\mu\text{m}$  average size after three PTCAP passes, where the processed samples showed the occurrence of recrystallization during the SPD process. This is consistent with the results of other Mg alloys processed by the PTCAP method such as AZ31 (Fata et al., 2017b) and AZ91 (Fata et al., 2017a). Figure 4.22 displays the comparison of the number of PTCAP passes and the grain size achieved in different Mg alloys between the current study and the previous studies (Fata et al., 2017a; Fata et al., 2017b).

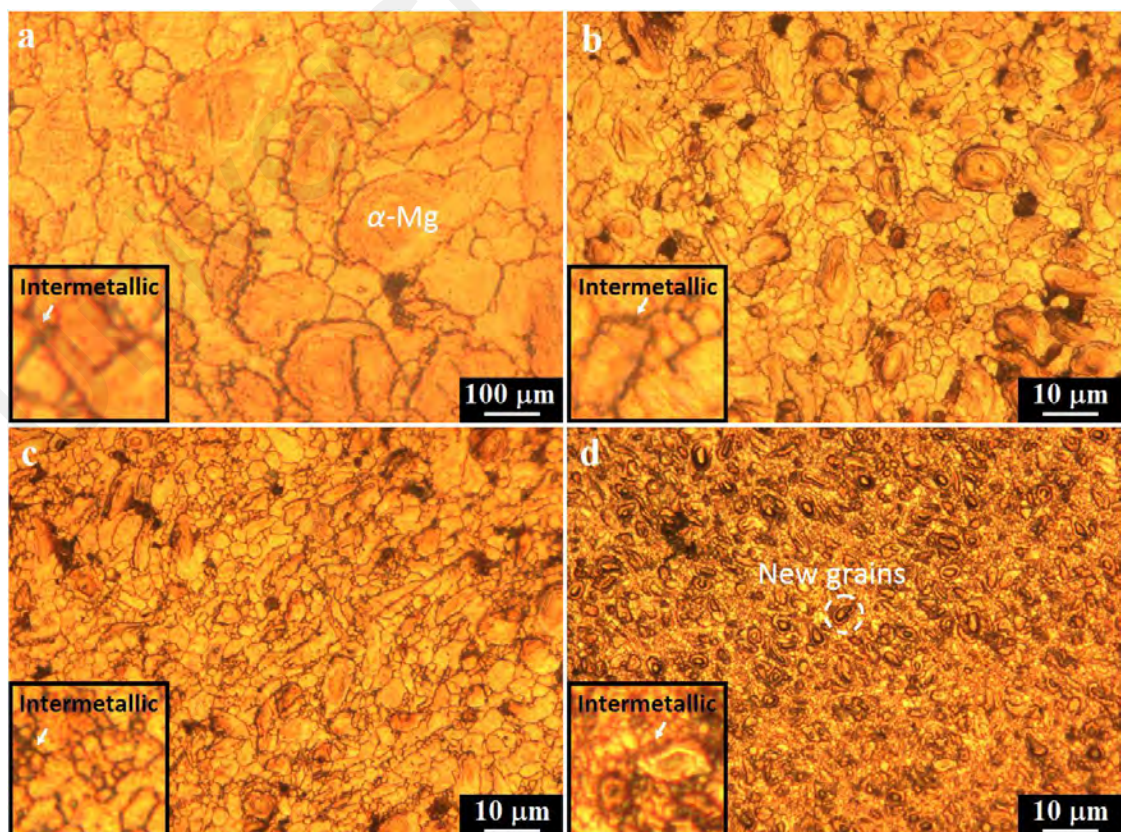


**Figure 4.21:** Optical micrographs of ZK60 Mg alloy perpendicular to the extrusion direction (a) before and after (b) one, (c) two and (d) three passes of PTCAP.

An increase in the number of passes up to two increases the volume fraction of dynamically recrystallized grains, resulting in an average particle size decrease to around 2  $\mu\text{m}$ . After implementing the third pass, a sizeable progression in recrystallization took place, thus an average grain size of 0.9  $\mu\text{m}$  was attained. Compared to the AZ31 and AZ91 Mg alloys, similar PTCAP passes result in a more refined microstructure in the ZK60 Mg alloy. As can be seen, after one PTCAP pass, the average grain size of AZ31 and AZ91 Mg alloys reached 11 and 9  $\mu\text{m}$ , while in the case of ZK60 the value is 9  $\mu\text{m}$ . By increasing the number of pass to two, the average grain sizes of AZ31, AZ91, and ZK60 Mg alloys further decrease to 8, 4.8 and 2  $\mu\text{m}$ , respectively. Ultimately, the lowest average grain size was found in the UFG–ZK60 Mg alloy after three PTCAP passes. This behaviour can be ascribed to the differences in initial grain size, the temperature of SPD processes as well as texture development (Segal, 2018).

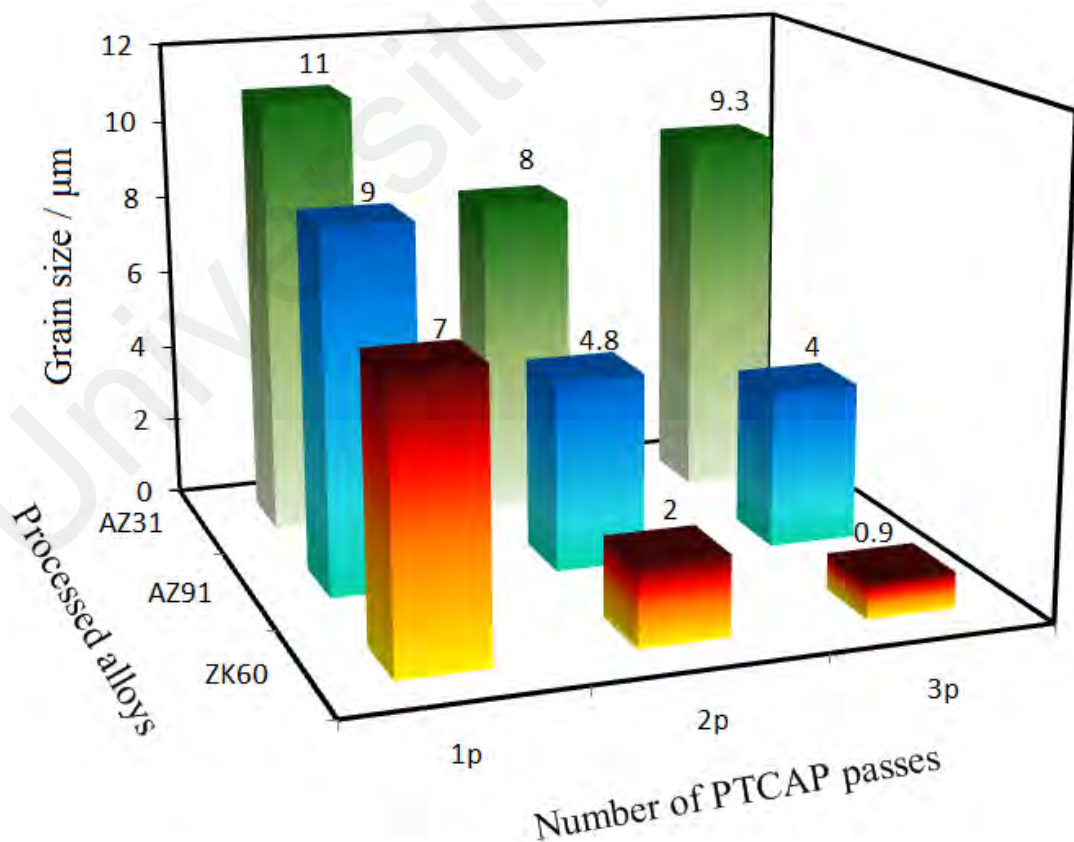


**Figure 4.22:** Comparing the number of PTCAP passes and the grain size achieved in different Mg alloys between the current study and the previous studies (Fata et al., 2017a; Fata et al., 2017b).

#### 4.3.3.2 SEM Analysis

Figure 4.23 displays a “NavCam” image for macro navigation and SEM images of the ZK60 Mg alloy before and after three passes along with the EDX spectra. In Figure 4.23(b), the unprocessed sample consists of almost coarse grains with a mean grain size of  $\sim 90 \mu\text{m}$ , which is consistent with the optical micrograph. The three-passed specimen possesses a more homogeneous and finer microstructure with a mean grain size of  $\sim 1.5 \mu\text{m}$  (Figure 4.23(c)). The microstructure also includes some precipitates ( $\text{MgZn}$ ,  $\text{MgZn}_2$ ,  $\text{ZrZn}_2$ , and  $\text{ZrZn}_3$ ) with a particle size of  $\leq 100 \text{ nm}$ , which are homogeneously distributed in the grain interior. This suggests that the three PTCAP passes resulted in intensive grain refinement of the UFG–ZK60 Mg tube. Similar refinement was also reported in the microstructural investigation of a commercially pure Cu, where a substantial grain refinement was attained even after one pass of PTCAP (Faraji et al., 2012a). To confirm the presence of the second phase, the EDX point analysis was performed (Figure 4.23(d)). The matrix regions nearby the grain boundaries are fairly rich with Zn, whereas the grain interiors are observed to be pure Mg. It should be noted that the dissimilarity between the different areas is attributable to Zn possessing (a higher atomic number element), producing a more intense (bright) BSE signal. The EDX results reveal that the microstructure of the three-passed sample consists of  $\alpha$ -Mg matrix along with different intermetallic phases, where Mg, Zn, and Zr are the main elements.

As shown in Figure 4.23(d), different elemental compositions and allocations of  $97.3\text{Mg}-2.2\text{Zn}-0.5\text{Zr}$ ,  $96.3\text{Mg}-3.6\text{Zn}-0.1\text{Zr}$ ,  $95.4\text{Mg}-4.1\text{Zn}-0.5\text{Zr}$ , and  $88.8\text{Mg}-9.8\text{Zn}-1.4\text{Zr}$  (at.%) are observed which are linked to the presence of  $\alpha$ -Mg and various intermetallic compounds. Based on the SEM micrographs and elemental compositions of different secondary-phase particles, three passes of PTCAP, not only increases the Zn solid solubility in the  $\alpha$ -Mg matrix but also results in greater crushing of the Mg–Zn, and Zn–Zr compounds and also better distribution in the alloy matrix.

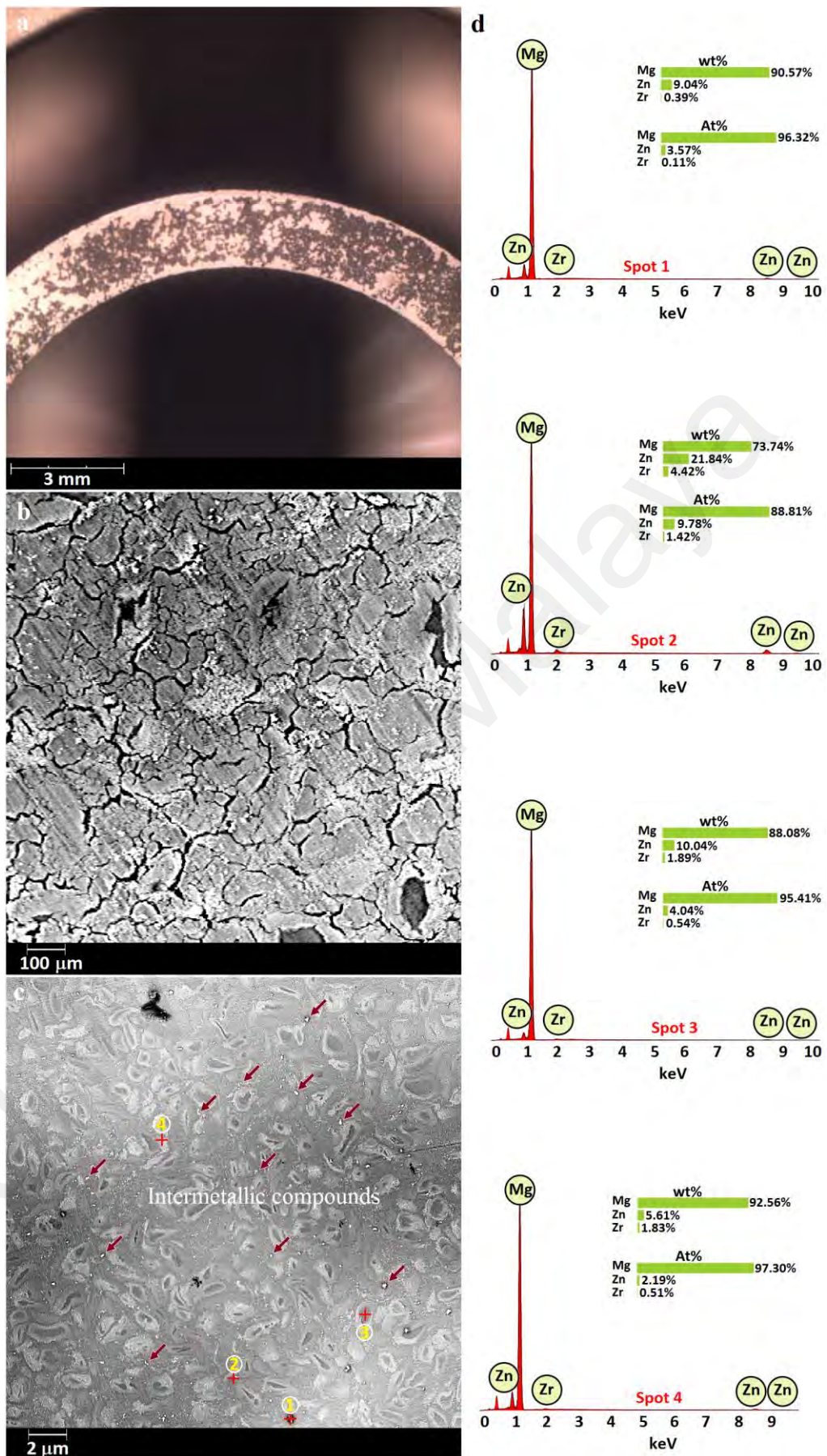


**Figure 4.23:** (a) “NavCam” image for macro navigation and SEM/EDS images of (b) as-received ZK60 Mg alloy (c) the processed tube perpendicular to the extrusion direction after third pass of PTCAP and (d) the EDX point analysis.

### 4.3.4 Mechanical Properties

#### 4.3.4.1 Vickers microhardness

Figure 4.24 shows the Vickers microhardness values across the wall thickness of the as-received and PTCAP-processed tubes, as well as the average values of Vickers microhardness for each sample compared to previous studies (Abdolvand et al., 2017b; Eftekhari et al., 2018; Faraji et al., 2017; Fata et al., 2017a; Fata et al., 2017b). As seen in Figure 4.24(a) and (b), after the primary pass of the PTCAP, the mean value of microhardness raised from  $77 \pm 2$  HV for the unprocessed sample to  $101 \pm 2$  HV, due to the dynamic recrystallization, accumulated shear strain and subsequent grain refinement throughout the SPD process.

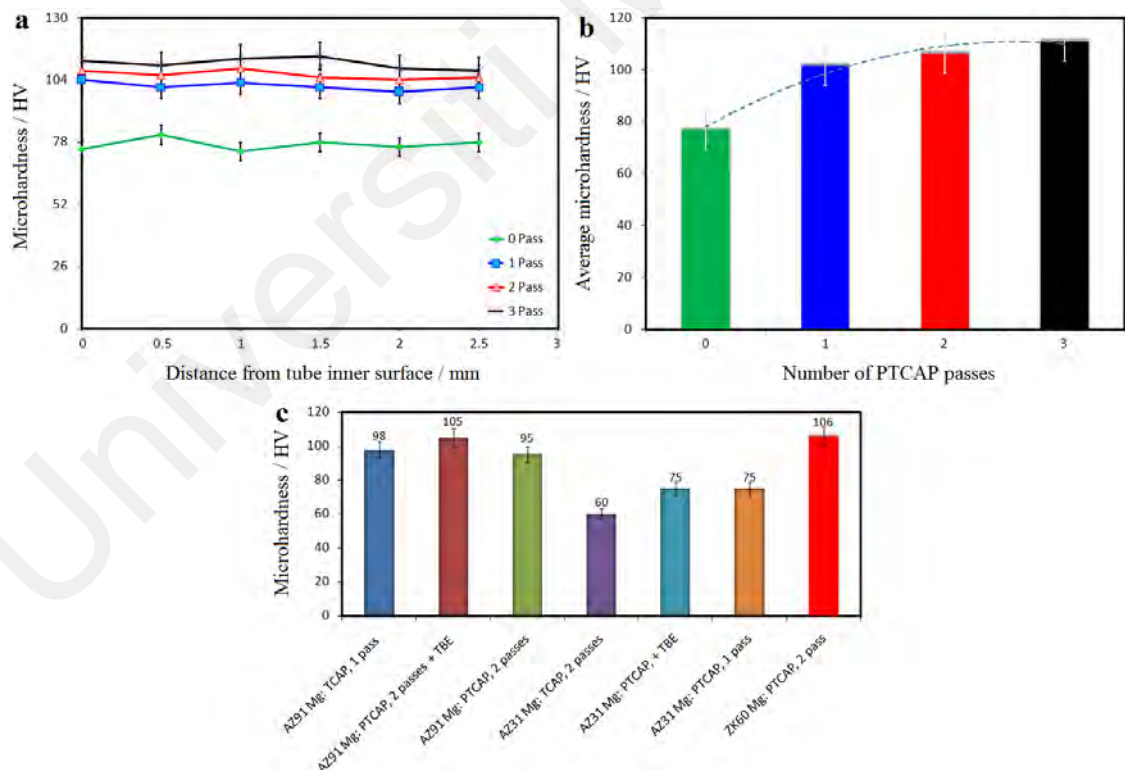


**Figure 4.24:** (a) Vickers microhardness values across the wall thickness of the as-received and PTCAP- processed tubes and (b) the average values of Vickers microhardness for each sample (c) compared to previous studies (Abdolvand et al., 2017b; Eftekhari et al., 2018; Faraji et al., 2017; Fata et al., 2017a; Fata et al., 2017b).

It is found that with the increase in the number of PTCAP passes and further grain refinement, the value of hardness increases due to further dynamic recrystallization. It is clear that there is a nearly 44% increase in the hardness magnitude of the three-passed specimen as compared to the as-received alloy, where the highest value of hardness ( $111 \pm 2$  HV) was detected among all the processed specimens. Here, the hardness enhancement is in good consistent with the microstructural observations, where more plastic strain caused by the increase of the number of PTCAP passes led to more grain refinement, better distribution of intermetallic particles and accordingly more hardness value (Fata et al., 2017b).

However, the increase of the hardness is not consistent with the increase in tensile test results (Third pass sample). This may attribute to the nature of the test procedure in microhardness measurement and tensile test. The hardness is measured in a very small area while the tensile test sample contains a large area of the sample. So, the probability of the existence of cracks/voids rise during the PTCAP process at the high number of passes in the tensile test sample is higher than that in the microhardness test measurement area. As depicted in Figure 4.24(c), the TCAP, PTCAP and a combination of PTCAP and TBE dramatically improves the microhardness of the Mg alloys by grain refining and work hardening. Besides, in accordance with this figure, the two-pass PTCAP processed ZK60 Mg alloy is harder than the processed AZ31 and AZ91 alloys (Abdolvand et al., 2017b; Eftekhari et al., 2018; Faraji et al., 2017; Fata et al., 2017a; Fata et al., 2017b).

#### **4.3.4.2 Stress-strain curve**

Figure 4.25(a) depicts the engineering stress–engineering strain curves of the as-received coarse-grained ZK60 material before and after PTCAP processing at room

temperature. The tensile test results of ZK60 Mg alloy after PTCAP process compared to different thermo-mechanical processes (Dumitru et al., 2014; Fouad et al., 2011; He et al., 2010; Mostaed et al., 2014; Müller et al., 2009; Nový et al., 2009; Orlov et al., 2011; Shahzad et al., 2007; Shahzad & Wagner, 2009; Vinogradov, 2017; Vinogradov et al., 2012) are also summarized in Table 4.7. Generally, the mechanical properties mainly depend on the microstructure, thus altering the microstructural features leads to dramatic changes in strength, toughness, ductility, and hardness. Based on the obtained data, all the PTCAP-processed specimens have higher  $\sigma_{YS}$  and  $\sigma_{UTS}$  than the as-received sample, which results from improved microstructure and increased dislocation density (Feng & Ai, 2009). The increased strength, especially  $\sigma_{YS}$  after the primary PTCAP pass, is caused by the effects of shear strain and the presence of dynamic recrystallization throughout the SPD process.

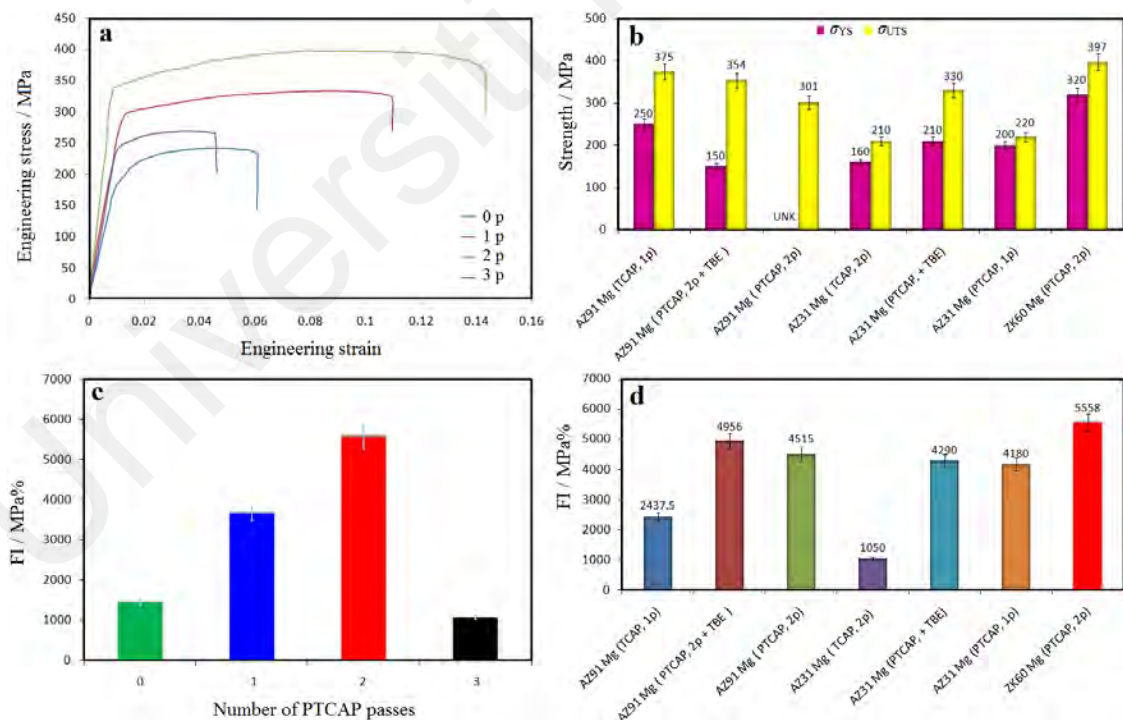


**Figure 4.25:** (a) Engineering stress–engineering strain curves for ZK60 Mg tube in the initial and PTCAP-processed conditions and (b) the strength variations of various Mg alloys processed by TCAP and PTCAP processes as well as (c) FI for the processed ZK60 (d) compared to previous studies (Abdolvand et al., 2017b; Eftekhari et al., 2018; Faraji et al., 2017; Fata et al., 2017a; Fata et al., 2017b).

It is observed that after different passes, the amount of  $\sigma_{UTS}$  is increased, which could be due to a finer microstructure and the increase in the percentage of the area occupied by finer grains. On the strength of the fine-grained materials, strength increases with decreasing grain size, consistent with the well-known Hall–Petch equation. Of course, this equation is invalid when the grain size is less than 20 nm (Phaniraj et al., 2007). Since the grain size is greater than 20 nm, this equation can be used to justify this improvement.

The PTCAP processing, not only enhances the strength but also causes a dramatic intensification in the ductility of the ZK60 Mg alloy. After one pass,  $\delta$  increased from around 6% of the as-received material to around 11%. In addition, both  $\sigma_{YS}$  and  $\sigma_{UTS}$  increased by  $\sim 49\%$  and  $38\%$ , respectively. After the second pass,  $\delta$ ,  $\sigma_{YS}$  and  $\sigma_{UTS}$  increased by  $\sim 14\%$ ,  $82\%$ , and  $65\%$ , respectively, which is ascribed to the concurrent fine grain strengthening mechanism and homogeneous distribution of the intermetallic phases in the  $\alpha$ -Mg matrix. With the increase of the strain in the third pass processed specimen,  $\delta$  decreased to 4% and the improvement in  $\sigma_{YS}$  and  $\sigma_{UTS}$  sharply decreased by 31% and 11%, respectively. Here, the specimen exposed to the temperature of 300° C during the process especially in higher number of passes that could influence the final grain size because of dynamic and static recrystallization.

However, the measured grain size showed that the grain size was decreased even in the three-pass processed sample while its mechanical properties were lessened. So, the loss in mechanical properties after the second pass may be related to the formation of cracks and voids which was mentioned in a number of studies (Amani & Faraji, 2018, 2019a; Amani et al., 2019b). The other reason might be related to the fracture, dissolution, and redistribution of the second phase at a long time at high-temperature exposure which normally enhances the mechanical properties. As represented in Table 4.7, different SPD-processed ZK60 Mg alloys exhibit great improvement in both strength and ductility

features, due to the grain refining, dislocation density increases and uniform spreading of tiny precipitates of the  $\beta$  phase after the SPD processes. For instance, the yield strength and the ultimate tensile strength of the processed Mg–Zn–Zr alloy by integrated extrusion and ECAP shows an increase of nearly 50% to  $\sigma_{YS} = 310$  MPa and  $\sigma_{UTS} = 351$  MPa, respectively (Vinogradov et al., 2012). The strength variations of various Mg alloys processed by the TCAP and PTCAP processes are illustrated in Figure 4.25(b).

This figure demonstrates that TCAP, PTCAP and a combination of PTCAP and tube backward extrusion (TBE) as a hybrid SPD can be applied on various Mg alloys to improve the mechanical strength through the development of UFG microstructure. In addition to this finding, it is obvious that the two-pass PTCAP processed ZK60 Mg alloy has the highest  $\sigma_{YS}$  and  $\sigma_{UTS}$  values compared to the AZ31 and AZ91 alloys (Abdolvand et al., 2017b; Eftekhari et al., 2018; Faraji et al., 2017; Fata et al., 2017a; Fata et al., 2017b). Multiplying the ultimate tensile strength ( $\sigma_{UTS}$ ) with elongation ( $E$ ) gives the Formability Index (FI) upon which the mechanical properties can be regulated as follows (Salandari-Rabori et al., 2017):

$$FI = \sigma_{UTS} E \quad (\text{Eq. 4.2})$$

The FI values calculated for each pass of the PTCAP process are illustrated in Figure 4.25(c). Prior to the deformation process, the as-received sample possesses a FI of 1446 MPa%, which increases to 3652 and 5558 MPa% after one and two PTCAP passes, respectively. Due to the abrupt decrease in the total elongation, the FI value decreases drastically and reaches a minimum of 1068 MPa% after three PTCAP passes. A similar trend was also reported in ZK60 Mg alloys by increasing the number of SPD passes (Mostaed et al., 2014). From Figure 4.25(d), the value of FI in the present work demonstrates the high potential of PTCAP in enhancing the formability of the ZK60 Mg

alloy compared to AZ31 and AZ91 alloys (Abdolvand et al., 2017b; Eftekhari et al., 2018; Faraji et al., 2017; Fata et al., 2017a; Fata et al., 2017b).

**Table 4.7:** The tensile test results of ZK60 Mg alloy after PTCAP process compared to different thermo-mechanical processes (Dumitru et al., 2014; Fouad et al., 2011; He et al., 2010; Mostaed et al., 2014; Müller et al., 2009; Nový et al., 2009; Orlov et al., 2011; Shahzad et al., 2007; Shahzad et al., 2009; Vinogradov, 2017; Vinogradov et al., 2012).

Series	Processing	$\sigma_{YS}$ (MPa)	$\sigma_{UTS}$ (MPa)	$\delta$ (%)	Ref.
0	As-received	176	241	6	Present
1	PTCAP, 1 pass, at 573 K	262	332	11	Present
2	PTCAP, 2 pass, at 573 K	320	397	14	Present
3	PTCAP, 3 pass, at 573 K	230	267	4	Present
4	ECAP, route Bc, 4 passes, at 523 K	~233	~316	~17	[165]
5	ECAP, route Bc, 4 passes, at 473 K	~216	~290	~21	[165]
6	ECAP, route Bc, 4 passes, at 423 K	~268	~300	~30	[165]
7	ECAP, route Bc, 8 passes, at 423 K	~216	~283	~24	[165]
8	ECAP, route Bc, 1 passes, at 523 K	~175	~290	~20	[114]
9	ECAP, route Bc, 2 passes, at 523 K	~175	~325	~25	[114]
10	ECAP, route Bc, 3 passes, at 523 K	~175	~320	~29	[114]
11	ECAP, route Bc, 4 passes, at 523 K	~140	~300	~30	[114]
12	ECAP, route Bc, 4 passes, at 513 K	120	221	28.1	[166]
13	ECAP, route Bc, 8 passes, at 513 K	125	226	35.1	[166]
14	ECAP, route Bc, 4 passes, at 513 K + ECAP, route Bc, 2 passes, at 453 K	160	236	28.9	[166]
15	ECAP, route Bc, 4 passes, at 513 K + ECAP, route Bc, 4 passes, at 453 K	175	266	31.9	[166]
16	DE for ER14 at 663 K	237	312	15.5	[163]
17	DE for ER14 at 663 K + T5 (423 K/24 h)	273	329	16.5	[163]
18	MIF 673 K	180	300	44	[167]
19	MIF 673 + 573 K	230	328	43	[167]
20	ECAP route Bc, 2 passes at 523 K	180	277	24	[167]
21	ECAP route Bc, 2 passes at 593 K + MIF 573 K	245	325	28	[167]
22	Hot pressed	222	264	7.4	[168]
23	DE for ER19 + ECAP, route C, 2 passes, at 623 K	310	351	17	[168]
24	DE for ER4.5 + DE for ER12 at 573 K	290	335	16	[169]
25	DE for ER4.5 + DE for ER44 at 573 K	280	340	19	[169]
26	DE for ER4.5 + DE for ER12 1 SW at 573 K	350	390	12	[169]
27	DE for ER12 at 623 K	300	335	15	[169]
28	DE for ER12 at 573 K	300	335	17	[170]
29	DE for ER12 at 523 K	325	355	14	[170]
30	DE for ER12 at 473 K	320	355	14	[170]
31	DE for ER12 at 448 K	275	330	21	[170]
32	DE for ER22 at 623 K	295	340	15	[171]
33	DE for ER22 at 623 K + ECAP, route Bc, 1st pass	285	335	16	[171]
34	at 523 K and 2nd pass at 513 K DE for ER22 at 623 K + ECAP, route Bc, 4 passes, 1st pass at 523 K, then reduced by 10 K for each pass	310	340	18	[171]

35	DE for ER22 at 623 K	288	337	16	[172]
36	DE for ER44 at 523 K	280	350	20	[173]
37	DE at 653 K	269	315	12.3	[174]
38	Multi-pass rolling at 673 K	~230	~285	~10.2	[174]
	ECAP, route Bc, 4 passes at 513 K + 4	266	175	31.9	
39	passes, route Bc at				[174]
	453 K				
40	HRDSR, 1p at 473 K	286	338	30.0	[174]
41	Twin roll cast + rolling at 573 K	390	445	8.3	[174]
42	DE of machined chips at 423 K	402	508	6.8	[174]

DE: direct extrusion, SW: swaging, ER: stands for extrusion ratio, MIF: multiaxial isothermal forging, HRDSR: high-ratio differential speed rolling.

## 4.4 Structural, Morphological and Mechanical Properties of WE43 Mg Tube Processed by PTCAP

### 4.4.1 Phase Composition and Interplanar Spacing

Figure 4.26 illustrates the XRD patterns of WE43 Mg alloy before and following one, two and three PTCAP passes as well as the influence of strain on the direction of XRD profiles and magnified XRD reflections in the range of  $30^\circ \leq 2\theta \leq 40^\circ$ . Similar to the ZK60 Mg alloy,  $\alpha$ -Mg (JCPDS#004-0770) was detected as the main characteristic peaks in all cases (Figure 4.26(a)). But unlike the processed ZK60, (1 0 1) peak remained stable as the main growth plane after the PTCAP process.

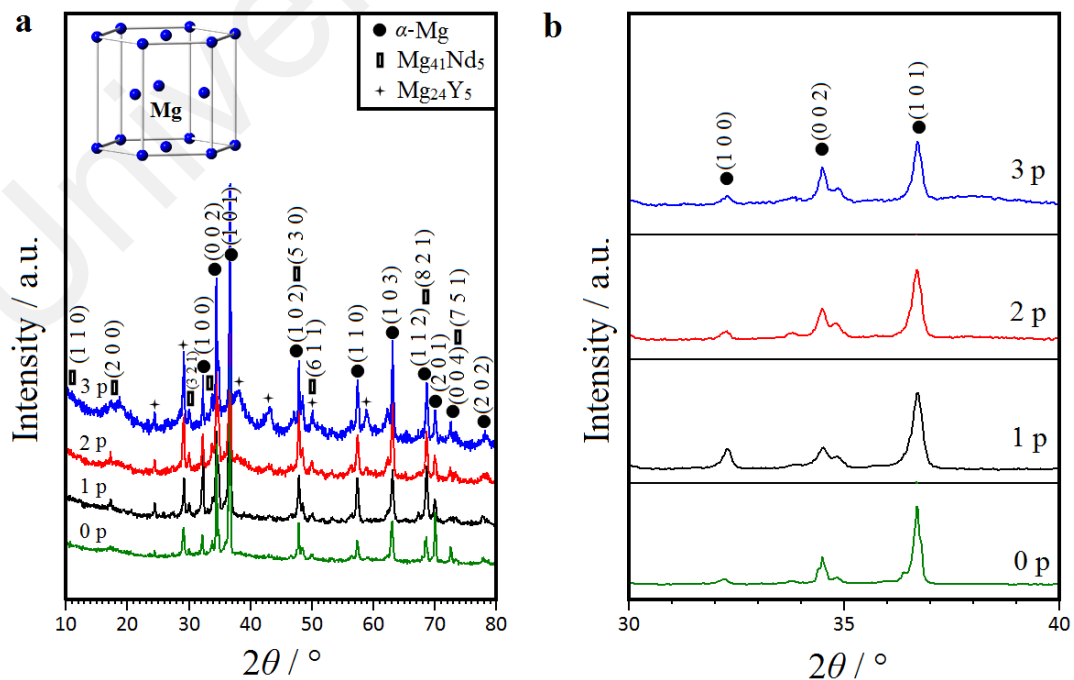


**Figure 4.26:** XRD patterns of WE43 Mg alloy (a) before and after one, two and three PTCAP pass as well as (b) the influence of strain on the direction of XRD profiles and (f) magnified XRD reflections in the range of  $30^\circ \leq 2\theta \leq 40^\circ$ .

In addition to  $\alpha$ -Mg, UFG–WE43 Mg tubes were composed of asymmetrical IMCs of  $Mg_{24}Y_5$  and  $Mg_{41}Nd_5$ . It should be noted that the noted peaks tend to be intensified in the processed tube. This shows that no dynamic dissolution process has occurred during the PTCAP of WE4360 Mg alloy (Jamili et al., 2017).

**Table 4.8:** Peak list of WE43 Mg alloy before and after different PTCAP passes.

Pass	No.	$2\theta$ ( $^\circ$ )	FWHM ( $^\circ$ )	h	k	l	$d_{hkl}$ -spacing ( $\text{\AA}$ )	Height (cts $s^{-1}$ )
0	1	32.2138	0.0888	1	0	0	2.77885	963.83
	2	34.4964	0.1023	0	0	2	2.60002	5088.13
	3	36.3733	0.0533	1	0	1	2.47006	2215.89
	4	48.5195	0.2132	1	0	2	1.87633	500.36
	5	57.4165	0.2132	1	1	0	1.60495	845.08
	6	63.0944	0.0711	1	0	3	1.4735	1850.51
	7	68.6437	0.065	1	1	2	1.36616	1179.51
1	1	32.294	0.1535	1	0	0	2.77213	2668.46
	2	34.509	0.1535	0	0	2	2.59911	2754.07
	3	36.7002	0.1791	1	0	1	2.4488	9939.97
	4	48.4985	0.2558	1	0	2	1.8771	494.13
	5	57.3965	0.3582	1	1	0	1.60546	1282.81
	6	63.0992	0.1535	1	0	3	1.4734	1628.81
	7	68.6411	0.2814	1	1	2	1.36734	1827.36
2	1	32.3001	0.1791	1	0	0	2.77162	676.75
	2	34.4873	0.1279	0	0	2	2.60069	2866.91
	3	36.6818	0.1791	1	0	1	2.44999	6659.83
	4	48.5072	0.2558	1	0	2	1.87678	579.98
	5	57.4199	0.2303	1	1	0	1.60486	965.27
	6	63.0932	0.1535	1	0	3	1.47353	2137.78
	7	68.6519	0.2047	1	1	2	1.36715	1097.79
3	1	32.2748	0.1535	1	0	0	2.77374	503.18
	2	34.4872	0.1279	0	0	2	2.60069	2268.24
	3	36.6948	0.1791	1	0	1	2.44915	3715.51
	4	48.5319	0.2558	1	0	2	1.87588	467.24
	5	57.4469	0.1535	1	1	0	1.60417	779.39
	6	63.1301	0.1279	1	0	3	1.47275	1439.8
	7	68.7139	0.2047	1	1	2	1.36607	874.9

As shown in this figure and Table 4.8, some differences are observed as the number of PTCAP passes increases. In fact, here are some changes in position, intensity and broadening the characteristic peaks. For instance, the Mg-derived XRD peaks are progressively moved to higher angles, suggesting that the PTCAP caused an isotropic

compression of the  $\alpha$ -Mg. This mobility also shows that a reduction has been made in the hexagonal close-packed unit cell of  $\alpha$ -Mg during PTCAP (Figure 4.26(b)). In addition, peak broadening took place on account of the reduction in the crystallite size and intensification in the micro-strain, where the sharpness of the diffraction peaks was changed because of differences in the crystallization capacity of the PTCAP-processed alloy (Sundeev et al., 2016). Figure 4.26(b) also illustrates that the direction of XRD reflections is influenced by both heterogeneous and homogeneous strains during different PTCAP passes, which has resulted in both peak broadening and peak shift.

#### 4.4.2 Structural Features

The structural evolution of the unprocessed and PTCAP-processed WE43 Mg alloy are explained in the following subsections.

##### 4.4.2.1 Lattice constants and unit cell volume

Using the Eqs. 3.3 and 3.5 mentioned in the previous chapter, the hexagonal close-packed unit cell and the lattice parameters of WE43 Mg alloy before and after PTCAP were determined and the obtained data are summarized in Table 4.9.

**Table 4.9:** Lattice constants, unit cell volume and lattice mismatch of the unprocessed and PTCAP-processed WE43 Mg alloy.

Number of passes	$a$ -axis (Å)	$b$ -axis (Å)	$c$ -axis (Å)	$V$ (Å <sup>3</sup> )	$\epsilon_a$ (%)	$\epsilon_c$ (%)
0	3.210(1)	3.210(1)	5.209(2)	46.47	0.016	-0.027
1	3.210(1)	3.210(1)	5.203(3)	46.73	0.016	-0.142
2	3.207(1)	3.207(1)	5.208(2)	46.38	-0.078	-0.046
3	3.207(1)	3.207(1)	5.206(2)	46.37	-0.078	-0.084

According to this table, the PTCAP gave rise to minor changes in the lattice constants and hexagonal close-packed unit cell, which is in good agreement with the findings of previous studies (Charfeddine et al., 2014). As already mentioned, the standard lattice parameters for Mg (JCPDS#004-0770),  $a_0$  and  $c_0$ , are 3.2095 and 5.2104 Å, respectively. In the case of the  $a$  constant, the same value of 3.210(1) Å was attained prior to and after the first pass of PTCAP. With increasing the number of PTCAP passes to two and three, a reduction from the initial value to 3.207(1) Å was observed. For the  $c$  constant, the alterations were not linear and therefore at first a diminution from the preliminary value of 5.209(2) Å for the unprocessed tube to 5.203(3) Å for the one PTCAP pass occurred. Then, this value increased to 5.208(2) Å after the second pass of PTCAP and again it fell to 5.206(2) Å. After the first pass of PTCAP, a sudden increase in unit cell volume was observed due to the Mg lattice distortion during the SPD process.

However, with increasing the number of PTCAP passes, the unit cell volume decreased somewhat and reached 46.37 Å<sup>3</sup> after the third pass. From this table, it is obvious that values of lattice mismatch of the processed specimens are trivial (~ 0.016–0.142%), where the uppermost values of  $\varepsilon_c$  (~ 0.142%) and  $\varepsilon_a$  (~ 0.078) were detected after the first and third pass of PTCAP, respectively. The negative values of the strain are evidence for the compressive in-plane and out-of-plane strains in the present cases (Cheong et al., 2014).

#### 4.4.2.2 Crystallite size and micro-strain

From the XRD patterns, a rise in the FWHM was observed with increasing the number of PTCAP passes, which resulted from a lessening of the crystallite size and an increase of the micro-strain  $\eta$  (Charfeddine et al., 2014). This behaviour can also be ascribed to

enhanced dislocation density as an influence of applying PTCAP processing (Jamili et al., 2017), which will be explained in the following sections.

Figure 4.27 illustrates the structural properties of the WE43 Mg alloy before and after one, two and three PTCAP passes. As shown in Figure 4.27(a), a significant refinement took place and the crystallite size decreased from the initial value of  $101 \pm 6$  nm for the unprocessed specimen to  $57 \pm 6$  and  $46 \pm 6$  nm with increasing the number of passes from 1 to 3, respectively. From Figure 4.27(b),  $\eta$  value for the unprocessed tube is 0.18% and reached a maximum of 0.29% after the third pass of PTCAP. This reveals that the UFG-WE43Mg tube processed by three passes of PTCAP is much more strained compared to the other tubes. Of course, as already mentioned, the structural assessments of the severe plastically deformed Mg-based alloys like WE43 are still in the early stages and thus further studies are needed to determine the optimal values.

#### 4.4.2.3 Volume fraction of the grain boundary

Based on the obtained data from Eq. 3.9 (Figure 4.27(c)), the PTCAP processing of WE43 Mg alloy resulted in a significant alteration in  $f$  value. As can be seen, volume fraction of the grain boundary increased notably from the primary value of 2.9% for the unprocessed tube to 5.1, 6.1 and 6.2% after the first, second and third pass of PTCAP, respectively. This result is consistent with the achieved data for the PTCAP-processed ZK60 Mg alloy in the present work.

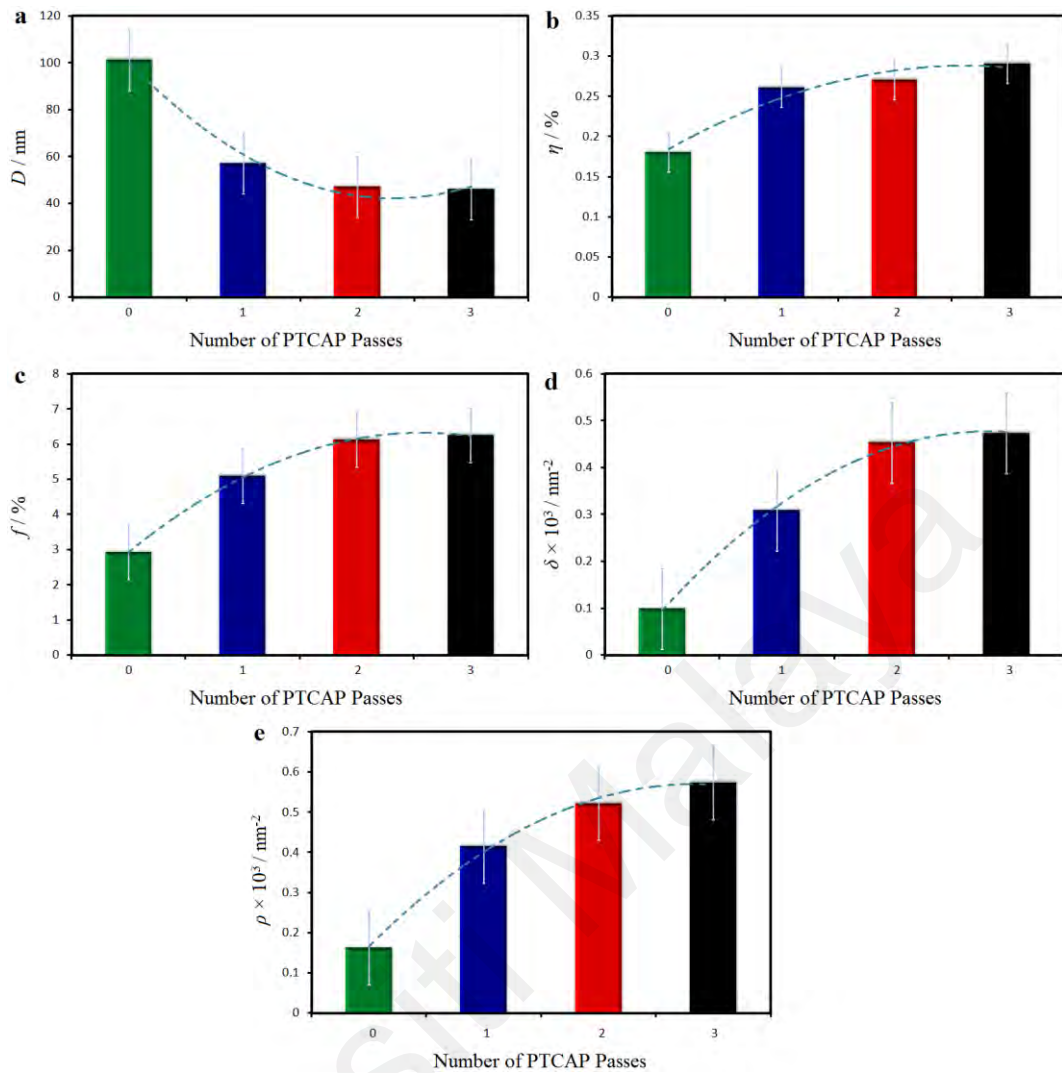


**Figure 4.27:** (a) Crystallite size ( $D$ ), (b) micro-strain ( $\eta$ ), (c) volume fraction of the grain boundary ( $f$ ), (d) defect density ( $D_d$ ), and (e) dislocation density ( $\rho$ ) of WE43 Mg alloy before and after one, two and three PTCAP passes.

#### 4.4.2.4 Defect and dislocation density

Figure 4.27(d) and (e) represents the progression of  $D_d$  as a result of an increase in the number of PTCAP passes so that the defect density and dislocation density increased by ~370% and ~256%, respectively, compared to the unprocessed workpiece. These variations can be explained on the basis of the processing circumstances. For instance, the level of equivalent strain in different passes of PTCAP, which gave rise to change the density of defects, such as density and feature of dislocations, concentration of vacancies, as well as fraction of grain boundaries (Bera et al., 2013). Therefore, the structural features and consequently the microstructure and mechanical behaviour of UFG WE43

Mg alloy can be modified using a proper selection of the PTCAP parameters. This finding is not only in good agreement with the results of UFG ZK60 Mg alloy, but also is consistent with the previous studies, showing an increase in defect density with increasing the number of SPD passes (Mesbah et al., 2014; Tyagi et al., 2017).

Based on the previous description about strengthening mechanisms of metallic alloys, different approaches exist depending on the chemical composition and production circumstances. For instance, solution strengthening, LPSO strengthening, and aging strengthening are the dominant mechanisms in Mg-based alloys (Tyagi et al., 2017). As mentioned already, the cutting of  $\beta'$  precipitates by dislocations is the main strengthening mechanism in the ZK60 Mg alloy (W.C. Liu et al., 2009).

Figure 4.28 shows the dynamic dissolution of second-phase particles within the matrix in WE43 Mg alloy. As it is schematically illustrated in this figure (left side), dislocation pile up at secondary phase particles results in a substantial amount of stress that may put in force the dislocations to cut through the secondary phase particles. This is where it seems that the level of requisite stress to shear the second phase can be attained during the PTCAP process taking into account the structural features of the eutectic second phase.

By passing dislocations through the secondary particles, an absolute shearing occurs and dislocation's Cottrell atmosphere may attract the impurity atoms and carry them through the matrix. In view of the initial and ultimate dislocations happening in particle shearing, the creation of fresh dislocations is essential to gratify the principle of Burgers-vectors preservation that was illustrated by yellow dislocation signs in Figure 4.28(a). It should be noted that cutting and dissolving the second phases may stop to a more active surface for diffusion that in turn would result in the dissolution process speeding up in a shorter period of time (Jamili et al., 2017).

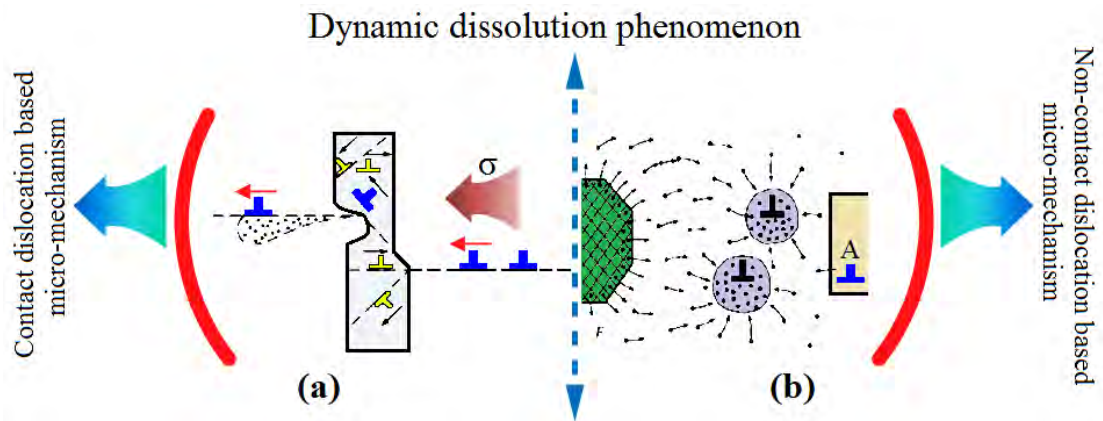


**Figure 4.28:** The dynamic dissolution of second-phase particles within the matrix in WE43 Mg alloy.

On the other hand, Frank-Read (FR) sources creating dislocations, which can be intensely activated during the PTCAP method, may also take action as a non-contact mechanism to dissolve the second phases (Vasil'ev et al., 2006), as shown in Figure 4.28(b). It appears that an elevated equivalent strain during the PTCAP may activate FR sources, where the newly created dislocations possessing no segregation can alter dislocations segregation equilibrium state into a none-equilibrium one.

It is worth noting that the high level of accumulation may speed up the diffusion process and following enough time for diffusion, the Cottrell atmosphere around the new created dislocations' cores attracts impurity atoms through the matrix. On the basis of this mechanism, diffusion fluxes are directed toward the dislocation's core atmospheres, and they make an effort to keep steady the impurity concentration in the overall matrix. This causes destruction of the equilibrium state between the dissolving phase and the matrix, leading to an elevated thermodynamic motivation for dissolution of dissolving phase. It should be mentioned that this dissolution mechanism possesses lesser energy-consuming owing to creating the dislocations at low exterior stresses (Vasil'ev et al., 2006). Based on these dynamic dissolutions of second-phase particles within the matrix, mechanical strength is expected to decrease; however, the substantial strengthening effects of grain refinement supported by Hall-Petch theory can prevail over the negative effect of

dynamic dissolution, which will be described in the following sections (Jamili et al., 2017).

#### 4.4.3 Microstructural Evolution Analysis

##### 4.4.3.1 Optical microscopy analysis

Figure 4.29 displays the optical micrographs of WE43 Mg alloy perpendicular to the extrusion direction before and after one, two and three passes of PTCAP. As can be seen in Figure 4.29(a), the unprocessed specimen is made up of coarse grains with  $\sim 75 \mu\text{m}$  in size. The typical microstructure of the unprocessed alloy is a  $\alpha$ -Mg matrix with some dispersed IMCs like  $\text{Mg}_{24}\text{Nd}_5$  and  $\text{Mg}_{41}\text{Nd}_5$  phases through the grains and grain boundaries (W. Liu et al., 2017). From Figure 4.29(b-e), by applying PTCAP and increasing the number of passes, the volume fraction of the recrystallized grains has enhanced, also resulted in arrays of fine new grains embedded in the elongated initial grains. The as-extruded alloy with the average grain size of  $75 \mu\text{m}$  has been replaced by fine grains of about  $2.4 \mu\text{m}$  mean size after three PTCAP passes. These OM images also disclose the presence of the second eutectic phase (Figure 4.29(e), which is mainly positioned at triple junctions and grain boundaries. These observations are consistent with previous SEM micrographs of the SPD-processed WE43 Mg alloys (Jamili et al., 2017; Torkian et al., 2018).

The microstructural observations indicated that new grains are primarily nucleated along the original grain boundaries. This is in line with previous researches (Fatemi-Varzaneh et al., 2007; Levinson et al., 2013). Moreover, prolific new-fangled grains may also be seen at the district of the eutectic phase particles. This is classically detected as several nucleations happened at the coarse particles. The eutectic particles with an average size coarser than  $1 \mu\text{m}$  may hinder dislocations. Furthermore, the interaction of

dislocations and particles would generate geometrically necessary dislocation, providing the powerful force for enhanced recrystallization (Salandari-Rabori et al., 2017).

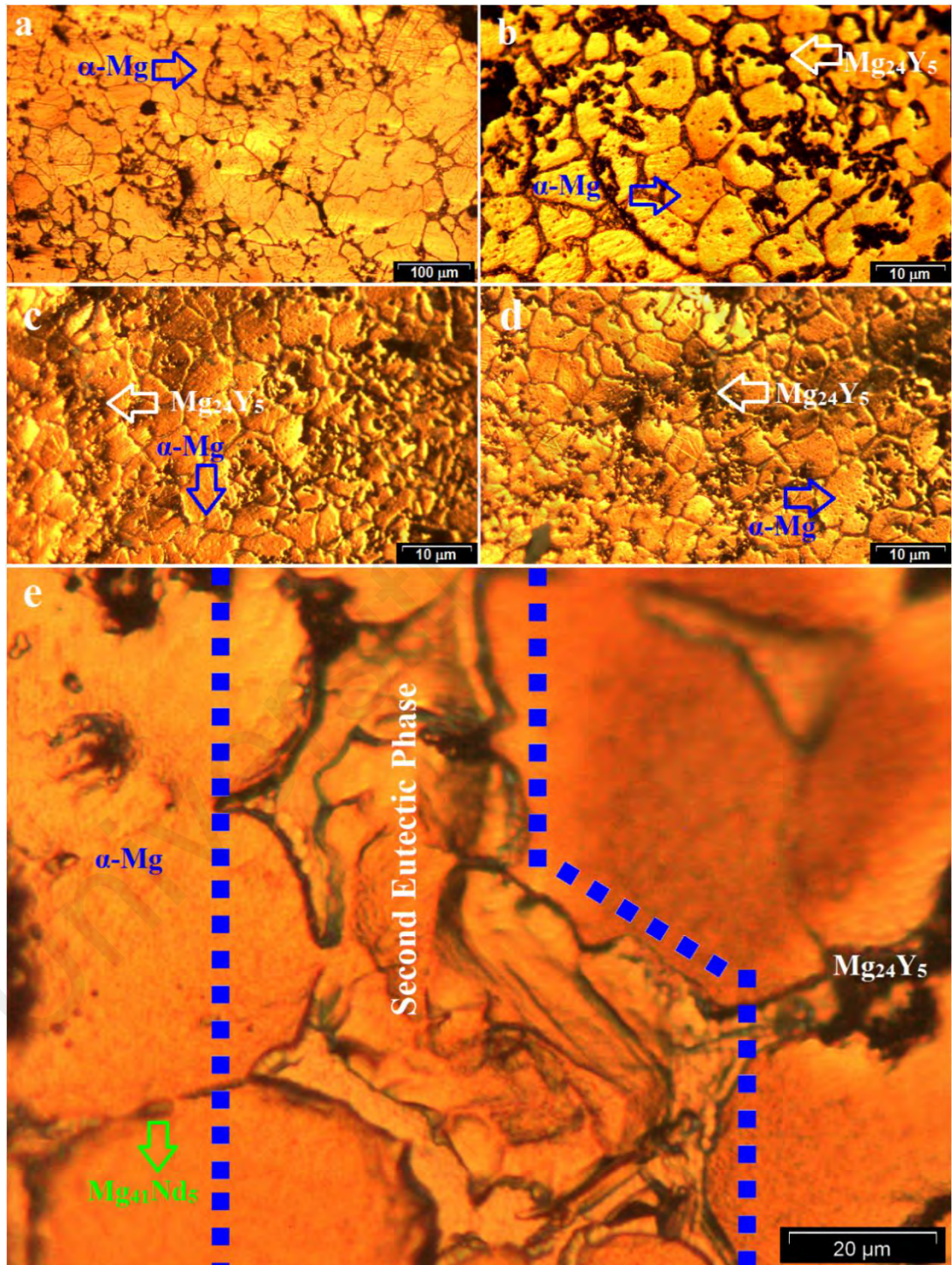


**Figure 4.29:** Optical micrographs of WE43 Mg alloy perpendicular to the extrusion direction (a) before and after (b) one, (c) two and (d,e) three passes of PTCAP.

#### 4.4.3.2 SEM Analysis

Figure 4.30 shows SEM micrographs of the WE43 Mg alloy prior to and following three PTCAP passes along with the EDX spectra. As can be seen in Figure 4.30(a), the unprocessed specimen is composed of almost coarse grains with a mean grain size of  $\sim 110 \mu\text{m}$ . This observation is in good agreement with the OM image. After the PTCAP process (3 passes), a more uniform and finer microstructure with an average grain size of  $\sim 1.5 \mu\text{m}$  was formed (Figure 4.30(c)). These observations reveal that the grain size determined by SEM has similar evolution as for the crystallite size; nonetheless, the grain size is several times larger than the crystallite size in PTCAP-processed UFG WE43 alloy (Gubicza, 2012), which can be described by the fact that coherently scattering domains (crystallites) correspond rather to subgrains in severely deformed microstructures (Gubicza, 2015).

In addition, the diminution in subgrain and grain sizes with increasing imposed strain is ascribed to the rise in dislocation density, as grain refinement during SPD processes like PTCAP generally begins by the arrangement of dislocations into low energy configurations, for instance, LAGBs. It should be mentioned that during SPD at elevated homologous temperatures dynamic recrystallization may also play a key role in grain refinement so that as the number of passes increases, the dislocation density reduces and the crystallite size enhances (Gubicza, 2012). For example, this behaviour has been observed in the SPD-processed Cu, which can be caused by the structural relaxation in grain/subgrain boundaries by the annihilation of extrinsic dislocations. This phenomenon is along with a reduction in the thickness of grain boundary in proportion to gradual changes from non-equilibrium boundaries to a more equilibrated configuration (Gubicza, 2015).

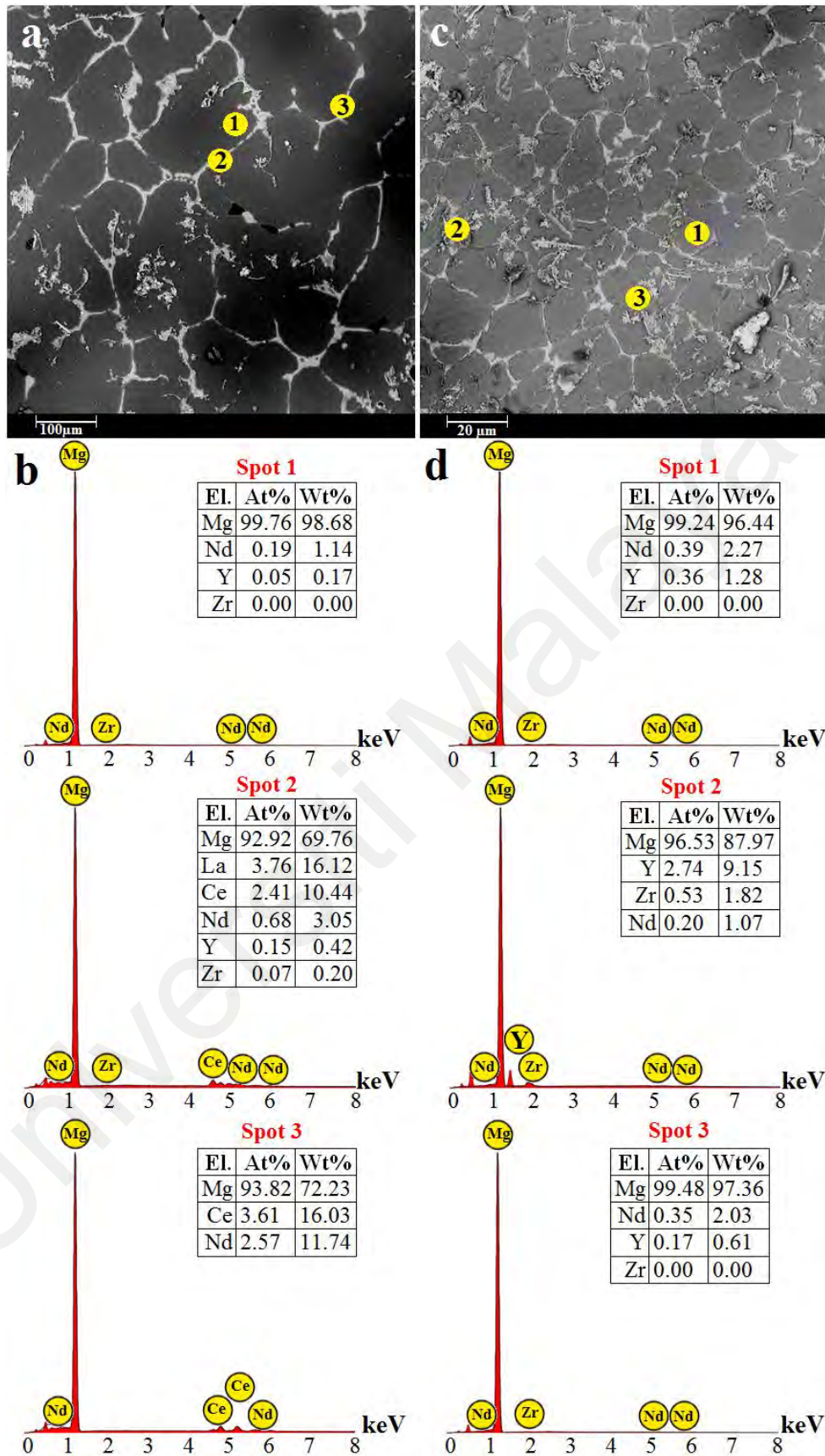


**Figure 4.30:** SEM micrographs and EDX spectra of the WE43 Mg alloy (a,b) prior to and (c,d) following three PTCAP passes.

To verify the presence of the second phase and rare elements (REs), the EDX point analysis was executed, as shown in Figure 4.30(b) and (d). These spectra show that the alloy consists of REs, like Y and Nd, as also observed in previous studies (Torkian et al., 2018). These rare elements restrain the motion of grain boundaries, which is recognized as Zener pinning effect. Following the third pass of PTCAP, grain refinement and better distribution of IMCs are obtained as shown in Figure 4.30(d).

Based on the microscopic observations in Figure 4.29 and Figure 4.30, the unprocessed specimen is composed of large equiaxed  $\alpha$ -Mg grains and dispersed IMCs phases. Following the first pass of PTCAP, new small Mg<sub>24</sub>Y<sub>5</sub> and Mg<sub>41</sub>Nd<sub>5</sub> phases and new dynamically recrystallized grains were developed along the primary grain boundaries. Further straining at higher passes resulted in the developing of more new finer recrystallized grains, where the fraction of the un-recrystallized  $\alpha$ -Mg has diminished.

#### **4.4.4 Mechanical Properties**

##### **4.4.4.1 Vickers microhardness**

Figure 4.31(a) displays the Vickers microhardness values along the thickness of the unprocessed and PTCAP-processed WE43 Mg tubes. From this figure, following the first pass of the PTCAP, the average value of microhardness increased from  $62 \pm 2$  HV for the unprocessed specimen to  $81 \pm 2$  HV, due to the dynamic recrystallization and significant strengthening effects of grain refinement (Gubicza, 2015). By increasing the number of PTCAP passes to two, the microhardness raised to  $85 \pm 2$  HV and finally with further straining at third pass it reached a maximum of  $89 \pm 2$  HV. This enhancement in microhardness is in good consistence with the microstructural results, where more plastic strain attributable to the increase of the number of PTCAP passes caused further grain

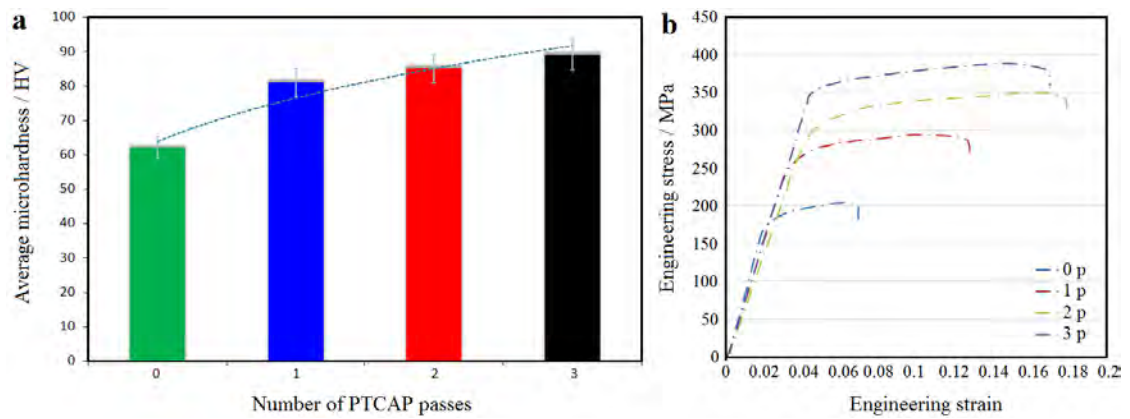


**Figure 4.31:** (a) Vickers microhardness values along the thickness and (b) engineering stress–engineering strain curves for WE43 Mg tube before and after one, two and three passes of PTCAP.

refinement, better spreading of IMCs and higher hardness value (Fata et al., 2017b). Moreover, this result is also inconsistent with the increase in mechanical strength in Figure 4.31(b). As illustrated in this figure, either the smaller grain size or the higher dislocation density following the third pass of PTCAP resulted in a higher  $\sigma_{YS}$  and  $\sigma_{UTS}$  compared to the unprocessed workpiece.

Regarding the intensification of the dislocation density and the diminution of the grain size, the mechanical strength of Mg-based alloys like WE43 tube processed by PTCAP enhances with increasing imposed strain (Valiev et al., 2006). At the same time, it is expected that the elongation to failure decreases owing to the loss of work hardening capability with increasing the defect density (Azushima et al., 2008). In some cases, the structural relaxation following high number of passes can cause an improvement of the ductility and a slight reduction of the  $\sigma_{YS}$ . Here, dislocations take part the main role in the hardening process attributable to SPD in fcc metals and solid solutions.

This behaviour can be described on the basis of a large fraction of grain boundaries that are composed of dislocations in SPD-processed metallic materials, therefore their hardening effect is also taken into account in the Taylor formula (Taylor, 1938). Thus, to attain higher mechanical strength during PTCAP, it should be elucidated what the central

factors are that induce the saturation dislocation density. In the present case, the solute atoms enhanced the mechanical strength directly by increasing the critical resolved shear stress of dislocation glide and also indirectly by enhancing the dislocation density. This signifies that solute atoms in PTCAP-processed alloys like WE43 tube can improve the mechanical strength by raising the density of dislocation (Gubicza, 2015). Based on this description, it can be concluded that not only the grain boundary configuration but also the total lattice defect arrangement should be generally considered by a suitable selection of the processing conditions of UFG alloys.

Universiti Malaya

## **CHAPTER 5: CONCLUSIONS AND SUGGESTIONS FOR FUTURE WORK**

In conclusion, microstructural evolution and mechanical properties of different Al, Mg and Cu-based alloys produced by TCAP and PTCAP processes were explored. The specific conclusions have been listed as follows:

### **5.1 Feasibility of Obtaining UFG Structure in TCAP and PTCAP Methods**

1. The formation of homogeneous UFG structures was confirmed with the minimum number of passes of 1 for Al-1060 and Brass70/30, as well as 3 for ZK60 and WE43 Mg alloys. The minimum mean grain sizes obtained in TCAP-processed Al, as well as PTCAP-processed brass, ZK60 and WE43 were respectively 0.48  $\mu\text{m}$ , 0.59  $\mu\text{m}$ , 0.9  $\mu\text{m}$ , and 2.2  $\mu\text{m}$ .
2. The dynamic recrystallization and breaking, as well as distribution of the precipitates at the newly formed grains, were the dominant phenomena in the TCAP and PTCAP process.

### **5.2 The Effect of Number of Passes on Microstructural Features**

The structural features, especially defect configuration of the TCAP and PTCAP processed UFG Al, Mg and Cu-based alloys were strongly influenced by the route (TCAP and PTCAP) and the strain of the processing. In most cases, a minimum in the crystallite size and unit cell volume and a maximum in the volume fraction of grain boundary and defect/dislocation density were obtained at the higher imposed strain (third pass). According to the optical, SEM, TEM, and EBSD observations, the mean grain sizes were decreased with the increase of the TCAP and PTCAP passes, reaching to their minimum

values following the third pass in both SPD processes.

### 5.2.1 TCAP-processed Al-1060

1. The high strains induced during the TCAP processing of Al 1060 resulted in reduced lattice constant from the initial value of 4.0600 Å for the unprocessed specimen to 4.0526, 4.0471 and 4.0510 Å following the first, second and third TCAP pass, respectively. Accordingly, the unit cell volume decreased from the initial value of 66.94 Å<sup>3</sup> for the unprocessed sample to 66.56, 66.29 and 66.48 Å<sup>3</sup> after the first, second and third TCAP pass, respectively.
2. The unprocessed sample presented a crystallite size and lattice strains of 364 ± 16 nm and 0.08%, respectively. However, after the first, second, and third TCAP passes these values respectively reached to 91 ± 16 nm and 0.1%, 68 ± 16 nm and 0.14%, as well as 60 ± 16 nm and 0.18%. This indicated a linear decreasing trend in crystallite size and increasing trend in lattice strain of the TCAP-processed Al-1060 alloy.
3. The TCAP processing of Al-1060 alloy also resulted in significant alterations in  $f$  from 0.8% for the unprocessed sample to 3.2, 4.3 and 4.8% in the one, two, and three-passed specimens, respectively. This dramatic increase in the fraction of grain boundary imparted substantial effects on the level of crystallographic defects such as dislocations, where the size and the orientation of different adjoining crystals showed a severe impact on dislocation nucleation and multiplication.
4. EBSD scans revealed a homogeneous ultrafine-grained microstructure after the third passes of the TCAP process. Apart from that, the mean grain sizes of the TCAP processed tubes were refined to 566 nm, 500 nm, and 480 nm, respectively

after the first, second and third passes from the preliminary grain size of 75  $\mu\text{m}$ . The results showed that after the three TCAP passes, the grain boundaries with a high angle comprised 78% of all the boundaries. This is in comparison to the first pass processed sample that includes approximately 20% HAGBs.

5. The TEM inspection afforded an appreciation of the role of very low-angle misorientation boundaries in the process of refining microstructure. The arrays of elongated subgrains observed in one pass processed sample have mostly transformed into nearly equiaxed subgrains and grains by the two-pass TCAP process. TEM analysis showed the formation of an array of elongated subgrains measuring  $\sim 460$  nm in size and high angle grain boundaries after the first TCAP pass. The second TCAP pass causes the transformation of the elongated subgrains to near equiaxed subgrains of  $\sim 320$  nm size. On the third pass, low angle equiaxed subgrains and grains are transformed into high angle equiaxed grains with  $\sim 310$  nm in size.

### 5.2.2 PTCAP-processed Brass70/30

1. The excessive strain in PTCAP contributed to a substantial shrinkage in lattice structure of  $\alpha$ -brass. The lattice constant value was decreased from the initial value of 3.6710  $\text{\AA}$  to 3.6690, 3.6660 and 3.6600  $\text{\AA}$  after the first, second, and third PTCAP pass. The reductions in lattice constants resulted in unit cell contraction from 49.47  $\text{\AA}^3$  for the unprocessed specimen to 49.39, 49.27 and 49.03  $\text{\AA}^3$  after the first, second and third PTCAP passes.
2. The structural variations of  $D$  and  $\eta$  in the brass alloy were linear, where the minimum values of both parameters were achieved in the third pass. Accordingly, the crystallite size reduced from  $106 \pm 16$  nm for the unprocessed sample to 102

$\pm 16$  nm after the first pass of PTCAP and then decreased to  $82 \pm 16$  nm and  $73 \pm 16$  nm after the second and third passes. In the other hand,  $\eta$  increased from 0.01% for the unprocessed workpiece to 0.02, 0.04, and 0.59% following the first, second and third pass of PTCAP, respectively.

3. The PTCAP processing of brass alloy caused substantial variations in  $f$  value from 2.8% for the unprocessed specimen to 2.9, 3.6 and 4.0% for the first, second and third pass, respectively. This structural evolution played an important role in nucleation and duplication of dislocation and thereby profoundly affected the microstructural features and mechanical performance of the PTCAP-processed Al-1060 alloy.
4. Moreover, based on the obtained results from EBSD, the grain size of 1 and 3 pass samples were refined to 780 and 590 nm from its initial size of 75  $\mu\text{m}$ . The fraction of the high-angle grain boundaries was increased from 30% in pass 1 to 66% in pass 3 of the PTCAP process.

### 5.2.3 PTCAP-processed ZK60 Mg Alloy

1. The PTCAP process resulted in a small decrease of the lattice parameters and volume of unit cell, where  $a$  was decreased from the initial value of 3.209(8)  $\text{\AA}$  in the unprocessed sample to 3.203(5), 3.202(5), and 3.200(2)  $\text{\AA}$  after the first, second and third passes. However, the changes in  $c$  parameter were not linear; first, it reduced from 5.208(1)  $\text{\AA}$  (unprocessed specimen) to 5.198(7)  $\text{\AA}$  after the first pass and then increased to 5.200(7)  $\text{\AA}$  following the second pass, and eventually reached a minimum value of 5.191(5)  $\text{\AA}$  in the three-passed sample.
2. A decrease in the unit cell volume was observed by the increase of the number of passes and reached a minimum of 46.03  $\text{\AA}^3$  after three passes. The results also

showed an insignificant lattice mismatch in the processed samples with small strain values ( $\sim 0.2\text{--}0.372\%$ ). The highest  $\varepsilon_a$  ( $\sim 0.296$ ) and  $\varepsilon_c$  ( $\sim 0.372\%$ ) values were related to the three-passed sample.

3. The PTCAP process led to the lattice distortions between 0.19 and 0.25% and severe refinements of the microstructure to nanometer crystallite size with an average of  $68 \pm 8$ ,  $61 \pm 8$  and  $51 \pm 8$  nm after one, two and three passes, respectively.
4. The minimum  $D$  and the maximum  $\eta$  values were attained after three passes, indicating that the UFG-ZK60Mg tube processed by three passes was significantly more strained compared to the other tubes.
5. The PTCAP processing of ZK60 Mg alloy led to changes in the  $f$  value from 4.3% for the one-passed sample to 4.8% for the two-passed specimen and finally reached a maximum of 5.7% after three PTCAP passes.
6. The  $D_d$  parameter increases linearly as the number of passes increases. This corroborated the effect of the number of passes on the  $D_d$  of the ZK60 Mg alloy, where the  $D_d$  of the three-passed sample increased by  $\sim 184\%$  compared to the unprocessed specimen.
7. The results showed that all the processed tubes had more refined microstructure with  $\sim 7$  to  $0.9 \mu\text{m}$  grain sizes, which consist of an average crystallite size between  $68 \pm 8$  and  $51 \pm 8$  nm, compared to the as-received specimen with a mean grain size of  $\sim 90 \mu\text{m}$ .

#### 5.2.4 PTCAP-processed WE43 Mg Alloy

1. The PTCAP process gave rise to minor changes in the lattice constants and hexagonal close-packed unit cell. In the case of the  $a$  constant, the same value of  $3.210(1) \text{ \AA}$  was attained prior to and after the first pass of PTCAP. With increasing

the number of PTCAP passes to two and three, a reduction from the initial value to 3.207(1) Å was observed. For the  $c$  constant, the alterations were not linear so that at first a diminution from the preliminary value of 5.209(2) for the unprocessed tube Å to 5.203(3) Å for the one PTCAP pass. Then, this value increased to 5.208(2) Å after the second pass of PTCAP and again it fell to 5.206(2) Å.

2. After the first pass of PTCAP, a sudden increase in unit cell volume was observed due to the Mg lattice distortion. However, with increasing the number of passes, the unit cell volume decreased somewhat and reached 46.37 Å<sup>3</sup> after the third pass.
3. A significant refinement and decreased crystallite size were detected from the initial value of  $101 \pm 6$  nm for the unprocessed specimen to  $57 \pm 6$  and  $46 \pm 6$  nm with increasing the number of passes from 1 to 3. The  $\eta$  value for the unprocessed tube was 0.18% and reached a maximum of 0.29% after the third pass. This revealed that the UFG–WE43 Mg tube processed by three passes of PTCAP was more strained compared to the other tubes.
4. The PTCAP processing of WE43 Mg alloy resulted in a significant increase in  $f$  value from the primary value of 2.9% for the unprocessed tube to 5.1, 6.1, and 6.2% after the first, second, and third passes. This result was consistent with the achieved data for the PTCAP-processed ZK60 Mg alloy in the present work. The defect density and dislocation density increased by  $\sim 370\%$  and  $\sim 256\%$ , respectively, compared to the unprocessed workpiece.
5. The presence of intermetallic compounds such as Mg<sub>24</sub>Y<sub>5</sub> and Mg<sub>41</sub>Nd<sub>5</sub> was confirmed along with the  $\alpha$ -Mg phase in the PTCAP-processed WE43 Mg alloy.

### 5.3 The Effect of Number of Passes on Mechanical Behaviour

With increasing the number of TCAP and PTCAP passes, microhardness, yield strength ( $\sigma_{\text{Yield}}$ ), ultimate tensile strength ( $\sigma_{\text{UTS}}$ ), and elongation to failure were significantly increased as a result of raised dislocation density, movement, and locking, as well as further microstructural refinement. In some cases, the elongation to failure decreased with increase of strain during SPD. Nonetheless, the structural relaxation following high number of passes resulted in an improvement of the ductility and a slight reduction of the  $\sigma_{\text{YS}}$ .

Based on the proposed strengthening mechanism, dislocations played an important role in hardening caused by TCAP and PTCAP. In precipitate-hardened UFG WE43 and ZK60 Mg alloys, the direct and indirect hardening contributions of precipitates were comparable.

#### 5.3.1 TCAP-processed Al-1060

1. A 50% increase in microhardness was observed after the first pass. The hardness of the processed tubes was improved from an initial value of 32.9 to 49.4 HV after one pass and no significant alteration was observed with further increase of the number of passes.
2. The yield and ultimate strengths were respectively increased 2.5 and 2.3 times as compared to the annealed specimen.

#### 5.3.2 PTCAP-processed Brass70/30

1. A significant rise in  $\sigma_{\text{YS}}$  and  $\sigma_{\text{UTS}}$  was detected for the PTCAP-processed specimens, caused by the grain refinement during the PTCAP processing. In

contrast, there was a substantial diminution in elongation to failure ( $\delta$ ) following the first and third pass of PTCAP.

2. The mean values of the elastic modulus and hardness of the processed brass after the first and third pass of PTCAP were  $75.1 \pm 1.65$  GPa and  $2.625 \pm 0.11$  GPa as well as  $103.86 \pm 3.36$  GPa and  $2.832 \pm 0.14$  GPa, respectively, which were significantly higher than those of the unprocessed tube with elastic modulus of  $64.08 \pm 1.34$  GPa and hardness of  $1.645 \pm 0.07$  GPa.

### 5.3.3 PTCAP-processed ZK60 Mg Alloy

1. The hardness of the processed tubes increased with the number of passes from  $77 \pm 2$  HV for the unprocessed alloy to a maximum of  $111 \pm 2$  HV at three PTCAP passes.
2. The PTCAP process not only increased the mechanical strength, but also the ductility of the processed tubes, where the highest yield strength (320 MPa), ultimate tensile strength (397 MPa), and elongation to failure (14%) values were obtained at the second pass. However, with increasing the number of passes to three, elongation to failure reached to 4%, while the yield strength and ultimate tensile strength decreased by 31% and 11%, respectively.

### 5.3.4 PTCAP-processed WE43 Mg Alloy

1. following the first pass of the PTCAP, the average value of microhardness increased from  $62 \pm 2$  HV for the unprocessed specimen to  $81 \pm 2$  HV, due to the dynamic recrystallization and significant strengthening effects of grain refinement. By increasing the number of PTCAP passes to two, the microhardness

raised to  $85 \pm 2$  HV and finally with further straining at the third pass, reached a maximum of  $89 \pm 2$  HV. This enhancement in microhardness was consistent with the microstructural results, where more plastic strain attributable to the increase of the number of PTCAP passes caused further grain refinement, better spreading of intermetallic compounds, and higher hardness value.

### **SUGGESTIONS FOR FUTURE WORK**

- Apply the process on larger scale tubes with more industrial capability
- Biocompatibility check for the processed Mg tubes for future applications

## REFERENCES

- Abdolvand, H., Faraji, G., Givi, M. B., Hashemi, R., & Riazat, M. (2015a). Evaluation of the microstructure and mechanical properties of the ultrafine grained thin-walled tubes processed by severe plastic deformation. *Metals and Materials International*, 21(6), 1068-1073.
- Abdolvand, H., Faraji, G., & Shahbazi Karami, J. (2017a). Microstructure and mechanical properties of AZ91 tubes fabricated by multi-pass parallel tubular channel angular pressing. *Journal of Ultrafine Grained and Nanostructured Materials*, 50(1), 16-22.
- Abdolvand, H., Faraji, G., Shahbazi Karami, J., & Baniasadi, M. (2017b). Microstructure and mechanical properties of fine-grained thin-walled AZ91 tubes processed by a novel combined SPD process. *Bulletin of Materials Science*, 40(7), 1471-1479.
- Abdolvand, H., Sohrabi, H., Faraji, G., & Yusof, F. (2015b). A novel combined severe plastic deformation method for producing thin-walled ultrafine grained cylindrical tubes. *Materials Letters*, 143, 167-171.
- Afrasiab, M., Faraji, G., Tavakkoli, V., Mashhadi, M., & Bushroa, A. (2014). Excellent energy absorption capacity of nanostructured Cu–Zn thin-walled tube. *Materials Science and Engineering: A*, 599, 141-144.
- Afrasiab, M., Faraji, G., Tavakkoli, V., Mashhadi, M., & Dehghani, K. (2015). The effects of the multi-pass parallel tubular channel angular pressing on the microstructure and mechanical properties of the Cu–Zn tubes. *Transactions of the Indian Institute of Metals*, 68(5), 873-879.
- Alizadeh, M., & Dashtestaninejad, M. K. (2018). Development of Cu-matrix, Al/Mn-reinforced, multilayered composites by accumulative roll bonding (ARB). *Journal of Alloys and Compounds*, 732, 674-682.
- Amani, S., & Faraji, G. (2018). Recrystallization and mechanical properties of WE43 magnesium alloy processed via cyclic expansion extrusion. *International Journal of Minerals, Metallurgy, and Materials*, 25(6), 672-681.
- Amani, S., & Faraji, G. (2019a). Processing and properties of biodegradable magnesium microtubes for using as vascular stents: A brief review. *Metals and Materials International*, 25(5), 1341–1359.
- Amani, S., Faraji, G., Kazemi Mehrabadi, H., & Baghani, M. (2019b). Manufacturing and mechanical characterization of Mg-4Y-2Nd-0.4 Zr-0.25 La magnesium microtubes by combined severe plastic deformation process for biodegradable vascular stents. *Proceedings of the Institution of Mechanical Engineers, Part B: Journal of Engineering Manufacture*, 233(4), 1196-1205.
- An, X., Han, W., Huang, C., Zhang, P., Yang, G., Wu, S., & Zhang, Z. (2008). High strength and utilizable ductility of bulk ultrafine-grained Cu–Al alloys. *Applied Physics Letters*, 92(20), 201915.

- Angella, G., Jahromi, B. E., & Vedani, M. (2013). A comparison between equal channel angular pressing and asymmetric rolling of silver in the severe plastic deformation regime. *Materials Science and Engineering: A*, 559, 742-750.
- Ashouri, S., Nili-Ahmadabadi, M., Moradi, M., & Iranpour, M. (2008). Semi-solid microstructure evolution during reheating of aluminum A356 alloy deformed severely by ECAP. *Journal of Alloys and Compounds*, 466(1-2), 67-72.
- Azushima, A., Kopp, R., Korhonen, A., Yang, D., Micari, F., Lahoti, G., Groche, P., Yanagimoto, J., Tsuji, N., & Rosochowski, A. (2008). Severe plastic deformation (SPD) processes for metals. *CIRP Annals*, 57(2), 716-735.
- Babaei, A., & Mashhadi, M. (2014a). Tubular pure copper grain refining by tube cyclic extrusion-compression (TCEC) as a severe plastic deformation technique. *Progress in Natural Science: Materials International*, 24(6), 623-630.
- Babaei, A., Mashhadi, M., & Jafarzadeh, H. (2014b). Tube cyclic expansion-extrusion (TCEE) as a novel severe plastic deformation method for cylindrical tubes. *Journal of Materials Science*, 49(8), 3158-3165.
- Badran, H., Yahia, I., Hamdy, M. S., & Awwad, N. (2017). Lithium-doped hydroxyapatite nano-composites: synthesis, characterization, gamma attenuation coefficient and dielectric properties. *Radiation Physics and Chemistry*, 130, 85-91.
- Basavaraj, V. P., Chakkingal, U., & Kumar, T. P. (2009). Study of channel angle influence on material flow and strain inhomogeneity in equal channel angular pressing using 3D finite element simulation. *Journal of Materials Processing Technology*, 209(1), 89-95.
- Benisek, A., Dachs, E., Salihović, M., Paunovic, A., & Maier, M. E. (2014). The vibrational and configurational entropy of  $\alpha$ -brass. *The Journal of chemical thermodynamics*, 71, 126-132.
- Bera, S., Chowdhury, S. G., Estrin, Y., & Manna, I. (2013). Mechanical properties of Al7075 alloy with nano-ceramic oxide dispersion synthesized by mechanical milling and consolidated by equal channel angular pressing. *Journal of Alloys and Compounds*, 548, 257-265.
- Bridgman, P. (1937). Flow phenomena in heavily stressed metals. *Journal of Applied Physics*, 8(5), 328-336.
- Cabibbo, M., Evangelista, E., & Scalabroni, C. (2005). EBSD FEG-SEM, TEM and XRD techniques applied to grain study of a commercially pure 1200 aluminum subjected to equal-channel angular-pressing. *Micron*, 36(5), 401-414.
- Charfeddine, S., Zehani, K., Besais, L., & Korchef, A. (2014). *Grain refinement and lattice imperfections in commercial aluminum alloy processed by severe plastic deformation*. Paper presented at the IOP Conference Series: Materials Science and Engineering.

- Cheong, Y., Yam, F., Ooi, Y., & Hassan, Z. (2014). Room-temperature synthesis of nanocrystalline titanium dioxide via electrochemical anodization. *Materials Science in Semiconductor Processing*, 26, 130-136.
- Chino, Y., Kobata, M., Iwasaki, H., & Mabuchi, M. (2003). An investigation of compressive deformation behaviour for AZ91 Mg alloy containing a small volume of liquid. *Acta materialia*, 51(11), 3309-3318.
- Cordero, Z. C., Knight, B. E., & Schuh, C. A. (2016). Six decades of the Hall–Petch effect—a survey of grain-size strengthening studies on pure metals. *International Materials Reviews*, 61(8), 495-512.
- Cullity, B. D., & Stock, S. R. (2001). *Elements of X-ray diffraction* (Vol. 3): Prentice hall New Jersey.
- Das, M., Das, G., Ghosh, M., Wegner, M., Rajnikant, V., GhoshChowdhury, S., & Pal, T. (2012). Microstructures and mechanical properties of HPT processed 6063 Al alloy. *Materials Science and Engineering: A*, 558, 525-532.
- Dumitru, F.-D., Higuera-Cobos, O. F., & Cabrera, J. (2014). ZK60 alloy processed by ECAP: Microstructural, physical and mechanical characterization. *Materials Science and Engineering: A*, 594, 32-39.
- Dyakonov, G., Mironov, S., Semenova, I., Valiev, R., & Semiatin, S. (2019). EBSD analysis of grain-refinement mechanisms operating during equal-channel angular pressing of commercial-purity titanium. *Acta materialia*, 173, 174-183.
- Edalati, K. (2019). Review on Recent Advancements in Severe Plastic Deformation of Oxides by High-Pressure Torsion (HPT). *Advanced Engineering Materials*, 21(1), 1800272.
- Edalati, K., Akiba, E., & Horita, Z. (2018). High-pressure torsion for new hydrogen storage materials. *Science and Technology of advanced Materials*, 19(1), 185-193.
- Eftekhari, M., Fata, A., Faraji, G., & Mashhadi, M. (2018). Hot tensile deformation behavior of Mg-Zn-Al magnesium alloy tubes processed by severe plastic deformation. *Journal of Alloys and Compounds*, 742, 442-453.
- El-Danaf, E., Soliman, M., Almajid, A., & El-Rayes, M. (2007). Enhancement of mechanical properties and grain size refinement of commercial purity aluminum 1050 processed by ECAP. *Materials Science and Engineering: A*, 458(1-2), 226-234.
- Elias, C. N., Meyers, M. A., Valiev, R. Z., & Monteiro, S. N. (2013). Ultrafine grained titanium for biomedical applications: An overview of performance. *Journal of Materials Research and Technology*, 2(4), 340-350.
- Estrin, Y., & Vinogradov, A. (2013). Extreme grain refinement by severe plastic deformation: A wealth of challenging science. *Acta materialia*, 61(3), 782-817.

- Faraji, G., & Asadi, P. (2011a). Characterization of AZ91/alumina nanocomposite produced by FSP. *Materials Science and Engineering: A*, 528(6), 2431-2440.
- Faraji, G., Babaei, A., Mosavi Mashhadi, M., & Abrinia, K. (2012a). Parallel tubular channel angular pressing (PTCAP) as a new severe plastic deformation method for cylindrical tubes. *Materials Letters*, 77, 82-85.
- Faraji, G., Besharati, M., Mosavi, M., & Kashanizadeh, H. (2008). Experimental and finite element analysis of parameters in manufacturing of metal bellows. *The International Journal of Advanced Manufacturing Technology*, 38(7-8), 641-648.
- Faraji, G., Ebrahimi, M., & Bushroa, A. (2014a). Ultrasonic assisted tubular channel angular pressing process. *Materials Science and Engineering: A*, 599, 10-15.
- Faraji, G., & Kim, H. (2017). Review of principles and methods of severe plastic deformation for producing ultrafine-grained tubes. *Materials Science and Technology*, 33(8), 905-923.
- Faraji, G., Mashhadi, M., Abrinia, K., & Kim, H. (2012b). Deformation behavior in the tubular channel angular pressing (TCAP) as a noble SPD method for cylindrical tubes. *Applied Physics A*, 107(4), 819-827.
- Faraji, G., Mashhadi, M., Bushroa, A., & Babaei, A. (2013a). TEM analysis and determination of dislocation densities in nanostructured copper tube produced via parallel tubular channel angular pressing process. *Materials Science and Engineering: A*, 563, 193-198.
- Faraji, G., Mashhadi, M., Dizadji, A., & Hamdi, M. (2012c). A numerical and experimental study on tubular channel angular pressing (TCAP) process. *Journal of mechanical science and technology*, 26(11), 3463-3468.
- Faraji, G., Mashhadi, M., & Kim, H. (2011b). Microstructure inhomogeneity in ultra-fine grained bulk AZ91 produced by accumulative back extrusion (ABE). *Materials Science and Engineering: A*, 528(13-14), 4312-4317.
- Faraji, G., & Mosavi Mashhadi, M. (2013b). Plastic deformation analysis in parallel tubular channel angular pressing (PTCAP). *Journal of Advanced Materials and Processing*, 1(4), 23-32.
- Faraji, G., Mosavi Mashhadi, M., Joo, S.-H., & Kim, H. S. (2012d). The role of friction in tubular channel angular pressing. *Review on Advanced Materials Science*, 31(2012), 12-18.
- Faraji, G., Mosavi Mashhadi, M., & Kim, H. S. (2011c). Tubular channel angular pressing (TCAP) as a novel severe plastic deformation method for cylindrical tubes. *Materials Letters*, 65(19-20), 3009-3012.
- Faraji, G., Mosavi Mashhadi, M., & Kim, H. S. (2012e). Deformation behavior in tubular channel angular pressing (TCAP) using triangular and semicircular channels. *Materials transactions*, 53(1), 8-12.

- Faraji, G., Mosavi Mashhadi, M., & Kim, H. S. (2012f). Microstructural evolution of UFG magnesium alloy produced by accumulative back extrusion (ABE). *Materials and Manufacturing Processes*, 27(3), 267-272.
- Faraji, G., Roostae, S., Nosrati, A. S., Kang, J., & Kim, H. (2015). Microstructure and mechanical properties of ultra-fine-grained Al-Mg-Si tubes produced by parallel tubular channel angular pressing process. *Metallurgical and Materials Transactions A*, 46(4), 1805-1813.
- Faraji, G., Yavari, P., Aghdamifar, S., & Mosavi Mashhadi, M. (2014b). Mechanical and microstructural properties of ultra-fine grained AZ91 magnesium alloy tubes processed via multi pass tubular channel angular pressing (TCAP). *Journal of Materials Science & Technology*, 30(2), 134-138.
- Fata, A., Eftekhari, M., Faraji, G., & Mosavi Mashhadi, M. (2018). Enhanced hot tensile ductility of Mg-3Al-1Zn alloy thin-walled tubes processed via a combined severe plastic deformation. *Journal of Materials Engineering and Performance*, 27(5), 2330-2337.
- Fata, A., Faraji, G., Mashhadi, M., & Abdolvand, H. (2017a). Evaluation of hot tensile behavior of fine-grained Mg-9Al-1Zn alloy tube processed by severe plastic deformation. *Transactions of the Indian Institute of Metals*, 70(5), 1369-1376.
- Fata, A., Faraji, G., Mashhadi, M., & Tavakkoli, V. (2016). Hot tensile deformation and fracture behavior of ultrafine-grained AZ31 magnesium alloy processed by severe plastic deformation. *Materials Science and Engineering: A*, 674, 9-17.
- Fata, A., Faraji, G., Mashhadi, M., & Tavakkoli, V. (2017b). Hot deformation behavior of Mg-Zn-Al alloy tube processed by severe plastic deformation. *Archives of Metallurgy and Materials*, 62(1), 159-166.
- Fatemi-Varzaneh, S., Zarei-Hanzaki, A., & Beladi, H. (2007). Dynamic recrystallization in AZ31 magnesium alloy. *Materials Science and Engineering: A*, 456(1-2), 52-57.
- Feng, X.-M., & Ai, T.-T. (2009). Microstructure evolution and mechanical behavior of AZ31 Mg alloy processed by equal-channel angular pressing. *Transactions of Nonferrous Metals Society of China*, 19(2), 293-298.
- Figueiredo, R. B., & Langdon, T. G. (2009). Principles of grain refinement and superplastic flow in magnesium alloys processed by ECAP. *Materials Science and Engineering: A*, 501(1-2), 105-114.
- Figueiredo, R. B., & Langdon, T. G. (2010). Grain refinement and mechanical behavior of a magnesium alloy processed by ECAP. *Journal of Materials Science*, 45(17), 4827-4836.
- Fouad, Y., Mhaede, M., & Wagner, L. (2011). Effects of mechanical surface treatments on fatigue performance of extruded ZK60 alloy. *Fatigue & Fracture of Engineering Materials & Structures*, 34(6), 403-407.

- Furukawa, M., Horita, Z., Nemoto, M., & Langdon, T. G. (2002). The use of severe plastic deformation for microstructural control. *Materials Science and Engineering: A*, 324(1-2), 82-89.
- Gubicza, J. (2012). *Defect structure in nanomaterials*: Elsevier.
- Gubicza, J. (2015). Correlation between processing conditions, lattice defect structure and mechanical performance of ultrafine-grained materials. *Acta Physica Polonica, A*, 128(4), 479-485.
- Gubicza, J., Balogh, L., Hellmig, R. J., Estrin, Y., & Ungár, T. (2005). Dislocation structure and crystallite size in severely deformed copper by X-ray peak profile analysis. *Materials Science and Engineering: A*, 400, 334-338.
- Gunderov, D., Polyakov, A., Semenova, I., Raab, G., Churakova, A., Gimaltdinova, E., Sabirov, I., Segurado, J., Sitdikov, V., & Alexandrov, I. (2013). Evolution of microstructure, macrotexture and mechanical properties of commercially pure Ti during ECAP-conform processing and drawing. *Materials Science and Engineering: A*, 562, 128-136.
- Haghshenas, M., Wood, J., & Klassen, R. (2012). Effect of strain-hardening rate on the grain-to-grain variability of local plastic strain in spin-formed fcc metals. *Materials Science and Engineering: A*, 552, 376-383.
- He, Y., Pan, Q., Qin, Y., Liu, X., Li, W., Chiu, Y., & Chen, J. J. (2010). Microstructure and mechanical properties of ZK60 alloy processed by two-step equal channel angular pressing. *Journal of Alloys and Compounds*, 492(1-2), 605-610.
- Hilšer, O., Rusz, S., Szkandera, P., Čížek, L., Kraus, M., Džugan, J., & Maziarz, W. (2018). Study of the microstructure, tensile properties and hardness of AZ61 magnesium alloy subjected to severe plastic deformation. *Metals*, 8(10), 776.
- Hirsch, J., & Al-Samman, T. (2013). Superior light metals by texture engineering: Optimized aluminum and magnesium alloys for automotive applications. *Acta materialia*, 61(3), 818-843.
- Hirsch, J., Lücke, K., & Hatherly, M. (1988). Overview no. 76: Mechanism of deformation and development of rolling textures in polycrystalline fcc metals—III. The influence of slip inhomogeneities and twinning. *Acta Metallurgica*, 36(11), 2905-2927.
- Hossein Nedjad, S., Meidani, H., & Nili Ahmadabadi, M. (2008). Effect of equal channel angular pressing on the microstructure of a semisolid aluminum alloy. *Materials Science and Engineering: A*, 475(1-2), 224-228.
- Huang, C. X., Hu, W., Wang, Q., Wang, C., Yang, G., & Zhu, Y. (2015). An ideal ultrafine-grained structure for high strength and high ductility. *Materials Research Letters*, 3(2), 88-94.
- Huang, Y., & Prangnell, P. (2007). Continuous frictional angular extrusion and its application in the production of ultrafine-grained sheet metals. *Scripta Materialia*, 56(5), 333-336.

- Jafarlou, D., Zalnezhad, E., Hassan, M., Ezazi, M., Mardi, N., Hamouda, A., Hamdi, M., & Yoon, G. H. (2016). Severe plastic deformation of tubular AA 6061 via equal channel angular pressing. *Materials & Design*, *90*, 1124-1135.
- Jamili, A., Zarei-Hanzaki, A., Abedi, H., Minárik, P., & Soltani, R. (2017). The microstructure, texture, and room temperature mechanical properties of friction stir processed Mg-Y-Nd alloy. *Materials Science and Engineering: A*, *690*, 244-253.
- Javdani, A., Pouyafar, V., Ameli, A., & Volinsky, A. A. (2016). Blended powder semisolid forming of Al7075/Al<sub>2</sub>O<sub>3</sub> composites: Investigation of microstructure and mechanical properties. *Materials & Design*, *109*, 57-67.
- Javidikia, M., & Hashemi, R. (2017). Mechanical anisotropy in ultra-fine grained aluminium tubes processed by parallel-tubular-channel angular pressing. *Materials Science and Technology*, *33*(18), 2265-2273.
- Jin, L., Lin, D., Mao, D., Zeng, X., & Ding, W. (2005). Mechanical properties and microstructure of AZ31 Mg alloy processed by two-step equal channel angular extrusion. *Materials Letters*, *59*(18), 2267-2270.
- Jining, Q., Di, Z., Guoding, Z., & Lee, J.-C. (2005). Effect of temperature on texture formation of 6061 aluminum sheet in equal-channel angular pressing. *Materials Science and Engineering: A*, *408*(1-2), 79-84.
- Kang, S.-H., Lee, Y., & Lee, J. (2008). Effect of grain refinement of magnesium alloy AZ31 by severe plastic deformation on material characteristics. *Journal of Materials Processing Technology*, *201*(1-3), 436-440.
- Karimzadeh, A., & Ayatollahi, M. (2014). Mechanical properties of biomaterials determined by nano-indentation and nano-scratch tests *Nanomechanical Analysis of High Performance Materials* (pp. 189-207): Springer.
- Kawasaki, M., Figueiredo, R. B., & Langdon, T. G. (2012). Twenty-five years of severe plastic deformation: recent developments in evaluating the degree of homogeneity through the thickness of disks processed by high-pressure torsion. *Journal of Materials Science*, *47*(22), 7719-7725.
- Kawasaki, M., Horita, Z., & Langdon, T. G. (2009). Microstructural evolution in high purity aluminum processed by ECAP. *Materials Science and Engineering: A*, *524*(1-2), 143-150.
- Kheradmand, N., Barnoush, A., & Vehoff, H. (2010). *Investigation of the role of grain boundary on the mechanical properties of metals*. Paper presented at the Journal of Physics: Conference Series.
- Kim, H. S. (2002). Finite element analysis of deformation behaviour of metals during equal channel multi-angular pressing. *Materials Science and Engineering: A*, *328*(1-2), 317-323.

- Kim, H. S., Seo, M. H., & Hong, S. I. (2001). Plastic deformation analysis of metals during equal channel angular pressing. *Journal of Materials Processing Technology*, 113(1-3), 622-626.
- Kim, W. J., & Sa, Y. (2006). Micro-extrusion of ECAP processed magnesium alloy for production of high strength magnesium micro-gears. *Scripta Materialia*, 54(7), 1391-1395.
- Kleiner, S., Beffort, O., & Uggowitzer, P. J. (2004). Microstructure evolution during reheating of an extruded Mg–Al–Zn alloy into the semisolid state. *Scripta Materialia*, 51(5), 405-410.
- Kruzic, J., Kim, D., Koester, K., & Ritchie, R. (2009). Indentation techniques for evaluating the fracture toughness of biomaterials and hard tissues. *Journal of the Mechanical Behavior of Biomedical Materials*, 2(4), 384-395.
- Langdon, T. G. (2007). The processing of ultrafine-grained materials through the application of severe plastic deformation. *Journal of Materials Science*, 42(10), 3388-3397.
- Langford, G., & Cohen, M. (1976). Fracture and flow in solids. *Trans. ASM*, 7, 623-632.
- Latysh, V., Krallics, G., Alexandrov, I., & Fodor, A. (2006). Application of bulk nanostructured materials in medicine. *Current Applied Physics*, 6(2), 262-266.
- Lee, S. H., Saito, Y., Tsuji, N., Utsunomiya, H., & Sakai, T. (2002). Role of shear strain in ultragrain refinement by accumulative roll-bonding (ARB) process. *Scripta Materialia*, 46(4), 281-285.
- Lee, Y.-K., Jin, J., & Ma, Y. (2007). Transformation-induced extraordinary ductility in an ultrafine-grained alloy with nanosized precipitates. *Scripta Materialia*, 57(8), 707-710.
- Levinson, A., Mishra, R. K., Doherty, R. D., & Kalidindi, S. R. (2013). Influence of deformation twinning on static annealing of AZ31 Mg alloy. *Acta materialia*, 61(16), 5966-5978.
- Lin, Huang, J., & Langdon, T. (2005). Relationship between texture and low temperature superplasticity in an extruded AZ31 Mg alloy processed by ECAP. *Materials Science and Engineering: A*, 402(1-2), 250-257.
- Lin, Y., Zhang, Y., Xiong, B., & Lavernia, E. J. (2012). Achieving high tensile elongation in an ultra-fine grained Al alloy via low dislocation density. *Materials Letters*, 82, 233-236.
- Liu, W., Zhang, J., Zhang, Z., Wang, D., Xu, C., Zong, X., & Nie, K. (2017). High-strength Mg<sub>95</sub>Y<sub>3</sub>Zn<sub>1</sub>Ni<sub>1</sub> alloy with LPSO structure processed by hot rolling. *Materials and Manufacturing Processes*, 32(1), 62-68.
- Liu, W. C., Dong, J., Zhang, P., Yao, Z., Zhai, C., & Ding, W. (2009). High cycle fatigue behavior of as-extruded ZK60 magnesium alloy. *Journal of Materials Science*, 44(11), 2916-2924.

- Mabuchi, M., Iwasaki, H., Yanase, K., & Higashi, K. (1997). Low temperature superplasticity in an AZ91 magnesium alloy processed by ECAE. *Scripta Materialia*, 36(6), 681-686.
- Mahmoodian, R., Annuar, N. S. M., Faraji, G., Bahar, N. D., Razak, B. A., & Sparham, M. (2019). Severe plastic deformation of commercial pure titanium (CP-Ti) for biomedical applications: A brief review. *The Journal of The Minerals, Metals & Materials Society*, 71(1), 256-263.
- Maki, K., Ito, Y., Matsunaga, H., & Mori, H. (2013). Solid-solution copper alloys with high strength and high electrical conductivity. *Scripta Materialia*, 68(10), 777-780.
- Mesbah, M., Fadaeifard, F., Karimzadeh, A., Nasiri-Tabrizi, B., Rafieerad, A., Faraji, G., & Bushroa, A. (2016). Nano-mechanical properties and microstructure of UFG brass tubes processed by parallel tubular channel angular pressing. *Metals and Materials International*, 22(6), 1098-1107.
- Mesbah, M., Faraji, G., & Bushroa, A. (2014). Characterization of nanostructured pure aluminum tubes produced by tubular channel angular pressing (TCAP). *Materials Science and Engineering: A*, 590, 289-294.
- Meshkabadi, R., Faraji, G., Javdani, A., Fata, A., & Pouyafar, V. (2017). Microstructure and homogeneity of semi-solid 7075 aluminum tubes processed by parallel tubular channel angular pressing. *Metals and Materials International*, 23(5), 1019-1028.
- Mohammadi, A. S., Mashhadi, M. M., & Faraji, G. (2015). The effect of pass numbers over microstructure and mechanical properties of magnesium alloy of AZ31C in the tubular channel angular pressing (TCAP) at temperature of 300° C. *Modares Mechanical Engineering*, 15(1), 126-130.
- Moharrami, N., & Bull, S. (2014). A comparison of nanoindentation pile-up in bulk materials and thin films. *Thin Solid Films*, 572, 189-199.
- Mohebbi, M., & Akbarzadeh, A. (2010). Accumulative spin-bonding (ASB) as a novel SPD process for fabrication of nanostructured tubes. *Materials Science and Engineering: A*, 528(1), 180-188.
- Mostaed, E., Hashempour, M., Fabrizio, A., Dellasega, D., Bestetti, M., Bonollo, F., & Vedani, M. (2014). Microstructure, texture evolution, mechanical properties and corrosion behavior of ECAP processed ZK60 magnesium alloy for biodegradable applications. *Journal of the Mechanical Behavior of Biomedical Materials*, 37, 307-322.
- Müller, J., Janeček, M., Yi, S., Čížek, J., & Wagner, L. (2009). Effect of equal channel angular pressing on microstructure, texture, and high-cycle fatigue performance of wrought magnesium alloys. *International Journal of Materials Research*, 100(6), 838-842.
- Murashkin, M., Medvedev, A., Kazykhanov, V., Krokhin, A., Raab, G., Enikeev, N., & Valiev, R. (2015). Enhanced mechanical properties and electrical conductivity in

- ultrafine-grained Al 6101 alloy processed via ECAP-conform. *Metals*, 5(4), 2148-2164.
- Nagasekhar, A., Tick-Hon, Y., & Seow, H. (2007). Deformation behavior and strain homogeneity in equal channel angular extrusion/pressing. *Journal of Materials Processing Technology*, 192, 449-452.
- Nasiri-Tabrizi, B. (2014). Thermal treatment effect on structural features of mechano-synthesized fluorapatite-titania nanocomposite: A comparative study. *Journal of Advanced Ceramics*, 3(1), 31-42.
- Nový, F., Janeček, M., Škorík, V., Müller, J., & Wagner, L. (2009). Very high cycle fatigue behaviour of as-extruded AZ31, AZ80, and ZK60 magnesium alloys. *International Journal of Materials Research*, 100(3), 288-291.
- Oliver, W. C., & Pharr, G. M. (1992). An improved technique for determining hardness and elastic modulus using load and displacement sensing indentation experiments. *Journal of Materials Research*, 7(6), 1564-1583.
- Orlov, D., Raab, G., Lamark, T. T., Popov, M., & Estrin, Y. (2011). Improvement of mechanical properties of magnesium alloy ZK60 by integrated extrusion and equal channel angular pressing. *Acta materialia*, 59(1), 375-385.
- Pérez, C. L. (2004). On the correct selection of the channel die in ECAP processes. *Scripta Materialia*, 50(3), 387-393.
- Phaniraj, M., Prasad, M., & Chokshi, A. (2007). Grain-size distribution effects in plastic flow and failure. *Materials Science and Engineering: A*, 463(1-2), 231-237.
- Pineau, A. (2015). Crossing grain boundaries in metals by slip bands, cleavage and fatigue cracks. *Philosophical Transactions of the Royal Society A: Mathematical, Physical and Engineering Sciences*, 373(2038), 20140131.
- Raju, K. S., Krishna, M. G., Padmanabhan, K., Muraleedharan, K., Gurao, N., & Wilde, G. (2008). Grain size and grain boundary character distribution in ultra-fine grained (ECAP) nickel. *Materials Science and Engineering: A*, 491(1-2), 1-7.
- Reihanian, M., Ebrahimi, R., Moshksar, M., Terada, D., & Tsuji, N. (2008a). Microstructure quantification and correlation with flow stress of ultrafine grained commercially pure Al fabricated by equal channel angular pressing (ECAP). *Materials Characterization*, 59(9), 1312-1323.
- Reihanian, M., Ebrahimi, R., Tsuji, N., & Moshksar, M. (2008b). Analysis of the mechanical properties and deformation behavior of nanostructured commercially pure Al processed by equal channel angular pressing (ECAP). *Materials Science and Engineering: A*, 473(1-2), 189-194.
- Reshadi, F., Faraji, G., Aghdamifar, S., Yavari, P., & Mashhadi, M. (2015). Deformation speed and temperature effects on magnesium AZ91 during tubular channel angular pressing. *Materials Science and Technology*, 31(15), 1879-1885.

- Rezaei, M. R., Toroghinejad, M. R., & Ashrafizadeh, F. (2011). Production of nano-grained structure in 6061 aluminum alloy strip by accumulative roll bonding. *Materials Science and Engineering: A*, 529, 442-446.
- Sabbaghianrad, S., Wongsan-Ngam, J., Kawasaki, M., & Langdon, T. G. (2014). An examination of the saturation microstructures achieved in ultrafine-grained metals processed by high-pressure torsion. *Journal of Materials Research and Technology*, 3(4), 319-326.
- Sabirov, I., Murashkin, M. Y., & Valiev, R. (2013). Nanostructured aluminium alloys produced by severe plastic deformation: New horizons in development. *Materials Science and Engineering: A*, 560, 1-24.
- Saito, Y., Utsunomiya, H., Tsuji, N., & Sakai, T. (1999). Novel ultra-high straining process for bulk materials—development of the accumulative roll-bonding (ARB) process. *Acta materialia*, 47(2), 579-583.
- Sakai, T., & Miura, H. (2011). Mechanical properties of fine-grained magnesium alloys processed by severe plastic forging. In F. Czerwinski (Ed.), *Magnesium alloys—design, processing and properties* (pp. 219-244). Rijeka, Croatia: InTech.
- Salandari-Rabori, A., Zarei-Hanzaki, A., Abedi, H., Lecomte, J., & Khatami-Hamedani, H. (2018). Micro and macro texture evolution during multi-axial forging of a WE43 magnesium alloy. *Journal of Alloys and Compounds*, 739, 249-259.
- Salandari-Rabori, A., Zarei-Hanzaki, A., Fatemi, S., Ghambari, M., & Moghaddam, M. (2017). Microstructure and superior mechanical properties of a multi-axially forged WE magnesium alloy. *Journal of Alloys and Compounds*, 693, 406-413.
- Salimyanfard, F., Toroghinejad, M. R., Ashrafizadeh, F., & Jafari, M. (2011). EBSD analysis of nano-structured copper processed by ECAP. *Materials Science and Engineering: A*, 528(16-17), 5348-5355.
- Schwartz, A. J., Kumar, M., Adams, B. L., & Field, D. P. (2000). *Electron backscatter diffraction in materials science*: Springer.
- Segal, V. (2002). Severe plastic deformation: Simple shear versus pure shear. *Materials Science and Engineering: A*, 338(1-2), 331-344.
- Segal, V. (2018). Modes and processes of severe plastic deformation (SPD). *Materials*, 11(7), 1175.
- Shahzad, M., Eliezer, D., Gan, W. M., Yi, S. B., & Wagner, L. (2007). *Influence of extrusion temperature on microstructure, texture and fatigue performance of AZ80 and ZK60 magnesium alloys*. Paper presented at the Materials Science Forum.
- Shahzad, M., & Wagner, L. (2009). Thermo-mechanical methods for improving fatigue performance of wrought magnesium alloys *Engineering Against Fracture* (pp. 249-257): Springer.

- Shapourgan, O., & Faraji, G. (2016). Rubber pad tube straining as a new severe plastic deformation method for thin-walled cylindrical tubes. *Proceedings of the Institution of Mechanical Engineers, Part B: Journal of Engineering Manufacture*, 230(10), 1845-1854.
- Shin, D. H., Kim, I., Kim, J., & Zhu, Y. T. (2002). Shear strain accommodation during severe plastic deformation of titanium using equal channel angular pressing. *Materials Science and Engineering: A*, 334(1-2), 239-245.
- Siddiq, A., & El Sayed, T. (2012). Ultrasonic-assisted manufacturing processes: Variational model and numerical simulations. *Ultrasonics*, 52(4), 521-529.
- Sitdikov, O., Sakai, T., Avtokratova, E., Kaibyshev, R., Tsuzaki, K., & Watanabe, Y. (2008). Microstructure behavior of Al–Mg–Sc alloy processed by ECAP at elevated temperature. *Acta materialia*, 56(4), 821-834.
- Sun, F., & Froes, F. S. (2002). Synthesis and characterization of mechanical-alloyed Ti–xMg alloys. *Journal of Alloys and Compounds*, 340(1-2), 220-225.
- Sundeev, R., Glezer, A., & Shalimova, A. (2016). Are the abilities of crystalline alloys to amorphization upon melt quenching and severe plastic deformation identical or different? *Materials Letters*, 175, 72-74.
- Taban, E., Gould, J. E., & Lippold, J. C. (2010). Dissimilar friction welding of 6061-T6 aluminum and AISI 1018 steel: Properties and microstructural characterization. *Materials & Design*, 31(5), 2305-2311.
- Tan, J., & Tan, M. (2003). Dynamic continuous recrystallization characteristics in two stage deformation of Mg–3Al–1Zn alloy sheet. *Materials Science and Engineering: A*, 339(1-2), 124-132.
- Tavakkoli, V., Afrasiab, M., Faraji, G., & Mashhadi, M. (2015). Severe mechanical anisotropy of high-strength ultrafine grained Cu–Zn tubes processed by parallel tubular channel angular pressing (PTCAP). *Materials Science and Engineering: A*, 625, 50-55.
- Tavakkoli, V., Faraji, G., Afrasiab, M., & Mashhadi, M. (2016). Severe plastic deformation of nanostructured Cu-30% Zn tubes at increased temperatures. *International Journal of Advanced Design and Manufacturing Technology*, 9(3), 85-91.
- Taylor, G. I. (1938). Plastic strain in metals. *J. Inst. Metals*, 62, 307-324.
- Tham, Y., Fu, M., Hng, H., Pei, Q., & Lim, K. (2007). Microstructure and properties of Al-6061 alloy by equal channel angular extrusion for 16 passes. *Materials and Manufacturing Processes*, 22(7-8), 819-824.
- Torabzadeh, H., Faraji, G., & Zalnezhad, E. (2016). Cyclic flaring and sinking (CFS) as a new severe plastic deformation method for thin-walled cylindrical tubes. *Transactions of the Indian Institute of Metals*, 69(6), 1217-1222.

- Torkian, A., Faraji, G., & Karimpour, M. (2018). Mechanical properties and microstructure of WE43 Mg alloy processed by warm ECAP followed by extrusion. *Archives of Metallurgy and Materials*, 63(3), 1093--1100.
- Tóth, L., Arzaghi, M., Fundenberger, J., Beausir, B., Bouaziz, O., & Arruffat-Massion, R. (2009). Severe plastic deformation of metals by high-pressure tube twisting. *Scripta Materialia*, 60(3), 175-177.
- Toth, L., & Gu, C. (2014). Ultrafine-grain metals by severe plastic deformation. *Materials Characterization*, 92, 1-14.
- Tyagi, A., & Banerjee, S. (2017). *Materials under extreme conditions: Recent trends and future prospects*: Elsevier.
- Ungár, T., Gubicza, J., Ribárik, G., & Borbély, A. (2001). Crystallite size distribution and dislocation structure determined by diffraction profile analysis: principles and practical application to cubic and hexagonal crystals. *Journal of applied crystallography*, 34(3), 298-310.
- Valiev, R. Z. (2004). Nanostructuring of metals by severe plastic deformation for advanced properties. *Nature materials*, 3(8), 511–516.
- Valiev, R. Z., Alexandrov, I., Zhu, Y., & Lowe, T. (2002). Paradox of strength and ductility in metals processed by severe plastic deformation. *Journal of Materials Research*, 17(1), 5-8.
- Valiev, R. Z., & Langdon, T. G. (2006). Principles of equal-channel angular pressing as a processing tool for grain refinement. *Progress in materials science*, 51(7), 881-981.
- Vasil'ev, L., Lomaev, I., & Elsukov, E. (2006). On the analysis of the mechanisms of the strain-induced dissolution of phases in metals. *The Physics of Metals and Metallography*, 102(2), 186-197.
- Verlinden, B. (2018). Severe plastic deformation of metals. *Metallurgical and Materials Engineering*.
- Vinogradov, A. (2017). Effect of severe plastic deformation on tensile and fatigue properties of fine-grained magnesium alloy ZK60. *Journal of Materials Research*, 32(23), 4362-4374.
- Vinogradov, A., Orlov, D., & Estrin, Y. (2012). Improvement of fatigue strength of a Mg–Zn–Zr alloy by integrated extrusion and equal-channel angular pressing. *Scripta Materialia*, 67(2), 209-212.
- Wang, C., Li, F., Wang, L., & Qiao, H. (2012). Review on modified and novel techniques of severe plastic deformation. *Science China Technological Sciences*, 55(9), 2377-2390.
- Wang, Y., Chen, M., Zhou, F., & Ma, E. (2002). High tensile ductility in a nanostructured metal. *Nature*, 419(6910), 912-915.

- Wang, Y., Jiao, T., & Ma, E. (2003). Dynamic processes for nanostructure development in Cu after severe cryogenic rolling deformation. *Materials transactions*, 44(10), 1926-1934.
- Wei, Q., Cheng, S., Ramesh, K., & Ma, E. (2004). Effect of nanocrystalline and ultrafine grain sizes on the strain rate sensitivity and activation volume: Fcc versus bcc metals. *Materials Science and Engineering: A*, 381(1-2), 71-79.
- Williamson, G., & Hall, W. (1953). X-ray line broadening from filed aluminium and wolfram. *Acta Metallurgica*, 1(1), 22-31.
- Xia, Q., Xiao, G., Long, H., Cheng, X., & Yang, B. (2014). A study of manufacturing tubes with nano/ultrafine grain structure by stagger spinning. *Materials & Design*, 59, 516-523.
- Xu, Wang, X., Shirooyeh, M., Xing, G., Shan, D., Guo, B., & Langdon, T. G. (2015). Microhardness, microstructure and tensile behavior of an AZ31 magnesium alloy processed by high-pressure torsion. *Journal of Materials Science*, 50(22), 7424-7436.
- Xu, C., Furukawa, M., Horita, Z., & Langdon, T. G. (2003). Using ECAP to achieve grain refinement, precipitate fragmentation and high strain rate superplasticity in a spray-cast aluminum alloy. *Acta materialia*, 51(20), 6139-6149.
- Xu, S., Zhao, G., Luan, Y., & Guan, Y. (2006). Numerical studies on processing routes and deformation mechanism of multi-pass equal channel angular pressing processes. *Journal of Materials Processing Technology*, 176(1-3), 251-259.
- Xu, S., Zhao, G., Ren, G., & Ma, X. (2008). Numerical simulation and experimental investigation of pure copper deformation behavior for equal channel angular pressing/extrusion process. *Computational materials science*, 44(2), 247-252.
- Xu, S. W., Matsumoto, N., Kamado, S., Honma, T., & Kojima, Y. (2009). Effect of Mg<sub>17</sub>Al<sub>12</sub> precipitates on the microstructural changes and mechanical properties of hot compressed AZ91 magnesium alloy. *Materials Science and Engineering: A*, 523(1-2), 47-52.
- Yadav, D., & Bauri, R. (2012). Effect of friction stir processing on microstructure and mechanical properties of aluminium. *Materials Science and Engineering: A*, 539, 85-92.
- Yoon, S. C., Horita, Z., & Kim, H. S. (2008). Finite element analysis of plastic deformation behavior during high pressure torsion processing. *Journal of Materials Processing Technology*, 201(1-3), 32-36.
- Zakiyuddin, A., & Lee, K. (2018). Microstructure and corrosion behaviors of biodegradable Mg-1Zn-1Zr-xSn alloys prepared by powder-in-tube rolling. *Archives of Metallurgy and Materials*, 63(3), 1467-1471.
- Zhao, Y., Bingert, J., Zhu, Y., Liao, X., Valiev, R., Horita, Z., Langdon, T., Zhou, Y., & Lavernia, E. (2008). Tougher ultrafine grain Cu via high-angle grain boundaries and low dislocation density. *Applied Physics Letters*, 92(8), 081903.

- Zhao, Y., Bingert, J. F., Liao, X. Z., Cui, B. Z., Han, K., Sergueeva, A. V., Mukherjee, A. K., Valiev, R. Z., Langdon, T. G., & Zhu, Y. T. (2006). Simultaneously increasing the ductility and strength of ultra-fine-grained pure copper. *Advanced Materials*, 18(22), 2949-2953.
- Zhao, Y., Liao, X., Zhu, Y., Horita, Z., & Langdon, T. (2005). Influence of stacking fault energy on nanostructure formation under high pressure torsion. *Materials Science and Engineering: A*, 410, 188-193.
- Zhao, Y., Zhu, Y., Liao, X., Horita, Z., & Langdon, T. G. (2007). Influence of stacking fault energy on the minimum grain size achieved in severe plastic deformation. *Materials Science and Engineering: A*, 463(1-2), 22-26.
- Zhilyaev, A. P., & Langdon, T. G. (2008). Using high-pressure torsion for metal processing: Fundamentals and applications. *Progress in materials science*, 53(6), 893-979.
- Zhu, Y. T., & Liao, X. (2004). Nanostructured metals: Retaining ductility. *Nature materials*, 3(6), 351-352.